LASER-INDUCED MILLISECOND HEATING OF POLYMERS AND SMALL MOLECULES FOR PATTERN DEVELOPMENT

A Dissertation

Presented to the Faculty of the Graduate School

of Cornell University

in Partial Fulfillment of the Requirements for the Degree of

Doctor of Philosophy

by

Byungki Jung

January 2014

LASER-INDUCED MILLISECOND HEATING OF POLYMERS AND SMALL MOLECULES FOR PATTERN DEVELOPMENT

Byungki Jung, Ph.D.

Cornell University 2014

Microlithography and laser spike annealing (LSA) are key techniques that have enabled continued dimension scaling of transistors used in the semiconductor industry. As minimum feature sizes reach sub-20 nm scale in patterning, control of chemical reactions and their kinetics for a given lithographic material becomes critical for all thermally-activated processes. For example, current chemically amplified resist (CAR) systems require a post-exposure bake (PEB) where thermally-activated side-group cleavage reactions and acid-catalyst diffusion compete to control both pattern resolution and line edge definition.

The use of LSA has been explored in this work as a potential PEB process, showing promise for multiple metrics of CAR system performance. This work explores the behavior of organic and small molecules under millisecond time frame laser-induced heating using far-infrared CO_2 laser (λ = 10.6 μm) and near-infrared laser diode (λ = 980 nm) sources. To explore LSA heating of polymers, thin-film platinum resistors were fabricated and used to directly measure temperature profiles during LSA with high spatial and temporal resolution. Measured resistance changes were calibrated to absolute temperatures using melting points of silicon and thin-film gold dots. Effective substrate temperatures were obtained for dwell times ranging from 0.25 to 10 ms under both CO_2 and diode laser irradiation. In addition, spatially dependent thermal profiles were obtained in sub-millisecond time frames at high spatial resolutions up to 20 μm.

LSA was used to heat thermally sensitive resist polymers at temperatures beyond their conventional limits in millisecond time frames. Due to the five orders of magnitude decrease in time from conventional heating duration, these organic systems extended their thermal stabilities by up to 800 °C. Lithographic patterning using LSA as a PEB was explored under both deep UV (DUV) and extreme UV (EUV) exposures. Compared to conventional hot-plate PEB, high resolution (up to 50 nm lines/spaces) patterns were achieved at up to 30 % lower UV exposure doses (sensitivity) by accelerating the reaction kinetics at higher temperatures. Under these same conditions, the pattern roughness was reduced 25 % by minimizing the heating duration.

The chemical reaction kinetics and pathways of a model resist system with a methyl adamantyl side-group were extensively studied over five orders of magnitude in heating duration, exhibiting non-Arrhenius behavior. The side-group cleavage kinetics were measured to follow first order at high temperatures associated with millisecond heating, while a more complex power law behavior was observed for seconds time frame heating near the polymer's glass transition. The responsible chemical change, affecting the active catalyst concentration during heating, was identified and mathematically modeled to explain the kinetic shift while providing fundamental understanding necessary for improving patterning performance.

An alternative use of the laser-induced heating was demonstrated for controlling the pattern roughness by hardbaking fully developed resist profiles at peak temperatures between 295-450 °C for 500 μs. Due to polymer flow above the glass transition temperature, surface and edge smoothing up to 30 % with a <1 nm change in pattern dimension was observed.

Laser spike annealing was also used to investigate the nucleation and

growth kinetics of amorphous silicon (a-Si) at temperatures above 850 °C for sub-millisecond time frames. An explosive crystallization of a-Si was observed containing a mix of fine-grained and large-grained polycrystalline phases, along with Si propagation in its liquid state to create a feather-like threads spanning over 100 μm orthogonal to the scan direction.

Results from this work highlight the utility of laser heating technique to characterize reaction kinetics over a wide range of temperature and time, while identifying key kinetic changes and the underlying mechanisms to gain fundamental understanding. Combined with existing methods to characterize material properties, LSA is a powerful technique for investigating reaction kinetics at high temperatures on millisecond time frames, not only for conventional semiconductor materials such as Si but also for thermally sensitive organic systems.

BIOGRAPHICAL SKETCH

Byungki Jung was born on February 1, 1984 in Seoul, Republic of Korea (South). He and his sister came to the United States in 1995 for education. At the age of 17, Byungki became the head of household when his mother returned home to South Korea. He spent his middle and high school years at Gill St. Bernard's School in Gladstone, NJ before transitioning to Ithaca, NY for his undergraduate enrollment at Cornell University in 2003. After completing his Sophomore year at Cornell University, he served in the Republic of Korea Army for two years and was discharged after fulfilling his service requirements on July 2007. He returned to Cornell as a Junior and gained his first research experience working with Professor George Malliaras. He obtained Bachelor's of Science degree in Materials Science and Engineering in May 2009. He was fortunate to meet Professor Michael Thompson and join his research group at the end of his Junior year, where he was inspired and motivated to research in pursuit of a Ph.D. degree. During the second year of his graduate school, Byungki met his lovely wife and married in June 2011. While performing his research at Cornell in collaboration with Intel Corporation and Semiconductor Research Corporation, Byungki interned with GLOBALFOUNDRIES in Albany, NY and IBM Corporation in Yorktown Heights, NY, where he gained industrial perspective and research applications. He decided to pursue his career in the semiconductor research and development by joining Intel Corporation upon graduation.

Dedicated to my wife and parents

ACKNOWLEDGEMENTS

This thesis would not have been possible without innumerable encouragement and support from family, colleagues, and friends. I sincerely thank my wife, Jina, for her patience and understanding my responsibilities as a graduate student. I am truly privileged to have been educated in the United States with sacrifices made by my parents, who I always keep in my thoughts. I also thank my sister, Jinie, for her love and encouragement.

I am truly fortunate to have met Professor Michael Thompson during my undergraduate years at Cornell. His work and dedication towards students are still an inspiration and taught me patience beyond military discipline. I am sincerely grateful to Professor Christopher Ober for his guidance in research and future directions, while allowing me to take part in his group. I will never forget the years spent in the Thompson and the Ober Group.

Throughout my graduate career, guidances in both organic and physical chemistries were required, and Professors William Dichtel and Ulrich Wiesner were always open for helpful discussions and suggestions. Their teachings made me a better student and a researcher. I am especially thankful to Professor Dichtel for his guidance in research while serving on my thesis committee.

I give special thanks to Michael Willemann, Jing Sha, and Shahyaan Desai for being great mentors and friends, where their guidance jump-started my graduate research. I am fortunate and thankful to Professor George Malliaras for his patience and for introducing me to academic research during my undergraduate years. Manish Chandhok and Todd Younkin from Intel Corporation are gratefully acknowledged for their mentoring and guidance on my graduate research and I am grateful to Intel Corporation and Semiconductor Research Corporation for their financial support.

All former and present CNF, CCMR, NBTC, and Cornell NMR facility members are gratefully acknowledged including Garry Bordonaro, John Treichler, Michael Skvarla, Noah Clay, Rob Ilic, Paul Pelletier, Jerry Drumheller, Meredith Metzler, Aaron Windsor; Paul Bishop, John Hunt, Philip Carubia; Penny Burke, Teresa Porri; Ivan Keresztes, and Anthony Condo. Working with them to solve technical problems on cutting-edge tools for research was a privilege for me.

Internships with GLOBALFOUNDRIES and IBM Corporation improved the knowledge required for my graduate research. I would like to thank my mentors, Gerard Schmid, Kenji Yoshimoto, Markus Brink, and Michael Guillorn, for their teachings and helpful discussions beyond academic environment.

It was my absolute pleasure to work and spend time with my Cornell colleagues, especially the Ober and Thompson Group members. Among them, Krishna Iyengar, Jing Jiang, Alan Jacobs, Pratima Satish, Florencia Paredes, Andrew Hurst, Dong Chen, Megan Hill, and Kwan Wee Tan are acknowledged for their current and past involvements on the laser project. I would also like to acknowledge my brothers at Phi Gamma Delta and my friends and faculty members including Peter and Randi Schmidt at Gill St. Bernard's School, who encouraged and supported my continued study at Cornell in pursuit of a Ph.D. degree. I will truly miss everyone.

I sincerely thank God for his blessing, whose immeasurable glory and power surpasses all science and human knowledge. I also thank Father Joseph Marcoux and parishioners at St. Catherine of Siena for guidance in spiritual faith over the years.

Finally, I thank you for your time to read this thesis and hope it presents help in your research.

CONTENTS

LIST OF TABLES

LIST OF FIGURES

CHAPTER 1

INTRODUCTION

1.1 Microlithography

1.1.1 Overview

Technological advancements and challenges that the microelectronics industry have overcome over the past four decades are astounding. Computers, once available as a computational tool only for engineers and scientists, have become a common household tool regardless of occupation or age, with the cost and the performance of semiconductor devices improving on a regular basis. Gordon E. Moore, a co-founder of Intel Corporation, recognized the rapid progress in 1965 and the trend, shown in Figure 1.1, is now commonly referred to as the "Moore's law." Moore's law today drives the scaling challenges in the patterning industry by promoting increase in transistor density per unit area on a regular basis.

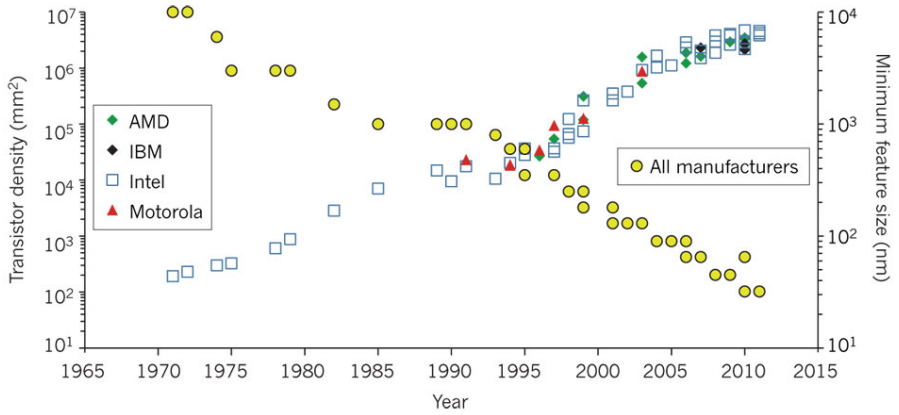

Figure 1.1: "Moore's Law" showing a linear trend in transistor density due to decreasing feature sizes over the past four decades. Reprinted with permission from [1]. Copyright 2011 Nature.

All semiconductor devices are fabricated using a patterning technique called microlithography, which has been a key driving force behind Moore's Law. The current generation of semiconductor devices uses a microlithography technique called photolithography, where a radiation sensitive polymer (resists) is patterned and used as protective template during the etching of underlying layers or devices as shown in Figure 1.2.

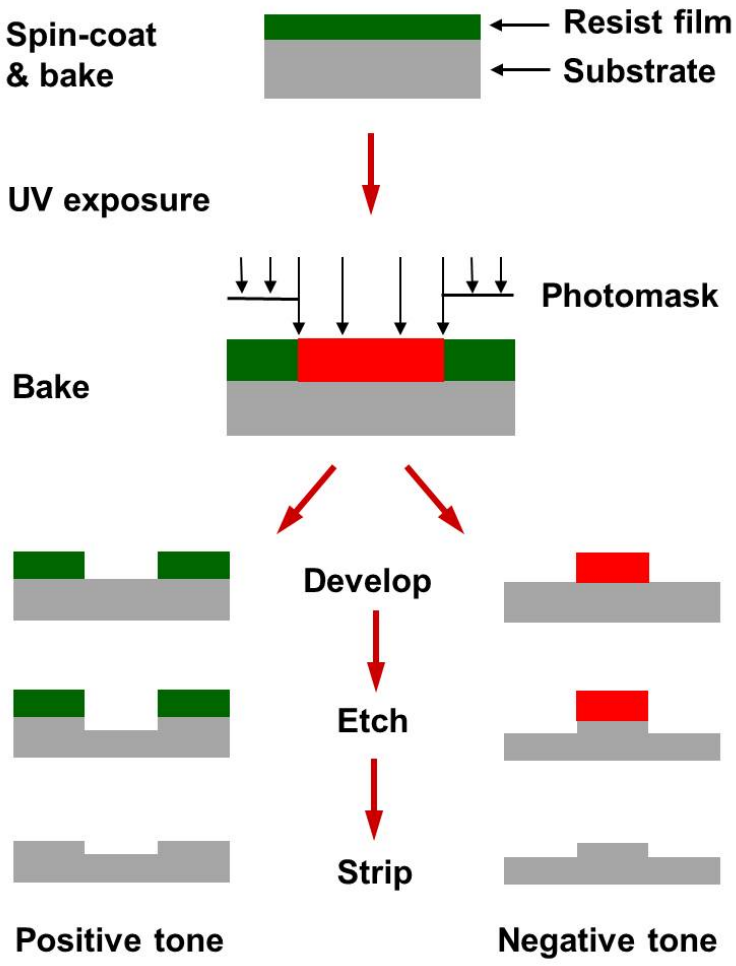

Figure 1.2: Typical lithographic imaging process.

Resist materials must meet demanding requirements to deliver the required features with minimal defects, a challenge that is becoming more stringent as pattern dimensions approach 10 nm scales. Requirements include high resolu-

tion, high sensitivity to UV exposure, high contrast, good etch resistance, high thermal stability, good solubility in a solvent, low cost, and good adhesion to various substrates [2, 3]. For example, one of the commonly used parameters for resist evaluation is the pattern contrast of the resist. Sensitivity curves (or contrast curves), schematically drawn for positive and negative resists in Figure 1.3, are often used to evaluate resists' patterning performances and their chemical reaction kinetics [2].

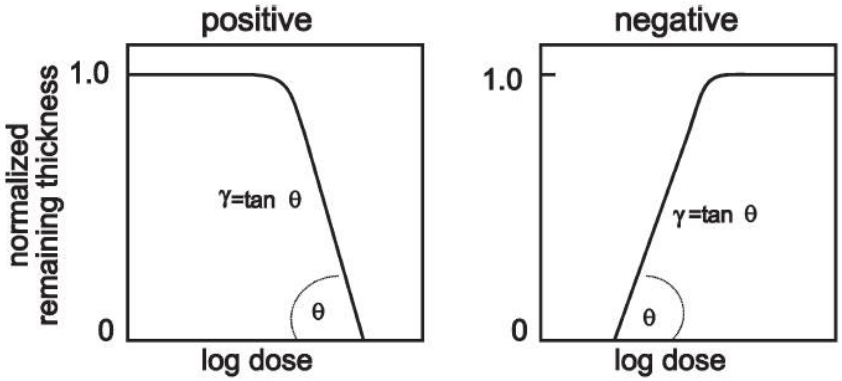

Figure 1.3: Sensitivity (or contrast) curves for positive or negative tone resists. For a positive tone resist, the UV dose required to completely remove the resist using a specific development condition is defined as the dose to clear, E_0. Reprinted with permission from [2]. Copyright 2005 Springer.

For a positive tone resist, the sensitivity is characterized by the dose to clear, E_0, which is the UV exposure dose required for complete removal of the resist using a specific development condition. Conversely, the sensitivity for a negative tone resist is the UV dose required to retain 50 % of the resist in the exposed area. For all resist materials, high resolution and sensitivity are simultaneously desired. In addition to the tone, resist materials are often classified by the radiation sources such as e-beam resists, EUV (13.5 nm) resists, and "photoresists" for g-line (436 nm), i-line (365 nm), KrF (248 nm), and ArF (193 nm) wavelengths.

1.1.2 Current and Future Lithography Techniques

The 193 nm immersion technique (Figure 1.4a) is the current workhorse in the semiconductor manufacturing industry, while potential next-generation lithography techniques include EUV lithography (Figure 1.4b), multiple e-beam direct-write patterning (Figure 1.4c), directed self-assembly (Figure 1.7), and imprint lithography (Figure 1.8).

193 nm immersion lithography takes the advantage of the higher refractive index of a fluid (n_{fluid}) compared to air ($n_{air} = 1$). For all optical lithography techniques, the resolution (R) and the depth of focus (DOF) are given approximately by

$$R = k_1 \frac{\lambda}{n \sin\theta} = k_1 \frac{\lambda}{\mathrm{NA}} \tag{1.1}$$

and

$$\mathrm{DOF} = k_2 \frac{\lambda}{n \sin^2\theta} = k_2 \frac{n\lambda}{\mathrm{NA}^2} \tag{1.2}$$

where $\mathrm{NA} = n \sin\theta$ is the numerical aperture, n is the refractive index of the medium, θ is the $\frac{1}{2}$ angle subtended by the first lens, λ is the wavelength of the exposing light, and k_1 and k_2 are Rayleigh coefficients that are dependent on the resist material, process technologies, and image formation technologies [10, 11]. Higher NA's and a shorter λ contribute to a higher resolution. For 193 nm immersion lithography, $n_{H_2O} \approx 1.44$ is greater than n_{air} but is less than $n_{resist} \approx 1.7$ enabling higher R and DOF by 30-40 %.

Figure 1.5 illustrates the impact of immersion on both R and DOF. For a given incident angle, the immersion technique increases the DOF compared to air as shown in Figure 1.5a and Equation 1.2. The increase in the refractive index of the medium between the lens and the resist substrate with water also increases

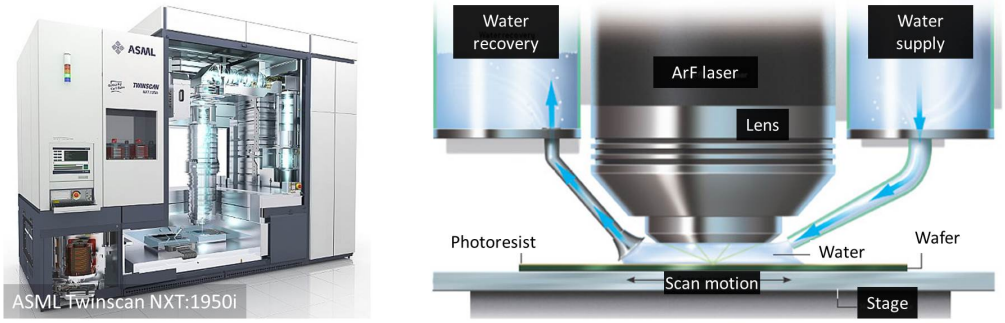

a) Current 193 nm immersion lithography tool by ASML [4]

b) Next-generation ASML EUV tool [5–8]

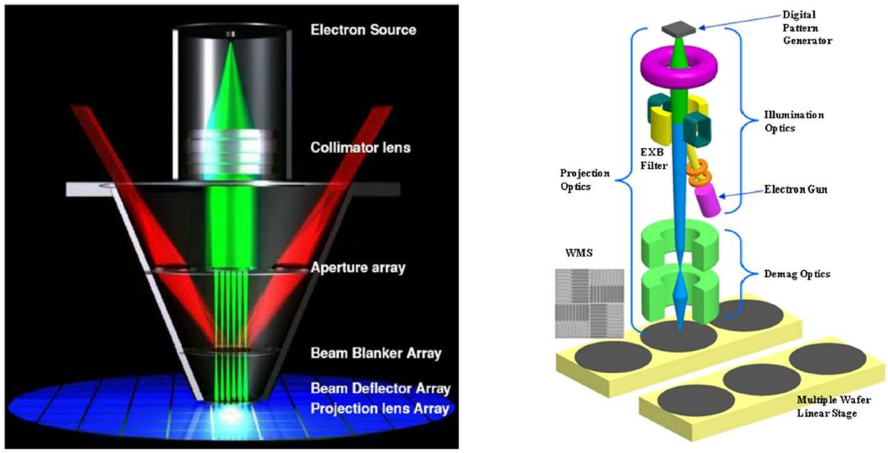

c) Mutiple e-beam direct-write systems. MAPPER (left) and KLA-Tencor REBL (right) [9]

Figure 1.4: Current and potential high resolution lithography options for sub-22 nm features. (a) 193 nm immersion lithography, (b) EUV (13.5 nm) lithography, and (c) two multiple e-beam direct-write techniques. Reprinted with permission from a) [4] copyright 2005 Precision Graphics, b) [5–8] copyright 2013 ASML, and c) [9] copyright 2013 MAPPER Lithography and KLA-Tencor.

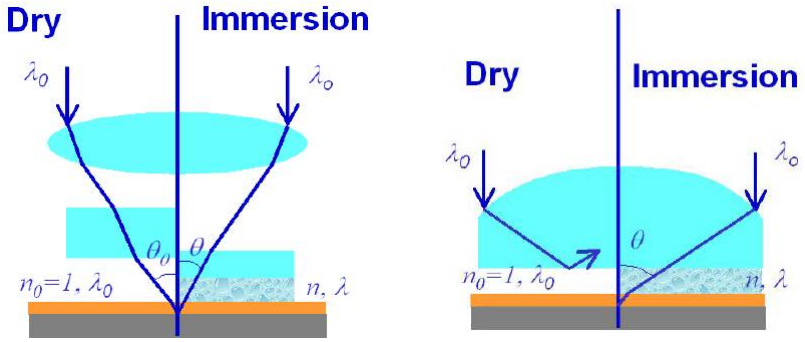

a) Increase in DOF by decreasing the incident angle in water

b) Enabling higher NA

Figure 1.5: Improvements in 193 nm immersion lithography enabling higher resolution patterns. Reprinted with permission from [12]. Copyright 2005 SPIE.

the critical angle at which the light is reflected at the resist interface through total internal reflection 1.5b. This technique allows light with higher spatial frequency to be coupled into the resist. For resolution below 32 nm, current 193 nm immersion lithography requires "double patterning" with two exposure steps for split layers, each containing resolution-limited features [13].

While the 193 nm double patterning technique has been able to achieve features far below the exposure wavelength, the process cost involving the second exposure and the fundamental resolution limit (Equation 1.1) inspired an extensive push for 13.5 nm EUV wavelength as a potential next-generation lithography technology. The current state of the art EUV tool, shown in Figure 1.4b, achieves sub-22 nm resolution (single exposure) with a projected throughput of 125 wafers per hour (wph) with moderately sensitive resist (15 mJ/cm^2), if EUV light source of sufficient brightness can be realized [7]. Since almost all materials absorb at 13.5 nm wavelength, optical components in the system must be mirrors. The challenges in optics have been largely overcome, but the light

source remains a major challenge. Two competing methods for generating EUV wavelengths are shown in Figure 1.6 [8, 14]. The laser-produced plasma (LPP)

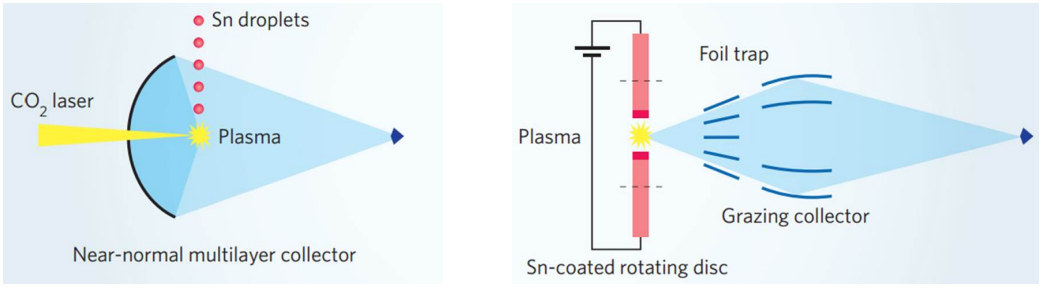

a) Laser-Produced Plasma (LPP) b) Laser-assisted Discharge Plasma (LDP)

Figure 1.6: Two competing 13.5 nm EUV source concepts for generating high power. Reprinted with permission from [8]. Copyright 2010 Nature.

technique uses a pre-pulse laser to vaporize a ~20 μm diameter molten Sn drop followed by irradiation of the Sn plasma using a high powered CO_2 laser with resulting spectrum filtered for exposure [15]. Debris generated from Sn droplets are mitigated using background gas or magnetic field. Another method for generating EUV wavelength is to ignite a Sn plasma at a high voltage using a laser-assisted discharge plasma (LDP) technique. Once generated, the debris is mitigated by a rotating foil trap [8, 14]. While EUV powers up to ~45 W and ~30 W have been achieved using LPP and LDP techniques respectively, a source power greater than 100 W is required to achieve the 125 wph throughput capability required for production.

EUV lithography has advanced tremendously since its inception in 1985. However, due to many remaining challenges and the cost of EUV lithography, multiple e-beam direct-write systems (Figure 1.4c) have also received considerable attention as a competing candidate for the next-generation lithography. E-beam lithography has been predominantly used to fabricate complex masks

for optical pattern generators, including for the 193 nm systems. Advances in digital electronics today allow gigabits per second (Gbs) data rates, improving the wafer throughput. Simultaneously, micro-mechanical components enable multiple parallel beams for e-beam lithography. However, the feasibility of this potential next-generation technology remains yet to be demonstrated due to the number of beams required. Existing demonstrations continue to suffer from a low wafer throughput.

While there are a number of multiple e-beam techniques, the Multiple Aperture Pixel by Pixel Enhancement of Resolution (MAPPER) claims a wafer throughput of ~10 wph with 1.1 m by 1.6 m footprint using 13,260 Gaussian beams on a high sensitivity resist (30 $\mu C/cm^2$). This technique uses a single source with a collimator which breaks a uniform beam into thousands of Gaussian beams. These beams are detected by photodiodes and are amplified by a complementary metal-oxide semiconductor (CMOS) circuits on the beam blanker array before being projected onto the wafer [16]. An alternate multiple e-beam technique is the Reflective E-Beam Lithography (REBL), which uses a digital (or dynamic) pattern generator consisting CMOS circuits where decelerated electrons are fired back onto the wafer substrate [7]. While both of these multiple e-beam direct-write systems boast high resolution lithography with DOF ~1 μm, their high volume manufacturing is ultimately limited by their wafer throughput.

Due to difficult challenges in achieving sub-22 nm features through conventional lithography techniques, alternatives such as the directed self-assembly (DSA) of block copolymers and imprint lithography have also received considerable attention. For DSA, diblock copolymers consisting two chemically

different polymer chains joined by a covalent bond have been used, taking the advantage of the chemical incompatibility between the two blocks, which spontaneously self-assemble into microphase-separated domains exhibiting ordered morphologies in nanometer scales at equilibrium [17, 18]. The relative chain length of the blocks determine the size of microdomains and lithographically-defined chemical or topographical pre-patterns on the substrate promote preferential alignment. Figure 1.7 schematically shows DSA of a diblock poly(styrene) and poly(methyl methacrylate) (PS-*b*-PMMA) copolymers through chemoepitaxy (using chemical pre-patterns) and graphoepitaxy (using topographical pre-patterns).

M. S. Onses *et al.* demonstrated DSA of 20 nm thick PS-*b*-PMMA after 5 min hot-plate heating at 220 °C for chemoepitaxy and at 250 °C for graphoepitaxy [19]. Two relative chain lengths (block ratio) are shown for 37-37 K and 25-26 K PS-*b*-PMMA, where the chain length dependent microdomains form lines/spaces of varying dimensions. Pre-patterns for chemoepitaxy contained lithography-defined and crosslinked PS (15 nm line, 84 nm spacings) separated by regions of random copolymer brushes (hydroxyl-terminated PS-*co*-PMMA). Graphoepitaxy pre-patterns were printed using e-beam lithography on 70 nm thick hydrogen silsequioxane. By inducing the phase separation of block copolymers to perform pattern multiplication, DSA is considered as a viable alternative for sub-20 nm microlithography. However, significant challenges arise in controlling point defects and dislocations in microdomains. Even a slight mismatch in surface energy between the guide patterns and the diblock copolymer can result in alignment defects.

A second unconventional route is pattern generation by imprint lithography.

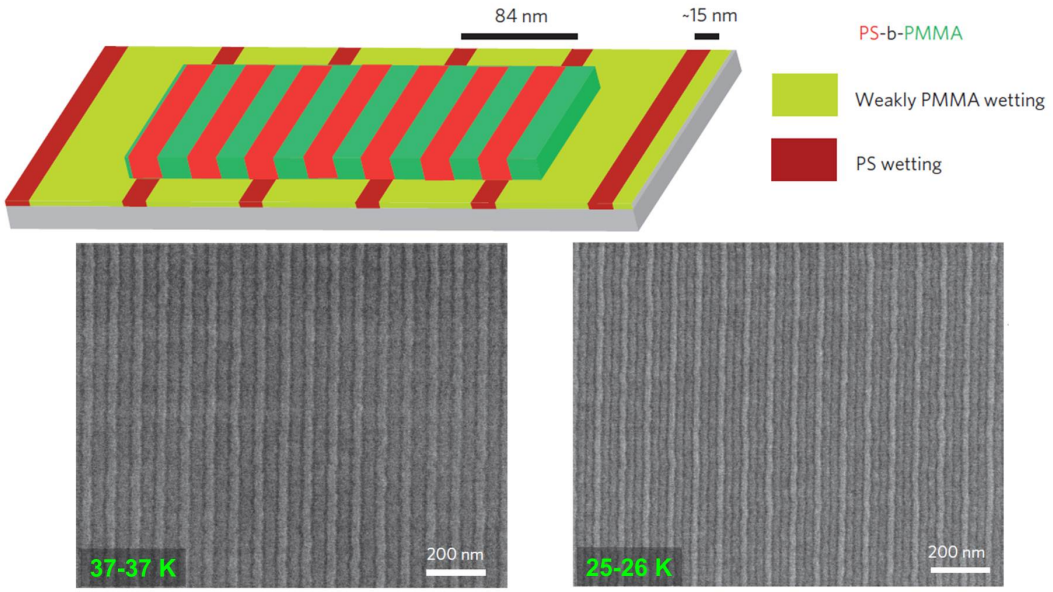

a) Directed self-assembly using chemoepitaxy

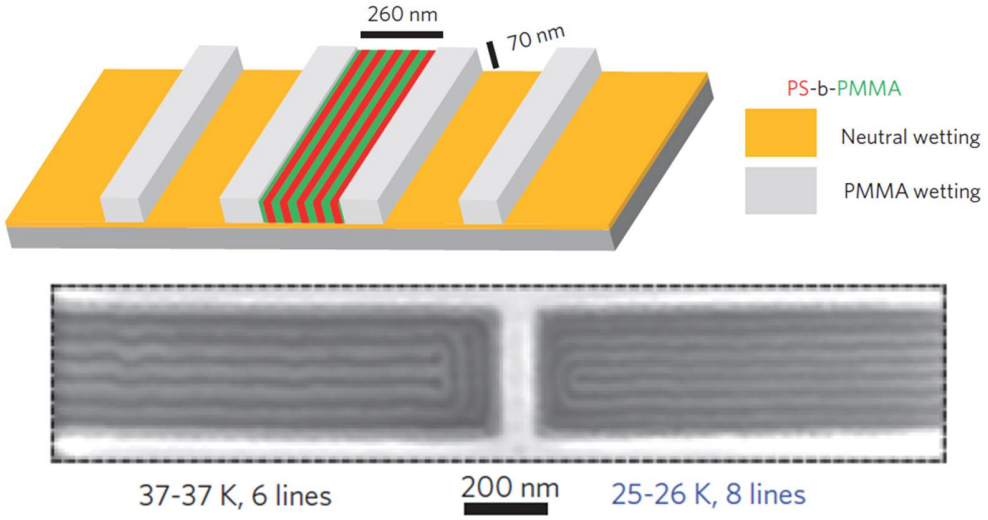

b) Directed self-assembly using graphoepitaxy

Figure 1.7: Directed self-assembly of 20 nm thick diblock PS-*b*-PMMA copolymers using lithographically defined by a) chemical pre-patterns (chemoepitaxy) and b) topographical pre-patterns (graphoepitaxy) upon substrate heating for 5 min at 220 °C and 250 °C respectively. Two relative chain length (block ratio) are shown for 37-37 K and 25-26 K PS-*b*-PMMA. Reprinted with permission from [19]. Copyright 2013 Nature.

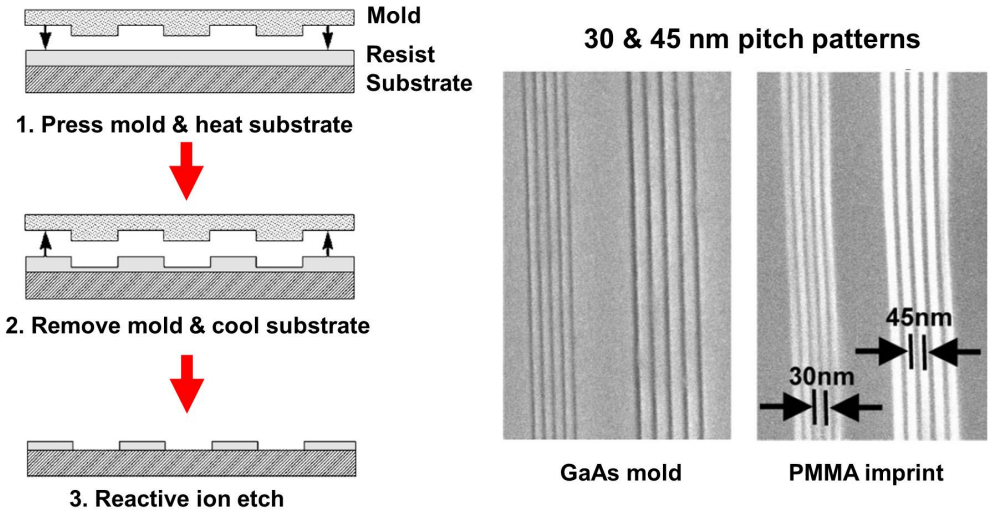

Figure 1.8: Schematics of imprint lithography in its simplest form. A mold (metal, dielectric, or semiconductor) used to deform the thermoplastic resist above its glass transition temperature. An example of high resolution imprint lithography is shown using GaAs mold on ~20 nm thick PMMA at ~200 °C and ~15 MPa. Reprinted with permission from [23]. Copyright 2004 American Institute of Physics.

This technique, represented schematically in Figure 1.8, takes the advantage of the thermoplastic character of resist polymers, where it is deformed upon contact with a mold while the substrate is heated above the polymer's glass transition temperature. The mold is removed when the resist is cooled below the glass transition temperature. Residual resist in the compressed area is removed using an anisotropic etching process such as reactive ion etching (RIE) [20–22]. Imprint lithography boasts of sub-10 nm and even molecular-level resolution, but the technique suffers from defect control during pattern transfer and consistency in imprint related to the frequent mold treatment during mass production [22, 24].

While EUV lithography, multiple direct-write e-beam lithography, directed

self-assembly of block copolymers, and imprint lithography show their viability for sub-20 nm lithography, their challenges in production call for additional innovative techniques that may help to drive the Moore's law down to 6 nm nodes.

1.1.3 Chemically Amplified Resists

Resists remain critical for the most of potential next-generation lithography techniques. Over the past three decades, chemically amplified photoresists have been widely used as resists for UV lithography due to their high sensitivity and excellent patterning performance. The process of pattern formation relies on generating spatially resolved acid-catalysts, which then diffuse and induce a series of side-group deprotection in the resist film during a heating step referred to as the post-exposure bake (PEB). This bake is generally performed above the resist's glass transition temperature (T_g) for 30 to 120 s. The solubility of the resist matrix changes with sufficient deprotection, after which the resist is selectively removed in a developing solvent. As patterns approach 10 nm dimensions, resist materials face numerous challenges including the control of acid-catalyst diffusion while still providing the thermally activated deprotection to reach the solubility switch during PEB.

A simplest chemically amplified resist system contains a polymer resin (or matrix) with an acid-generating component called the photo-acid generator (PAG). These two components are generally mixed into a common solvent and are spun onto a wafer substrate with thicknesses comparable to the exposure wavelength. The very first resist designed for this acid-catalyzed deprotection

was a two component system containing poly(4-*t*-butoxycarbonyloxystyrene) (PBOCST) and a PAG. The acid-catalyzed deprotection scheme of this resist is represented schematically in Figure 1.9. As shown in Figure 1.9a, acid-catalysts

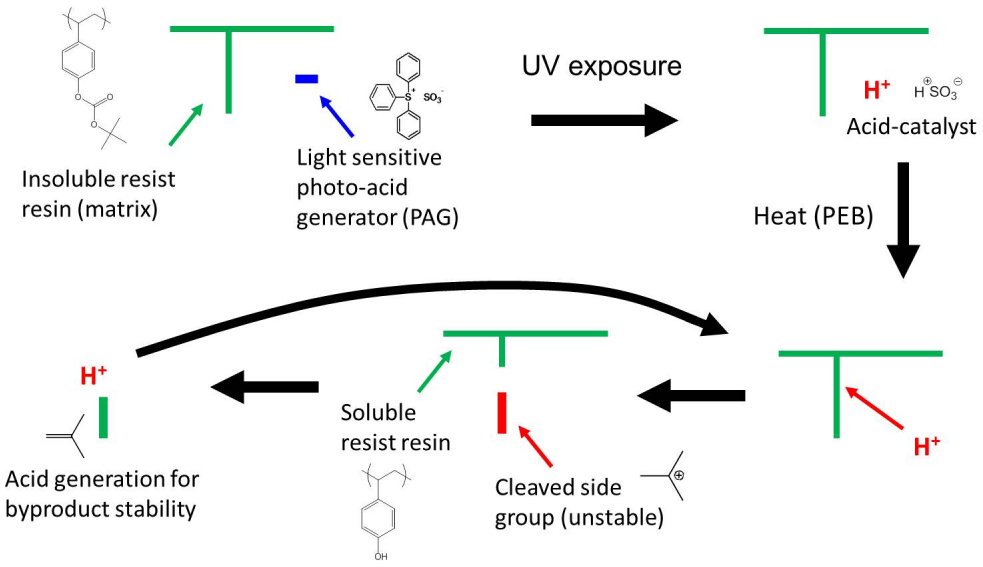

a) Cartoon representation of a chemical amplification scheme

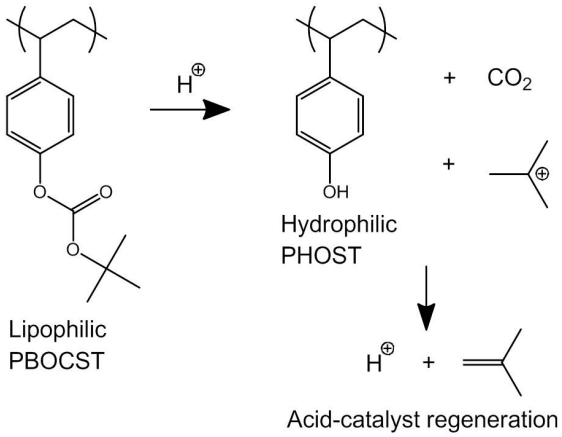

b) Acid-catalyzed deprotection using PBOCST

Figure 1.9: Acid-catalyzed deprotection for solubility change in the resist polymer resin [2, 25].

are generated from PAGs upon UV exposure. During PEB, these acids and their counter ions (SO_3^- in Figure 1.9) diffuse in the resist polymer resin and cleave a side-group (or "protecting group") in a deprotection reaction which changes the

polarity of the resin. The deprotected side-group is unstable and must regenerate the acid-catalyst in order to reach its thermodynamically and kinetically stable form. The regenerated acid diffuses within the polymer resin to deprotect another protecting group, resulting in a chemical amplification scheme until the heating source is removed. Typically, this amplification results in 100-1000 deprotection reactions per generated acid [26]. The actual chemical structures are shown in Figure 1.9b. The *t*-butyl groups are deprotected by an acid-catalyst upon PEB, with the lipophilic PBOCST becoming a hydrophilic PHOST. The reaction byproduct releases another acid in order to form a stable isobutene. Once deprotected, the hydrophilic PHOST resin can be removed in an alcohol or aqueous developing solvent for positive-tone development [2].

Through the chemical amplification technique, the sensitivity of resist polymers used for the 248 nm and 193 nm lithography were drastically improved. However as feature sizes decreased to sub-32 nm in resolution, excessive diffusion of acid-catalysts began to create edge roughnesses in the resist profiles as shown in Figure 1.10. This variation, known as the line-edge roughness (LER), is the 3σ deviation along one edge of the printed line with respect to a straight line. Another widely used term for quantifying roughness in lithographic pattern is the line-width roughness (LWR), which is the variation in the width of the printed line between the two edges. In general, LWR can be estimated as $\text{LWR} \sim \sqrt{2} \cdot \text{LER}$ [27].

LER is caused by a number of statistical fluctuations including shot noise (photon flux variations) during UV exposures, random walk nature of the acid-catalyze diffusion in the resist polymer resin, and swelling of the resin during the development process. Upon pattern transfer onto the underlying substrate

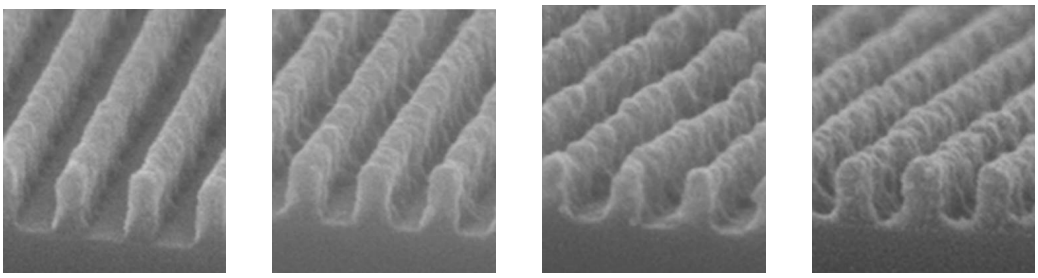

a) 0 % Scattering b) 20 % Scattering c) 30 % Scattering d) 40 % Scattering

Figure 1.10: Roughness induced on a 50 nm half pitches by a range of EUV scattering (flare). As photon scattering level increase, both LER and LWR increases. For example, the LWR increases from 3σ = 7 nm to 11 nm for 0 to 20 % flare levels. Reprinted with permission from [28]. Copyright 2008 Elsevier.

by etch, the LER and irregularities in features ultimately generate fluctuations in the gate voltage and threshold current in completed devices. These issues demonstrate the importance of resist materials and processing techniques including PEB, pattern development, and etch [29–31].

The International Technology Roadmap for Semiconductors (ITRS) periodically updates an assessment of the semiconductor industry's future technology requirements, including specifications for the resist materials. The target resolution of flash with LWR requirements are shown below in Table 1.1. Requirements for the critical dimension (CD) and LWR for each targeted flash node approach sub-nanometer scales, making the process control critical. In addition, resist materials must be sufficiently thick to act as a stencil, and must also be relatively insensitive to temperature in order to prevent pattern collapse and/or dimension change during PEB, development, and etch.

Although ITRS assessment provides a goal for the materials research and development for the targeted nodes, it is worth noting that manufacturing solutions beyond 2018 are essentially unknown. In addition to the resolution

Table 1.1: ITRS patterning requirements for resist materials [32]

Year of production	2015	2018	2021	2025
Flash half pitch (node) [nm]	15	12	9	5
Critical dimension (CD) control 3σ [nm]	1.7	1.3	1.0	0.8
Line width roughness (LWR) 3σ [nm]	1.8	1.3	0.9	0.6
Resist thickness [nm]	35-65	20-45	15-35	15-30
PEB temperature sensitivity [nm/°C]	0.8	0.6	0.4	0.4
Physical gate length after etch [nm]	17	13	10	6.6

requirements, resist materials must be sensitive enough to support the high wafer throughput. These sensitivity requirements are summarized in Table 1.2. Solving these challenges require extensive understanding of resists' chemical

Table 1.2: ITRS sensitivity requirements for resist materials [32]

Exposure technology	Sensitivity
248 nm KrF lithography	20-50 mJ/cm^2
193 nm ArF lithography	20-50 mJ/cm^2
EUV (13.5 nm) lithography	10-20 mJ/cm^2
High voltage e-beam (50-100 kV)	50-60 μC/cm^2
Low voltage e-beam (1-5 kV)	30-60 μC/cm^2

reactions and their kinetics. Although the lithography process is extremely reliable, the chemical reaction paths and kinetics of chemically amplified resists are not fully understood. Like many organic thin-films, difficulties in characterizing the reaction kinetics arise due to the limited thermal stability, limiting study to a narrow range of temperatures. In this work, a laser-induced millisec-

ond heating is explored for both patterning performance and kinetic analysis of model chemically amplified resist systems used for 248 nm, 193 nm, and EUV (13.5 nm) lithography. By working in the milliseconds time frame, the range of temperatures explored was dramatically improved, allowing the determination of critical reaction behavior.

1.2 Millisecond Annealing for Shallow Junctions

1.2.1 Shallow Junction Annealing and Diffusion Control

Introducing impurity atoms (dopants) into a semiconductor material by diffusion marked the beginning of the electronics age. Specifically, the silicon age was heralded by the invention of pn junctions in the 1940's, where traces of boron and phosphorus dopants were found in bulk silicon [33]. Techniques for introducing dopants into silicon substrates have become well-established, with low energy ion implantation becoming dominant over the past decade for shallow implantations [34]. Impurities such as boron diffuse by an interstitial mechanism and the initial rapid displacement of impurities occur during the first annealing step following implantation. This displacement, referred to as the enhanced transient diffusion (TED), is a significant issue for ultra-shallow junctions with critical dimensions approaching sub-20 nm features [35]. A. E. Michel *et al.* showed that TED could be reduced while increasing the electrical activation by annealing at high temperatures for short times [36]. The continued decrease in pn junction dimensions according to the scaling trend (Moore's law) have pushed the substrate annealing into the millisecond times at temperatures

approaching the substrate melt, to limit the excessive diffusion while improving dopant activation levels [37–39].

For annealing technologies down to 100 nm nodes, the rapid thermal annealing (RTA) tools have been dominant, achieving 100 ms durations with peak temperatures of 1100 °C [40, 41]. Dopant activation in the millisecond times and below have been achieved using flash lamp annealing (FLA), direct surface annealing, or laser spike annealing (LSA), which are three major competing techniques for the solid-phase (non-melt) substrate annealing [37, 42–44]. All three techniques utilize a very large increase in the ramp rate from the RTA predecessor in order to fully minimize the TED. Millisecond FLA, introduced in the 1980's, uses an array of broad-band xenon arc flash lamps ignited by a high voltage pulse which allows substrates to be annealed in the range of 100 μs to 500 ms [42, 45]. Combined with the conventional spike RTA, the FLA has demonstrated reduction in TED [45, 46]. However, the FLA currently suffers from non-uniformity issues caused by variations in reflectivity of different features on the wafer substrate [46].

Direct surface annealing and LSA are similar but competing laser-based millisecond spike annealing techniques, which differs in the laser sources, wavelengths, and scanning modes. Both techniques use a line-focused continuous wave (CW) laser beam that is scanned across the substrate to locally heat and anneal the radiated area. In the case of the direct surface annealing, diode laser stacks with λ = 810 nm are used to scan a stationary wafer in the millisecond time frames [44, 47]. For LSA, a CO_2 gas laser (λ = 10.6 μm) is used where the peak annealing temperature is set by the laser power density and the heating duration is the beam dwell time (τ_{dwell}), defined as the short axis of the laser

beam divided by the scanning velocity. In general, anneal durations ranging from 10 μs to 10 ms can be achieved for temperatures up to and beyond silicon melt [37]. Figure 1.11 shows the typical diffusion lengths of dopants (Δx_j) and the resulting decrease in the sheet resistance (R_s) of the substrate after milliseconds dopant activation using LSA [48].

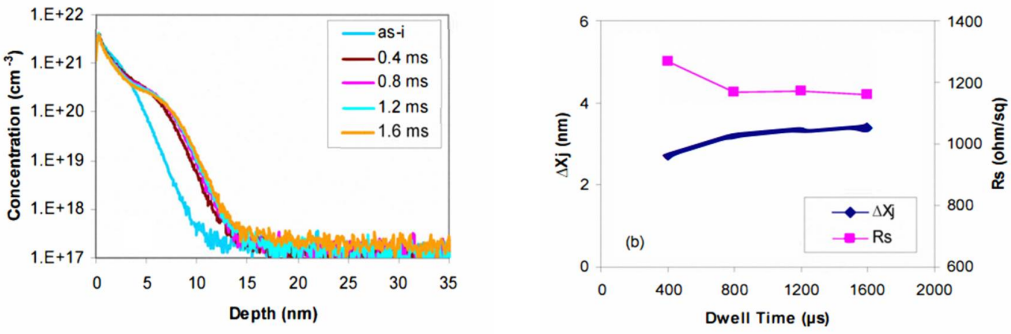

a) Secondary ion mass spectrometry analysis before and after LSA

b) Diffusion into junction depth and sheet resistance comparison

Figure 1.11: Boron dopant activation in Ge substrates using millisecond LSA technique at 1240 °C at varying τ_{dwell}. a) Secondary ion mass spectrometry analysis for the 10^{15} cm^{-2} boron samples at 200 eV. b) Sheet resistance (R_s) and diffusion length into junction depth Δx_j) at multiple dwell times. X_j is defined at 5×10^{18} cm^{-3}. Reprinted with permission from [48]. Copyright 2010 IEEE.

Both figures show impurity movement of ≈2.7 nm in the first 0.4 ms of the LSA and saturates at ~3.4 nm for a factor of 4 longer τ_{dwell}. This observation suggests that in order to minimize TED while fully activating the dopant species, annealing must be performed in the sub-millisecond time frames. For this reason, LSA shows great potential and promise for the next-generation junction annealing.

1.2.2 Laser Spike Annealing System at Cornell

Two Ultratech laser spike annealing systems were donated to Cornell by Intel Corporation in 2008. These alpha demo tools were equipped with a 120 W far-infrared CO_2 laser (λ = 10.63 μm), necessary optics for millisecond anneals, and a linear motion stage (Aerotech ES14663-1) capable of traveling up to 400 mm/s. The system was reconstructed to accommodate a 250 W fiber-coupled near-infrared diode laser (λ = 980 nm) in addition to the CO_2 laser. The completed laser setup is shown in Figure 1.12, where the red line represents the beam path for the CO_2 laser while the green line represents the optical fiber coupling the 980 nm beam. For the all of the following experiments, laser scans were performed in and out of the page plane.

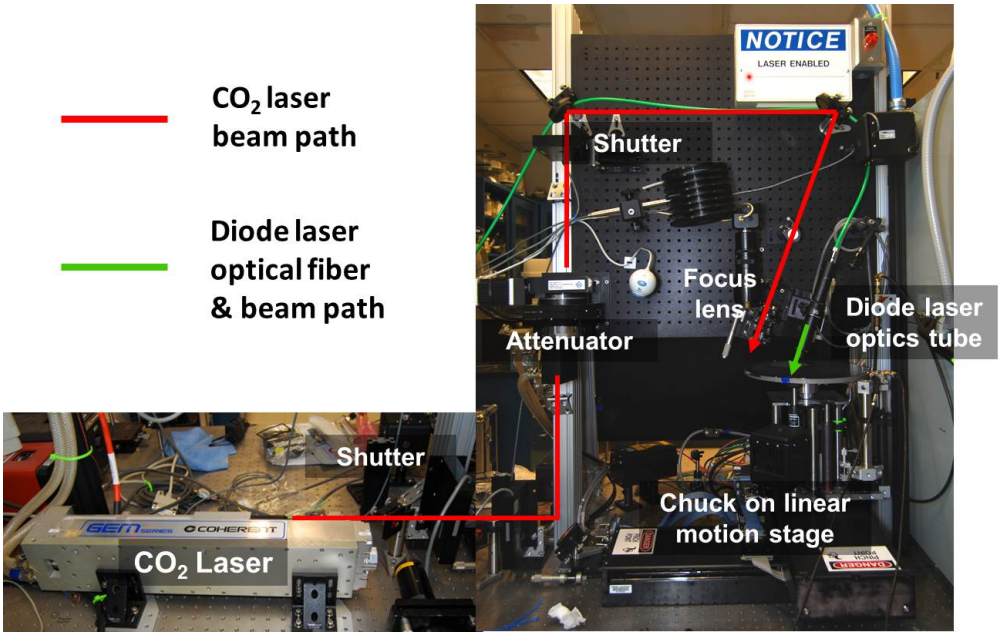

Figure 1.12: Laser spike annealing system at Cornell as of December 2013.

1.2.3 10.6 μm CO_2 Gas Laser

The beam shape of the CO_2 gas laser (Coherent GEM-100L) is originally circular with a 3.8 ± 0.4 mm diameter. This beam is focused into a line with the beam full width half maximum (FWHM) at approximately 90 μm by 600 μm using two lenses as schematically shown in Figure 1.13. The CO_2 beam, with radius

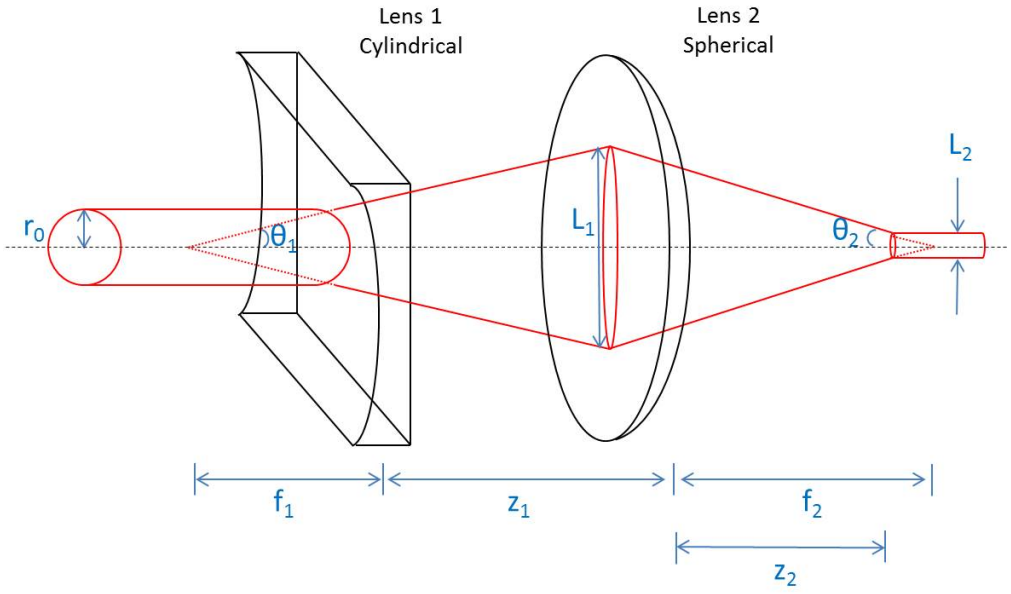

Figure 1.13: Focusing schematics for CO_2 laser into a line-shape.

$r_0 \approx 1.9$ mm enters a cylindrical plano-concave lens with an effective focal length f_1, where it expands in one axis with a half-angle θ_1 of r_0/f_1. At z_1, a spherical lens focuses the asymmetric beam. The expanded dimension is focused to near the diffraction limit, while the narrow width axis forms the long dimension of the beam.

This line-focused beam is profiled using a photodiode detector (Figure 1.14a). A 50 μm pinhole, capable of resisting up to 100 kW/mm^2, was placed on top of a 10.6 μm detector to protect the photodiode detector during laser

scans as shown in Figure 1.14b.

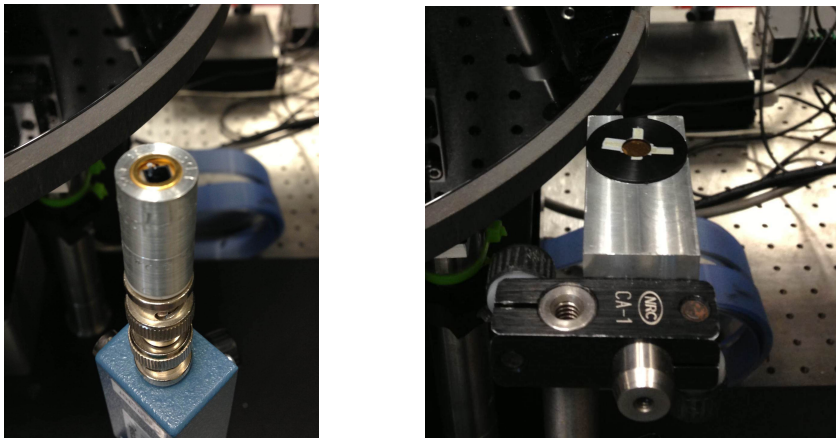

a) Photodiode detector b) 50 μm pinhole

Figure 1.14: Experimental setup for beam intensity profiling for both CO_2 and diode laser. a) A photodiode detector is used with its signal amplified for 10.6 μm or 980 nm. b) A 50 μm pinhole sits on top of the photodiode detector to resist high-power laser scans. To profile a 1-3 mm wide laser beams, linear motion stage was used to meet a high spatial resolution of 20 μm.

Figure 1.15 shows a typical intensity profile of the line-focused CO_2 laser at 20 W for a 100 mm/s scan speed. The beam intensity profile shows that the beam length along the long axis has a FWHM of 588 μm while the short axis has a FWHM of 90 μm. The scan duration, the time at which the beam "dwells" at a position, is the dwell time (τ_{dwell}) defined as the FWHM of the short axis divided by the scan speed. Since this beam profile was performed at a scan speed of 100 mm/s, the translated scan duration is $\tau_{dwell} \approx 900$ μs.

Ideally, the laser beam would have a Gaussian intensity profile corresponding to the theoretical lowest-order transverse mode (TEM_{00}). While the CO_2 beam is not a perfect Gaussian due to optics contamination and refractive index gradients, the measured intensity profile is nearly Gaussian and is an adequate approximation for spike annealing experiments [49].

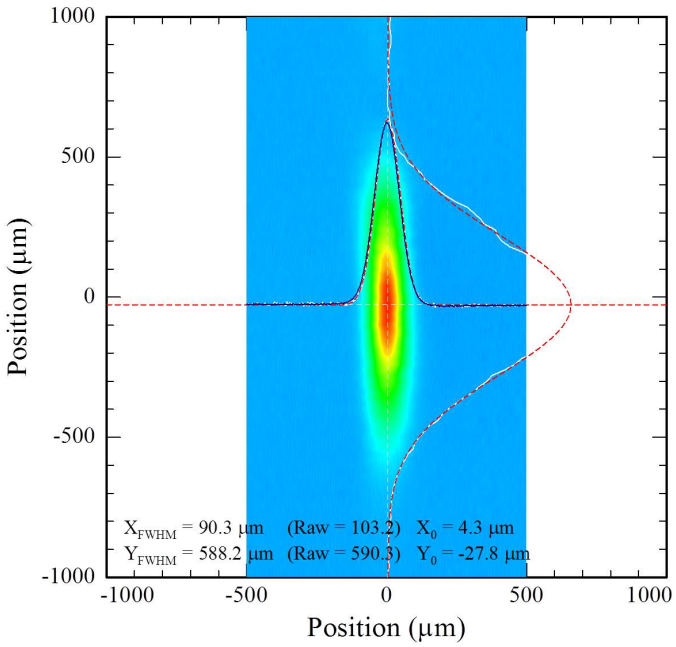

Figure 1.15: Beam intensity profile of a line-focused CO_2 laser at Cornell.

The intensity of the CO_2 laser is controlled by the rotation angle of a polarizer-analyzer-attenuator (as shown in Figure 1.12) containing a series of ZnSe plates. These plates are set at Brewster's angle with respect to the incident beam. As the beam passes through the series of plates, all horizontally polarized (s-polarized) components are reflected to a water-cooled beam dump while vertically polarized (p-polarized) components are transmitted [50]. The effective laser power on the stage chuck is

$$P = P_{min} + (P_{max} - P_{min})\,|\sin(\theta - \phi_0)|^2 \tag{1.3}$$

where θ is the angle of the ZnSe plates inside the attenuator, P_{min} and P_{max} are the minimum and maximum output power from the attenuator, and ϕ_0 is the plate angle which P_{min} is achieved. A typical power calibration for the CO_2 laser is shown in Figure 1.16.

Power at the wafer plane is typically measured by thermopile sensors as

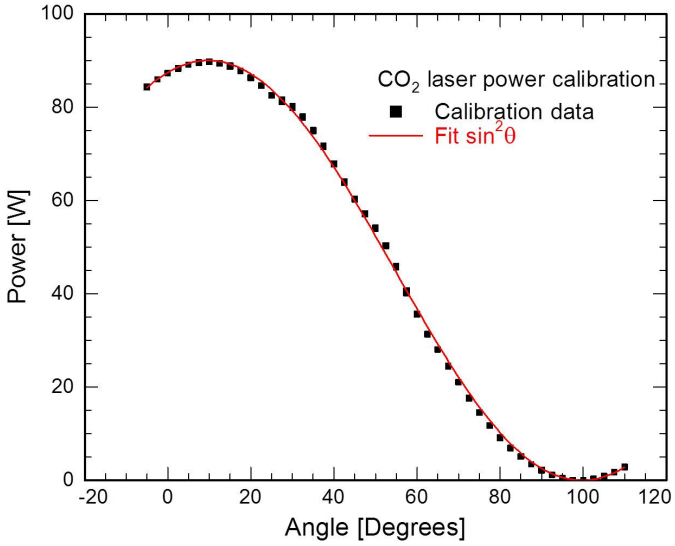

Figure 1.16: A typical CO_2 power calibration showing the angle of ZnSe plates inside an attenuator as a function of output power. The output power follows a $\sin^2\theta$ relationship.

a function of the attenuator angle. Equation 1.3 is then fitted to yield typical values of $P_{max} \approx 94$ W, $P_{min} = 0$ W, and $\phi_0 \approx 87.0\,^\circ$. Since the output power of the CO_2 laser is sensitive to the temperature of the water-cooled laser medium, the laser power was routinely calibrated.

1.2.4 980 nm Solid-State Diode Laser

Unlike the CO_2 laser which requires mirrors to direct the beam path, the solid-state diode laser at 980 nm is fiber-coupled through total internal reflection (fiber represented as a green wire in Figure 1.12). The 250 W diode laser (Jenoptik JOLD-250-CPXF-2P2) has a fiber core of ~400 μm which can be directly connected to a tube containing a quartz homogenizer and focus lenses. As schematically shown in Figure 1.17, a fiber-coupled beam with $r_0 \approx 200\,\mu$m enters a 2 mm thick quartz homogenizer. Total internal reflection from the top and bottom

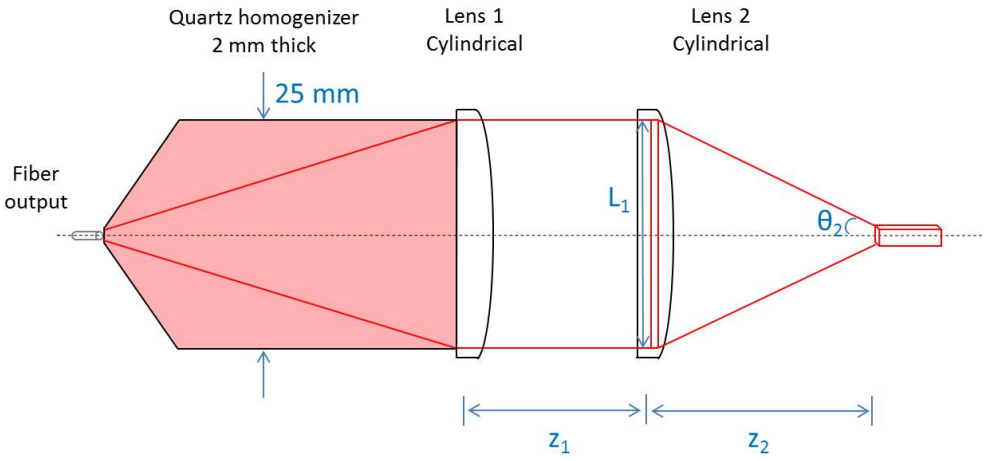

Figure 1.17: Focusing schematics for a diode laser into a homogenized line-shape. A 2 mm thick quartz homogenizer creates a flat-top with a uniform intensity in the long axis of the beam.

faces of the homogenizer results in a uniform intensity profile across the exit face. The thickness of the slab is imaged onto the surface yielding a uniform "long" axis of the beam. In the axis depicted in Figure 1.17, the output face of the 400 μm fiber is imaged to the sample, yielding the short axis of the beam profile. Figure 1.18 shows the flat-top diode beam profile obtained using a photodiode detector.

The beam is nearly flat along the long axis while super-Gaussian in the narrow axis, mirroring the intensity profile in the laser fiber coupling. The flat-top intensity profile spans greater than 2 mm. The "step" near the bottom of the long axis is likely due to imperfect machining at the quartz homogenizer edge.

The short axis width of the beam also displays a small area where beam intensity is uniform followed by a Gaussian-like tail with a FWHM of 236.3 μm. This short axis width is nearly three times greater than that of the CO_2 beam, which increases the τ_{dwell} by the same amount at a constant scan velocity. Due

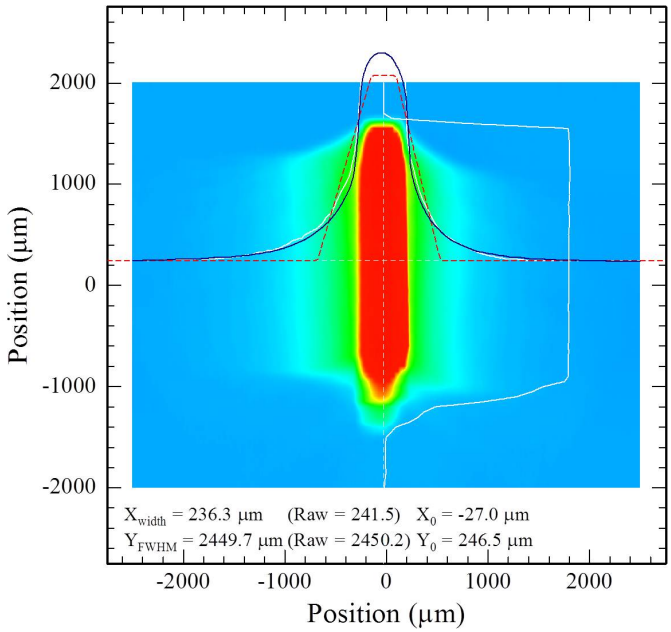

Figure 1.18: Beam intensity profile of a line-focused diode laser at Cornell.

to this reason, the fastest τ_{dwell} for the diode laser using the linear motion of the stage was limited to 1 ms (236.3 mm/s).

The power of the solid-state diode laser is controlled by the input current. A high power laser diode current source (ILX Lightwave LDX-36125-12) was used to generate up to 110 A of current for the 250 W laser. The optical power from the laser diode can be described by the following relationship,

$$P = m\,(I - I_{thresh}) \tag{1.4}$$

where I is the input current, I_{thresh} is the threshold current needed for stimulated emission, and m is the slope $\frac{dP}{dI}$. The threshold behavior of the diode laser output can be described using a simple IV curve as shown in Figure 1.19a. For voltages beyond ~5.3 V, the curve essentially becomes linear up to the maximum input current at 110 A, showing excellent stability of a solid-state laser even at high powers.

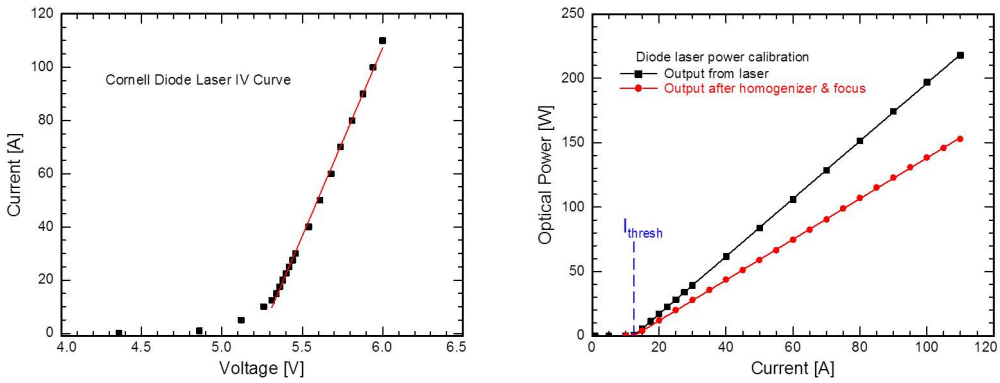

a) Diode Laser IV Curve

b) Diode Laser Power Calibration

Figure 1.19: A typical diode laser power calibration. a) IV characteristics of the diode laser, where the input current must be above a threshold to begin lasing. b) Optical power output as a function of input current. While the laser itself can reach up to 220 W at maximum supply current (110 A), there is a ~30 % power loss when the beam passes through the homogenizer and focusing lenses.

At maximum current, the diode laser couples 220 W into the fiber which can be directed to the sample chuck. While Figure 1.19b shows ~30 % power loss as the beam travels through the fiber, homogenizer, and focus lenses, the optical power in both curves show perfect linearity as a function of input current, with the same I_{thresh} value. The effective laser power on the stage chuck is the curve in red, where the following values were obtained for experimental calibration according to Equation 1.4: m = 1.59 W/A and I_{thresh} = 12.44 A.

1.2.5 Laser Spike Annealing for Polymer Heating

Using the LSA technique, CW laser heating sources can transiently heat polymer thin-films without damage to temperatures approaching 1000 °C, well above their conventional decomposition temperatures. Analogous to the appli-

cations in junction annealing where dopant activation levels are improved while limiting TED using short time annealing, laser-induced heating can potentially enhance the thermally-activated reaction kinetics of resist polymers at temperatures well above conventional heating methods (hot-plate or furnace). This laser-induced heating of polymer thin-films, inspired by the LSA technique, is schematically shown in Figure 1.20. A line-focused CW laser is scanned over the substrate to rapidly heat the surface for durations ranging from microseconds to milliseconds, followed by cooling through the thermal conduction into the substrate.

The biggest merit and interest in using this LSA-inspired technique for thermally-sensitive polymers is the ability to reach a high peak temperature with an ultra-fast rate followed by the subsequent quench rate on the same order. This short time behavior with a fast ramp and quench rates are schematically shown in Figure 1.21. This novel approach can drastically reduce the heating time for thin-film polymer processing such as the PEB of resist polymers used in lithography, while taking advantage of the rapid heating and quenching rates to analyze the reaction kinetics of polymers in their thermally stable form after high temperature heating [51–53]. For a conventional PEB, the substrate is heated at 100 K/s for tens of seconds, whereas a laser-induced PEB utilizes rapid heating to a peak temperature at 10^4-10^5 K/s. For example, PEB is performed on a hot-plate at 70-150 °C for 30-120 s, while the laser-induced PEB can be extended to temperatures of 560 °C with duration correspondingly reduced to 200 μs. The ability to reach high temperature for millisecond time frames offers the potential to explore previously estimated kinetics and models for thermally-sensitive polymeric materials.

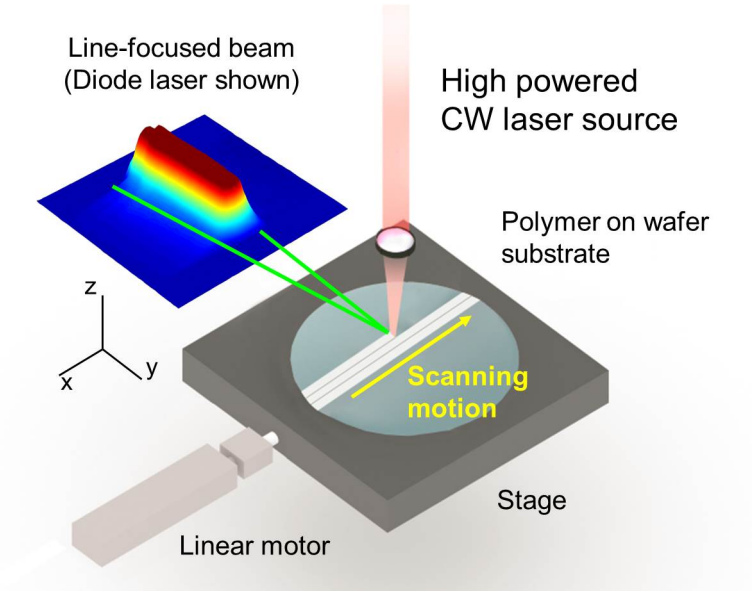

a) Laser-induced millisecond polymer heating

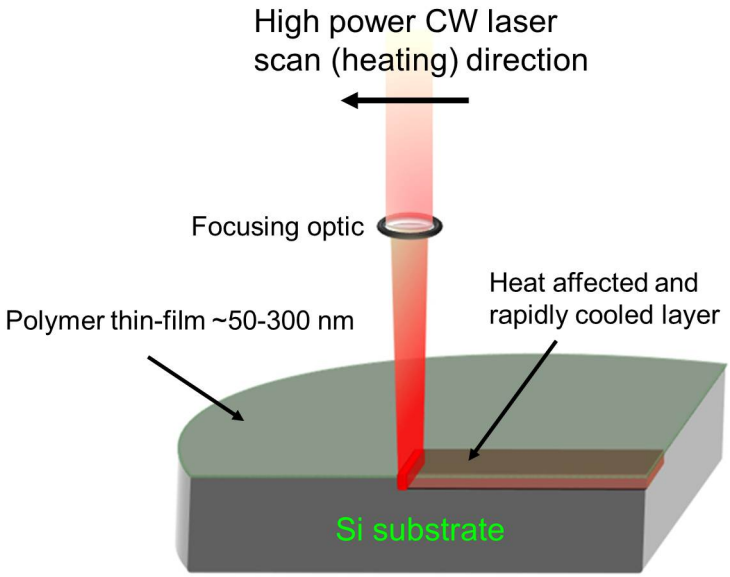

b) Cross-section view of millisecond heating

Figure 1.20: Millisecond characterization method using a line-focused, continuous wave CO_2 or diode laser systems. Schematic drawing shows a line-focused beam scanning the substrate. The top ~100 μm of the substrate surface is rapidly heated and cooled through the thermal diffusion into the silicon substrate. Reprinted with permission from [51]. Copyright 2012 American Chemical Society.

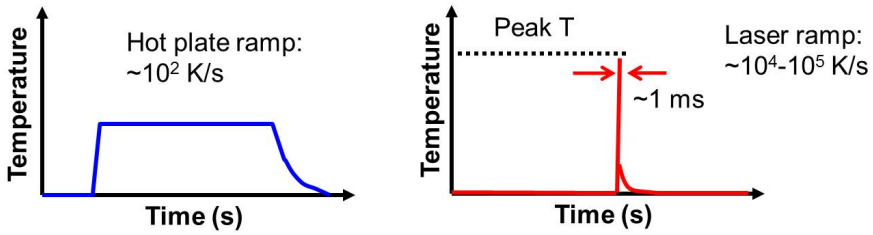

Figure 1.21: Schematic comparison of heating profile during hot-plate and laser-induced heating on a polymer film.

1.3 Thesis Outline

Both polymers and small molecules are more sensitive to temperature compared to metal or semiconductor thin-films. Chapter 2 will discuss the methodology for measuring the substrate temperature using a micron-scale platinum resistor. The measured temperatures are used for analysis in the remaining chapters in this thesis. Chapter 3 explores the thermal stability of polymers in the laser-induced sub-millisecond time frames. At 50 μs, stability of organic, conjugated, and Si-containing polymers approach 1000 °C, which is at least 400 °C above the conventional decomposition limit during the seconds duration heating.

The extended thermal stability using laser-induced heating is then applied in Chapter 4 to lithographically pattern chemically amplified resist systems. While conventional PEB uses a hot-plate to induce thermally-activated and acid-catalyzed deprotection reactions at 70-150 °C for 30-120 s, laser-induced PEB can shift the conditions to 200-560 °C for 50-2000 μs. Compared to the conventional methods, results show simultaneous improvements in sensitivity (up to 60 %) and edge definitions (up to 30 %) using laser PEB. The chemical reaction kinetics giving rise to this improvement is investigated in Chapter 5, where a fundamental understanding in the deprotection reaction and the acid

diffusion is developed and discussed.

The laser-induced heating is then used in Chapter 6 as a post-development process that can reduce roughness on existing polymer patterns. The polymer is heated above its T_g, where it flows to minimize the surface energy resulting in roughness reduction. However, the excessive flow of the polymer, which damages high resolution patterns, is controlled and prevented by keeping the duration short in the sub-millisecond time frames.

In Chapter 7, LSA is used to crystallize amorphous silicon in millisecond times, where rapid heating and cooling results in an explosive crystallization behavior. The growth kinetics and yielding morphologies are investigated. Conclusions and suggestions for future work are given in Chapter 8.

References

[1] I. Ferain, C. A. Colinge, and J. P. Colinge, "Multigate transistors as the future of classical metal-oxide-semiconductor field-effect transistors", *Nature*, vol. 479, pp. 310–316, 2011.

[2] H. Ito, "Chemical amplification for microlithography", *Adv. Polym. Sci.*, vol. 172, pp. 27–245, 2005.

[3] C. G. Willson, R. A. Dammel, and A. Reiser, "Photoresist materials: a historical perspective", *Proc. SPIE*, vol. 3051, pp. 28–41, 1997.

[4] G. Stix, "Shrinking circuits with water", *Sci. Am.*, vol. 293, pp. 64–67, 2005.

[5] H. Meiling, H. Meijer, V. Banine, R. Moors, R. Groeneveld, H. J. Voorma, U. Mickan, B. Wolschrijn, B. Mertens, G. van Baars, P. Kürz, and N. Harned, "First performance results of the ASML alpha demo tool", *Proc. SPIE*, vol. 6151, p. 615 108, 2006.

[6] H. Meiling, W. de Boeij, F. Bornebroek, N. Harned, I. de Jong, P. Kürz, M. Lwish, H. Meijer, D. Ockwell, R. Peeters, E. van Setten, J. Stoeldraijer, C. Wagner, S. Young, and R. Kool, "From performance validation to volume introduction of ASML's NXE platform", *Proc. SPIE*, vol. 8322, 83221G, 2012.

[7] R. Peeters, S. Lok, E. van Alphen, N. Harned, P. Kuerz, M. Lowisch, H. Meijer, D. Ockwell, E. van Setten, G. Schiffelers, J. W. van der Horst, J. Stoeldraijer, R. Kazinczi, R. Droste, H. Meiling, and R. Kool, "ASML's NXE platform and volume introduction", *Proc. SPIE*, vol. 8679, 86791F, 2013.

[8] C. Wagner and N. Harned, "EUV lithography: Lithography gets extreme", *Nature Photonics*, vol. 4, pp. 24–26, 2010.

[9] B. J. Lin, "Future of multiple-e-beam direct-write systems", *J. Micro/Nanolith. MEMS MOEMS*, vol. 11, no. 3, p. 033 011, 2012.

[10] S. Okazaki, "Resolution limits of optical lithography", *J. Vac. Sci. Technol. B*, vol. 9, no. 6, p. 2829, 1991.

[11] B. J. Lin, "The k3 coefficient in nonparaxial λ/NA scaling equations for resolution, depth of focus, and immersion lithography", *J. Micro/Nanolith. MEMS MOEMS*, vol. 1, no. 1, pp. 7–12, 2002.

[12] J. H. Chen, L. J. chen, T. Y. Fang, T. C. Fu, L. H. Shiu, Y. T. Huang, N. Chen, D. C. Oweyang, M. C. Wu, S. C. Wang, J. C. Lin, C. K. Chen, W. M. Chen, T. S. Gau, B. J. Lin, R. Moerman, W. G. van Ansem, E. van der Heijden, F. de Jong, D. Oorschot, H. Boom, M. Hoogendorp, C. Wagner, and B. Koerk, "Characterization of ArF immersion process for production", *Proc. SPIE*, vol. 5754, pp. 13–22, 2005.

[13] M. Maenhoudt, J. Versluijs, H. Struyf, J. van Olmen, and M. van Hove, "Double patterning scheme for sub-0.25 k1 single damascene structures at $NA = 0.75$, $\lambda = 193$ nm", *Proc. SPIE*, vol. 5754, pp. 1508–1518, 2005.

[14] H. Meiling, "From performance validation to volume introduction of ASML's NXE platform", SEMICON West, San Francisco, CA, 2012.

[15] D. C. Brandt, I. V. Fomenkov, A. I. Ershov, W. N. Partlo, D. W. Myers, R. L. Sandstrom, B. L. F. amd M. J. Lercel, A. N. Bykanov, N. R. Böwering, G. O. Vaschenko, O. V. Khodykin, S. N. Srivastava, I. Ahmad, C. Rajyaguru, P. Das, V. B. Fleurov, K. Zhang, D. J. Golich, S. D. Dea, R. R. Hou, W. J. Dunstan, C. J. Wittak, P. Baumgart, T. Ishihara, R. D. Simmons, R. N. Jacques, and R. A. Bergstedt, "LPP source system development for HVM", *Proc. SPIE*, vol. 7969, 79691H, 2011.

[16] G. de Boer, M. P. Dansberg, R. Jager, J. J. M. Peijster, E. Slot, S. W. H. K. Steenbrink, and M. J. Wieland, "MAPPER: progress towards a high volume manufacturing system", *Proc. SPIE*, vol. 8680, 86800O, 2013.

[17] M. Park, C. Harrison, P. M. Chaikin, R. A. Register, and D. H. Adamson, "Block copolymer lithography: periodic arrays of ~10^{11} holes in 1 square centimeter", *Science*, vol. 276, no. 5317, pp. 1401–1404, 1997.

[18] R. Ruiz, H. Kang, F. A. Detcheverry, E. Dobisz, D. S. Kercher, T. R. Albrecht, J. J. de Pablo, and P. F. Nealey, "Density multiplication and improved lithography by directed block copolymer assembly", *Science*, vol. 321, no. 5891, pp. 936–939, 2008.

[19] M. S. Onses, C. Song, L. Williamson, E. Sutanto, P. M. Ferreira, A. G. Alleyne, P. F. Nealey, H. Ahn, and J. A. Rogers, "Hierarchical patterns of three-dimensional block-copolymer films formed by electrohydrodynamic jet printing and self-assembly", *Nat. Nanotechnol.*, vol. 8, no. 9, pp. 667–675, 2013.

[20] S. Y. Chou, P. R. Krauss, and P. J. Renstrom, "Imprint of sub-25 nm vias and trenches in polymers", *Appl. Phys. Lett.*, vol. 67, no. 21, pp. 3114–3116, 1995.

[21] S. Y. Chou, P. R. Krauss, and P. J. Renstrom, "Imprint lithography with 25-nanometer resolution", *Science*, vol. 272, no. 5258, pp. 85–87, 1996.

[22] S. Y. Chou, P. R. Krauss, W. Zhang, L. Guo, and L. Zhuang, "Sub-10 nm imprint lithography and applications", *J. Vac. Sci. Technol. B*, vol. 15, no. 6, pp. 2897–2904, 1997.

[23] M. D. Austin, H. Ge, W. Wu, M. Li, Z. Yu, D. Wasserman, S. A. Lyon, and S. Y. Chou, "Fabrication of 5 nm linewidth and 14 nm pitch features by

nanoimprint lithography", *Appl. Phys. Lett.*, vol. 84, no. 26, pp. 5229–5301, 2004.

[24] F. Hua, Y. Sun, A. Gaur, M. A. Meitl, L. Bilhaut, L. Rotkina, J. Wang, P. Geil, M. Shim, J. A. Rogers, and A. Shim, "Polymer imprint lithography with molecular-scale resolution", *Nano Lett.*, vol. 4, no. 12, pp. 2467–2471, 2004.

[25] H. Ito, C. G. Willson, and J. M. J. Frechet, "New UV resists with negative or positive tone", *Digest of Technical Papers of 1982 Symposium on VLSI Technology*, vol. 82, pp. 86–87, 1982.

[26] V. M. Prabhu, S. Sambasivan, D. Fischer, L. K. Sundberg, and R. D. Allen, "Quantitative depth profiling of photoacid generators in photoresist materials by near-edge x-ray absorption ïňąne structure spectroscopy", *Appl. Surf. Sci.*, vol. 253, no. 2, pp. 1010–1014, 2006.

[27] G. M. Gallatin, P. P. Naulleau, and R. Brainard, "Modeling the effects of acid amplifiers on photoresist stochastics", *Proc. SPIE*, vol. 8322, p. 83221C, 2012.

[28] C. Gustin, L. H. A. Leunissen, A. Mercha, S. Decoutere, and G. Lorusso, "Impact of line width roughness on the matching performances of next-generation devices", *Thin Solid Films*, vol. 516, no. 11, pp. 3690–3696, 2008.

[29] A. Asenov, S. Kaya, and A. R. Brown, "Intrinsic parameter fluctuations in decananometer MOSFETs introduced by gate line edge roughness", *Electron Devices, IEEE Transactions on*, vol. 50, no. 5, pp. 1254–1260, 2003.

[30] G. M. Gallatin, "Resist blur and line edge roughness", *Proc. SPIE*, vol. 5754, pp. 38–52, 2005.

[31] P. Oldiges, Q. Lin, K. Petrillo, M. Sanchez, M. Ieong, and M. Hargrove, "Modeling line edge roughness effects in sub 100 nanometer gate length devices", in *Simulation of Semiconductor Processes and Devices, 2000. SISPAD 2000. 2000 International Conference on*, 2000, pp. 131–134.

[32] (2012). International technology roadmap for semiconductors, [Online]. Available: `www.itrs.net`.

[33] M. Riordan and L. Hoddeson, "The origin of the pn junction", *IEEE Spectrum*, vol. 34, no. 6, pp. 46–51, 1997.

[34] A. T. Fiory and K. K. Bourdelle, "Electrical activation kinetics for shallow boron implants in silicon", *Appl. Phys. Lett.*, vol. 74, no. 18, pp. 2658–2660, 1999.

[35] C. S. Rafferty, G. H. Gilmer, M. Jaraiz, D. Eaglesham, and H. J. Gossmann, "Simulation of cluster evaporation of transient enhanced diffusion in silicon", *Appl. Phys. Lett.*, vol. 68, no. 17, pp. 2395–2397, 1996.

[36] A. E. Michel, W. Rausch, P. A. Ronsheim, and R. H. Kastl, "Rapid annealing and the anomalous diffusion of ion implated boron into silicon", *Appl. Phys. Lett.*, vol. 50, no. 7, pp. 416–418, 1987.

[37] S. Talwar, D. Markle, and M. Thompson, "Junction scaling using lasers for thermal annealing", *Solid State Technol.*, vol. 46, no. 7, pp. 83–86, 2003.

[38] A. Shima, Y. Wang, D. Upadhyaya, L. Feng, S. Talwar, and A. Hiraiwa, "Dopant profile engineering of CMOS devices formed by non-melt laser spike annealing", *Dig. Tech. Pap. Symp. VLSI Technol.*, vol. 8B, no. 4, pp. 144–145, 2005.

[39] T. Yamamoto, T. Kubo, T. Sukegawa, E. Takii, Y. Shinmamune, N. Tamura, T. Sakoda, M. Nakamura, H. Ohta, T. Miyahita, H. Kurata, S. Satoh, M. Kase, and T. Sugii, "Junction profile engineering with a novel multiple laser spike annealing scheme for 45-nm node high performance and low leakage CMOS technology", *Int. El. Devices Meet.*, vol. 1, pp. 143–146, 2007.

[40] T. E. Seidel, D. J. Lischner, C. S. Pat, R. V. Knoell, D. M. Maher, and D. C. Jacobson, "A review of rapid thermal annealing (RTA) of B, BF_2 and As ions implanted into silicon", *Nucl. Instrum. Meth. B*, vol. 7-8, no. 1, pp. 251–260, 1985.

[41] L. Csepregi, E. F. Kennedy, T. J. Gallagher, J. W. Mayer, and T. W. Sigmon, "Reordering of amorphous layers of si implanted with ^{31}P, ^{75}As, and ^{11}B ions", *J. Appl. Phys.*, vol. 48, no. 10, pp. 4234–4240, 1977.

[42] T. Gebel, M. Voelskow, W. Skorupa, G. Mannino, V. Privitera, F. Priolo, E. Napolitani, and A. Carnera, "Flash lamp annealing with millisecond pulses for ultra-shallow boron profiles in silicon", *Nucl. Instrum. Meth. B*, vol. 186, no. 1-4, pp. 287–291, 2002.

[43] C. Wündisch, M. Posselt, B. Schmidt, V. Heera, T. Schumann, A. Mücklich, R. Grötzschel, W. Skorupa, T. Clarysse, E. Simoen, and H. Hortenbach, "Millisecond flash lamp annealing of shallow implanted layers in Ge", *Appl. Phys. Lett.*, vol. 95, no. 25, p. 252 107, 2009.

[44] M. Bidaud, H. Bono, C. Chaton, B. Dumont, V. huard, P. Morin, L. Proencamota, R. Ranica, and G. Ribes, "High-activation laser anneal process for the 45 nm CMOS technology platform", in *Advanced Thermal Processing of Semiconductors, 2007. RTP 2007. 15th International Conference on*, 2007, pp. 251–256.

[45] F. Lanzerath, D. Buca, H. Trinkaus, M. Goryll, S. Mantl, J. Knoch, U. Breuer, W. Skorupa, and B. Ghyselen, "Boron activation and diffusion in silicon and strained silicon-on-insulator by rapid thermal and flash lamp annealings", *J. Appl. Phys.*, vol. 104, no. 4, p. 044 908, 2008.

[46] T. Miyashita, T. Kubo, Y. S. Kim, M. Nishikawa, Y. Tamura, J. Mitani, M. Okuno, T. Tanaka, H. Suzuki, T. Sakata, T. Kodama, T. Itakura, N. Idani, T. Mori, Y. Sambonsugi, A. Shimizu, H. Kurata, and T. Futatsugi, "A study on millisecond annealing (MSA) induced layout dependence for flash lamp annealing (FLA) and laser spike annealing (LSA) in multiple msa scheme with 45 nm high-performance technology", *Int. El. Devices. Meet.*, pp. 1–4, 2009.

[47] Y. He, B. Wu, G. Yu, Y. C., H. Liu, W. Lu, J. Wu, D. W. Zhang, C. Wang, J. Y. Tang, and G. Zhao, "Process match between DSA and LSA for ultra-shallow junction formation", in *Junction Technology (IWJT), 2012 12th International Workshop on*, 2012, pp. 77–80.

[48] S. Chen, X. Wang, M. Thompson, Y. Wang, C. Lu, and J. McWhirter, "Characterization of dopant activation, mobility and diffusion in advanced millisecond laser spike annealing", in *Advanced Thermal Processing of Semiconductors (RTP), 2010 18th International Conference on*, 2010, pp. 66–70.

[49] J. T. Verdeyen, *Laser Electronics*. Upper Saddle River, New Jersey: Prentice Hall, Inc., 1995, pp. 8–62.

[50] M. Born and E. Wolf, *Principles of optics: electromagnetic theory of propagation interference and diffraction of light*. Cambridge, UK: Cambridge University Press, 2003, pp. 286–312.

[51] B. Jung, J. Sha, F. Paredes, M. Chandok, T. R. Younkin, U. Wiesner, C. K. Ober, and M. O. Thompson, "Kinetic rates of thermal transformation and diffusion in polymer systems measured during sub-millisecond laser-induced heating", *ACS Nano*, vol. 6, no. 7, pp. 5830–5836, 2012.

[52] J. Sha, B. Jung, M. O. Thompson, C. K. Ober, M. Chandhok, and T. R. Younkin, "Submillisecond post-exposure bake of chemically amplified resist by CO_2 laser spike annealing", *J. Vac. Sci. Technol. B*, vol. 27, no. 6, pp. 3020–3024, 2009.

[53] B. Jung, J. Sha, F. Paredes, C. K. Ober, M. O. Thompson, M. Chandhok, and T. R. Younkin, "Sub-millisecond post exposure bake of chemically amplified resists by CO_2 laser heat treatment", *Proc. SPIE*, vol. 7639, pp. 1–9, 2010.

CHAPTER 2

THIN PLATINUM RESISTORS FOR SPATIAL AND TEMPORAL PROFILES DURING MILLISECOND LASER SPIKE ANNEALING

2.1 Introduction and Motivation

Laser spike annealing (LSA) is a potential solution for limiting the enhanced transient diffusion (TED) of dopants while improving their activation levels as the critical dimensions of shallow junctions push toward 10 nm dimensions [1–4]. The technique utilizes a line-focused continuous wave (CW) laser beam, which is scanned across the substrate to reach peak temperatures approaching the substrate melting point in dwell times (τ_{dwell}) as short as 10 μs. The surface of the substrate is rapidly heated at 10^4-10^5 K/s for dopant activation followed by rapid quenching of the surface through the thermal conduction into the substrate.

Temperature and time control for dopant activation is critical, regardless of the annealing method. For spike annealing techniques including LSA and flash lamp annealing (FLA), both the dopant activation levels and lateral diffusion of species depend heavily on a peak temperature. For this reason, temperature measurements during millisecond annealing techniques are important for eliminating the uncertainties associated with the coupling of laser radiation into the substrate surface and the complexities in heat transport across thin-film structures above the substrates.

Several techniques have been established in the past to measure the absolute temperatures during the rapid thermal processes. Optical pyrometry, which

measures the thermal radiation emitted from the substrate during the anneal, is popular [5]. For millisecond LSA, the radiation is collected by optics placed above the annealing substrate, which is converted to temperature for a real-time temperature measurement [6]. However, this non-contact technique is challenging due to the long absorption length of IR wavelengths in Si substrates, coupled with steep temperature gradients during millisecond τ_{dwell}. In addition, optical pyrometry is an indirect measurement of temperatures and low temperature measurements are particularly challenging [7].

For direct contact temperature measurements during rapid thermal processing, thermocouples on Si wafers and thin-film resistors have been well-established. While thermocouples on Si wafers provide absolute temperatures for chamber based annealing techniques, such as rapid thermal annealing (RTA) in ~100 ms time frames, they are difficult to fabricate and measure with high spatial resolution in micrometer scale and with sub-ms temporal resolution [8]. Alternatively, thin-film based resistors offer advantages in both spatial and temporal resolution [9, 10]. These sensitive resistors can be patterned at sub-micron dimensions while maintaining high sensitivity and bandwidth. Spatial scales can be defined lithographically and the time response is limited only by the RC time constant of the system, which can be designed to MHz levels [11].

In this work, platinum thin-film resistors were fabricated and utilized for direct temperature measurements during the millisecond LSA of Si wafer substrates. These resistor devices (hereby referred to as "thermistors") are thermally small compared to the incident laser beam, enabling high spatial resolution and temperature profiles. Characterization including fabrication, calibration, and analysis methodologies are presented in detail. Temperature data

obtained from this work were used to understand laser-induced heating of polymers and small molecules.

2.2 Fabrication and Characterization Methods

2.2.1 Device Fabrication

Thermistor devices were lithographically patterned on thermally oxidized (100 nm) Si wafers. Boron-doped wafers with $\rho \sim 0.01$-0.02 Ω·cm were used for the CO_2 laser (λ = 10.6 μm) to couple the far-infrared beam with the Si substrate through free-carrier generation at room temperature. Lightly doped Si substrates $\rho \sim$ 10-20 Ω·cm were used for profiling the near-infrared diode laser (λ = 980 nm).

Two mask levels were used to pattern the thermistor through contact lithography. First, the device layer (Figure 2.1a) was patterned by lift-off using a Shipley 1805 resist patterned on top of LOR5A polymer to enhance undercut during lift-off. Approximately 40 nm thick Pt film was deposited on a 2 nm Cr adhesion layer. The resistor devices were formed using Shipley 1165 stripper to remove the lift-off resist. To reduce series and contact resistances, the Pt contact pads were strapped by an additional 250 nm of Ni using a second mask layer as shown in Figure 2.1b. The center of the thermistor device consisted of six different probes: two device probes along with additional probes at top and bottom for two separate 4-pt measurements (Figure 2.1c). At the center, the thermistor device was designed to be ~2 μm wide and 40 nm thick. The length between top contact wires at center were designed to be 10 μm long while bottom con-

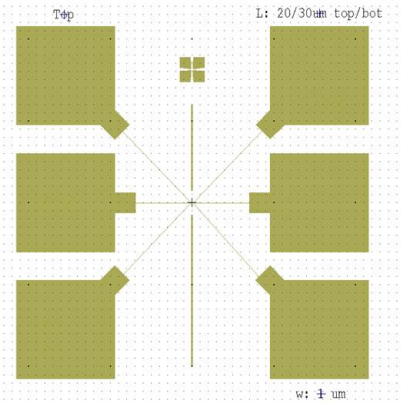

a) Device layer (Pt)

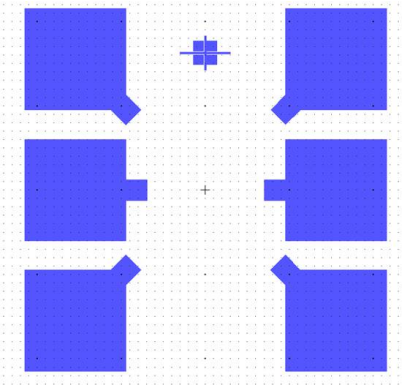

b) Contact layer (Ni)

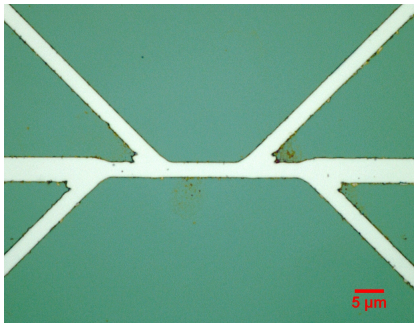

c) 4-Terminal device

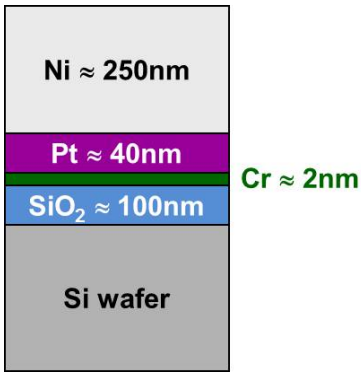

d) Cross-section schematics of a contact pad

Figure 2.1: Layout used for thermistor fabrication. Dimension of individual device is a 9 mm square. Platinum device at center was designed to be 2 μm in width and 40 nm thick. The length between top contact wires were designed to be 10 μm long while bottom contact wires are 30 μm, giving calculated resistance of 13.25 Ω and 39.75 Ω respectively.

tact wires were 30 μm long, giving calculated resistances of 13.25 Ω and 39.75 Ω respectively.

Patterned wafers were diced into 9 mm square devices and were furnace annealed for 5 min at 500 °C in N_2 environment to reduce resistance at the Pt and Ni interface. Each device was subsequently epoxy glued to a dual in-line package and wire-bonded for rigid measurements as shown in Figure 2.2a. Due

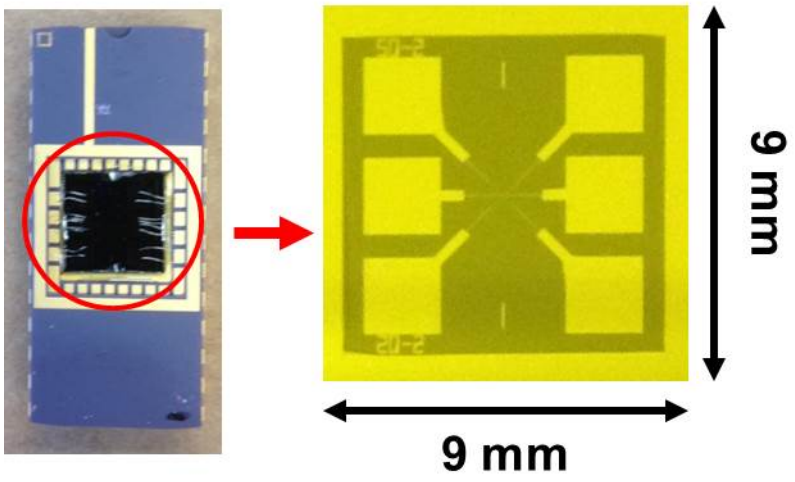

a) Fabricated and packaged thermistor

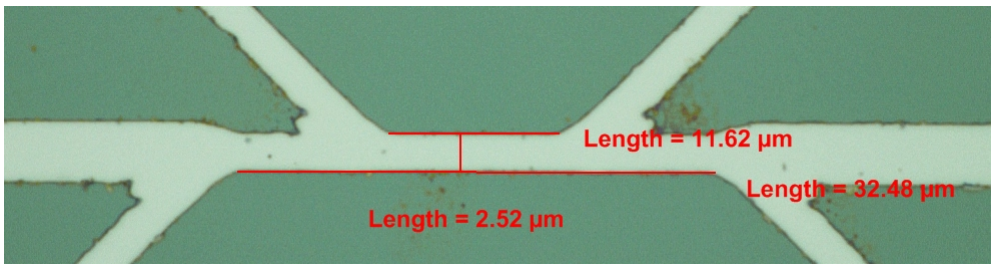

b) Actual dimensions of fabricated 4-pt device

Figure 2.2: Devices used for temperature measurements. Actual dimension of the device used for this study was 2.52 ± 0.13 μm in width and 40 nm thick. Distance between top contact wires were 11.9 ± 0.68 μm while the bottom contact wires were 32.6 ± 0.43 μm. The measured resistances were 36.2 ± 1.5 Ω using top contact wires and 64.2 ± 2.3 Ω respectively.

to the variations in lithographic patterning and Pt thicknesses, the measured resistance between devices varied slightly. As shown in Figure 2.2b, fabricated devices used for this study had a device width of 2.52 ± 0.13 μm with 40 nm thick Pt. Measured distances between top contact wires were 11.9 ± 0.68 μm, while the bottom contact wires were 32.6 ± 0.43 μm. On average, the measured 4-pt resistance of the top contact was 36.2 ± 1.5 Ω, while the bottom contact was 64.2 ± 2.3 Ω.

2.2.2 Data Acquisition and Signal Amplification

Each device was irradiated on the LSA system (Figure 2.3) with either CO_2 or diode laser. For the CO_2, the incident beam was line-focused with a Gaussian full width half maximum (FWHM) of 90 μm in the scan direction and 588 μm in the lateral direction (Figure 1.15). The diode laser was also line-focused and homogenized in order to give a 2.45 mm "flat-top" intensity profile in the lateral direction and a 236 μm FWHM in the scan direction (Figure 1.18).

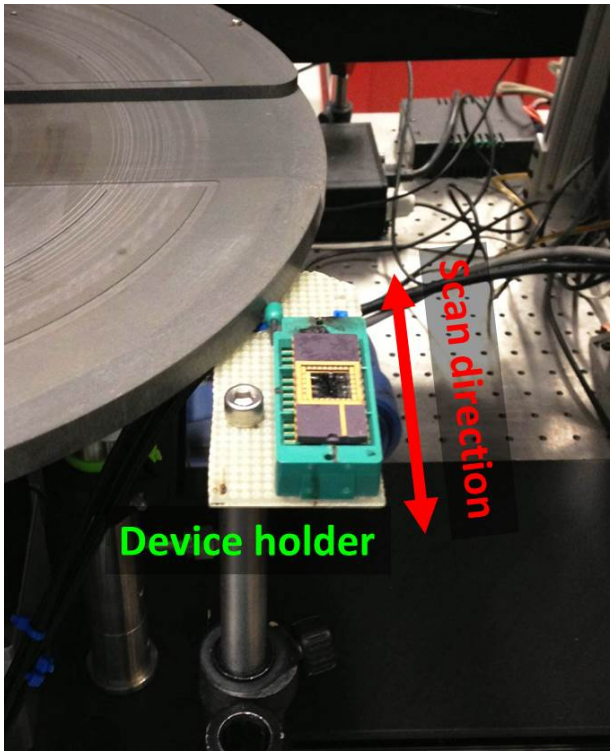

Figure 2.3: Packaged thermistor device and stage holder for resistance change measurements during millisecond laser spike annealing.

The spatial resolution of the thermistor device is determined by the dimension perpendicular to the scan direction. As shown in Figure 2.1c, 10 and 30 μm device lengths are sufficiently small compared to the long axis length of both

laser beams. The temporal resolution on the other hand is determined by the width of the device in the scan direction. The temporal resolution can be approximated by dividing this width by the scanning velocity. Given that the scanning velocity for the millisecond LSA ranged from 20 mm/s to 400 mm/s over a 2.5 μm wide thermistor device, the temporal resolution is on the order of 6.25 to 125 μs. These temporal resolutions are also sufficiently small compared to the analyzed τ_{dwell} ranging from 250 μs to 10 ms. For measuring the resistance change (current and voltage changes) as shown schematically in Figure 2.4, an oscilloscope (Tektronix TDS2012) with 3 ns response time was used.

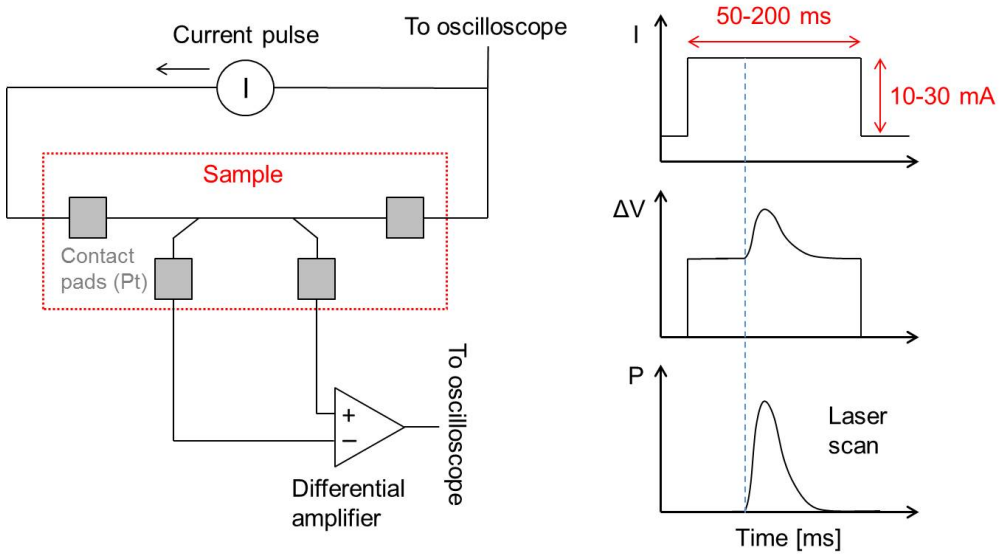

Figure 2.4: Schematics of thermistor measurement. The current in the thermistor is pulsed on prior to laser scan. The differential voltage on the 4-pt taps respond to temperature changes as the laser scan crosses the device. The current pulse is terminated to prevent I^2R heating of the sample on seconds time frame.

The full circuit for current and voltage measurements are shown in Figure 2.5. To prevent I^2R heating of the thermistors, a pulser (Stanford DG535) was used to bias the system to +1 V for a short duration ranging from 50 ms

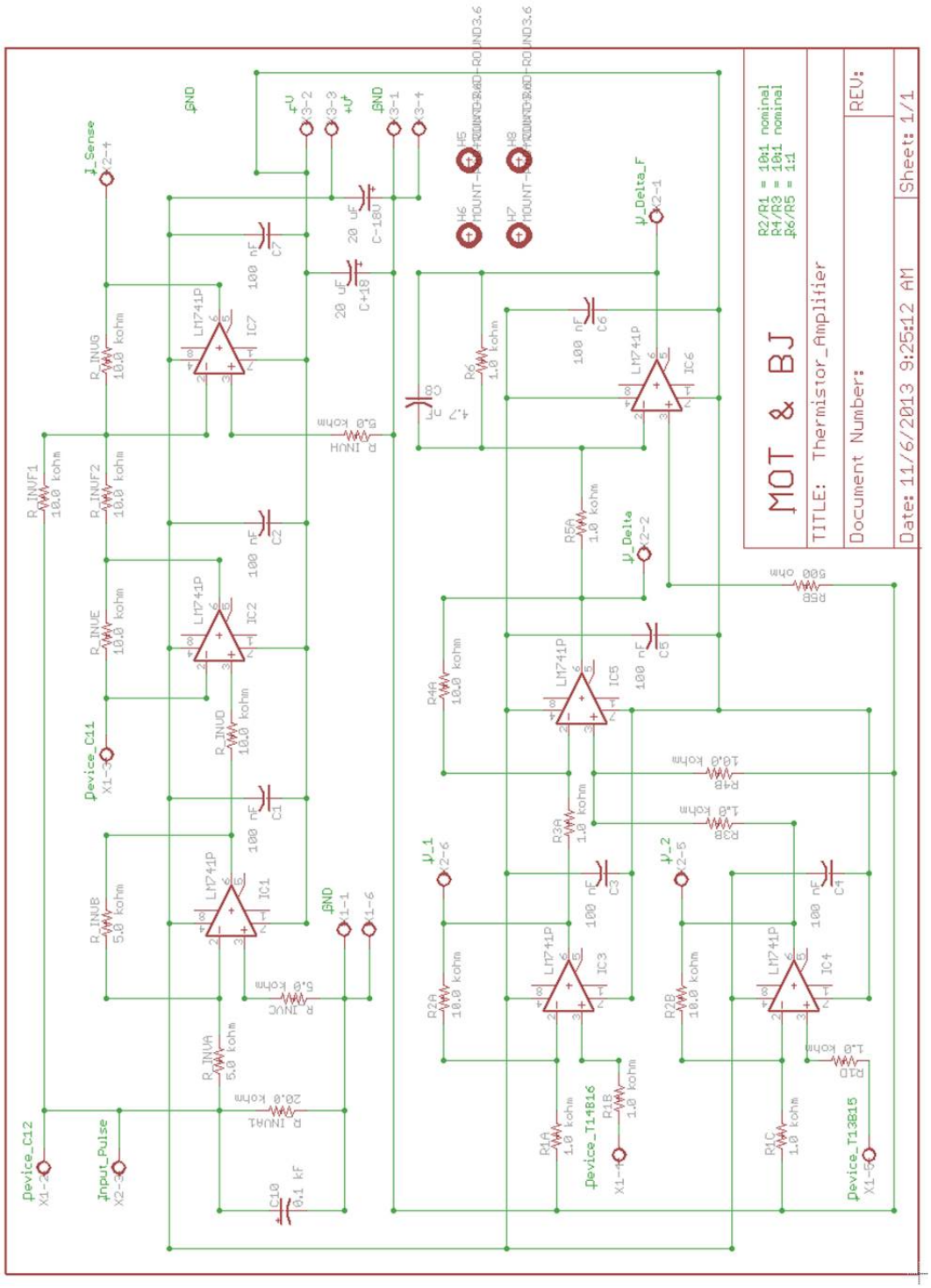

Figure 2.5: Schematic of the full circuit used to amplify current and voltage change of Pt thermistors during millisecond LSA. Both current and differential voltages are amplified for capture with a high-speed oscilloscope.

to 200 ms with the laser scan contained within these time frames. Since noise in measurements are inevitable due to the stability of the scanning hardware (linear motion stage and mechanical shutters), a series of operational amplifiers (LM741CN) were used to amplify the current and voltage changes during millisecond LSA.

Figure 2.6 shows an example of typical signals collected from the oscilloscope. The current and voltage drops across the thermistor were measured during each laser scan. Resistance change is obtained from these two curves through Ohm's law, demonstrating that peak resistance change at a power and dwell can be obtained at high temporal resolutions (25 μs for the shown τ_{dwell} = 900 μs). To increase the accuracy of the resistance measurement, at least three measurements for every LSA power at τ_{dwell} were averaged to produce peak temperatures from the temporal profiles.

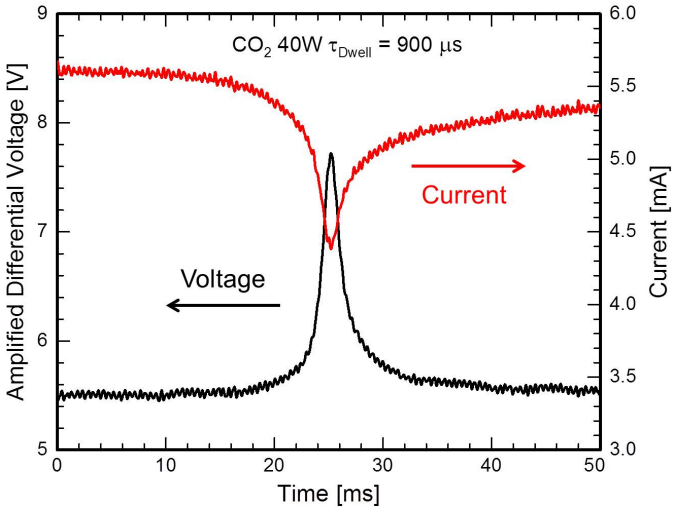

Figure 2.6: Typical data obtained from a single thermistor scan at 40 W (≈1050 °C) at τ_{dwell} = 900 μs. Amplified differential voltage from the thermistor and current were obtained to calculate the resistance change. As the laser heats the thermistor, the increased temperature reduces the current and increases the voltage delta between the taps.

2.2.3 Resistance Measurements and Absolute Calibrations

Typical Resistance Measurements

For a single laser scan over the thermistor device at a given power and τ_{dwell}, the peak resistance change (ΔR_{max}) can be measured. Figure 2.7a shows the temporal profile during a 250 μs dwell, where ΔR_{max} can be obtained for τ_{dwell} = 250 μs. The measured ΔR_{max} can also be obtained as a function of laser power for a

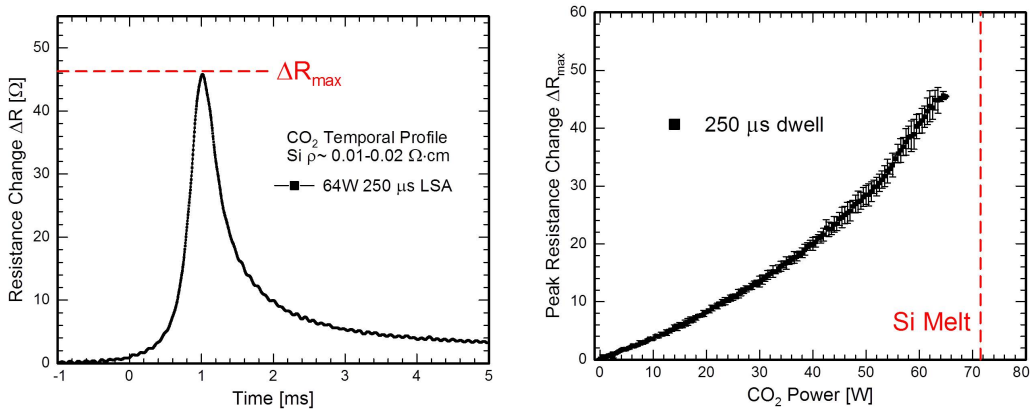

a) CO_2 temporal profile

b) Peak resistance change vs. power

Figure 2.7: Identifying the peak resistance change ΔR_{max} from a thermistor device. a) Resistance change which corresponds to substrate temperature change can be obtained as a function of time at a high resolution, showing rapid heating and cooling in a few milliseconds. A single laser scan at τ_{dwell} = 250 μs is shown. b) Collected ΔR_{max} as a function of power for a 250 μs dwell. The curve deviates from the expected linearity potentially due to the slip in atomic planes of Si substrates, limiting carrier motion near melt.

given dwell time, as shown Figure 2.7b for 250 μs. The ΔR_{max} is a continuous function with temperature as expected. To correlate the measured ΔR_{max} with temperatures, a calibration using a reference point is required as discussed below.

Using the Temperature Coefficient of Resistance

For obtained resistance changes, it is extremely important to identify an absolute temperature for a given power at τ_{dwell}. The resistance change of Pt film is expected to be directly related to temperature by the following relation,

$$R = R_0 (1 + \alpha \Delta T) \tag{2.1}$$

where α is the temperature coefficient of resistance (TCR) for Pt, ΔT is $T - T_0$, and R_0 is the Pt resistance at a reference temperature T_0 [12]. At sufficiently low temperatures up to ~300 °C, the TCR is expected to be a constant [13]. Since the resistance change of Pt is expected to be linear with temperature, each thermistor device was initially calibrated under known temperatures up to 200 °C using a hot-plate. Once the TCR was obtained from a thermistor device, it can be linearly extrapolated to the laser-induced heating regimes up to the Si melt threshold.

TCR data obtained from the hot-plate heating on two thermistor devices are shown in Figure 2.8a. For temperatures up to 200 °C, the calibration data fit extremely well to give a constant TCR value of $1.83 \times 10^{-3} \pm 8.6 \times 10^{-5}$ °C^{-1}. This value is lower than the reported TCR value of 3.85×10^{-3} °C^{-1}) for bulk Pt and 3.16×10^{-3} °C^{-1} for 350 nm thick Pt on a Si substrate [14]. The TCR obtained from the hot-plate calibration can be extrapolated up to the resistance change (ΔR) that corresponds to the Si melt at 1414 °C. Ideally this TCR is a constant for the fabricated thermistor device, and the measured peak ΔR at a laser power and τ_{dwell} can be referred to a peak temperature using the extrapolated curve. This analysis is shown in Figure 2.8b for three dwells at temperatures just below the substrate melt threshold. In this plot, the extrapolation of the hot-plate data indicated an expected resistance change of 65.5 Ω at the Si melting point

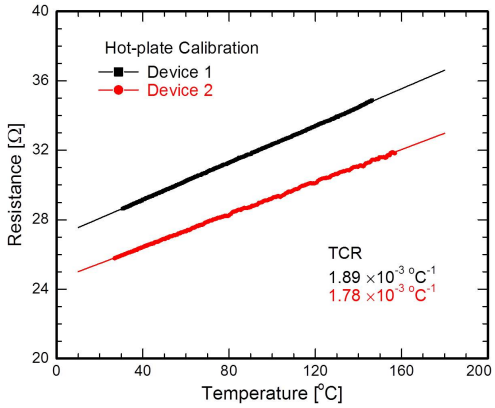

a) Hot-plate calibration of thermistor

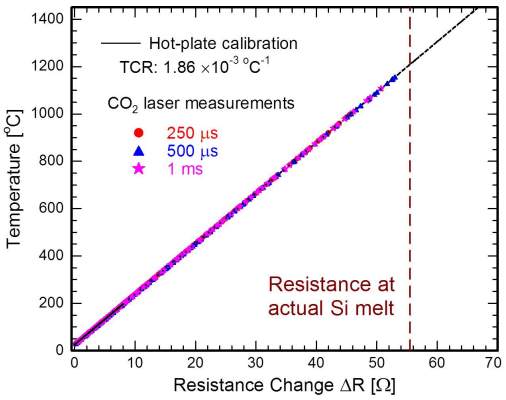

b) Measured resistance change and inferred temperatures during CO_2 laser scans

Figure 2.8: Attempts to quantify the absolute temperature of resistance change for thermistors. a) Resistance as a function of temperature for two thermistor devices using hot-plate heating under known temperatures. b) Measured resistance change and inferred temperature obtained from the hot-plate calibration for three dwells. TCR extrapolations at actual Si melt (1414 °C) are low by ≈200 °C.

(1414 °C). However, experimental measurements near the melt laser power gave $\Delta R \approx 55.5\ \Omega$ at 1414 °C, suggesting an alternate calibration method must be used in order to establish the absolute temperature from the measured ΔR.

Using the Absolute Melt of Silicon and Gold

The observed resistance change (Figure 2.7b) were calibrated to absolute melt temperatures of the Si substrate and deposited Au thin-films. To observe the Si melting point, tracks following a laser scan were analyzed using optical dark field. The melt is expected to occur starting at the center of the beam which has the highest beam intensity giving rise to a peak substrate temperature. As an example, Si melt threshold is shown as a function of laser power for 500 μs in Figure 2.9.

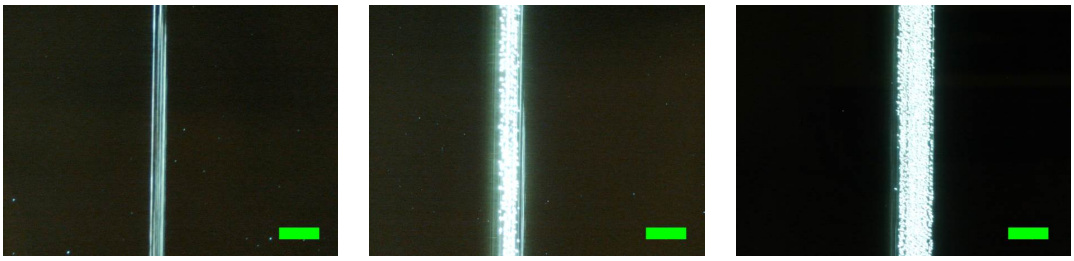

a) CO_2 60.8 W 500 μs b) CO_2 63 W 500 μs c) CO_2 66 W 500 μs

Figure 2.9: Identifying the Si melt threshold using dark field images of optical microscope. The Si melt tracks are visible starting from 60.8 W of CO_2 intensity. All scale bars correspond to 20 μm.

The Si melt tracks can be identified with distinction due to light scattering from the roughened surface of melted Si substrate. As laser powers increase beyond 60.8 W (Si melt threshold), the width of the melt track increases due to the expansion of the beam area, which corresponds to temperatures beyond Si melt at 1414 °C. The threshold power for Si melt is expected to change as a function of dwell time, and Table 2.1 summarizes the observed melt during either CO_2 or diode LSA. While the Si melt threshold can be achieved for τ_{dwell} = 0.2-10 ms using a CO_2 laser at 120 W, the diode laser at Cornell was limited to a source with 155 W cap in laser power which prevented melt analysis below 7.5 ms dwell.

Using the observed melt threshold values, the observed ΔR_{max} was converted to absolute temperature. Measured ΔR_{max} values were extrapolated linearly to the Si melt power, which was assigned as 1414 °C. Linearity of ΔR_{max} with temperature was assured. For ΔR_{max} values obtained using CO_2 for 250 μs (Figure 2.7b), the non-linear curve was calibrated to the Si melt threshold at 71.5 W, resulting in Figure 2.10. The ΔR_{max} and the resulting temperature are limited only up to ~15 % of the observed Si melt due to thermally generated dislocations in the substrate and/or the atomic agglomeration at the Pt and Cr interface [13].

Table 2.1: Observed threshold for Si melting during either CO_2 or diode LSA. Silicon substrate resistivity were 0.01-0.02 Ω·cm and 10-20 Ω·cm for CO_2 and diode LSA respectively. All substrate thickness was 500-550 μm.

τ_{dwell} [ms]	CO_2 power [W]	Diode power [W]
0.25	71.5	-
0.50	60.8	-
0.75	56.5	-
1.0	53.5	-
2.0	47.5	-
3.0	45.9	-
5.0	44.8	-
7.5	-	152
8.75	-	135
9.5	-	128
10.0	42.8	124

To confirm the temperature calibration using the absolute melting point of Si, a second calibration point was introduced using Au melt. Aluminum was also investigated, but a significant oxidation was observed near the melting temperatures which made the identification of melt threshold difficult. To identify Au melt power thresholds during LSA, 2 μm and 5 μm Au squares spaced 20 μm apart (center to center spacing) were deposited onto the Si substrate as a 50 nm film. The size of the Au squares were sufficiently small to minimize IR reflection.

The Au squares were scanned with either CO_2 or diode laser until the threshold power at a dwell for melt was identified. For powers up to melt threshold,

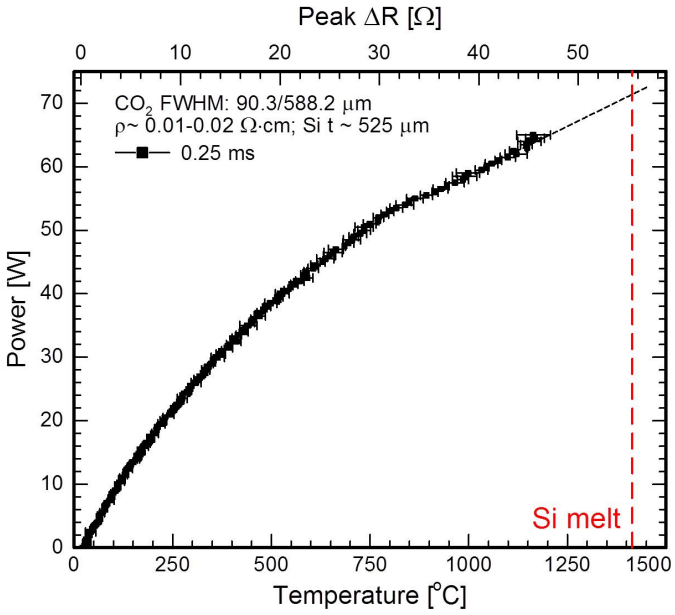

Figure 2.10: Substrate temperature during a 250 μs CO_2 laser scan. Resistance change was calibrated to the absolute melt of Si at 71.5 W, which corresponds to 1414 °C.

no significant structural changes were observed under either optical microscope or SEM (Figure 2.11). These chemically inert Au squares show minimal oxidation below its melt, and immediately form spheres once a threshold power is reached as shown in Figure 2.11i. Au melt threshold powers were collected as a function of dwell times and were used as a second calibration point to confirm the temperature calibration obtained using Si melt. No significant difference in the Au melt threshold was observed between the 2 and 5 μm squares, confirming the minimal impact of the squares on the thermal behavior.

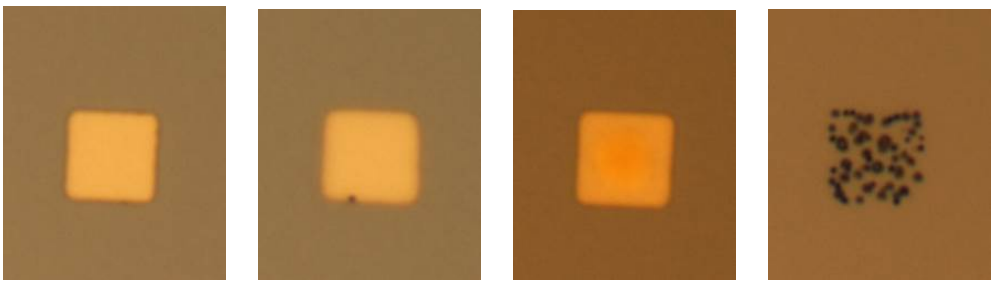

a) No laser b) 70 % to threshold c) 80 % to threshold d) Melt threshold

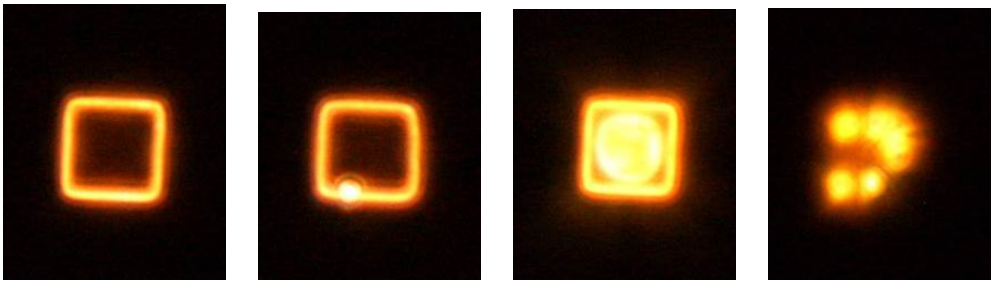

e) No laser f) 70 % to threshold g) 80 % to threshold h) Melt threshold

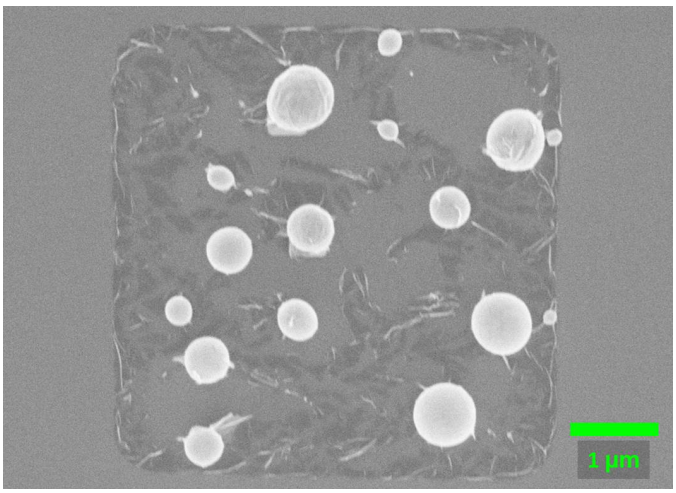

i) SEM image at melt threshold

Figure 2.11: Identifying the Au melt threshold using bright field optical, dark field optical, and scanning electron microscopes. The Au melt thresholds are clearly defined as it is chemically inert where oxidation is minimal. Au squares form spheres beyond melt threshold. CO_2 laser was used for melt calibration shown above. All gold squares are 5 μm in size and 50 nm thick.

2.3 Results and Discussion

2.3.1 CO_2 Laser Temperature Measurements and Behavior

The peak resistance change ΔR_{max} can be obtained from the temporal profiles along with the relationship between power and temperature as shown in Figure 2.10 for a 250 μs CO_2 laser heating. To ensure and confirm correct temperature calibration, Au melt threshold at 250 μs was identified at 60 W (equivalent to T_{melt} at 1064 °C) which overlaps the calibrated curve as shown in Figure 2.12a.

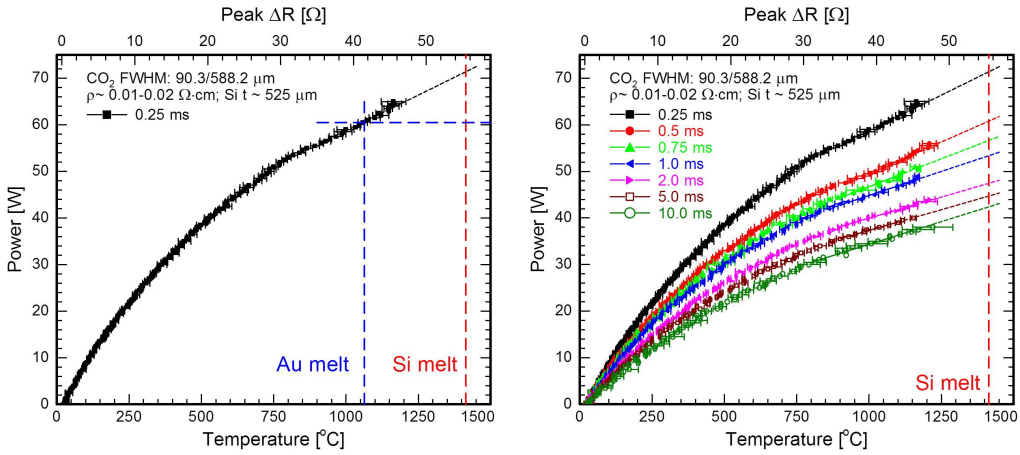

a) Confirming 250 μs calibration

b) CO_2 peak temperatures

Figure 2.12: CO_2 temperature calibration. a) Confirming correct temperature calibration using the observed melt of gold. b) Temperature calibration shown for dwell times ranging from 250 μs to 10 ms.

These curves can be replicated for virtually all dwell times as long as the stage is capable of moving at respective velocities. As an example, power vs. temperature for dwell times ranging from 250 μs to 10 ms is shown in Figure 2.12b. While the curve shapes are similar, the temperature corresponding to the absolute power is a strong function of dwell time for 1 ms and below.

This power vs. τ_{dwell} relationship can be explicitly described at a constant ΔR_{max} (constant peak temperature) or at the absolute melt of Si and Au as shown in Figure 2.13.

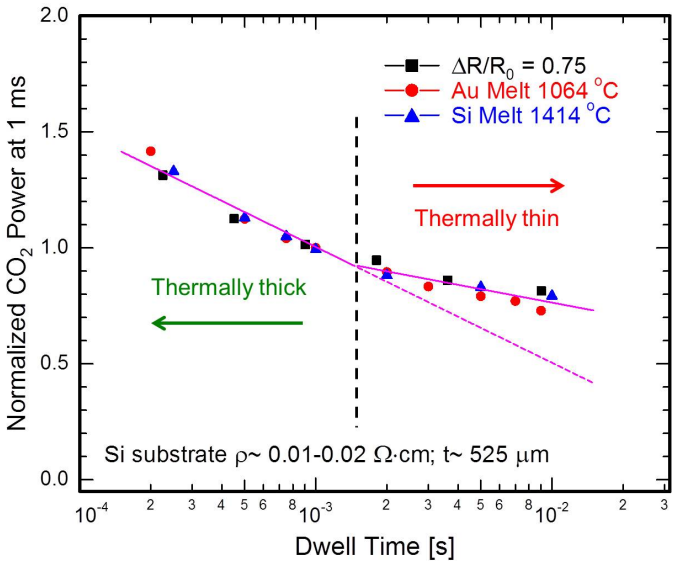

Figure 2.13: Power vs. dwell relationship for the millisecond CO_2 LSA using Au melt, Si melt, or a constant peak temperature (peak resistance change) of a thin-film Pt resistor.

In Figure 2.13, CO_2 laser powers for Au melt, Si melt, and thermistor $\Delta R/R_0$ were normalized to the respective powers at τ_{dwell} = 1 ms. These powers are plotted as a function of dwell time on a logarithmic scale. Two distinct behaviors are observed before and after ~1.5 ms dwell, suggesting a change in the quench behavior through thermal conduction into the Si substrate. The thermal diffusion length for substrate quenching following LSA can be estimated. The thermal diffusivity of Si is 0.8 cm^2/s and the thermal diffusion length $L \sim \sqrt{4 D \tau_{dwell}}$ for quench is ~690 μm for 1.5 ms τ_{dwell}, which is comparable to a standard 4 inch Si wafer thickness at ~525 μm. Below τ_{dwell} = 1.5 ms, the wafer is "thermally thick" and heat flow can assume the substrate to be infinite. Above τ_{dwell} = 1.5 ms, the finite thickness of the substrate is "felt" and

enters the "thermally thin" regime, where the heat flow becomes dependent on the quality of heat sinking to the wafer chuck.

As long as the substrate resistivity is constant, the power vs. τ_{dwell} plot is a powerful tool for estimating the peak substrate temperature at any LSA τ_{dwell}, corresponding to a known power at τ_{dwell}. For a ~525 μm thick Si substrate with resistivity $\rho \sim 0.01\text{-}0.02\ \Omega\cdot$cm, the relationship between the CO_2 power and τ_{dwell} shown in Figure 2.13 can be described by $P = -0.499\,\tau_{dwell} - 0.493$ and $P = -0.192\,\tau_{dwell} - 0.379$ for τ_{dwell} less than and greater than 1.5 ms respectively.

The large thermal diffusion length at long τ_{dwell} has a significant impact on ΔR measurement during the millisecond LSA. Ideally, the resistance change is directly proportional to the substrate temperature, which results in identical curve-shapes when the normalized ΔR is plotted as a function of the normalized laser power for any τ_{dwell}. This curve is shown in Figure 2.14a for τ_{dwell} = 0.25-1 ms. The normalized resistance curves for all dwell times overlap with each other. While the resistance curves are non-linear with substrate temperature (laser power), they remain directly proportional to each other during the sub-millisecond LSA. However, as the substrate becomes "thermally thin" for τ_{dwell} >1.5 ms, the proportionality constant between resistance and temperature shifts. Figure 2.14b shows an additional resistance curve at 2 ms, where the absolute ΔR is much higher than the expected values due to the chuck heat transfer effect. The large variations in the resistance behavior in Figure 2.14b further confirms the importance of identifying Si and Au melts to calibrate the measured ΔR, rather than relying on conventional approach using TCR extrapolations.

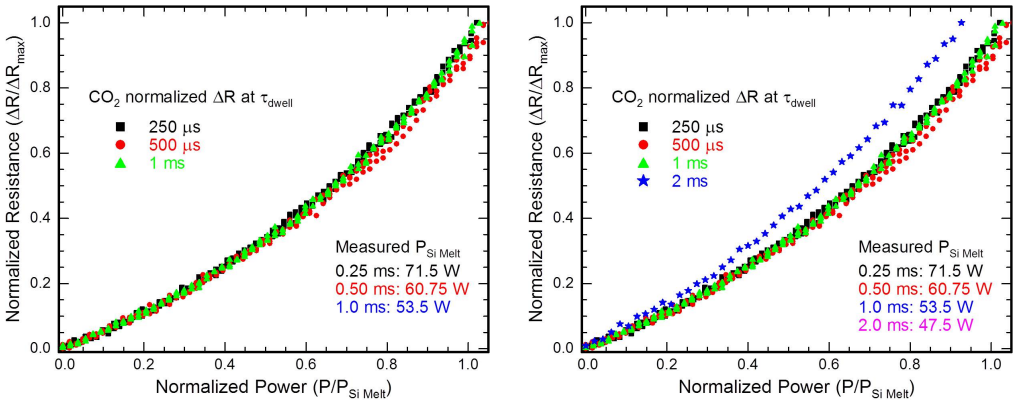

a) Resistance directly proportional to power

b) Thermally thin for τ_{dwell} >2 ms

Figure 2.14: Normalized resistance change as a function of the normalized power for a range of τ_{dwell}. The resistance is non-linear with LSA powers (temperatures), but remains directly proportional. a) Consistent curve-shape is observed for dwell times up to 1 ms. b) Thermally thin behavior is observed for 2 ms.

2.3.2 Effects of substrate slip at high temperatures

Thermal-induced generation and propagation of dislocation arrays in Si substrates have been extensively studied since the 1970's [15–17]. At temperatures beyond 1000 °C, the thermal stresses across the temperature gradient generates dislocations, which propagates to show "slip lines" upon selective etching of the substrate. Dislocations formed in devices, such as pn junctions, can increase leakage current and affect the overall device yield.

When annealing thermistors at high peak temperatures, generated dislocations can also affect the resistance measurements while permanently damaging the device through plastic deformation. Once the thermistor is damaged, the resistance measurement on the same device cannot be reproduced as shown in Figure 2.15.

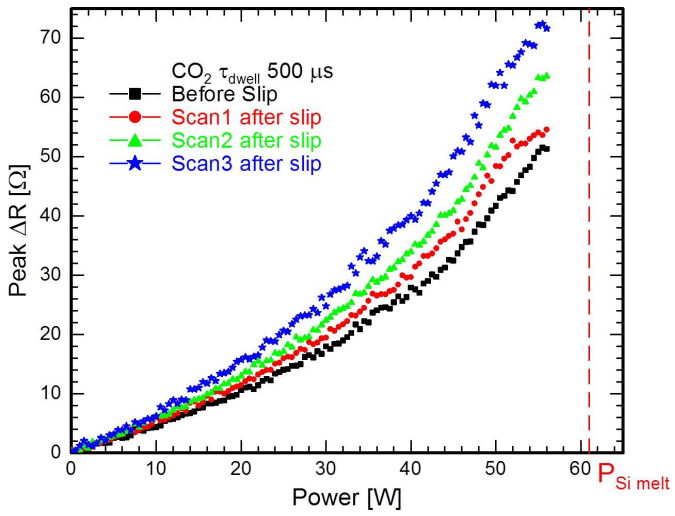

Figure 2.15: Effects of thermal stress on peak ΔR measurements. Generated dislocations ("slip lines") damages the thermistor device, where the resistance measurements cannot be reproduced.

A fresh thermistor device was measured up to 95 % of the Si melt threshold at 500 μs (58 W). The absolute ΔR on the first scans were comparable to other devices (Figure 2.12). However, subsequent scans showed increasing resistance as shown in Figure 2.15. The shape of the resistance curve remained the same, but the absolute ΔR values increase as the damaged device is subsequently annealed. This observation suggests additional generation of dislocations and/or propagation of existing dislocations for every laser scan beyond its slip threshold.

Experimentally, it is critical to stay sufficiently low in laser power to avoid slip and to confirm consistent ΔR during multiple scans over the same thermistor device. In general, laser powers up to 80 % of the Si melt threshold prevented change in ΔR. For temperature calibrations up to Si melt, the thermistor device must be sacrificed.

2.3.3 Diode Laser Temperature Measurements and Behavior

Methods for temperature calibration using the 980 nm diode laser were identical to that of the CO_2 laser. However, the substrate resistivity for the diode laser was much higher ($\rho \sim$ 10-20 Ω·cm) as beam coupling to the substrate does not require absorption through free carrier generation using heavily doped substrates. Identical thermistors were fabricated using lightly doped samples for the ΔR measurements using the diode laser.

Peak resistance change values, ΔR_{max}, were collected from the temporal curves and were calibrated to the absolute melt of Si, with temperatures as a function of power shown in Figure 2.16. This relationship between temperature

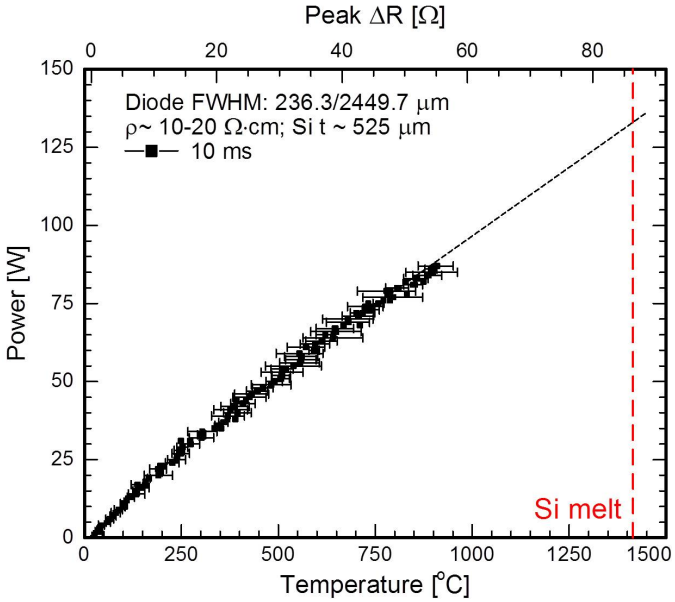

Figure 2.16: Diode laser temperature calibration for 10 ms τ_{dwell}.

and power can be obtained for dwell times within the stage velocity limits. For 10 ms τ_{dwell}, the curve shape is comparable to that observed for the CO_2 laser (Figure 2.12b). The power corresponding to any given temperature is higher for

the diode laser as the beam in much larger.

To effectively correlate the temperature vs. τ_{dwell}, the absolute melt of the Si substrate was obtained as a function of dwell time on a logarithmic scale as shown in Figure 2.17. Unlike the CO_2 laser power vs. τ_{dwell} where two distinct

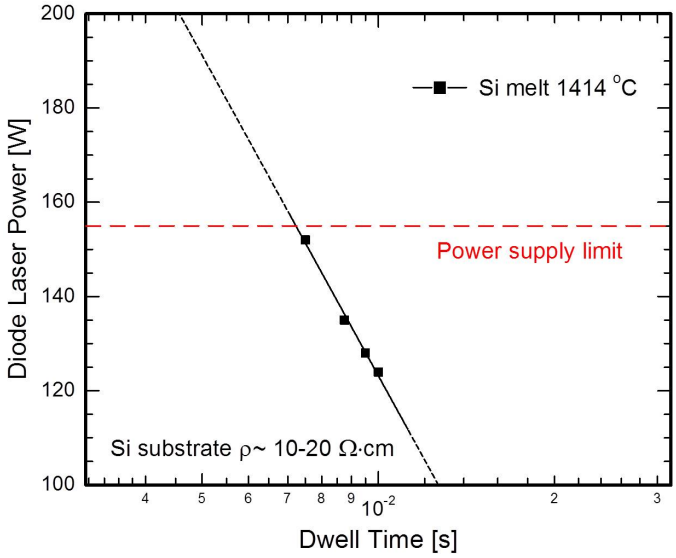

Figure 2.17: Power vs. dwell relationship for diode LSA obtained from observing Si melt. Higher laser power is required to achieve Si melt for τ_{dwell} < 7.5 ms.

slopes were observed due to the transition from thermally thick to thin, the diode power vs. τ_{dwell} relationship exhibits linearity with a steep slope between τ_{dwell} ranging from 7.5 ms to 10 ms. Due to the limitations in laser power supply, Si melt could not be obtained for τ_{dwell} < 7.5 ms. The thermal diffusion length is ~1500 μm for τ_{dwell} = 7.5 ms, far greater than the Si substrate thickness (~525 μm). This comparison confirms that the power vs. τ_{dwell} should be almost independent of τ_{dwell} between 7.5 ms and 10 ms as it remain in the thermally thin limit.

As long as the substrate resistivity is consistent, the power vs. τ_{dwell} is a

powerful tool to estimate the effective substrate temperature at any LSA τ_{dwell}. For Si substrate with resistivity $\rho \sim$ 10-20 Ω·cm, the relationship between the diode laser power vs. τ_{dwell} shown in Figure 2.17 can be described by P = $-226\,\tau_{dwell} - 330$.

2.3.4 Temporal Temperature Profiles

Using the Pt resistor devices, the temporal profile experienced by the sample during the millisecond LSA can be obtained for both CO_2 and diode lasers. Figure 2.18 shows the temporal profile using the CO_2 laser. For τ_{dwell} = 250 μs, the

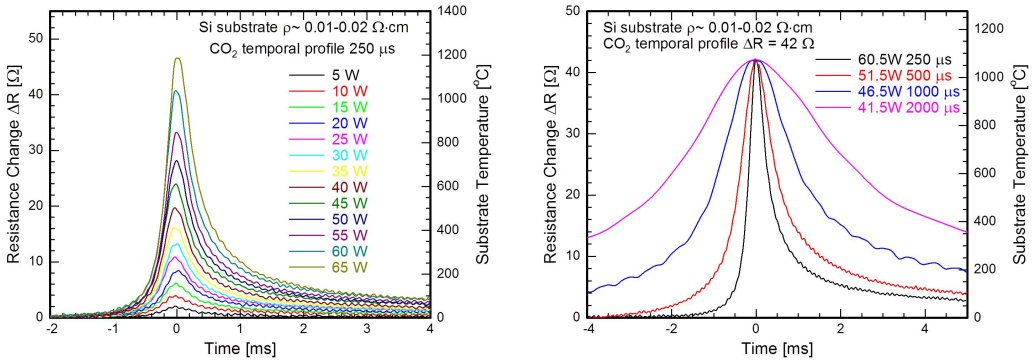

a) Temporal profile at constant τ_{dwell}

b) Temporal profile at constant peak temperature

Figure 2.18: Temporal profiles during CO_2 LSA as a function of a) power for constant τ_{dwell} at 250 μs, and b) τ_{dwell} at constant substrate temperature (ΔR_{max} obtained from a thermistor device.

substrate temperature begins to rise ~1 ms prior to the peak. After the laser passes, the sample begins to immediately cool through thermal conduction into the substrate bulk. After ~4 ms, the temperature drops to <100 °C. As the laser powers increase, the spike annealing behavior becomes more apparent as both heating and quenching rates increase dramatically.

The temporal profiles are plotted as a function of τ_{dwell} in Figure 2.18b, at a constant peak temperature. Significant broadening of the profile is observed for increasing τ_{dwell} due to the longer heating duration and thermal diffusion length, $L \sim \sqrt{4\,D\,\tau_{dwell}}$. This length is increased by 65 % as τ_{dwell} is increased from 250 μs to 2 ms.

Similar temporal profiles can be measured using the diode laser as shown in Figure 2.19 for τ_{dwell} = 10 ms. While the temporal profile for the diode laser show

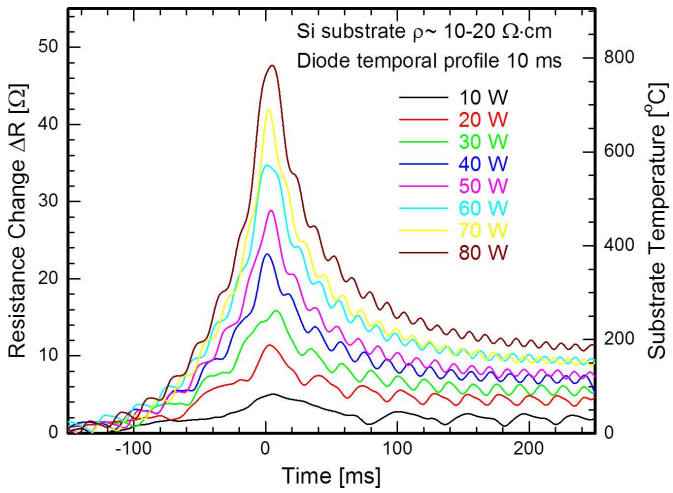

Figure 2.19: Temporal profile measured as a function of laser power during diode LSA for τ_{dwell} = 10 ms. Periodic waves are observed throughout all powers due to external effects.

similar rapid heating and quenching behaviors observed from the CO_2 temporal profiles (Figure 2.18), periodic waves are observed throughout all curves. These oscillations are potentially caused by the ripples from the power supply used for the differential amplifiers. The undesirable power frequency may become visible during long laser scans (τ_{dwell} = 10 ms), where the entire heating and cooling process can extend beyond 100 ms. However, these oscillations is not detrimental to the peak temperature measurements as demonstrated and shown previously in Figure 2.16.

2.3.5 Spatial Temperature Profiles

In the previous chapter, both CO_2 and diode laser profiles were obtained by measuring the beam intensities using photodiodes (Figures 1.15 and 1.18). While the beam intensity profiles provide good estimates for the beam dimensions and FWHM, the temperature profiles and gradient along the lateral direction (along the beam long axis) depend on the thermal diffusion into the substrate. The small device size of the thermistor allows measurement at the long axis profile.

The temperature profile along the long axis of the CO_2 beam on a B-doped Si ($\sim 5 \times 10^{18}$ cm^{-3}) and InP substrates were measured by stepping the thermistor device across the beam (Figure 2.20). Both spatial temperature and intensity

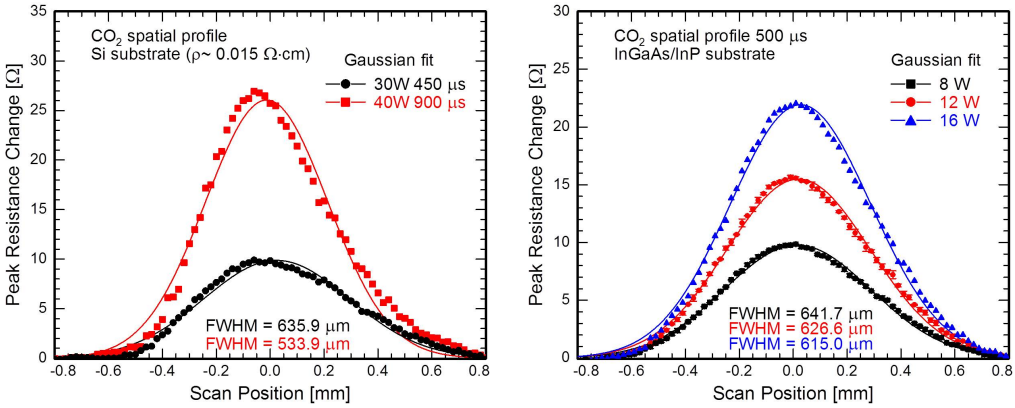

a) Si substrate b) InGaAs/InP substrate

Figure 2.20: Spatial temperature profiles during CO_2 LSA on a) B-doped Si substrate and b) InGaAs/InP substrates. On Si substrates, the measured FWHM between optical intensity profile and thermal profiles vary by less than 10 %. The variation in FWHM between Si and InP substrates are due to the differences in thermal diffusion broadening.

profiles can be approximated using a Gaussian function,

$$P_G(x \mid \mu, \sigma) = \frac{1}{\sqrt{2\pi\sigma^2}} \exp\left[-\frac{(x-\mu)^2}{2\sigma^2}\right] \tag{2.2}$$

with a mean μ and a standard deviation σ. The Gaussian exhibits a FWHM of $\sqrt{8\ln 2}\,\sigma \approx 2.355\,\sigma$. The observed FWHM from temperature profiles measured on both Si or InP substrates are 610 ± 44 μm, which is comparable to the FWHM obtained from intensity profiles at 588 μm.

Small variations in the FWHM between Si and InP substrates are due to the difference in InP thermal conductivity and thermal broadening. However, both substrates exhibit a decrease in FWHM as the laser power increases. For example, the FWHM at 8 W on InP substrate decreases by ~4.2 % when the laser power is raised to 16 W. The increase in FWHM at low powers suggests a wider thermal spread during the millisecond heating. This effect likely arise from the decrease in the substrate thermal conductivity with increasing temperature [18, 19]. During the millisecond LSA, only the top ~100 μm of the substrate is heated followed by quenching through the thermal conduction into the substrate. As the laser power increases, the thermal conductivity in these regions decreases and the lateral thermal diffusion becomes limited, subsequently making the temperature profile steeper resulting in a smaller FWHM.

Under the laser diode at millisecond dwells, substantially greater thermal broadening is expected. The spatial temperature profile of the homogenized diode laser was also measured. The diode beam intensity profile (Figure 1.18) exhibited an almost flat 2450 μm beam. Figure 2.21 shows the measured temperature profile for dwells from 1 to 10 ms. The temperature profiles follow a Gaussian-like distribution with a FWHM of 2300 ± 200 μm. Unlike the intensity profile which showed a uniform flat-top across 2.5 mm, lateral cooling by ther-

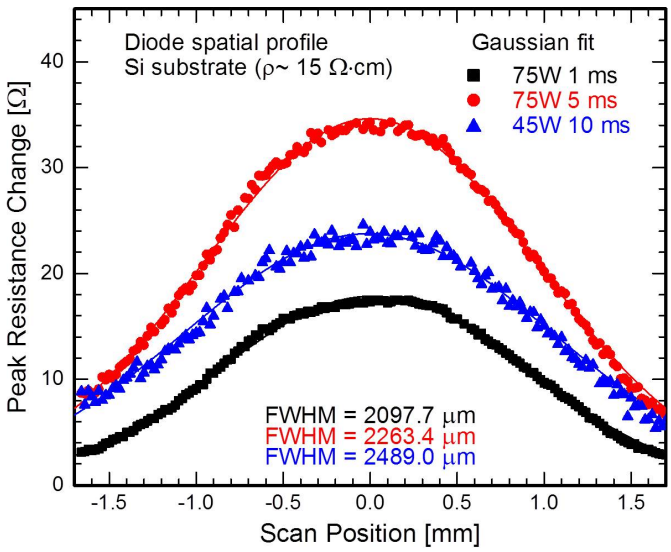

Figure 2.21: Spatial temperature profiles for diode LSA on an Si substrate. While the beam intensity is homogeneous across a 2450 μm width, lateral thermal conduction results in temperature profile that follows a Gaussian-like distribution.

mal conduction gives rise to the observed temperature profiles. As observed for CO_2 scans, the diode-induced temperature profiles also show an increase in FWHM at low powers. Experimentally, it is critical to acknowledge the existing temperature gradient across the long axis of diode laser beam despite the uniform laser intensity.

2.3.6 Comparison with Simulation

Temperature calibrations and measurements were compared with simulated data using a previously developed software, Cornell Laser Annealing Simulation Package (CLASP). The CLASP software was initiated and developed by K. Iyengar and M. O. Thompson, with key features including the ability to simulate the substrate thermal property during LSA, to model the CO_2 absorption

through the thermal and free carrier generation, and to provide information on optical coupling which rises from thin-films on the substrate [10, 20].

The laser absorption by thermal and free carrier generation are based on Klaassen's model for the absorption dependence on carrier concentration [21]. Input parameters such as the Si substrate reflectivity, line power density (W/cm), and doping concentrations were measured or calculated as shown in Appendix A.

Using CLASP, temporal profiles during a 500 μs CO_2 LSA were simulated and plotted as shown in Figure 2.22a. The shape of the simulated profiles are

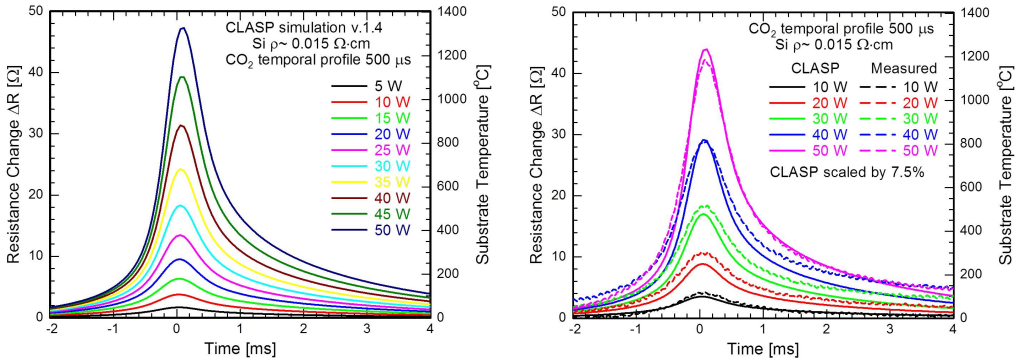

a) Simulated temporal profile CO_2 250 μs

b) Comparison between simulation and measurement

Figure 2.22: Temporal profiles during CO_2 LSA on a B-doped Si substrate ($\rho \sim 0.015$ Ω·cm. a) Simulated temporal profiles for a 500 μs dwell. b) Comparison between the simulated profiles and the measured profiles using Pt resistors. The simulated and the measured profiles are extremely comparable. Laser power was offset by 7.5 % to correspond with the experimentally observed Si melt and the measured temperatures.

similar compared to that of measured shown in Figure 2.18a, where the leading edge and the trailing edge of the profile (before and after the peak temperature) is consistent at a given power. As laser powers increase, the broadening of the profile due to the limited thermal conduction becomes apparent. The simulated

data is compared with the measured data in Figure 2.22b. While the profile shapes resulting from heating and quenching during LSA are similar, it was necessary to scale the laser power and compensate the quantitative differences between the simulated and the measured temperatures. The simulated peak temperatures as a function of τ_{dwell} from 250 μs to 1 ms are shown as a function of laser power in Figure 2.23a.

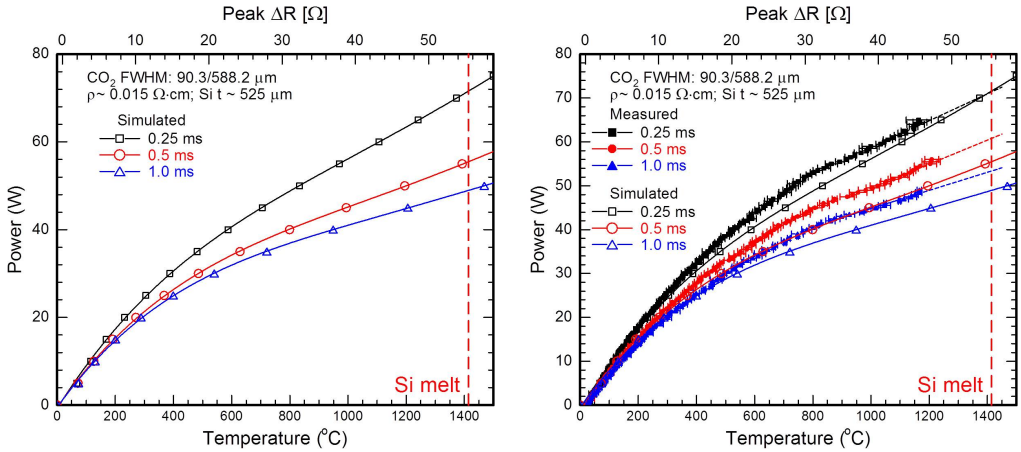

a) Simulated temperature during CO_2 LSA b) Temperature comparison between simulation and measurement

Figure 2.23: Temperature calibration of CO_2 LSA for τ_{dwell} ranging from 250 to 1000 μs. a) Simulated relationship between temperature and power. b) Comparison between simulated and measured temperature during a CO_2 LSA. An offset in peak temperatures are observed for longer τ_{dwell}.

As observed experimentally, the temperature versus power is non-linear due to the temperature-dependent properties. Compared to the actual measurement shown in Figure 2.23b, the temperature curve shapes between the simulated and measured are similar for all τ_{dwell}. As τ_{dwell} increases, a variation in the absolute peak temperature is observed. The simulated temperature vs. power for 500 and 1000 μs exhibit a significant deviation from the measured Si melt, which estimates higher substrate temperatures than the measured data at a given power.

When all simulated powers at dwell were scaled by a factor of 1.08 (7.5 % increase), the simulated curves match the experimental values extremely well for all τ_{dwell} as shown in Figure 2.24. The temperature variation for 250 μs near the Si melt may be due to the substrate damage (dislocation slip) near its melting temperature. The 7.5 % variation between the simulated and the measured temperature profiles may arise from errors in the laser power, physical properties, Si absorption for the 4.8×10^{18} cm^{-3} doping concentration, and/or the decrease in the thermal conductivity with doping.

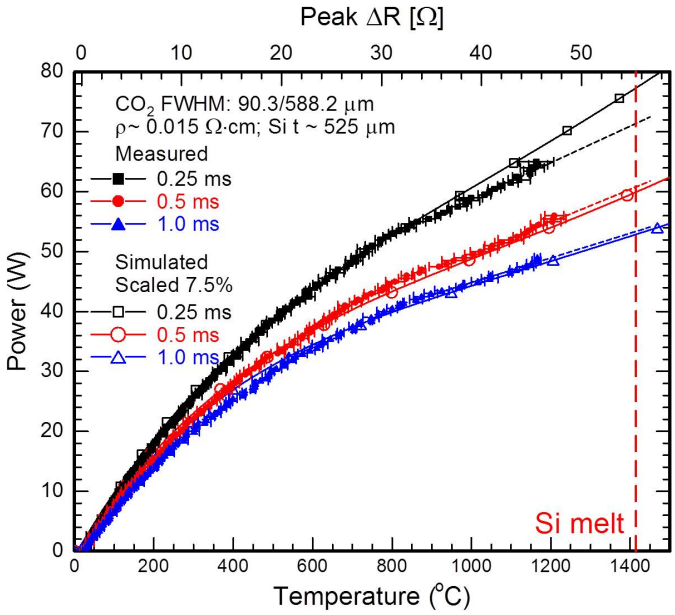

Figure 2.24: Simulated temperatures of CO_2 LSA for τ_{dwell} ranging from 250 to 1000 μs, where the simulated power is increased by 7.5 % to match the experimentally observed values. Data match extremely well for all dwells, but the variation for 250 μs at high temperature is likely due to the substrate damage (dislocation slip) near the melting temperature.

Overall, the measured temperature of the Si substrate using Pt resistors matches the simulated values and behavior using CLASP. This ability to measure the substrate temperature during sub-millisecond LSA, while confirming

the rapid heating and quenching behaviors using computational analysis, is a powerful tool for characterizing dopant activation in the Si bulk and thin-film layers on the Si substrate.

2.4 Conclusions

A method for measuring spatial and temporal profiles during sub-millisecond and millisecond laser spike annealing was developed using a thin-film Pt resistors. Resistance changes, ΔR, were measured and calibrated using the Si and Au melts to determine peak substrate temperatures during CO_2 and diode LSA in the millisecond regime. The measured spatial profiles followed a Gaussian distribution with FWHM values that are comparable to the beam intensity profiles.

A transition from thermally thick to thermally thin behavior was observed for τ_{dwell} greater than 1.5 ms. However, the experimental values were obtained for τ_{dwell} up to 10 ms. Comparison of the measured temperatures with the simulated temperatures showed only a small deviation, confirming the validity of both.

Substrate temperatures, spatial profiles, and temporal profiles measured using Pt thin-film resistor is a powerful characterization tool for understanding the spike annealing behavior during the sub-millisecond LSA. The measured surface temperatures are critical not only for dopant activation studies in the substrate bulk, but also for kinetic analysis of thermally sensitive materials on the substrate surface as discussed in subsequent chapters.

2.5 Acknowledgments

Semiconductor Research Corporation (Task ID: 1870.001) provided funding for this work. This work would not have been possible without the experimental support and helpful discussions from Krishna Iyengar, Michael Willemann, Florencia Paredes, and Megan Hill. This work made use of facilities in the Cornell Center for Materials Research (NSF-DMR 0520404) and the Cornell NanoScale Science and Technology Facility (NSF-ECS 0335765). Cornell Laser Annealing Simulation Package (CLASP) was initiated and developed by Michael O. Thompson, Krishna Iyengar, and Paulette Clancy. Garry Bordonaro and Shahyaan Desai are acknowledged for their contributions on initial thermistor fabrication and guidance.

References

[1] S. Talwar, D. Markle, and M. Thompson, "Junction scaling using lasers for thermal annealing", *Solid State Technol.*, vol. 46, no. 7, pp. 83–86, 2003.

[2] A. Shima, Y. Wang, D. Upadhyaya, L. Feng, S. Talwar, and A. Hiraiwa, "Dopant profile engineering of CMOS devices formed by non-melt laser spike annealing", *Dig. Tech. Pap. Symp. VLSI Technol.*, vol. 8B, no. 4, pp. 144–145, 2005.

[3] T. Yamamoto, T. Kubo, T. Sukegawa, E. Takii, Y. Shinmamune, N. Tamura, T. Sakoda, M. Nakamura, H. Ohta, T. Miyahita, H. Kurata, S. Satoh, M. Kase, and T. Sugii, "Junction profile engineering with a novel multiple laser spike annealing scheme for 45-nm node high performance and low leakage CMOS technology", *Int. El. Devices Meet.*, vol. 1, pp. 143–146, 2007.

[4] C. S. Rafferty, G. H. Gilmer, M. Jaraiz, D. Eaglesham, and H. J. Gossmann, "Simulation of cluster evaporation of transient enhanced diffusion in silicon", *Appl. Phys. Lett.*, vol. 68, no. 17, pp. 2395–2397, 1996.

[5] S. Nishino, J. A. Powell, and H. A. Will, "Production of large area singe crystal wafers of cubic SiC for semiconductor devices", *Appl. Phys. Lett.*, vol. 42, no. 5, pp. 460–462, 1983.

[6] S. Chen, J. Hebb, A. Jain, S. Shetty, and Y. Wang, "Wafer temperature measurement and control during laser spike annealing", in *Advanced Thermal Processing of Semiconductors, 2007. RTP 2007. 15th International Conference on*, 2007, pp. 239–244.

[7] X. Xu, C. P. Grigoropoulos, and R. E. Russo, "Nanosecond time resolution thermal emission measurement during pulse excimer laser interaction with materials", *Appl. Phys. A*, vol. 62, no. 1, pp. 51–59, 1996.

[8] K. G. Kreider and G. Gillen, "High temperature materials for thin-film thermocouples on silicon wafers", *Thin Solid Films*, vol. 376, no. 1-2, pp. 32–37, 2000.

[9] A. Rajagopal, S. Walavalkar, S. Chen, L. Guo, T. Gwinn, and A. Scherer, "Microscales and nanoscaled platinum sensors", *Appl. Phys. Lett.*, vol. 97, no. 13, p. 133 109, 2010.

[10] K. Iyengar, B. Jung, M. Willemann, P. Clancy, and M. O. Thompson, "Experimental determination of thermal profiles during laser spike annealing with quantitative comparison to 3-dimensional simulations", *Appl. Phys. Lett.*, vol. 100, no. 21, p. 211 915, 2012.

[11] J. A. Kittl, R. Reitano, M. J. Aziz, D. P. Brunco, and M. O. Thompson, "Time resolved temperature measurements during rapid solidification of sias alloys induced by pulsed laser melting", *Appl. Phys. Lett.*, vol. 73, no. 8, pp. 3725–3733, 1993.

[12] J. N. Fox, "Temperature coefficient of resistance", *Phys. Educ.*, vol. 25, no. 3, pp. 167–169, 1990.

[13] R. B. Belser and W. H. Hicklin, "Temperature coefficients of resistance of metallic films in the temperature range 25° to 600°C", *J. Appl. Phys.*, vol. 30, no. 3, pp. 313–322, 1959.

[14] K. G. Kreider, D. C. Ripple, and W. A. Kimes, "Thin-film resistance thermometers on silicon wafers", *Meas. Sci. Technol.*, vol. 20, no. 4, pp. 1–6, 2009.

[15] S. M. Hu, "Defects in silicon substrates", *J. Vac. Sci. Technol.*, vol. 14, no. 1, pp. 17–31, 1977.

[16] B. Leory and C. Plougonven, "Warpage of silicon wafers", *J. Electrochem. Soc.*, vol. 127, no. 4, pp. 961–970, 1980.

[17] M. A. Tavel and E. W. Hearn, "An interactive computer simulation of heating and cooling a row of silicon wafers", *J. Electrochem. Soc.*, vol. 135, no. 5, pp. 1266–1271, 1988.

[18] W. Kim, J. Zide, A. Gossard, D. Klenov, S. Stemmer, A. Shakouri, and A. Majumdar, "Thermal conductivity reduction and thermoelectric figure of merit incrase by embedding nanoparticles in crystalline semiconductors", *Phys. Rev. Lett.*, vol. 96, no. 4, p. 045 901, 2006.

[19] C. J. Glassbrenner and G. A. Slack, "Thermal conductivity of silicon and germanium from 3K to the melting point", *Phys. Rev.*, vol. 134, no. 4A, A1058–A1069, 1964.

[20] K. Iyengar, "Modeling sub-millisecond laser spike annealing processes", PhD thesis, Cornell University, 2012.

[21] D. B. M. Klaassen, "A unified mobility model for device simulation - I. Model equations and concentration dependence", *Solid-State Electron.*, vol. 35, no. 7, pp. 953–959, 1992.

CHAPTER 3

STABILITY OF POLYMER SYSTEMS AT LASER-INDUCED HIGH TEMPERATURES

3.1 Introduction and Motivation

Of all the classes of materials such as metals, semiconductors, and ceramics, the least thermally stable materials is generally acknowledged to be organic polymers [1, 2]. Due to their extreme sensitivity to heating conditions, thermal decomposition of organic polymers and their kinetics have been extensively studied using methods such as thermogravimetric analysis (TGA) and differential scanning calorimetry (DSC), Fourier transform infrared spectrometry (FTIR), and mass spectrometry (MS) [3–8].

In general, organic polymer systems begin to decompose near 200-400 °C and the most stable polymeric systems, such as polyurethane, begin to degrade at 300 °C and completely decompose by 700 °C [9, 10]. The thermal threshold for decomposition is identified as the temperature at which the polymer begins to experience mass loss. Any mass loss of the sample at low temperatures (~300 °C) changes the physical and chemical properties of the polymer, including its reaction kinetics and behavior. This thermal instability of organic systems and small molecules limits the temperature range over which polymers can be studied or processed.

In both metallurgical and polymer communities, it is well known that material properties and reaction kinetics depend heavily on the heating conditions, including the ramp and quench rates. For example, martensitic transformations

in iron-carbon steel occurs during rapid quench of the alloy, which limits the diffusion of carbon atoms and makes the alloy harder [1, 11]. The glass transition in organic polymers can also shift by 80 °C as quench rate is increased from 5 K/min to ~10^5 K/min [12]. Most of these property changes and their underlying reaction kinetics follow Arrhenius behavior, where high temperatures accelerate and enhance the transformation as long as the material does not degrade.

Sub-millisecond laser spike annealing (LSA) (Figure 1.20) is capable of heating Si substrates to peak temperatures beyond the Si melt (1414 °C) for dwell times (τ_{dwell}) ranging from 50 μs to 20 ms at ramp and quench rates on the order of 10^4-10^5 K/s. By using a CO_2 laser (λ = 10.6 μm), thin-film polymers can be heated indirectly from the underlying Si substrate due to the transparency of most organic thin-films at the CO_2 wavelength [13].

This chapter explores the thermal stability and decomposition kinetics of various organic polymer systems using sub-millisecond laser-induced heating at temperatures well above their conventional thermal limits.

3.2 Materials and Sample Preparation

Two classes of organic polymers were selected for thermal stability and decomposition kinetics investigations using laser-induced heating. The first class includes simple organic polymers commonly used in the current optical lithography, phase segregation of block copolymers, and directed self-assembly. The second class includes conjugated and Si-containing polymers. Figure 3.1 shows the polymers in the first class chosen for decomposition studies.

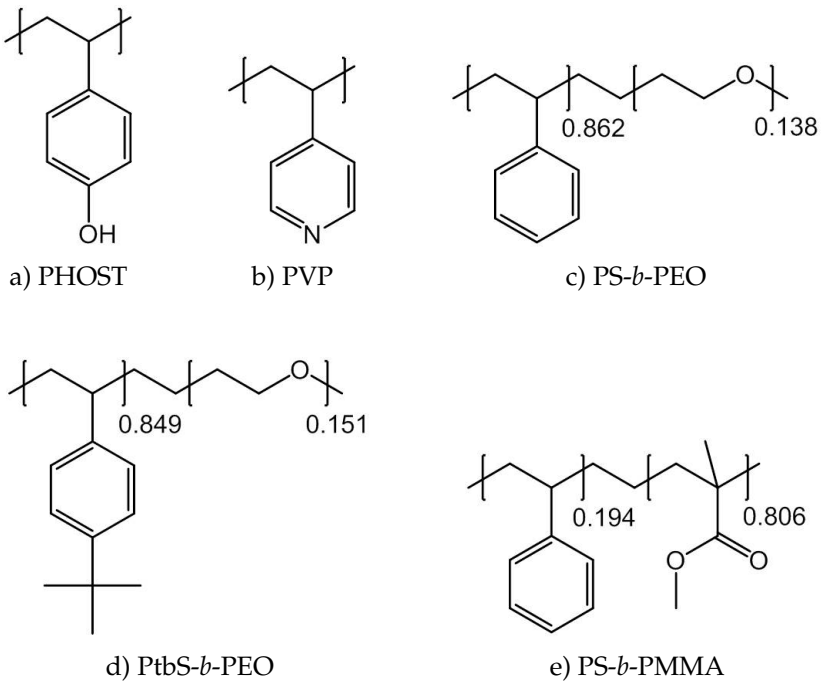

a) PHOST b) PVP c) PS-*b*-PEO

d) PtbS-*b*-PEO e) PS-*b*-PMMA

Figure 3.1: Typical organic systems related to photolithography and phase segregation studies. These polymers were selected due to their high thermal stability and wide applications. a) poly(4-hydroxystyrene) (PHOST), b) poly(4-vinylpyridine) (PVP), c) poly(styrene)-*b*-poly(ethylene oxide) (PS-*b*-PEO), d) poly(4-*t*-butyl styrene)-*b*-poly(ethylene oxide) (PtbS-*b*-PEO), and e) poly(styrene)-*b*-poly(methyl methacrylate) (PS-*b*-PMMA).

The selected polymers were poly(4-hydroxystyrene) (PHOST), poly(4-vinylpyridine) (PVP), poly(styrene)-*b*-poly(ethylene oxide) (PS-*b*-PEO), poly(4-*t*-butyl styrene)-*b*-poly(ethylene oxide) (PtbS-*b*-PEO), and e) poly(styrene)-*b*-poly(methyl methacrylate) (PS-*b*-PMMA). Aside from their application in lithography and phase segregation studies, these polymers also exhibit high thermal stability, up to at least ~300 °C under 5 °C/min heating using TGA.

Due to the variations in polarity, the polymers were dissolved in different solvents. PHOST was dissolved in propylene glycol monomethyl ether acetate (PGMEA), PtbS-*b*-PEO, PS-*b*-PEO, and PS-*b*-PMMA were dissolved in tetrahy-

drofuran (THF), and PVP was dissolved in methanol. The polymer concentration was ~3 wt.% with respect to (w.r.t.) the solvent, with a target thickness of ~150 nm for spin-coating on Si substrates. Thin-films were baked on a vacuum-chuck hot-plate at 130 °C for PGMEA or at 60 °C for THF and methanol to evaporate the solvent from the film. To induce CO_2 absorption at 10.6 μm through free carrier generation, B-doped Si substrates with $\rho \sim 0.01-0.02$ Ω·cm were employed.

The second class of polymers were selected from conjugated or Si-containing polymers with significantly different backbones (Figure 3.2). These polymers were expected to exhibit in different activation energies for decomposition. Selected materials were poly(3,4-ethylene dioxythiophene): poly(styrene sulfonate) (PEDOT:PSS), sodium poly(styrene sulfonate) (PSS), poly(2-methoxy-5-(2-ethyl hexyloxy)-1,4-phenylene vinylene) (MEH-PPV), and poly(styrene)-*b*-poly(dimethylsiloxane) (PS-*b*-PDMS). PEDOT:PSS, PSS, and MEH-PPV are conjugated polymers, where PEDOT:PSS is an acceptor material and MEH-PPV is a donor material, commonly used in organic light emitting diodes (OLEDs). PSS is often used to remove ions from water, where the sulfonate group neutralizes calcium Ca^{2+} and magnesium Mg^{2+} ions to soften water. PS-*b*-PDMS is a hybrid compound that has received attention in the lithography community because of microphase segregation and preferential alignment for sub-20 nm patterning applications [14].

To spin-coat these materials on Si substrates, PEDOT:PSS and PSS were dissolved in deionized water, while MEH-PPV and PS-*b*-PDMS were dissolved in toluene. To promote adhesion between the Si surface and PEDOT:PSS, the substrate was cleaned and oxidized using a piranha solution (a mixture of hydrogen

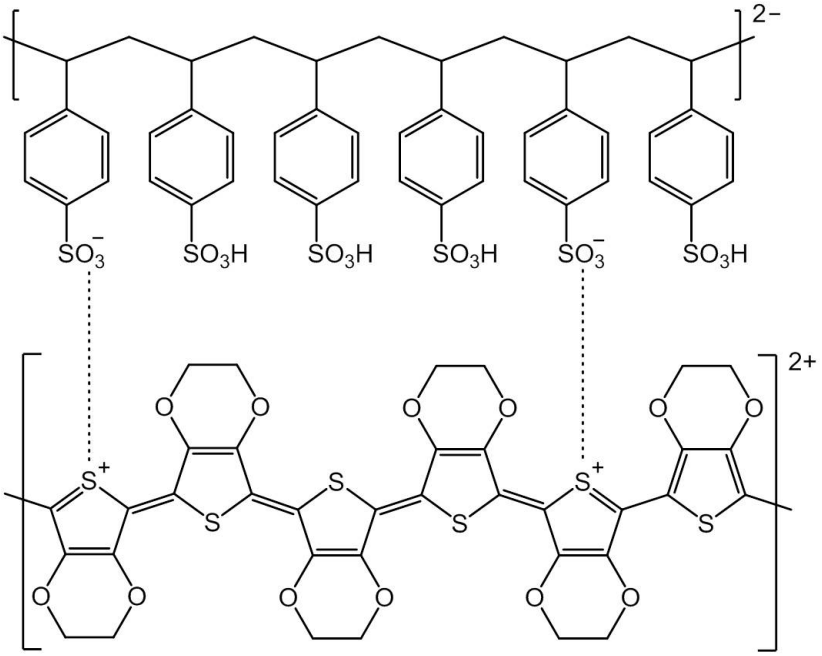

a) PEDOT:PSS

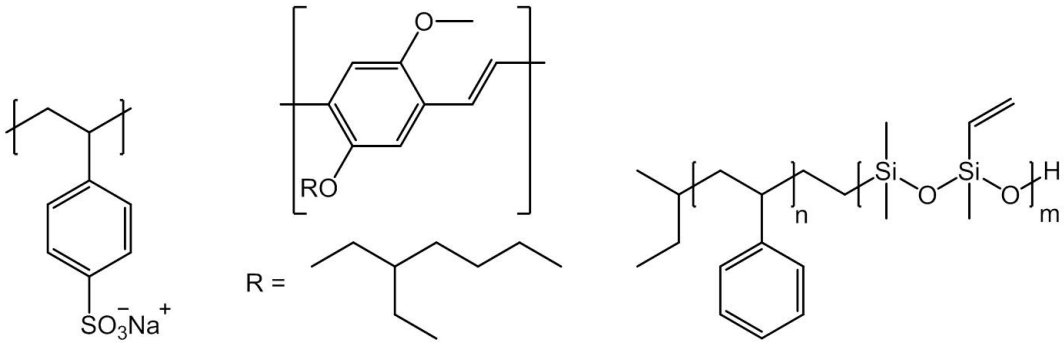

b) PSS c) MEH-PPV d) PS-*b*-PDMS

Figure 3.2: Second group of polymers used for decomposition analysis. These polymers and small molecules were selected due to the chemical complexities which are expected to exhibit different activation energies for decomposition. a) Poly(3,4-ethylene dioxythiophene) poly(styrene sulfonate) (PEDOT:PSS), b) sodium poly(styrene sulfonate) (PSS), c) poly(2-methoxy-5-(2-ethyl hexyloxy)-1,4-phenylene vinylene) (MEH-PPV), and d) a vinyl functionalized poly(styrene)-*b*-poly(dimethylsiloxane) (PS-*b*-PDMS).

peroxide H_2O_2 and sulfuric acid H_2SO_4) to make the surface hydrophilic. After spin-coating, solvents were evaporated through a soft bake at 90 °C for 120 s for deionized water or at 100 °C for 90 s for toluene. The target thickness for each polymer film was 100 nm.

All polymer thin-films were heated using a conventional hot-plate at temperatures 50-600 °C for 15-60 s or using a laser-induced heating at temperatures 200-1000 °C for 50-1000 μs. To quantify the thermal stability, film thickness was measured using a Woollam spectroscopic ellipsometer (WVASE32), Filmetrics (F50-EXR), and Tencor P10 profilometer. These thermal stability data were confirmed using TGA by Seiko Instruments, Inc. (Exstar TG/DTA 6200). While thickness measurements were performed in ambient air, TGA was performed in flowing N_2 gas. Additional decomposition characterization was performed using an Fourier transform infrared (FTIR) spectroscopy by Bruker (Hyperion 2000 Tensor 27).

3.3 Results and Discussion

3.3.1 Thermogravimetric Analysis and Degradation Thresholds

Thermogravimetric analysis (TGA) is an accepted technique to determine the decomposition threshold of bulk organic polymers and small molecules by observing their mass change as a function of heating temperature [3–5, 15]. As an example, a TGA curve for PHOST during a 5 °C/min heating ramp to 500 °C

is shown in Figure 3.3. By 300 °C, approximately 10 % of the polymer weight

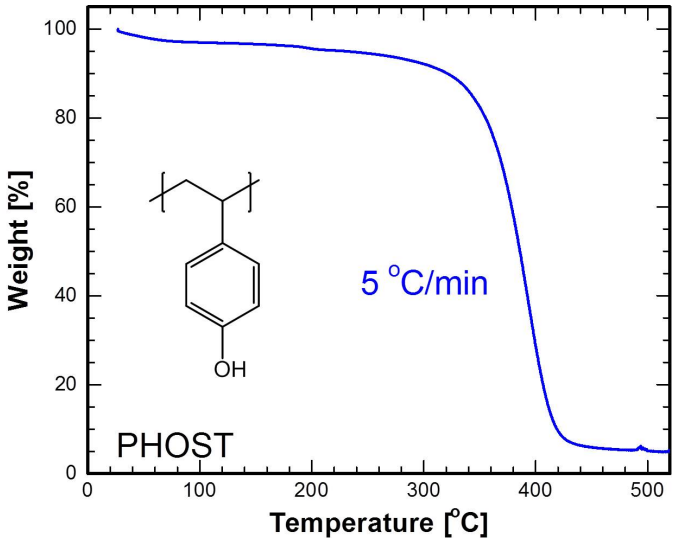

Figure 3.3: Weight loss percent as a function of heating temperature for PHOST using TGA at a 5 °C ramp rate. Each drop in polymer weight represents decomposition of different components of PHOST.

is lost as the least thermally stable hydroxyl components volatilize [6, 16, 17]. While the majority of the moisture and hydroxyl groups at the surface become volatile in the first 100 °C, the steady decrease in weight at higher temperature is likely due to the evaporation of trapped water vapor within the bulk. At ~350 °C, a significant drop in weight is observed suggesting the decomposition of the polymer as weight drops to essentially zero by ~420 °C.

While the relationship between bulk polymer weight and heating temperature is easily obtained using the conventional TGA, weight measurements during laser-induced heating at high ramp rates (10^4–10^5 K/s) are difficult since polymer heating must occur on a Si substrate rather than in a bulk form. However, since the relative change in mass and volume of the polymer are comparable [18], the relative weight change of the bulk polymer can also be described by the normalized thickness change of a 150 nm film. This comparison is shown

in Figure 3.4 for PHOST.

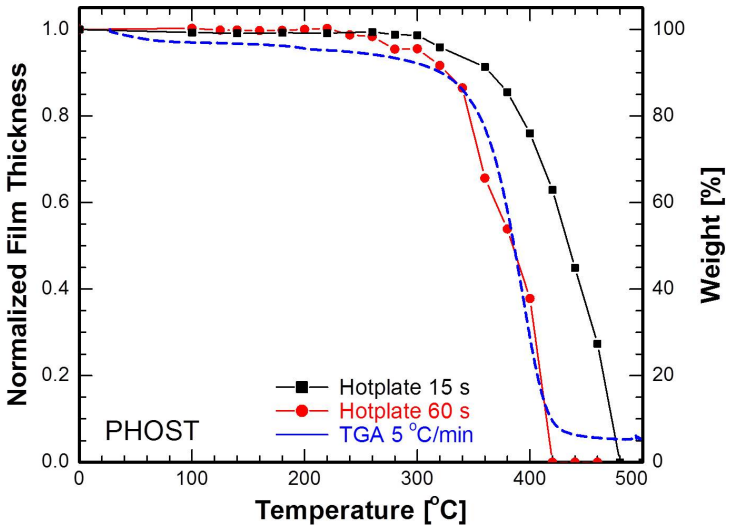

Figure 3.4: Normalized PHOST film thickness on a Si substrate as a function of heating temperature using a vacuum-chuck hot-plate. The drop in polymer thickness is comparable to the weight percent as plotted on the right axis.

The normalized film thickness was plotted as a function of heating temperature using a vacuum-chuck hot-plate for 15 and 60 s durations. As a comparison, weight percent of the bulk PHOST is plotted against the right axis. The weight loss during TGA with a 5 °C/min ramp rate is essentially equivalent to the normalized thickness loss during hot-plate heating for 60 s. The curve shape remains essentially similar including the threshold temperature for the drop in both thickness and weight, suggesting an equivalent decomposition behavior of the polymer. As expected, the curve shifts by ~60 °C as the heating duration is reduced from 60 s to 15 s.

The result shown in Figure 3.4 demonstrates two great potentials for sub-millisecond heating. First, the TGA curve, which characterizes the decomposition behavior of a polymer, can be equivalently replicated by measuring the film thickness loss during heating. This relationship opens up the possibility to

characterize the decomposition behavior in the sub-millisecond time frames by measuring the film thickness during the transient laser-induced heating. Second, the thermal stability of the polymer can potentially be extended to a much higher temperatures when the heating duration is simultaneously reduced into the sub-millisecond time frames. This behavior is comparable to the increase in the thermal stability of polymers during fast heating ramp rates as demonstrated by A. A. Minakov *et al.* [12], but more powerful since the full thickness (or weight) profile is easily obtained after higher temperature and/or sub-millisecond time frames.

For all investigated polymers, the mass measured during a 5 °C/min TGA was similar or equivalent to the normalized film thickness on Si substrates heated using a conventional hot-plate for 60 s (Appendix B). Each polymer thin-film was heated using a hot-plate for seconds time frames or a laser-induced heating for the sub-millisecond time frames to characterize the decomposition behavior.

3.3.2 Extension in Thermal Stability of Organic Systems and Decomposition Kinetics

Organic polymers during sub-millisecond heating

To characterize and compare the decomposition behavior of organic polymers between seconds and sub-millisecond heating, thickness loss of a ~150 nm film on Si substrates were measured as a function of heating temperature. As an example, PHOST and PS-*b*-PMMA thickness losses are shown in Figure 3.5. While

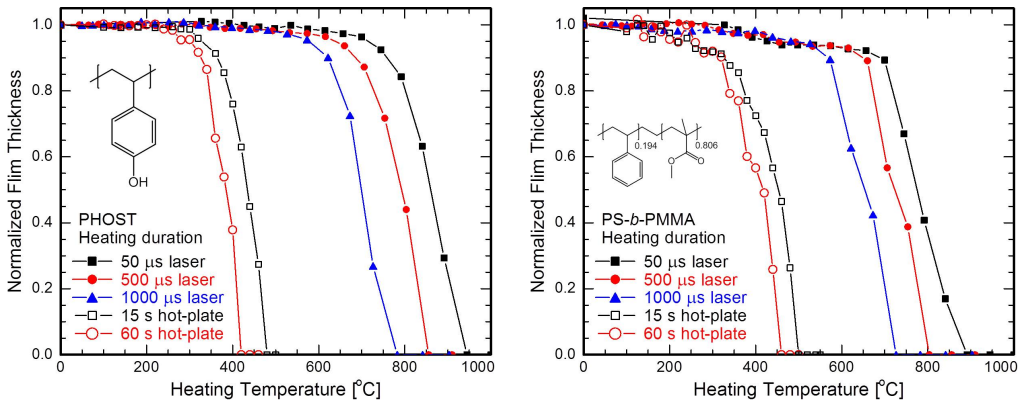

a) PHOST b) PS-*b*-PMMA

Figure 3.5: Polymer film thickness loss as a function of temperature during hot-plate seconds and laser-induced sub-millisecond heating for a) PHOST and b) PS-*b*-PMMA. Curve shapes between the two heating durations are essentially equivalent, suggesting a similar decomposition behavior of the respective polymers. The decomposition threshold are extended to 950 °C for PHOST and 900 °C for PS-*b*-PMMA when the heating duration is reduced to 50 μs.

the curve shape describing the decomposition behavior remain identical for all heating durations on a given polymer, a large shift in temperature is observed between second and sub-millisecond time frames. When heating duration is reduced from 60 s to 50 μs, the thermal stability of PHOST and PS-*b*-PMMA are extended up to ~950 °C and ~900 °C respectively. This difference corresponds to a ~525 °C and ~450 °C change in the respectable stabilities for a six orders of magnitude faster heating durations.

Both polymers are initially stable at low temperatures, losing less than 10 % of their initial thickness. A rapid drop in thickness is observed at a temperature threshold, where the entire polymer decomposes including the backbone itself. The activation characteristics for this decomposition is expected to follow Arrhenius behavior, as the decomposition rate is simply the inverse of heating duration (decomposition rate = $\left[\text{heating duration}\right]^{-1}$). Figure 3.6 plots the de-

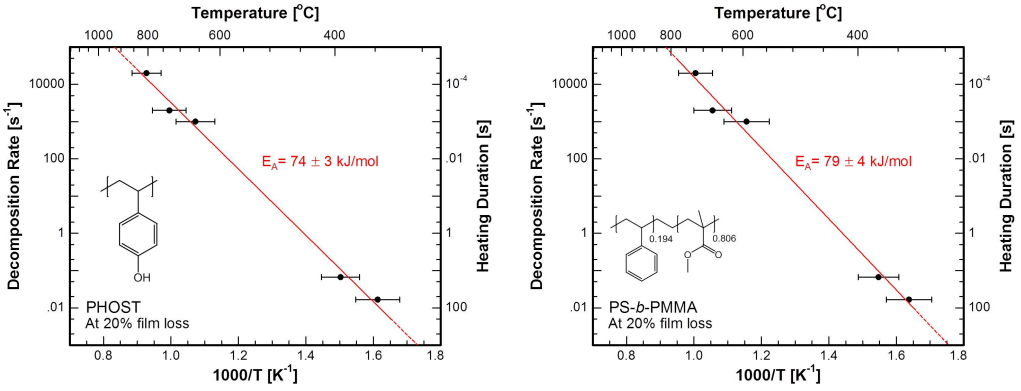

a) PHOST b) PS-*b*-PMMA

Figure 3.6: Polymer decomposition rate as a function of inverse temperature at 20 % thickness loss for a) PHOST and b) PS-*b*-PMMA. The decomposition rate is Arrhenius for hot-plate induced and laser-induced temperatures. The activation energy between two systems are similar due to the common organic backbone for both systems (74 ± 3 kJ/mol and 79 ± 4 kJ/mol for PHOST and PS-*b*-PMMA respectively).

composition rate at 20 % film thickness loss as a function of inverse temperature for these two polymer systems.

The decomposition follows Arrhenius behavior spanning over 500 degrees in temperature across the hot-plate and laser-induced heating regimes. The observed activation energy (E_A) for decomposition on both polymers are comparable at 74 ± 3 kJ/mol for PHOST and 79 ± 4 kJ/mol for PS-*b*-PMMA, suggesting the decomposition of similar polymer groups. For all investigated polymer systems with organic backbone including PVP, PS-*b*-PEO, and PtbS-*b*-PEO, the thermal stability limits using laser-induced sub-millisecond heating and the respective E_A for decomposition are summarized in Table 3.1.

The extension in thermal stability (ΔT) is achieved as all polymer systems can be characterized at >900 °C as long as the heating duration is reduced to the sub-millisecond time frames using laser heating. The similarity in E_A is

Table 3.1: Thermal stability limits of organic polymers and resulting activation energies (E_A) for decomposition

Polymer	T_{limit} 60 s	T_{limit} 50 μs	$\Delta T^{20\ \%\ film\ loss}_{60\ s\ vs.\ 50\ \mu s}$	$E_A^{decomposition}$
PHOST	420 °C	945 °C	~460 °C	74 ± 3 kJ/mol
PVP	440 °C	1000 °C	~510 °C	75 ± 4 kJ/mol
PS-*b*-PEO	380 °C	1000 °C	~530 °C	70 ± 1 kJ/mol
PtbS-*b*-PEO	400 °C	~1000 °C	~535 °C	66 ± 2 kJ/mol
PS-*b*-PMMA	460 °C	890 °C	~385 °C	79 ± 4 kJ/mol

likely due to the decomposition of similar organic backbone shared by all of the investigated polymers. However, the observed E_A is only half of the previously reported ~160 kJ/mol for crystalline polyethylene [19, 20]. This difference in E_A may be due to the decomposition occurring in a free-flowing polymer above 200 °C, well above the typical glass transition temperature of the investigated systems [21].

To ensure that the decomposition mechanism are equivalent between hot-plate and laser heating, FTIR spectroscopy was used to observe ester, ether, and alcohol peaks as a function of heating temperature. Peaks for PHOST is shown as an example in Figure 3.7. Analysis of FTIR peaks corresponding to ester and ether shown in Figures 3.7a and 3.7b suggest thermal stabilities up to ~320 °C for 60 s hot-plate and ~660 °C for 500 μs laser heatings. The difference confirms the ~400 °C extension in thermal stability of PHOST in the sub-millisecond time frames as previously demonstrated using the thickness analysis (Figure 3.5a). The gradual decrease in peaks at high temperatures suggest the same decomposition mechanism between two heating durations, also confirming the Arrhenius decomposition behavior over the seven orders of magnitude in decompo-

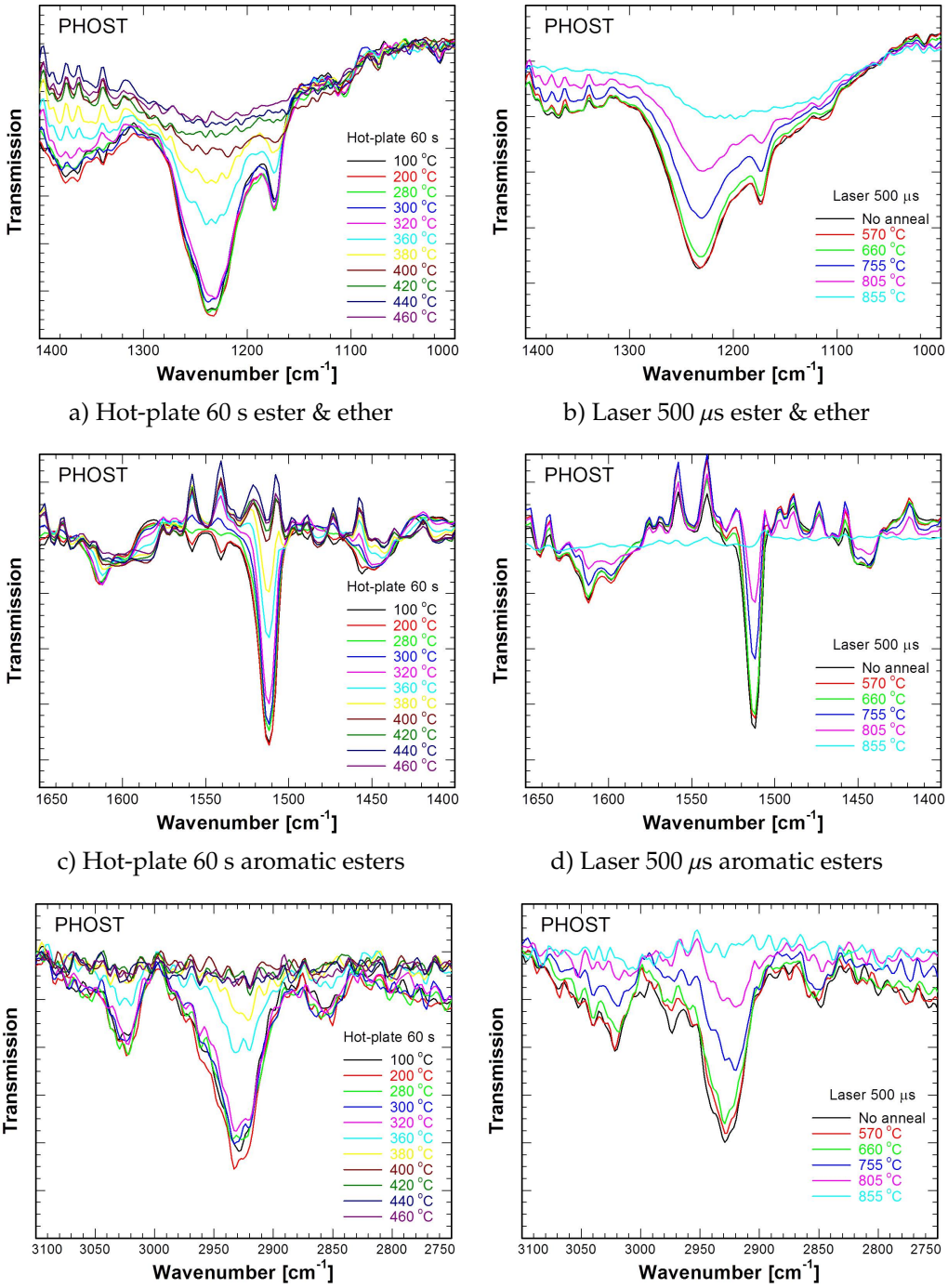

a) Hot-plate 60 s ester & ether

b) Laser 500 μs ester & ether

c) Hot-plate 60 s aromatic esters

d) Laser 500 μs aromatic esters

e) Hot-plate 60 s alcohol

f) Laser 500 μs alcohol

Figure 3.7: FTIR peak comparison between hot-plate and laser heating for vibration stretches of a,b) ester and ether, c,d) aromatic ester, and e,f) alcohol for PHOST. All peaks decrease as a function of heating temperature.

sition rate (Figure 3.6a).

While the alcohol peaks for PHOST exhibit similar decrease as the esters and ethers, the formation of additional peaks at the highest temperature for the aromatic esters in PHOST is observed for both heating methods. To quantify this change, all peaks were integrated and were plotted as a function of heating temperature as shown in Figure 3.8.

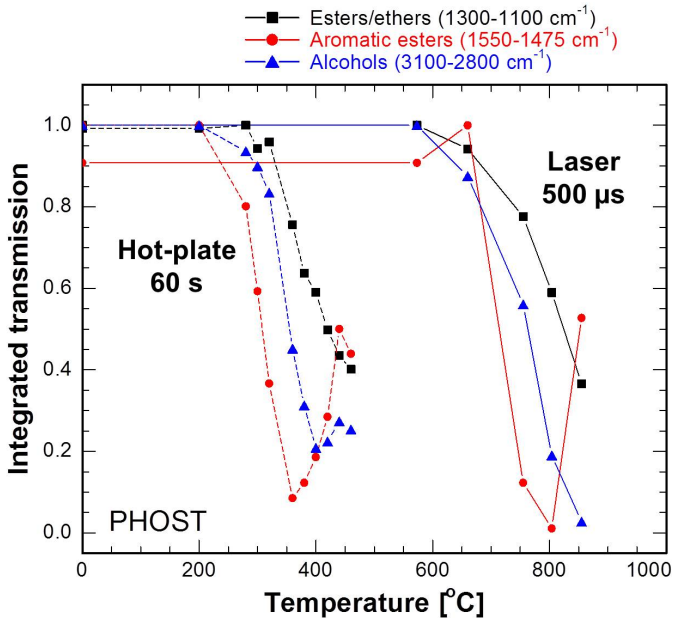

Figure 3.8: Integrated FTIR peaks for PHOST resulting from a 60 s hot-plate or a 500 μs laser heating. While ester/ether and alcohol peaks show consistent decrease in peaks as a function of temperature, a sharp increase in the aromatic esters is observed for both heating methods. The increase in C=O peaks suggests their formation through the decomposition of PHOST components.

Integrated peaks for PHOST show consistent decrease in all peaks with increasing temperature regardless of the heating method, due to the equivalent decomposition mechanism. Out of all components, however, a sharp increase in the aromatic esters is observed. This increase suggests the formation of alkenyl

groups from the decomposition of other components, potentially through radical generations. The FTIR analysis was performed for all investigated organic, conjugated, and Si-containing polymers, where a comparable decomposition behavior was observed between hot-plate and laser-induced heating as shown in Appendix B.

Overall, the thermal stability of simple organic polymers was extended up to 1000 °C using sub-millisecond laser-induced heating. The decomposition behavior of these organic polymers was characterized, revealing comparable E_A's for decomposition resulting from similar organic backbones. This result motivated an investigation on more complex systems, such as the conjugated and Si-containing polymers.

Conjugated and Si-containing polymers during sub-millisecond heating

Thermal stability tests during sub-millisecond LSA were extended to both conjugated and Si-containing polymers as previously shown in Figure 3.2. For all systems, film thicknesses were recorded as a function of heating temperature for both hot-plate seconds heating and laser-induced sub-millisecond heating.

Figure 3.9 shows the weight percent obtained using TGA and film thickness loss for MEH-PPV and PS-*b*-PDMS, showing correlation between two properties for both conjugated and Si-containing polymers. The measured TGA curve for MEH-PPV conjugated polymer is comparable to the reported analysis, where short polymer chains completely decompose at ~400 °C and longer chains decompose at ~800 °C [22]. The initial thickness and weight at ~200 °C is due to the decomposition of 2-ethyl hexane, which assists the dispersion and dissolution

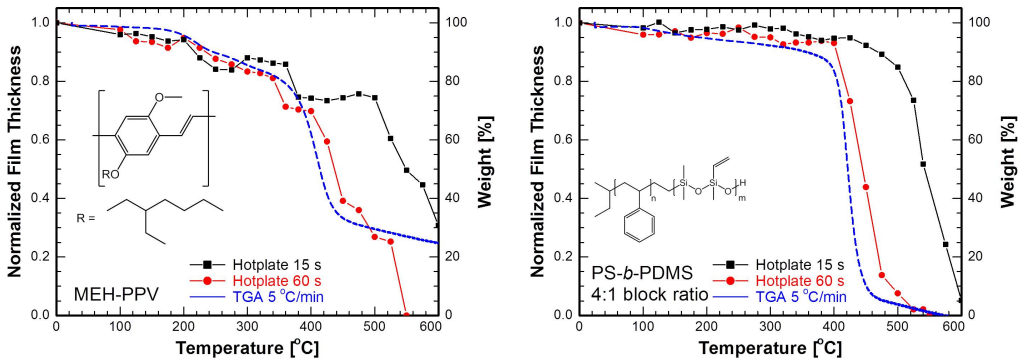

a) MEH-PPV b) PS-*b*-PDMS (4:1 block ratio)

Figure 3.9: Normalized film thickness on a Si substrate as a function of heating temperature using a vacuum-chuck hot-plate for a) MEH-PPV and b) PS-*b*-PDMS (4:1 block ratio). The drop in polymer thickness is comparable with the weight percent as plotted on the right axis.

of MEH-PPV in toluene. The weight loss measured by 5 °C/min TGA correlates well with the normalized film thickness loss up to 550 °C. The premature thickness drop at 550 °C is potentially due to the accelerated decomposition of MEH-PPV long chains in its thin-film form, or more likely due to the variations in the heating environment, where polymer films are annealed in ambient air while the TGA was performed in nitrogen environment. For PS-*b*-PDMS shown in Figure 3.9b, the weight percent overlapped the normalized film thickness during a 60 s hot-plate heating.

Having correlated the TGA analysis and the film thickness, polymer thin-films were subjected to either a hot-plate or laser-induced heating. Figure 3.10 shows the normalized thickness measured as a function of heating temperature for MEH-PPV and PS-*b*-PDMS. Under laser-induced heating, the decomposition of MEH-PPV and PS-*b*-PDMS exhibit curve shapes that are comparable for all heating durations into the sub-millisecond time frames, including the two step decomposition behavior observed for the short and long chain MEH-PPVs.

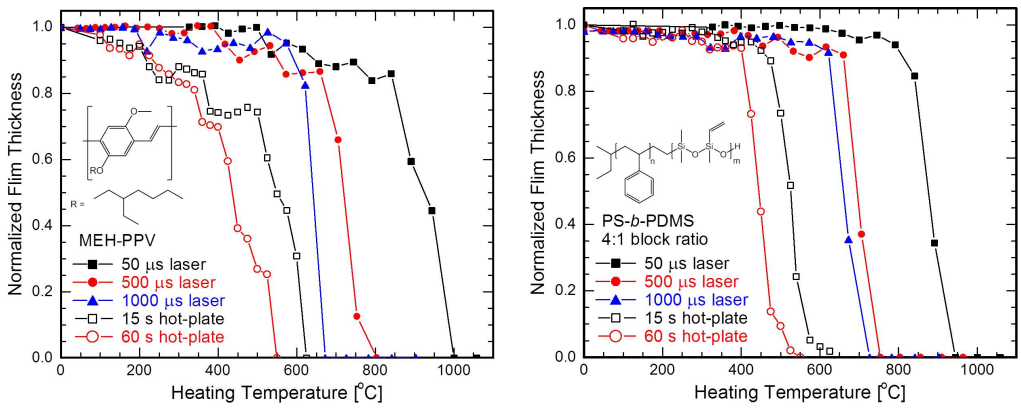

a) MEH-PPV b) PS-*b*-PDMS (4:1 block ratio)

Figure 3.10: Polymer film thickness loss as a function of temperature during hot-plate seconds or laser-induced sub-millisecond heating for a) MEH-PPV and b) PS-*b*-PDMS (4:1 block ratio). Curve shapes between the two heating durations are comparable, suggesting a similar decomposition behavior of the respective polymers. The decomposition threshold for both are extended up to 1000 °C for MEH-PPV and 900 °C for PS-*b*-PDMS as the heating duration was reduced to 50 μs.

The conjugated polymer also exhibits a similar shift in temperature across time regimes, with the thermal stability of MEH-PPV extended to 1000 °C at 50 μs. A similar extension is observed for PS-*b*-PDMS system to ~950 °C at 50 μs.

The activation energy for decomposition is shown in Figure 3.6. Over 500 degrees, the decomposition rate follows Arrhenius behavior. However, the observed E_A for MEH-PPV and PS-*b*-PDMS are significantly different at 71 ± 4 kJ/mol and 103 ± 15 kJ/mol respectively. Data for all investigated polymers are summarized in Table 3.2. TGA analysis, decomposition curves, and FTIR analysis are included in Appendix B.

Similar to the polymer systems with a common organic backbone, the extension in thermal stability (ΔT) is achieved, as both conjugated and Si-containing polymers can be characterized up to ~950 °C in the sub-millisecond time frames.

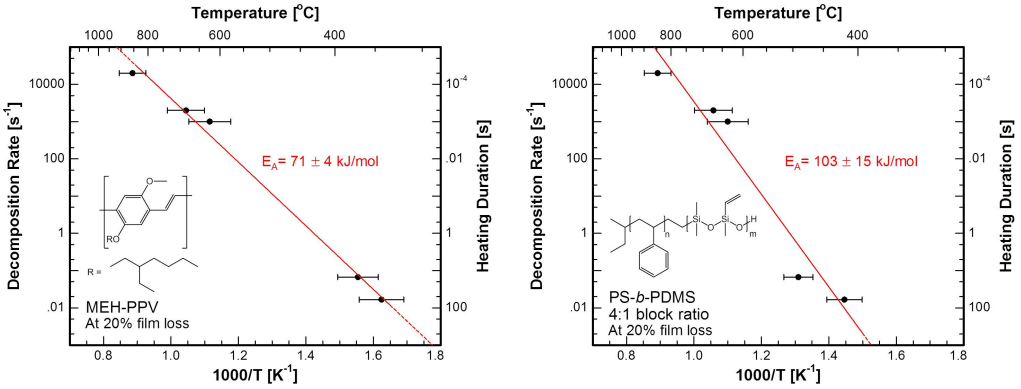

a) MEH-PPV b) PS-*b*-PDMS (4:1 block ratio)

Figure 3.11: Polymer decomposition rate as a function of inverse temperature at 20 % thickness loss for a) MEH-PPV and b) PS-*b*-PDMS (4:1 block ratio). The decomposition rate exhibit Arrhenius behavior for hot-plate and laser-induced temperatures. The activation energy between two systems are different due to the inorganic element Si incorporated into the backbone of PDMS (71 ± 4 kJ/mol and 103 ± 15 kJ/mol for MEH-PPV and PS-*b*-PDMS respectively).

Table 3.2: Thermal stability limits of conjugated and Si-containing polymers and resulting activation energies (E_A) for decomposition

Polymer	T_{limit} 60 s	T_{limit} 50 μs	$\Delta T^{20\ \%\ film\ loss}_{60\ s\ vs.\ 50\ \mu s}$	$E_A^{decomposition}$
MEH-PPV	550 °C	1000 °C	~510 °C	71 ± 4 kJ/mol
PS-*b*-PDMS (4:1)	550 °C	940 °C	~430 °C	103 ± 15 kJ/mol
PS-*b*-PDMS (16:13)	550 °C	940 °C	~425 °C	107 ± 19 kJ/mol
PEDOT:PSS	475 °C	~1050 °C	~420 °C	86 ± 9 kJ/mol

While the decomposition E_A for MEH-PPV is similar to that of the previous systems, the E_A is increased up to 30 % for Si-containing PS-*b*-PDMS and S-containing PEDOT:PSS.

The change in decomposition E_A can be attributed to the backbone elements and the attached side groups. While it is often difficult to separate the role of the

backbone and side-groups in heat resistance, individual component behavior can be hypothesized [23]. For example, PDMS has reported activation energies for decomposition at ~175 kJ/mol [24] and ~100 kJ/mol [25] for amorphous and crosslinked polymers respectively. The investigated PDMS system contains a vinyl group on the backbone, where G. Deshpande *et al.* has shown that the addition of vinyl components to PDMS can lower its activation barrier down to 23 kJ/mol, depending on the concentration of vinyl groups on the PDMS [25]. While the measured E_A for PDMS corresponds well with the reported values, its increase from the organic systems may be due to the Si incorporation to the polymer backbone [23, 26, 27].

In contrast to the Si-containing polymers, the two conjugated polymers, MEH-PPV and PEDOT:PSS, show distinct E_A's for decomposition. While MEH-PPV is aliphatic, PEDOT and PSS are held through ionic bonds and contain a skeletal sulfur atom. For the aliphatic MEH-PPV, the decomposition E_A at 71 ± 4 kJ/mol is comparable to the organic polymers such as PHOST and PS-*b*-PMMA (74 ± 3 and 79 ± 4 kJ/mol). In addition, MEH-PPV has a relatively large 2-methoxy-5-(2-ethylhexyloxy) side-group compared to the ionic-bound PEDOT:PSS, which increases the free volume and reduces the heat resistance for MEH-PPV [28]. In a previous study by E. Vitoratos *et al.*, the ionic nature of PEDOT:PSS allowed a grain formation of PEDOT oligomers at elevated temperatures, raising the activation barrier for both electrical conduction and decomposition [29]. However, further investigation is required to identify the responsible mechanism for the enhanced thermal stability of PS-*b*-PDMS and PEDOT:PSS.

3.4 Conclusions

The thermal decomposition of organic, conjugated, and Si-containing polymers was investigated using the laser-induced sub-millisecond heating. Decomposition behavior of selected polymers was studied by correlating the weight loss obtained from TGA with the film thickness loss of a ~100 nm film. At elevated temperatures, similar losses in both weight and film thickness was observed and suggested comparable decomposition of chemical components within the polymer. With heating durations reduced by five orders of magnitude from the conventional seconds time frame, the stability of all examined polymer systems were extended up to 1050 °C, enabling kinetic studies of thin-film polymers at high temperatures for sub-millisecond times.

Decomposition activation energies were obtained for a variety of organic, conjugated, and Si-containing polymers. While polymers with organic backbones, such as PHOST and PS-*b*-PMMA, showed consistent decomposition activation around 65-75 kJ/mol, Si-containing polymers such as PS-*b*-PDMS and conjugated polymers such as PEDOT:PSS exhibited higher activation barriers at ~105 and 86 kJ/mol respectively. The E_A increase in PS-*b*-PDMS is potentially due to the Si in the backbone. For PEDOT:PSS, the ionic nature of both PEDOT and PSS can potentially increase the activation barrier for decomposition.

Overall, the laser-induced heating presents an opportunity to characterize the chemical reaction properties of thermally sensitive polymer systems at previously unattainable heating conditions. This extension in thermal stability during laser-induced heating can be utilized to extend the fundamental understanding of thermal decomposition and reaction kinetics of organic, conjugated,

and Si-containing polymers.

3.5 Acknowledgments

Kwan Wee Tan and Professor Ulrich Wiesner are gratefully acknowledged for the experimental contribution and helpful discussions. Hiroaki Sai, Joerg Werner, Brendan Wenning, David Moore, Alan Jacobs, and Jing Jiang are acknowledged for providing materials that made these experiments possible.

References

[1] W. D. Callister, *Materials Science and Engineering: An Introduction*. New York, NY: John Wiley & Sons, Inc., 2007, pp. 5–14.

[2] S. I. Stupp and P. V. Braun, "Molecular manipulation of microstructures: biomaterials, ceramics, and semiconductors", *Science*, vol. 277, no. 5330, pp. 1242–1248, 1997.

[3] E. S. Freeman and B. Carroll, "The application of thermoanalytical techniques to reaction kinetics: the thermogravimetric evaluation of the kinetics of the decomposition of calcium oxalate monohydrate", *J. Phys. Chem.*, vol. 62, no. 4, pp. 394–397, 1958.

[4] A. W. Coats and J. P. Redfern, "Kinetic parameters from thermogravimetric data", *Nature*, vol. 201, no. 4914, pp. 68–69, 1964.

[5] H. L. Friedman, "Kinetics of thermal degradation of char-forming plastics from thermogravimetry. Application to a phenolic plastic", *J. Polym. Sci. Pol. Sym.*, vol. 6, no. 6, pp. 183–195, 1964.

[6] K. Pielichowski and J. Njuguna, *Thermal degradation of polymeric materials*. Shawbury, UK: Rapra Technology Limited, 2005, pp. 3–29.

[7] M. J. O'Neill, "Measurement of specific heat functions by differential scanning calorimetry", *Anal. Chem.*, vol. 38, no. 10, pp. 1331–1336, 1966.

[8] W. Xie, Z. Gao, W. P. Pan, D. Hunter, A. Singh, and R. Vaia, "Thermal degradation chemistry of alkyl quaternary ammonium montmorillonite", *Chem. Mater.*, vol. 13, no. 9, pp. 2979–2990, 2001.

[9] I. B. Johns, E. A. McElhill, and J. O. Smith, "Thermal stability of some organic compounds", *J. Chem. Eng. Data*, vol. 7, no. 2, pp. 277–281, 1962.

[10] S. Duquesne, M. L. Bras, S. Bourbigot, R. Delobel, G. Camino, B. Eling, C. Lindsay, and T. Roels, "Thermal degradation of polyurethane and polyurethane/expandable graphite coatings", *Chem. Mater.*, vol. 74, no. 3, pp. 493–499, 2001.

[11] Z. Nishiyama, M. Fine, M. Meshii, and C. Wayman, *Martensitic transformation*. New York, NY: Academic Press, Inc., 1978, pp. 2–124.

[12] A. A. Minakov, D. A. Mordvintsev, and C. Schick, "Melting and reorganization of poly(ethylene terephthalate) on fast heating (1000 K/s)", *Polymer*, vol. 45, no. 11, pp. 3755–3763, 2004.

[13] R. M. Silverstein, G. C. Bassler, and T. C. Morrill, *Spectrometric identification of organic compounds*. New York, New York: John Wiley & Sons, Inc., 1991, pp. 91–132.

[14] K. W. Gotrik and C. A. Ross, "Solvothermal annealing of block copolymer thin flims", *Nano. Lett.*, vol. 13, no. 11, pp. 5117–5122, 2013.

[15] C. D. Doyle, "Estimating thermal stability of experimental polymers by empirical thermogravimetric analysis", *Anal. Chem.*, vol. 33, no. 1, pp. 77–79, 1961.

[16] A. A. Apostolov, S. Fakirov, E. Vassileva, R. D. Patil, and J. E. Mark, "DSC and TGA studies of the behavior of water in native and crosslinked gelatin", *J. Appl. Polym. Sci.*, vol. 71, no. 3, pp. 465–470, 1999.

[17] M. Kamruddin, P. Ajikumar, R. Nithya, G. Mangamma, A. Tyagi, and B. Raj, "Effect of water of crystallization on synthesis of nanocrystalline ceria by non-hydrolytic method", *Powder Technol.*, vol. 161, no. 2, pp. 145–149, 2006.

[18] R. J. Young and P. A. Lovell, *Introduction to polymers*. Boca Raton, FL: CRC Press, 1991, pp. 11–108.

[19] D. A. Anderson and E. S. Freeman, "The kinetics of the thermal degradation of polystyrene and polyethylene", *J. Polym. Sci.*, vol. 54, no. 159, pp. 253–260, 1961.

[20] A. Marcilla and M. Beltrn, "Kinetic study of the thermal decomposition of polystyrene and polyethylene-vinyl acetate graft copolymers by thermogravimetric analysis", *Polym. Degrad. Stabil.*, vol. 50, no. 1, pp. 117–124, 1995.

[21] K. Chen, E. J. Saltzman, and K. S. Schweizer, "Segmental dynamics in polymers: from cold melts to ageing and stressed glasses", *J. Phys.: Condens. Matter*, vol. 21, no. 50, pp. 1–20, 2009.

[22] P. Prajongtat, S. Suramitr, M. P. Gleeson, K. Mitsuke, and S. Hannongbua, "Enhancement of the solubility, thermal stability, and electronic properties of carbon nanotubes functionalized with MEH-PPV: a combined experimental and computational study", *Monatsh. Chem.*, vol. 144, no. 7, pp. 925–935, 2013.

[23] H. R. Allcock, "Inorganic - organic polymers", *Adv. Mater.*, vol. 6, no. 2, pp. 106–115, 1994.

[24] T. H. Thomas and T. C. Kendrick, "Thermal analysis of polysiloxanes. II. Thermal vacuum degradation of polysiloxanes with different substituents on silicon and in the main siloxane chain", *J. Polym. Sci. A2.*, vol. 8, no. 10, pp. 1823–1830, 1970.

[25] G. Deshpande and M. E. Rezac, "Kinetic aspects of the thermal degradation of poly(dimethyl siloxane) and poly(dimethyl diphenyl siloxane)", *Polym. Degrad. Stabil.*, vol. 76, no. 1, pp. 17–24, 2002.

[26] D. A. Foucher, R. Ziembinski, B. Z. Tang, P. M. Macdonald, J. Massey, C. R. Jaeger, G. J. Vancso, and I. Manners, "Synthesis, characterization, glass transition behavior, and the electronic structure of high-molecular-weight, symmetrically substituted poly(ferrocenylsilanes) with alkyl or aryl side groups", *Macromolecules*, vol. 26, no. 11, pp. 2878–2884, 1993.

[27] J. M. Nelson, H. Rengel, and I. Manners, "Ring-opening polymerization of [2]ferrocenophanes with a hydrocarbon bridge: synthesis of poly(ferrocenylethylenes)", *J. Am. Chem. Soc.*, vol. 115, no. 15, pp. 7035–7036, 1993.

[28] J. S. Vrentas and J. L. Duda, "Diffusion in polymer - solvent systems. I. Reexamination of the free-volume theory", *J. Polym. Sci.*, vol. 15, no. 3, pp. 403–416, 1997.

[29] E. Vitoratos, S. Sakkopoulos, E. Dalas, N. Paliatsas, D. Karageorgopoulos, F. Petraki, S. Kennouc, and S. A. Choulis, "Thermal degradation mechanisms of PEDOT:PSS", *Org. Electron.*, vol. 10, no. 1, pp. 61–66, 2009.

CHAPTER 4

PATTERNING USING MILLISECOND LASER POST EXPOSURE BAKE

4.1 Introduction and Motivation

Over the past three decades, chemically amplified resists (CARs) have been widely used as patterning materials for 248 and 193 nm optical lithography due to their high sensitivity and excellent patterning performance [1, 2]. Following generation of photoacids by UV irradiation, polymer backbone deprotection occurs during a post exposure bake (PEB). Photo-generated acids diffuse and deprotect the acid-labile protecting groups in the polymer matrix, eventually inducing a solubility switch of the resist in a developing media [3]. PEB is conventionally achieved by heating the resist using a hot-plate at temperatures of 90-150 °C for 30-120 s. Excessive PEB conditions leads to deleterious diffusion of photoacids with negative consequences on line width roughness [4].

4.1.1 Trade-off in Resolution, Roughness, and Sensitivity

The International Technology Roadmap for Semiconductor (ITRS) requirements for resist material (Tables 1.1 and 1.2) show a uniform control in the critical dimension (CD) and line width roughness (LWR) of <1 nm for 16 nm half pitch resolution and below. For optical lithography and EUV lithography, an empirically observed trade-off between resolution, LER (or LWR), and sensitivity exists [5, 6]. More famously known as the "RLS trade-off" (resolution, LER, and

sensitivity), this empirically observed behavior follows the relationship,

$$\sigma_{LER} \approx \text{constant} \times \left(\frac{I(x)}{\partial_s I(x)} \right)_{edge} \sqrt{\frac{1}{\rho_{PAG}\, \alpha\, Q\, \nu\, E_{size}\, R^3\, \exp(-\alpha\, Q\, \nu\, E_{size})}} \tag{4.1}$$

where σ_{LER} is the 1σ variation from a straight edge of the resist, $I(x)$ is the 1-D image intensity (assuming thin resist and 1-D resist line), ∂_s is the derivative in the direction perpendicular to the developed resist edge, ρ_{PAG} is the PAG loading (# molecules/volume), α is the resist absorption coefficient ($1/\mu$m), Q is the quantum yield (# acid generated/# photons absorbed), R is the pattern resolution, ν is the photo-acid interaction volume, and E_{size} is the resist sensitivity (exposure dose) required to print the pattern at targeted resolutions. The dependence of σ_{LER} on $\exp(-\alpha\, Q\, \nu\, E)$ accounts for the saturation of acid generation when all PAGs in the resist resin are activated [6–8].

To clarify the RLS trade-off, Equation 4.1 can be simplified to

$$\sigma_{LER} \propto \frac{1}{\sqrt{\alpha\, Q\, E\, R^3}} \tag{4.2}$$

which suggests that an improvement of one parameter (resolution, LER, or sensitivity) will come at the expense of one or both of the other two. This trade-off can be seen for a 30 nm target line width as shown in Figure 4.1. This behavior exists for all types of lithography involving chemically amplified resists, as there are no fundamental differences between 193 nm ArF, e-beam, and EUV resist once acid-catalyzed latent images form during PEB. Two potential solutions exist for bypassing this RLS trade-off. First, the acid formation is controlled by the choice and design of the resist material and the acid formation mechanisms are different between the three lithography process [6]. A proposed reaction mechanism for acid generation is shown in Table 4.1 [9, 10].

248 nm KrF and 193 nm ArF lithography use 5.0 eV and 6.4 eV photons respectively during UV exposure, to activate the PAG through a near optically

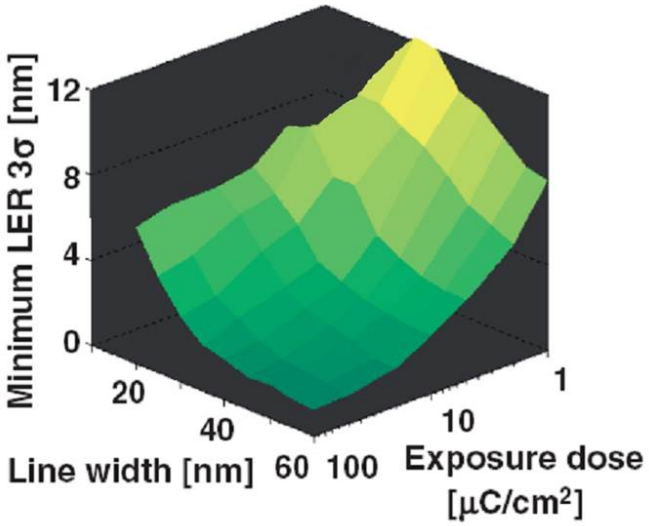

Figure 4.1: Simulation of line width as a function of exposure dose and LER for a target CD of 30 nm. Plot show that an improvement in one parameter is possible at the compensation of the other two parameters. Reprinted with permission from [6]. Copyright 2009 The Japan Society of Applied Physics.

Table 4.1: A proposed reaction mechanism for acid generation [9, 10]

Litho Technique	Energy absorber	Acid generation mechanism
KrF & ArF	PAG	Excitation of PAG
EUV (13.5 nm)	Mainly polymer	Multi-spur reaction
E-beam	Mainly polymer	Isolated-spur reaction

transparent resist resin. In contrast, EUV photons at 13.5 nm (91.8 eV) ionize the resist polymer upon impact and generate additional catalysts through a multi-spur reaction, which includes ionization of polymers, dissociative electron attachment of PAGs, and recombination of protons and anions. The development a next-generation EUV or e-beam resist, to compensate such effects, would require a full understanding of the deprotection reaction and catalyst diffusion kinetics.

A second method to bypass the RLS trade-off is to optimize the deprotection and diffusion of the acid-catalyst during the PEB process. For example, the resist deprotection reaction can be accelerated at an extremely high temperature, while the excessive acid-catalyst diffusion is subsequently decreased by minimizing the PEB duration necessary to reach the solubility switch. This concept involves using resist materials that have a critical activation characteristics. If the side-group deprotection and acid diffusion are considered as separate processes, they are expected to have different activation energies (E_A).

This work focuses on comparing chemically amplified resists with varying side-groups and PAGs (resulting in varying E_A). Laser-induced heating ultimately improves the patterning performance by raising the PEB temperature to accelerate the deprotection kinetics while pushing down to milliseconds duration.

4.1.2 E_A's in Chemically Amplified Resists

Key kinetic processes during PEB include the resist deprotection, acid diffusion, and acid quench, which are all thermally activated. With temperature, the relative rates of these three processes diverge due to differences in the activation energies as shown schematically in Figure 4.2 [11, 12].

Deprotection rates increase with temperature, leading to an enhanced resist sensitivity. However, if the heating duration is not simultaneously reduced, diffusion will be excessive and image quality will be lost [13]. The minimum time required at temperature is inversely related to the deprotection rate, while the acid diffusion distance (image resolution loss) is proportional to the square

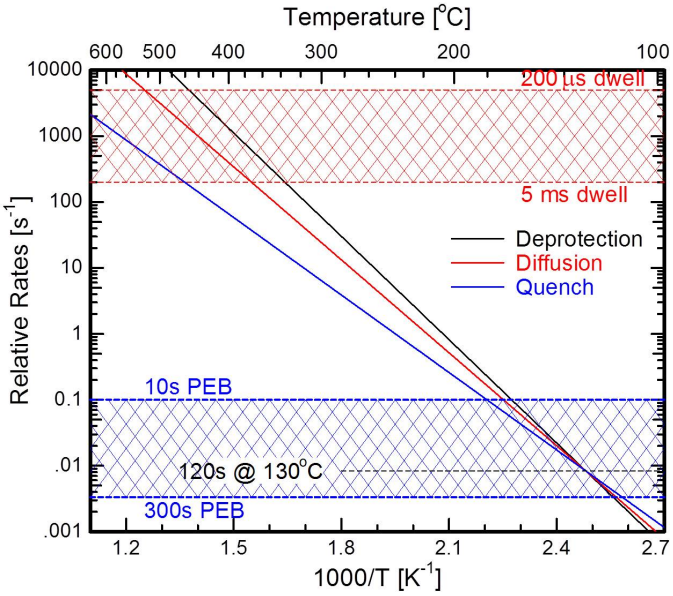

Figure 4.2: Schematic plot of the kinetic competition between resist's side-group deprotection, acid diffusion, and amine-induced acid quenching. As PEB temperatures increase, the competition window between diffusion and deprotection becomes much wider [11, 12]. For this illustration, the relative rates were normalized to a conventional hot-plate PEB condition at 130 °C for 120 s and the E_A values were 100, 90, and 75 kJ/mol for deprotection, diffusion, and quench respectively.

root of the diffusivity ($L \sim \sqrt{Dt}$). As long as the activation energy of diffusion ($E_A^{Diffusion}$) is less than that of deprotection ($E_A^{Deprotection}$), higher temperatures will accelerate the deprotection reaction while the millisecond heating duration compensates and results in reduced diffusion.

Using the conventional hot-plate PEB, however, heating durations shorter than a few seconds are not accessible. To access this millisecond time frames (and higher temperatures), an alternate PEB technique is required [14]. This work utilizes the line-focused CO_2 laser-induced heating system to achieve PEB durations of millisecond time frames at temperatures up to the thermal decomposition limit of the resist.

4.2 Materials and Methods

Three resist polymer resins (Figure 4.3) and three PAGs (Figure 4.4) were used in various combinations in this study. A model resist for 248 nm KrF lithography poly(4-hydroxystyrene-*co*-styrene-*co*-*t*-butyl acrylate) and a model resist for 193 nm ArF lithography poly(2-methyl-2-adamantyl methacrylate-*co*-γ-butyrolactone-2-yl methacrylate) were chosen due to their high thermal stability. Poly(4-*t*-butoxycarbonyloxystyrene), also known as PBOCST, was also chosen due to its wide application as the first chemical amplified system [3]. The PAGs include two ionic salts triphenylsulfonium nonaflate (TPS-NF) and triarylsulfonium hexafluoroantimonate salt (THSb) and a non-ionic PAG *n*-hydroxynaphthalimide trifluoromethanesulfonate (NHN-TF).

This combination generated a total of nine different chemically amplified resist systems which were investigated and compared under hot-plate PEB and laser PEB. Solutions of 5 wt.% resist in propylene glycol monomethyl ether acetate (PGMEA) were spun onto hexamethyldisilazane (HMDS) primed Si wafers. Target thickness for all films was 100 nm. The PAG concentration was 5 wt.% or 10 wt.% with respect to (w.r.t.) the resist polymer resin. The coated substrate was then heated on a hot-plate at 130 °C for 90 s as a post apply bake (PAB) to remove the remaining PGMEA in the film.

For initial sensitivity and acid diffusion studies requiring flood (blank) exposures, the samples were either exposed with a broadband DUV (235-260 nm) at Cornell Nanoscale Science & Technology Facility (CNF) or with extreme ultraviolet (EUV: 13.5 nm) at Professor Denbeaux lab in College of Nanoscale Science and Engineering (CNSE) in Albany, NY. For high resolution patterning, sam-

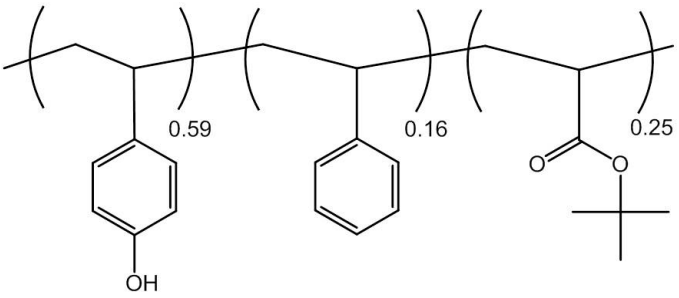

a) A 248 nm resist

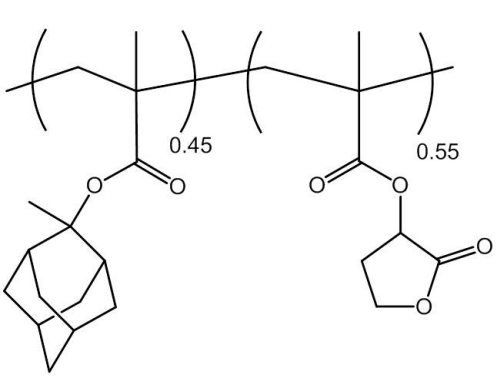

b) A 193 nm resist

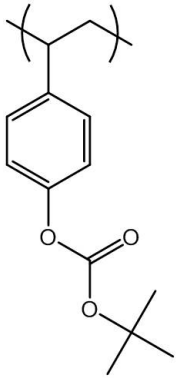

c) PBOCST

Figure 4.3: Deep UV photoresist polymers used for patterning analysis. a) A model 248 nm resist (poly(4-hydroxystyrene-*co*-styrene-*co*-*t*-butyl acrylate)), b) a model 193 nm resist (poly(2-methyl-2-adamantyl methacrylate-*co*-γ-butyrolactone-2-yl methacrylate)), and c) PBOCST (poly(4-*t*-butoxycarbonyloxystyrene)).

ples were exposed with either the ASML 300C DUV stepper at 248 nm in CNF or with EUV at Lawrence Berkeley National Laboratory Advanced Light Source (LBNL ALS).

After DUV and EUV exposures, samples underwent PEB using either a vacuum-chuck hot-plate or CO_2 laser heating. Hot-plate PEB was carried out for 60 s at temperatures varying from 115 °C to 150 °C and laser PEB was processed for 500 μs at temperatures varying from 265 °C (18 W) to 450 °C (30 W). After PEB, all films were developed in 0.26 N tetramethylammonium hydroxide (TMAH) for 60 s and were rinsed with de-ionized water.

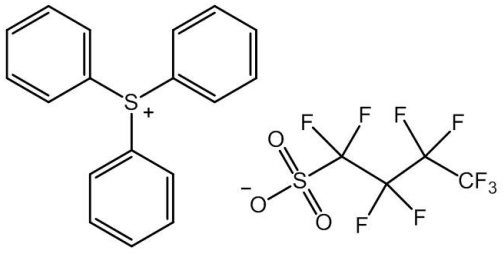

a) TPS-NF

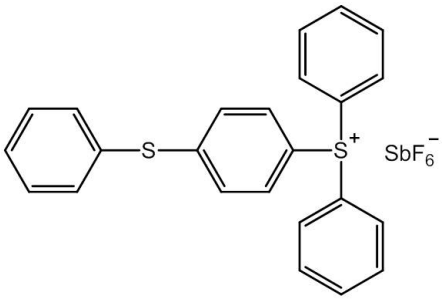

b) THSb

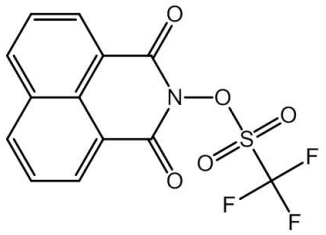

c) NHN-TF

Figure 4.4: PAGs used for patterning analysis. a) TPS-NF (triphenylsulfonium nonaflate), b) THSb (triarylsulfonium hexafluoroantimonate salt), and c) NHN-TF (*n*-hydroxynaphthalimide trifluoromethanesulfonate).

To quantify the acid diffusion, resist bilayers were fabricated by bringing resist-coated polydimethylsiloxane (PDMS) stamps and a silicon wafer in contact at 70 °C for 20 s as shown in Figure 4.5 [15, 16]. Resulting bilayers had PAG-containing top layers and PAG-free bottom layers, each with a target thickness of 100 nm. Film thicknesses were characterized using a Filmetrics optical measurement system (F50-EXR) confirmed through a profilometer (KLA-Tencor P10).

An example of the bilayer data is shown in Figure 4.6, where the acid diffusion length at a heating condition can be determined. Once exposed with sufficient dose and then baked, the generated acids initiate the deprotection reaction and complete the solubility switch on the PAG-containing top layer. Diffusion of

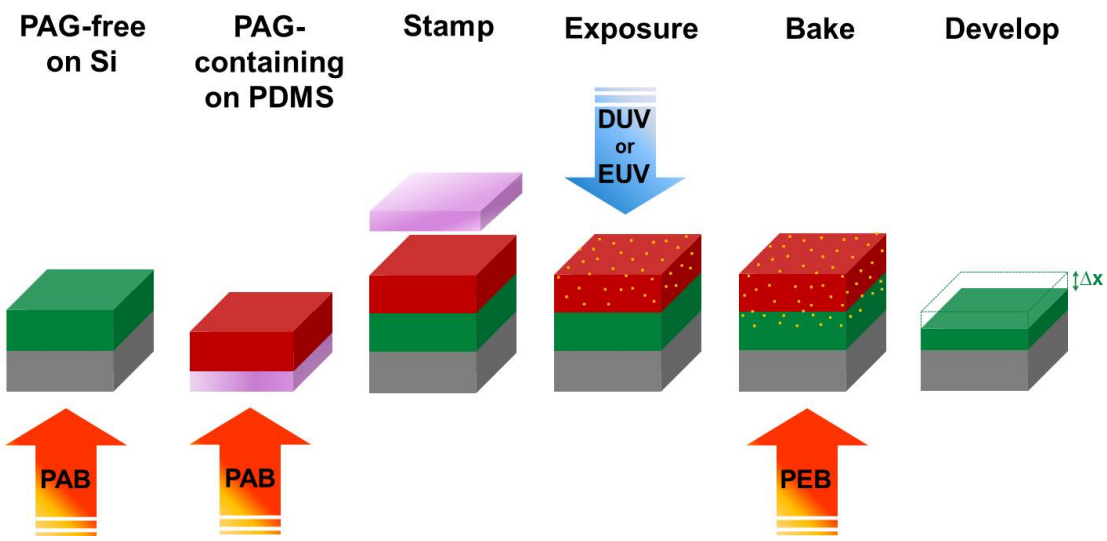

Figure 4.5: Measuring acid diffusion length using bilayer fabrication through a PDMS stamping technique. A PAG-free resist solution is spun on the silicon wafer while a PAG-containing resist solution is spun on the PDMS substrate. PDMS is stamped and peeled off to create a resist bilayer structure. Upon UV exposure and PEB, acids from the PAG-containing layer diffuse into the PAG-free layer, which subsequently induce deprotection. Thickness loss of the PAG-free bottom layer is measured after development and is quantified as the acid diffusion length.

acids into the underlying PAG-free layer induces additional deprotection, leading to the dissolution of a fraction of this layer upon development (Figure 4.5). Consequently, the diffusion of acids can be quantified by this additional dissolution. Under laser PEB at 385 °C for 500 μs for example, the local acid diffusion saturates after deprotecting approximately 50 % of the bottom layer, where the relative acid diffusion length, Δx, between heating conditions can be measured and estimated for diffusivity measurements.

To confirm the patterning performance using the millisecond laser PEB, a commercial EUV resist was patterned using a 13.5 nm (EUV) exposure at CNSE Albany followed by either a millisecond laser PEB or hot-plate PEB on-site. Due

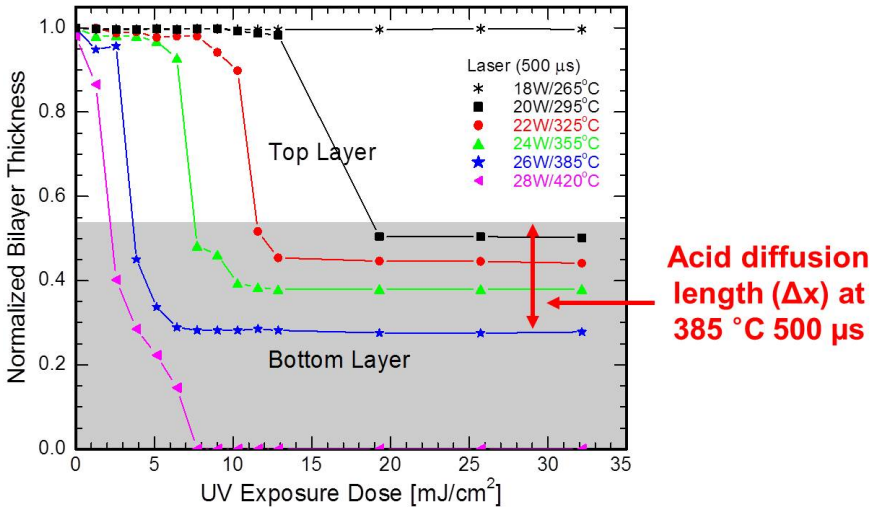

Figure 4.6: Example of a resist bilayer analysis. The PAG-free layer is represented in gray while the PAG-containing top layer is represented in white. With a sufficient acid concentration defined by the UV exposure dose, the solubility switch occurs from the top layer and the excess acids diffuse to partially deprotect the bottom layer until the local acid diffusion is saturated. The thickness loss of the bottom layer at temperature can be quantified as the acid diffusion length Δx.

to confidentiality issues, the supplier and structure of the commercial EUV resist cannot be revealed, but the system is chemically amplified and contains an acrylate-based resin, PAG, and a base quencher with a low glass transition temperature (T_g) ~100 °C.

A LEO 1550 FESEM was used for SEM imaging of critical dimensions (CD) >100 nm, while a Hitachi CD-SEM (CG5000) was used for CDs <100 nm.

4.3 E_A Validation using DUV Lithography

4.3.1 Stability of Resist and PAG

Each intrinsic resist polymer (without PAG) was heated at varying laser powers in order to determine the thermal stability during laser PEB. Figure 4.7 shows the film thickness of the 193 nm resist after laser PEB, both before and after development. There are two limiting power densities for the thermal stability. The laser PEB temperature, at which the complete loss of the intrinsic resist (without PAG) occurs before development, is defined as T_{decomp} (thermal decomposition). Similarly, T_{depro} (thermal deprotection) is defined as the laser PEB temperature at which the deprotection of the intrinsic resist occurs purely through a thermal process. For PEB above T_{depro}, the intrinsic resist is removed after development. For the 193 nm resist, both T_{depro} and T_{decomp} are above 675 °C (42 W). This temperature is well above both the polymer's T_g (~160 °C) and conventional thermal decomposition limits at (~400 °C) [17]. The resist stability at these high temperatures is enabled by the sub-millisecond duration of the laser PEB.

Laser powers and the peak temperature required for thermal decomposition and deprotection are shown in Table 4.2, along with the T_g of each investigated systems. For these systems, higher T_g corresponded to higher T_{decomp} and T_{depro}. The thermal stability of the PAGs was also examined using laser PEB. Coumarin 6 (C6) was added as an acid sensitive dye into poly(4-hydroxystyrene) (PHOST), which was chemically insensitive to the C6 and closely representative of the DUV resist resin. In the presence of an acid, the absorption wavelength of C6 shifts from ~470 nm to ~540 nm, and thus can be used as a quantitative detector of PAG thermal activation [18]. Figure 4.8 shows the absorption curves for un-

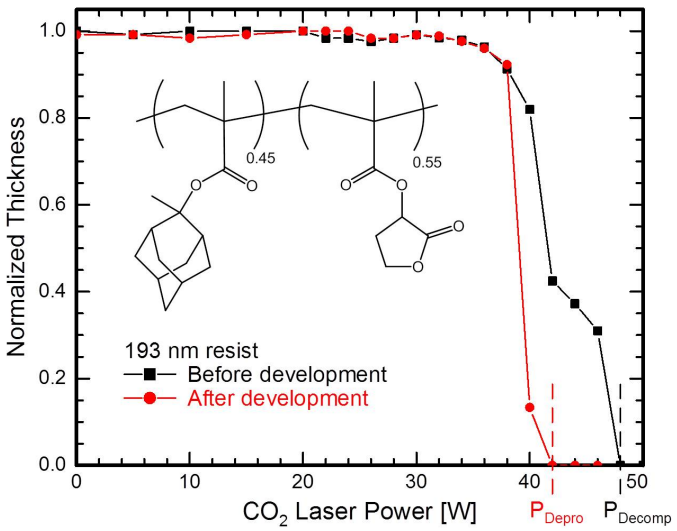

Figure 4.7: An example of finding thermal stability using laser PEB for an intrinsic 193 nm resist (without PAG).

Table 4.2: Laser PEB temperature required for thermal decomposition (T_{decomp}) and deprotection (T_{depro}) under millisecond heating for three resist systems and their T_g

Intrinsic Resist	T_{depro} [°C]	T_{decomp} [°C]	T_g [°C]
193 nm resist	675 (42 W)	760 (46 W)	160
248 nm resist	635 (40 W)	675 (42 W)	147
PBOCST	520 (34 W)	595 (38 W)	125

exposed resists as a function of laser PEB temperature at 500 μs. No significant variation is observed up to 540 °C (35 W) of laser power.

At high temperatures, there is a loss of the 470 nm peak but no measurable peak at 540 nm. This result indicates that the PAG remains thermally stable to powers above 540 °C (35 W), with either the PHOST or C6 decomposing and subsequently decreasing the absorption signal. The thermal stability of THSb and NHN-TF were qualitatively similar.

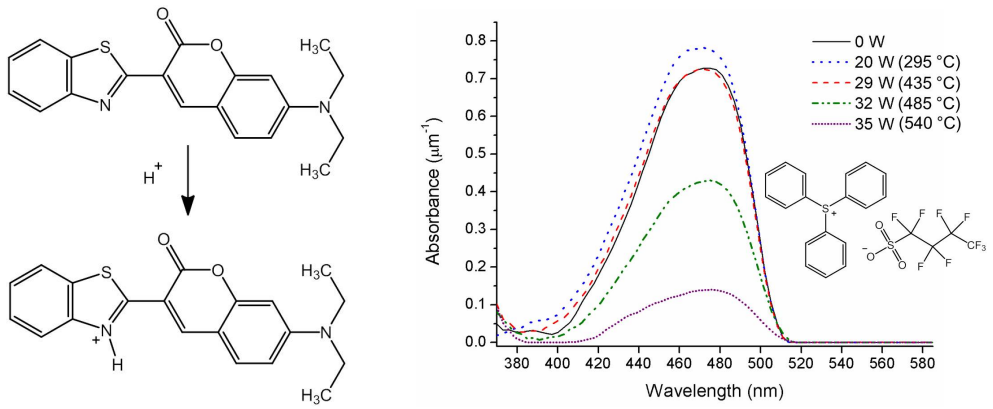

a) Coumarin 6 b) Stability of TPS-NF

Figure 4.8: An example of finding thermal stability using laser PEB for a PAG. Coumarin 6 was used as an acid sensitive dye for testing the thermal stability of TPS-NF. If acid is thermally activated from TPS-NF, a wavelength shift will occur from ~470 nm to ~540 nm [18, 19].

4.3.2 Resist Selection for Appropriate E_A Characteristics

The sensitivity enhancements of CARs have enabled substantial performance improvements in DUV lithography. Since the sensitivity is highly dependent on PEB conditions, it is critical for laser PEB to have comparable sensitivity with hot-plate PEB at temperatures below thermal deprotection, T_{depro}. The sensitivity, characterized by the dose to clear a large area of a resist polymer (E_0), of the different resist systems were compared using laser PEB and conventional hot-plate PEB. As an example, data for the 193 nm resist with 10 wt.% loading of THSb PAG under DUV exposures are shown in Figure 4.9.

The laser-induced millisecond PEB allows the deprotection reaction to complete even at temperatures well above the conventional thermal stability limit (~400 °C) [17]. For laser PEB at 355 °C (24 W), the solubility switch in the resist polymer is achieved at $E_0 \sim 1.5$ mJ/cm^2. At 385 °C (26 W), the E_0 for laser PEB

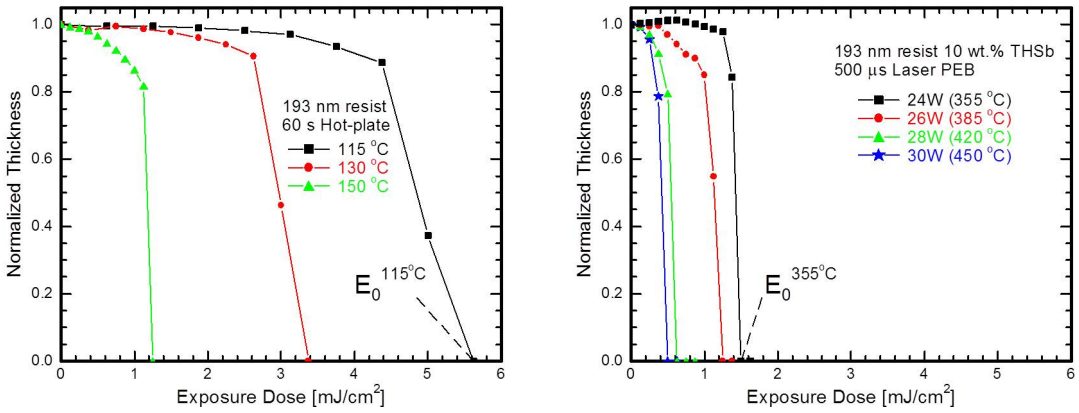

a) Hot-plate sensitivity b) Laser sensitivity

Figure 4.9: Contrast curves of 193 nm model resist with 10 wt.% THSb PAG loading under broadband DUV exposures followed by a) hot-plate PEB at 60 s, and b) laser PEB for 500 μs.

is almost identical to the E_0 for hot-plate PEB at 150 °C, although there is a five orders of magnitude difference in the PEB duration. When compared with a typical hot-plate temperature of 115 °C for this resist polymer, the E_0 for laser PEB at moderate temperatures requires only 10 % of the dose, which is a 10x improvement in sensitivity.

To compare E_0 between hot-plate PEB and laser PEB, we define E_0^{HP} as the E_0 required for hot-plate PEB at 115 °C for 60 s (typical PEB condition for this polymer). For laser PEB, T_0^{Laser} is defined as the laser PEB temperature where $E_0^{Laser} = E_0^{HP}$, which means that T_0^{Laser} is the minimum temperature that must be used for laser PEB to achieve a sensitivity equal to the typical hot-plate conditions. At higher temperatures, the laser PEB achieves higher sensitivity at a potential risk of the excessive acid diffusion. Table 4.3 shows the list of observed E_0^{HP} for all nine investigated resist systems.

As a reference point, the PEB conditions to obtain E_0^{HP} were fixed for the 193 nm resist, which had the highest T_{decomp}, T_{depro}, and T_g. This PEB condi-

Table 4.3: DUV exposure dose required to clear the chemically amplified systems using hot-plate PEB at 115 °C for 60 s (E_0^{HP}).

E_0^{HP} [mJ/cm^2]	TPS-NF	THSb	NHN-TF
193 nm resist	1.5	10	>15
248 nm resist	0.25	0.75	0.125
PBOCST	1.25	2	1

tion is higher compared to the typical conditions used for the 248 nm resist and PBOCST, which would increase the sensitivity due to the increased acid mobility at higher temperatures. As a result, the 248 nm resist, which contains more co-polymeric components (more free volume upon PEB), is a factor of 4-10 more sensitive than either of the other resist systems for all investigated PAGs. However, there is no consistent behavior of the PAGs within a given resist system. For example, TPS-NF (small PAG) in the 193 nm resist has a low E_0^{HP}, while both THSb (larger PAG) and NHN-TF (smaller PAG) have relatively high E_0^{HP}.

Table 4.4: The laser PEB temperature, T_0^{Laser}, at which $E_0^{Laser} = E_0^{HP}$ according to Table 4.3. T_0^{Laser} is the minimum temperature for laser PEB to achieve comparable sensitivity to the standard hot-plate conditions.

T_0^{Laser} [°C]	TPS-NF	THSb	NHN-TF
193 nm resist	385 (26 W)	295 (20 W)	<325 (<22 W)
248 nm resist	400-450 (27-30 W)	420 (28 W)	>400 (>27 W)
PBOCST	400-450 (30-33 W)	>450 (>30 W)	>485 (>32 W)

In order to gain maximum enhancement from laser PEB, T_0^{Laser} should be minimized. T_0^{Laser} for the nine resist systems are given in Table 4.4. Due to the high $E_0^{HP} = 10$ mJ/cm^2, T_0^{Laser} is low (295-325 °C) for the 193 nm resist with ei-

ther THSb or NHN-TF PAGs. For laser PEB conditions above T_0^{Laser}, the resist sensitivity will be improved compared to the hot-plate PEB at 115 °C for 60 s. However, the acid diffusion is also exponential with temperature, so heating temperatures must be minimized. To evaluate the acid diffusion of the nine resist systems, the bilayer structure was used to measure the diffusivity as discussed previously (Figure 4.6). Bilayers for each resist system were exposed using DUV, followed by PEB using a hot-plate or laser. Data for the 193 nm resist system with TPS-NF PAG are shown in Figure 4.10.

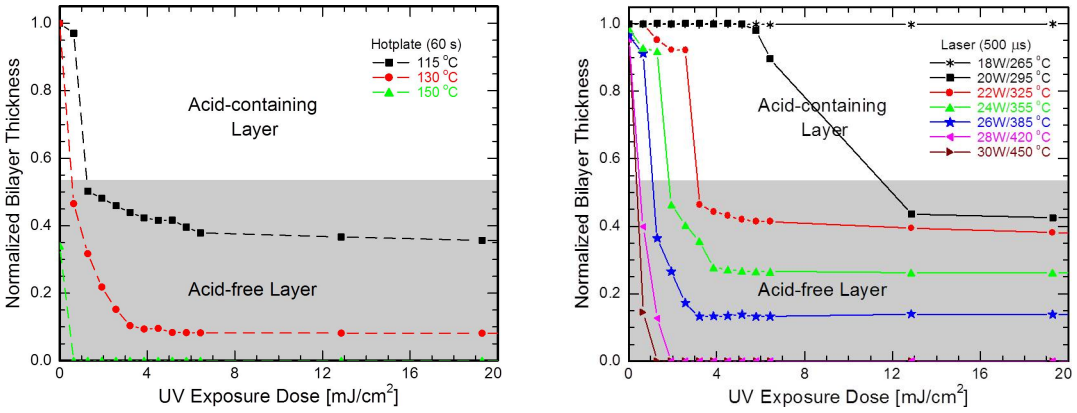

a) Hot-plate bilayer b) Laser bilayer

Figure 4.10: Bilayer data for 193 nm resist with 5 wt.% TPS-NF PAG loading only on the top layer (~100 nm) under DUV exposures followed by a) hot-plate PEB at 60 s, and b) laser PEB for 500 μs.

Using hot-plate PEB, a significant acid diffusion is observed even at 115 °C suggesting highly mobile acid. Increasing the PEB temperature to 130 °C results in additional diffusion, and nearly all of the bottom PAG-free layer is lost by 150 °C. For laser PEB, temperatures up to 325 °C (22 W) show no significant acid diffusion, while substantial diffusion occurs by 420 °C (30 W) which is comparable to the hot-plate induced diffusion at 150 °C. The saturation in diffusion lengths at high temperature and exposure doses are potentially due to the saturation in the local diffusion of acids. As no acids are generated in the bot-

tom layer during the UV exposure and are transported only by diffusion from the top layer, the dissolution of the PAG-free layer should be independent of exposure dose. This observation suggests an additional diffusion that is dependent on the acid-concentration, possibly linked to the saturation of acid traps or amine quench. Similar behavior was observed for both 248 nm and PBOCST resins with all investigated PAGs.

To compare resist systems, the highest hot-plate and laser temperatures, where the thickness profile of the bottom layer saturated within ~20 % of the original thickness, were defined as T_{MD}^{HP} (minimal diffusion) and T_{MD}^{Laser} respectively. For the 193 nm resist with TPS-NF system, T_{MD}^{HP} is <115 °C. Table 4.5 gives T_{MD}^{Laser} for the nine investigated systems.

Table 4.5: Highest laser PEB temperature resulting in minimal diffusion under DUV exposure (T_{MD}^{Laser}).

T_{MD}^{Laser} [°C]	TPS-NF	THSb	NHN-TF
193 nm resist	340 (23 W)	385 (26 W)	450 (30 W)
248 nm resist	310 (21 W)	355 (<24 W)	265 (18 W)
PBOCST	<340 (<23 W)	295 (<20 W)	<295 (<20 W)

For lithographic patterning using laser PEB, the optimal system for laser PEB is one with a T_0^{Laser} less than T_{MD}^{Laser}, resulting in a process window that has a higher sensitivity than the typical hot-plate PEB condition with minimal acid diffusion. The 193 nm resist with THSb PAG satisfies these criteria with T_0^{Laser} at 295 °C (20 W) and T_{MD}^{Laser} at 385 °C (26 W). These criteria also suggest that the 193 nm resist with the THSb PAG meets the activation energy requirements where $E_A^{Deprotection} > E_A^{Diffusion}$ for the high temperature and millisecond time PEB as schematically shown in Figure 4.2.

4.3.3 Validation through Imaging Performance

For lithography, the imaging quality is the ultimate test of a resist system and its PEB condition. Figure 4.11 compares the imaging after DUV (248 nm) exposure followed by either hot-plate PEB or laser PEB.

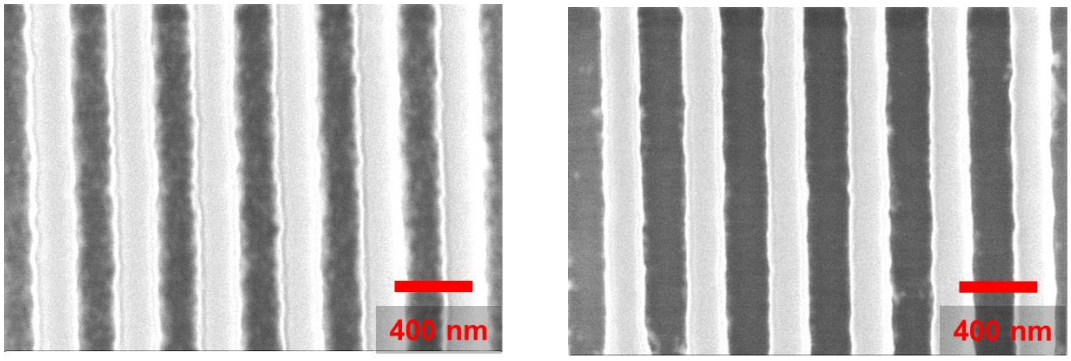

a) DUV & hot-plate PEB

b) DUV & laser PEB

Figure 4.11: SEM images of patterned 193 nm resist with THSb PAG at 250 nm half-pitches using 248 nm DUV exposures followed by a) hot-plate PEB at 115 °C for 60 s (20.0 mJ/cm^2) and b) laser PEB at 295 °C (20 W) for 500 μs (10.8 mJ/cm^2). For comparable CD at 250 nm, laser PEB simultaneously achieves ~2x increase in sensitivity and ~28 % reduction in LWR (30.9 and 22.2 nm for hot-plate and laser PEB respectively).

The DUV exposure dose required, for the comparable 250 nm critical dimension (CD) between hot-plate and laser PEB, are 20 mJ/cm^2 and 10.8 mJ/cm^2 respectively. By achieving high temperatures using laser PEB, the sensitivity is increased by a factor of two. Furthermore, the LWR values are 30.9 nm for hot-plate PEB and 22.2 nm for laser PEB, showing a 28 % decrease due to the 10^5 s shorter PEB duration.

This simultaneous improvement in sensitivity and roughness using laser PEB suggests that the RLS trade-off established in the seconds time frame is shifted favorably in the millisecond time frame. The improvement in patterning

performance using laser PEB is purely thermal (Appendix C) and is expected to be independent of the exposure wavelength. However, the activation characteristics of the resist material must meet the requirement $E_A^{Deprotection} > E_A^{Diffusion}$, with the laser PEB temperature falling between T_0^{Laser} and T_{MD}^{Laser}.

4.4 Patterning performance using EUV with Laser PEB

Compared to hot-plate PEB, the 193 nm resist with THSb PAG showed significant patterning improvement using DUV exposures and laser PEB. Although the improvement is thermal (as shown in Appendix C), the mechanism for deprotection (sensitivity) and acid generation may be different between 5.0 eV photons for 248 nm DUV exposures and 91.8 eV photons for 13.5 nm EUV exposures. Contrast (sensitivity) curves for the 193 nm resist with THSb PAG obtained using a flood (blank) EUV exposure are shown in Figure 4.12.

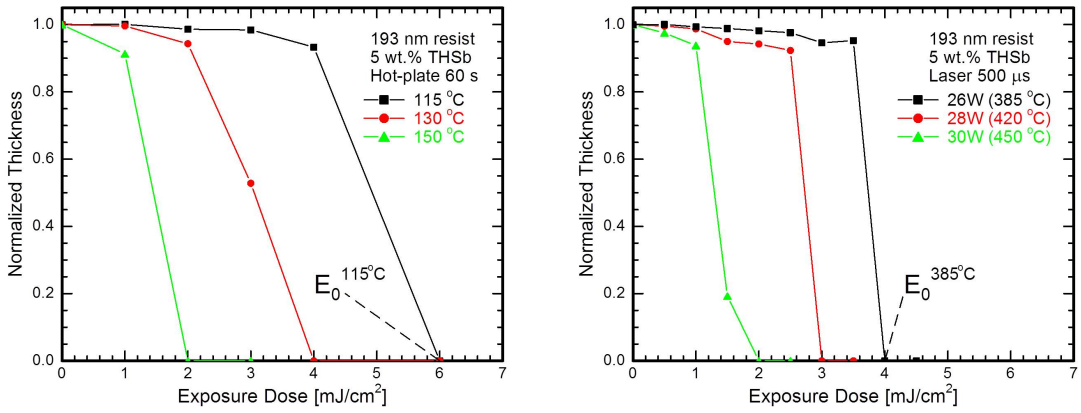

a) Hot-plate sensitivity b) Laser sensitivity

Figure 4.12: Contrast curves of the 193 nm resist with 5 wt.% THSb PAG loading using 13.5 nm EUV exposures followed by a) hot-plate PEB at 60 s and b) laser PEB for 500 μs.

Deprotection kinetics are not significantly different from the DUV exposures

(Figure 4.9). E_0^{HP} is ~5 mJ/cm^5 which corresponds to a T_0^{Laser} of <385 °C (<26 W). At 385 °C (30 W) laser PEB, the response is equivalent to a hot-plate PEB at 150 °C for 60 s. Compared to DUV exposures, the E_0 for the this resist system is ~2 times lower for hot-plate PEB, but is comparable using laser PEB. To prevent the excessive acid diffusion during laser PEB, resist bilayers were also EUV exposed followed by laser PEB as shown in Figure 4.13 to set the limit on PEB temperature (T_{MD}^{Laser}).

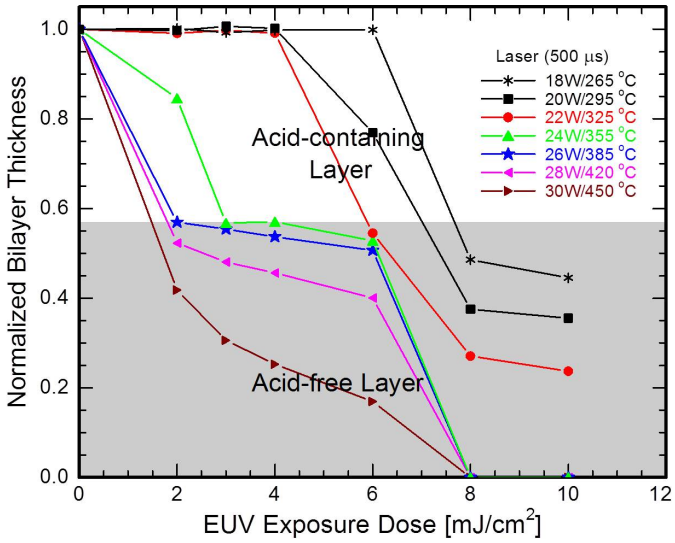

Figure 4.13: Sample bilayer data for 193 nm resist with 5 wt.% THSb PAG loading only on the top layer (~100 nm) under EUV exposures followed by a) hot-plate PEB at 60 s, and b) laser PEB for 500 μs.

Overall, the deprotection behavior observed using the contrast curve and acid diffusion using the bilayer studies do not look significantly different from the DUV counterpart (Figures 4.9 and 4.10). However, the extent of the deprotection reaction is much greater than that of the DUV counterpart, due to the 91.8 eV photons generating more initial acid concentration at comparable exposure doses. Since there were no significant difference in deprotection and acid diffusion behavior, patterning performance was tested using EUV followed by

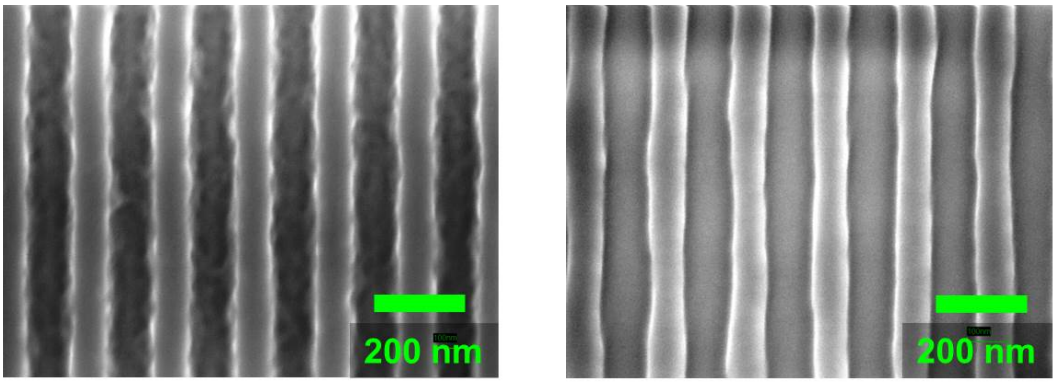

a) EUV & hot-plate PEB b) EUV & laser PEB

Figure 4.14: SEM images of patterned 193 nm resist with 5 wt.% THSb PAG at 100 nm half-pitches using 13.5 nm EUV exposures followed by a) hot-plate PEB at 115 °C for 60 s (9.04 mJ/cm^2) and b) laser PEB at 325 °C (22 W) for 800 μs (3.86 mJ/cm^2). For comparable CDs at 100 nm, laser PEB simultaneously achieves ~2.5x increase in sensitivity and ~20 % reduction in LWR (10 and 7 nm for hot-plate and laser PEB respectively).

either hot-plate PEB and laser PEB as shown in Figure 4.14.

To pattern 100 nm half-pitch features, the EUV exposure dose required for the typical hot-plate PEB condition (115 °C for 60 s) was 9.04 mJ/cm^2, while a moderate laser PEB condition (325°C for 800 μs) required 3.86 mJ/cm^2. This sensitivity is a 2.5x improvement for laser PEB, which is similar to the DUV observations. In addition, approximately 20 % reduction in roughness is visible for the laser PEB patterns, where the quantified LWR values are 10 and 7 nm for hot-plate and laser PEB respectively.

The ultimate resolution is also a critical metric for any resist system or process technology. The previously tested 193 nm resist with THSb PAG as the only additive (no base quenchers) was not capable of achieving sub-100 nm patterns. For test below this resolution using laser PEB, a well-characterized commercial EUV resist was used. This resist was an acrylate-based chemically amplified

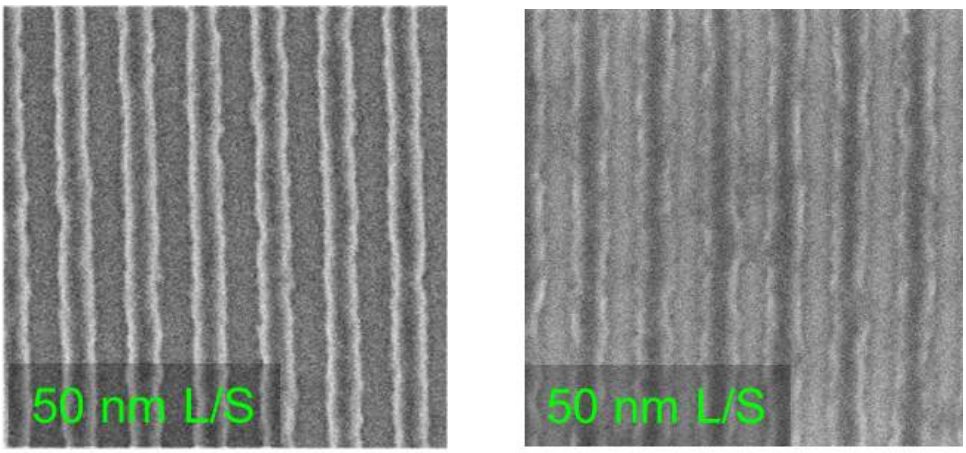

a) 85 °C hot-plate PEB b) 90 °C hot-plate PEB

Figure 4.15: SEM images of patterned commercial EUV resist (chemically amplified) at 50 nm half-pitches using 13.5 nm EUV exposures followed by a) hot-plate PEB at 85 °C for 60 s (14.0 mJ/cm^2) and b) hot-plate PEB at 90 °C for 60 s (9.72 mJ/cm^2). This resist system is thermally sensitive as 5 °C change in PEB temperature induces excessive acid diffusion.

system with a PAG and a base-quencher, with a sufficiently low T_g (~100 °C). The low T_g makes this resist extremely sensitive to temperature as shown in Figure 4.15.

The EUV resist resolves 50 nm CD with 8.2 nm LWR (5.6 nm LER) at 14.0 mJ/cm^2 of EUV exposure dose using the typical hot-plate PEB condition for this resist (85 °C for 60 s). When the PEB condition is raised by 5 °C, the exposure dose required to achieve the comparable 50 nm CD is reduced to 9.7 mJ/cm^2 as expected. However, due to the trade-off between sensitivity and LER, the roughness is significantly increased to 12.8 nm LWR and 6.9 nm LER.

For laser PEB, the simultaneous improvement in both sensitivity and roughness is expected. As a demonstration, samples with this commercial resist were EUV exposed and immediately post-exposure baked using either CO_2 laser-

induced PEB or diode laser-induced PEB, and then compared with hot-plate PEB at 85 °C for 60 s. Results are shown in Figure 4.16. Similar to the 193 nm resist system, this commercial EUV resist shows ~30 % increase in sensitivity with a 10 % roughness reduction. The suppression of acid diffusion results in lower LWR and LER using laser PEB. While sensitivity improvements are purely thermal, roughness decrease is dependent on the resist. The 193 nm resist system with THSb PAG was chosen for its appropriate activation characteristics, $E_A^{Deprotection} > E_A^{Diffusion}$. The commercial EUV resist system, in contrast, is designed and tailored specifically for the low temperature, seconds time frame heating.

Using hot-plate PEB, generated acid-catalysts have sufficient time to diffuse within the resist matrix. To minimize LWR and LER for hot-plate PEB, resist systems with $E_A^{Diffusion} > E_A^{Deprotection}$ are required, which is the opposite in requirement for high temperature laser heating as schematically shown in Figure 4.17. For conventional hot-plate PEB, sufficient acid-catalyzed deprotection leading to solubility switch is easily obtained during 30-120 s durations. Since the LER and LWR, induced by the excessive diffusion, are the limiter for 10 nm dimension patterning, commercial resist systems are tailored to have a higher activation for diffusion relative to deprotection (Figure 4.17a). While laser PEB was able to show patterning improvements for 50 nm half-pitch features (Figure 4.16), the activation characteristics of this commercial EUV system becomes less favorable for laser PEB as resolution approach 30 nm scale as shown in Figure 4.18.

Resolution down to 30 nm can be achieved using hot-plate PEB due to the favorable activation characteristics $E_A^{Diffusion} > E_A^{Deprotection}$. However, this activa-

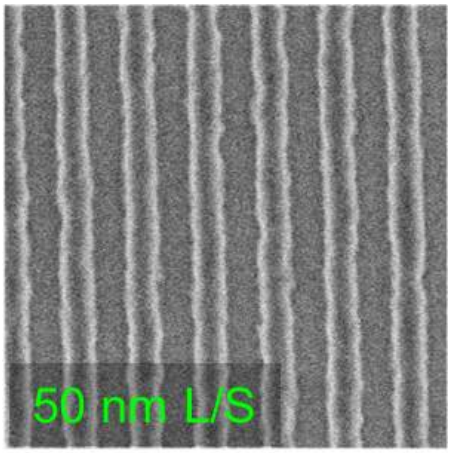

a) 85 °C 60 s hot-plate PEB

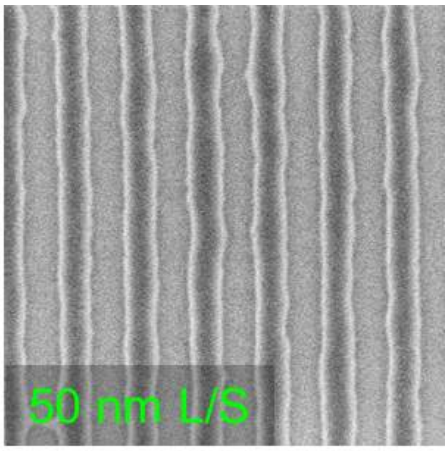

b) 315 °C 500 μs CO_2 laser PEB

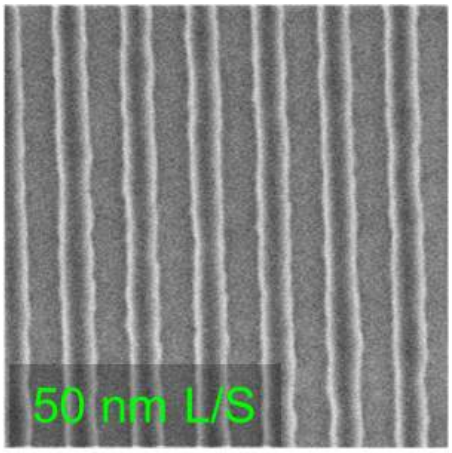

c) 225 °C 2 ms diode laser PEB

Figure 4.16: SEM images of patterned commercial EUV resist (chemically amplified) at 50 nm half-pitches using 13.5 nm EUV exposures followed by a) hot-plate PEB at 85 °C for 60 s (14.0 mJ/cm^2), b) CO_2 laser PEB at 315 °C for 500 μs (10.0 mJ/cm^2), and c) diode (980 nm) laser PEB at 225 °C for 2 ms (12.0 mJ/cm^2). Analyzed LWR values are 8.19 nm, 7.7 nm, and 6.88 nm while LER values are 5.6 nm, 3.9 nm and 4.5 nm for hot-plate, CO_2, and diode PEB respectively.

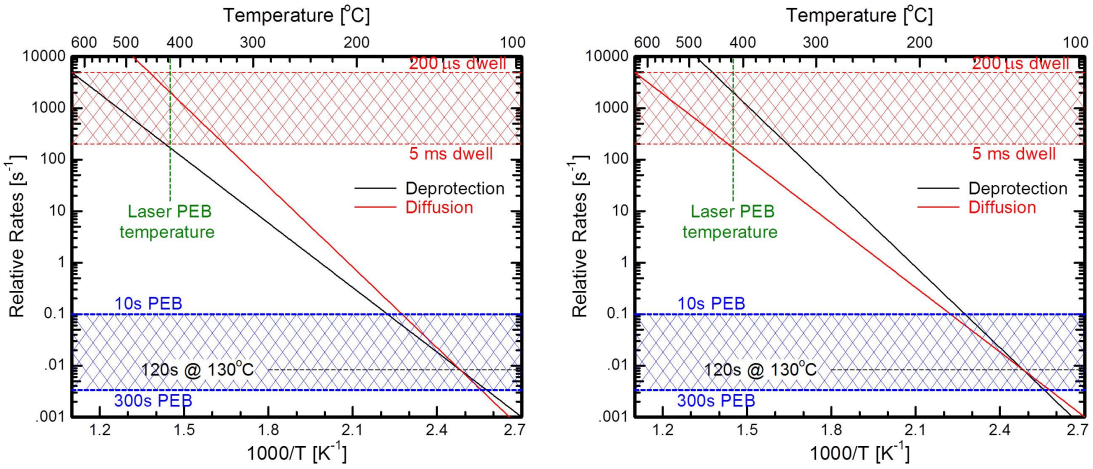

a) Ideal resist system for hot-plate

b) Ideal resist system for laser

Figure 4.17: Schematic plots of the kinetic competition between deprotection and acid diffusion of ideal resists for a) hot-plate PEB ($E_A^{Diffusion} > E_A^{Deprotection}$) and b) laser PEB ($E_A^{Deprotection} > E_A^{Diffusion}$). For these illustrations, the relative rates were normalized to a conventional hot-plate PEB condition at 130 °C for 120 s and the E_A values were 100 and 80 kJ/mol for either deprotection or diffusion.

tion characteristics is not ideal for laser PEB conditions. While patterning performance (sensitivity, LWR, and LER) are better or equivalent using laser PEB for 50 nm or 40 nm resolution patterns respectively, significant pattern roughness, pattern bridging, and collapse are observed for 30 nm features. This observation suggests that while laser PEB shows great potential, resist materials designed and tailored with protecting groups and PAGs optimized for the high temperature regime are required [20].

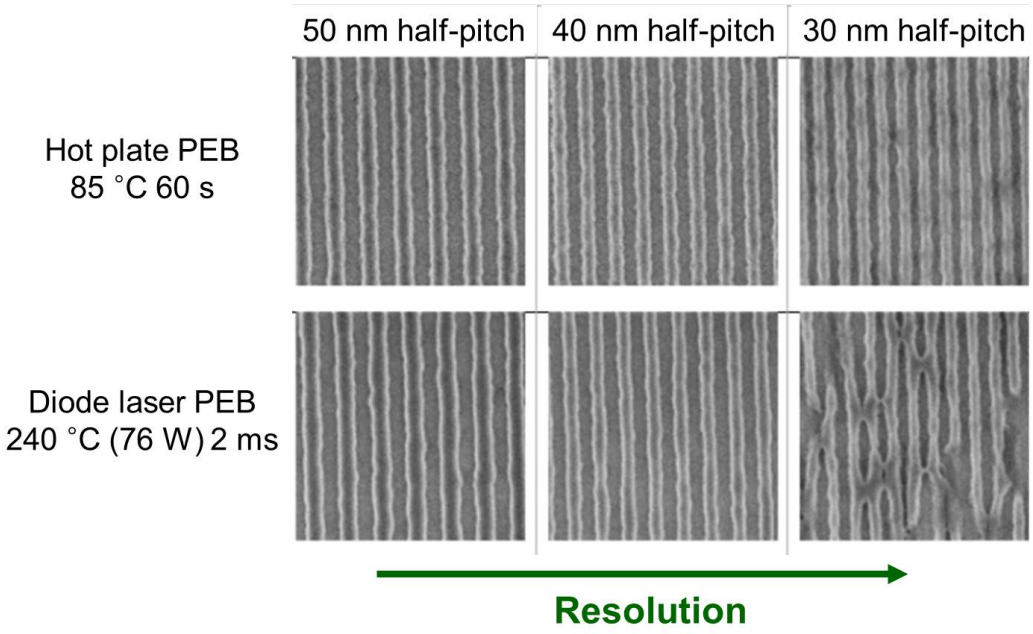

Figure 4.18: EUV exposure followed by hot-plate or laser PEB on commercial EUV resist system as a function of resolution. Excessive acid diffusion for hot-plate PEB is suppressed due to favorable activation characteristics ($E_A^{Diffusion} > E_A^{Deprotection}$). However, the same activation characteristics is detrimental for laser PEB conditions, where patterning performance becomes worse for higher resolution patterns.

4.5 Base Quenchers and Post-Exposure Delay for Laser PEB

4.5.1 Patterning Improvements with Base Quenchers

Commercial resist systems include small molecule additives that quench low concentration of the generated acid-catalysts. These small molecules are commonly referred to as base quenchers and are generally comparable in size with the acid-generating PAGs. The major role of base quenchers is to limit the chemical amplification during PEB in order to minimize the pattern roughness [21–23].

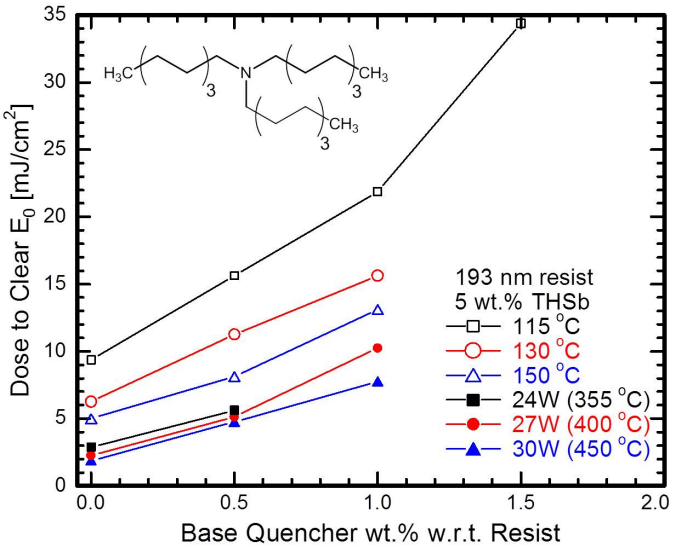

Figure 4.19: Structure of trioctylamine (TOA) base quencher and deprotection data for a 193 nm resist, 5 wt.% THSb PAG loading, and a range of TOA base quencher. Samples were exposed using a broadband DUV (235-260 nm) followed by either hot-plate PEB for 60 s or laser PEB for 500 μs.

Since base quencher molecules, and their kinetics, have been optimized to work with seconds time frame hot-plate PEB, it was important to investigate the quenching behavior using laser PEB. For this analysis, the change in resist deprotection was probed by the dose to clear (E_0) and was measured as a function of base quencher concentration using the 193 nm system with 5 wt.% THSb PAG w.r.t. the resist resin. Trioctylamine (TOA) with concentrations ranging from 0.5-2 wt.% w.r.t. the resist was used to match typical concentrations used for patterning applications. The structure of TOA and the deprotection data using a broadband DUV (235-260 nm) followed by either 500 μs CO_2 laser PEB or 60 s hot-plate PEB are shown in Figure 4.19.

For all PEB conditions, regardless of hot-plate or laser PEB, a small addition of the TOA base quencher significantly increases the exposure dose required to achieve the solubility switch. This increase in E_0 is a direct result of cata-

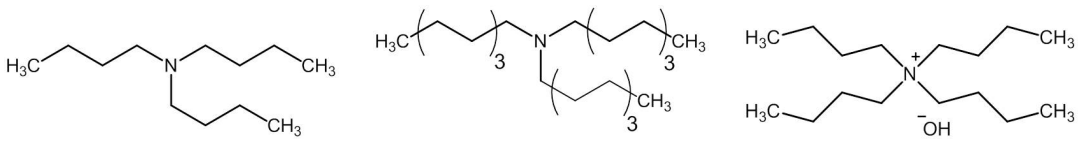

a) Tributylamine (TBA) b) Trioctylamine (TOA) c) Tetrabutyl ammonium hydroxide (TBAH)

Figure 4.20: Three base quencher molecules tested for optimal patterning performance using 248 nm DUV lithography and laser PEB.

lyst quenching during the PEB process. Even at a high laser PEB temperature of 450 °C (30 W), the acid concentration required to achieve the same amount of deprotection increases by a factor of two when 1 wt.% of base quencher is added. As PEB temperatures decrease, the curve shape describing the acid quench remains similar but shifts up requiring higher E_0. This behavior is comparable to the quenching effects observed for hot-plate PEB, suggesting that imaging performance can be improved even further for laser PEB if base quenchers are added to the chemically amplified systems.

For patterning evaluation using base quencher and laser PEB, three types of base quenchers were used based on their chemical properties as shown in Figure 4.20. Tributylamine (TBA) was chosen for its low boiling point and its racemic properties which makes it optically transparent. Previously tested TOA base quencher is non-ionic and has a long alkane chain that increases the molecule's boiling point and the optical opacity. Tetrabutyl ammonium hydroxide (TBAH) has a very similar property in size and optical property as the TOA, but is an ionic molecule.

Patterning performances using each base quenchers were tested for both hot-plate PEB and laser PEB. For comparable base quenching, equimolar base weights were calculated and added into the chemically amplified system con-

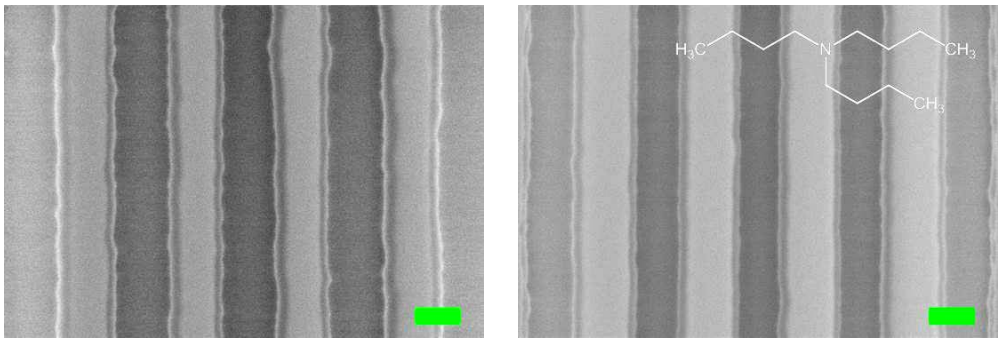

a) No base

b) TBA

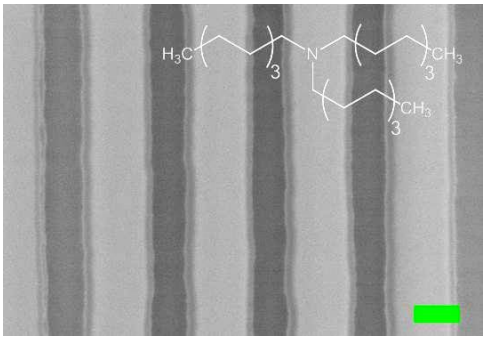

c) TOA

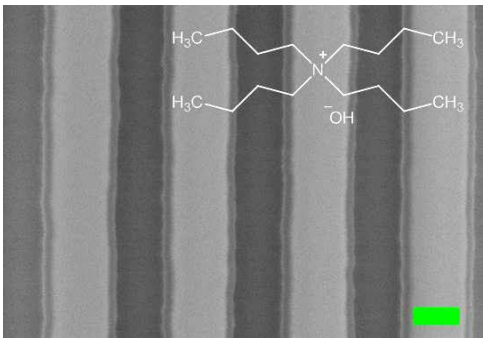

d) TBAH

Figure 4.21: SEM Images of 193 nm resist with 5 wt.% THSb along with equimolar weights of quenchers. Images were patterned using 248 nm DUV exposures followed by laser PEB at 295 °C (20 W) for 500 μs with target CD of 300 nm. Figure 4.21a is the point of reference pattern without any base additives. At comparable CD, patterns with TBA base additives show lowest LER value of 4.7 nm compared to 13.0 nm for TOA and 11.8 nm for TBAH. All scales bars correspond to 200 nm.

taining 193 nm resist with 5 wt.% THSb. As a reference point for the equimolar base weights, TOA concentration was set at 0.5 wt.% w.r.t. resist, which resulted in ~0.26 wt.% TBA w.r.t. resist and ~0.37 wt.% TBAH w.r.t. resist. Developed patterns using 248 nm exposures followed by laser PEB (295 °C (20 W) for 500 μs) are shown in Figure 4.21.

For a comparable CD of 300 nm, required exposure doses were 2.6 mJ/cm^2 without any base additive and 4.4-4.8 mJ/cm^2 with a small concentration of base

additives. While the sensitivity between all three base quencher types remains similar, the patterns developed with TBA additives showed the smallest LER value of 4.7 nm, while patterns generated using the other two base quenchers showed LER greater than 10 nm. This result suggests that the smallest non-ionic base is the most effective for neutralizing the acid-catalysts in the sub-millisecond PEB regime.

The incorporation of base quenchers show decrease in roughness and sharper features even for the laser PEB. While base additives show promising results for further improving patterns resolved using laser PEB, fundamental understanding on the role of base additives and their quenching mechanism is still required.

4.5.2 Post-Exposure Delay Effect on Laser PEB

Upon UV exposure, an initial concentration of acid-catalysts is established. If exposed samples do not undergo PEB immediately, the acid concentration in the resist matrix will be slowly quenched depending on the sample environment and potential exposure to airborne contamination including amines [24–26]. This effect, referred as the post-exposure delay (PED), is dependent on the time between exposure and PEB.

For initial EUV exposures performed at LBNL, there was a ~2-3 hrs PED due to the unavailability of the laser heating tool on-site. To estimate the impact of PED, controlled experiments were made with DUV exposures. Figure 4.22a shows the sensitivity and the acid diffusion length change as a function of PED after DUV exposure. Regardless of PEB temperature, E_0 values increase drasti-

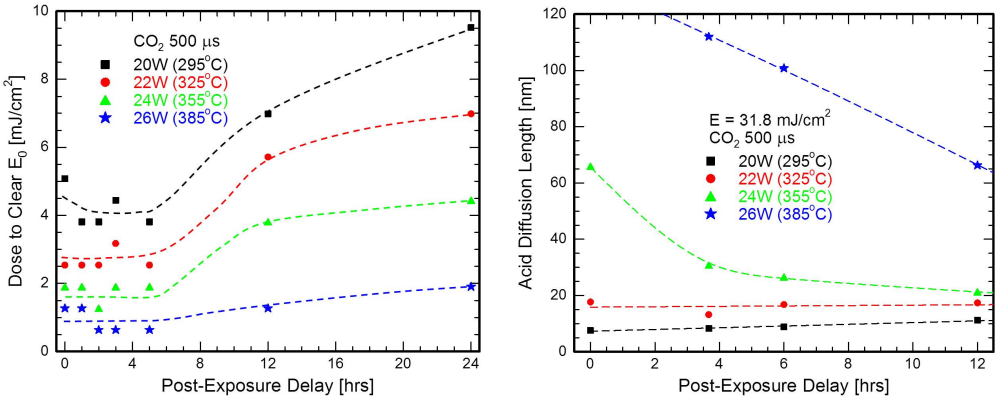

a) PED on deprotection

b) PED on acid diffusion length

Figure 4.22: Changes in the dose to clear (E_0) and acid diffusion length of a 193 nm resist system with 5 wt.% THSb system due to post-exposure delay (PED) after DUV exposures. While a clear trend is not observed, significant change in E_0 and acid diffusion are observed for hours of PED. Samples were exposed using a broadband DUV (235-260 nm) followed by laser PEB for 500 μs. Curves are drawn for illustration purposes only.

cally for PED beyond 5 hrs. While the change in sensitivity may seem minimal for PED less than 4 hrs, a 10 % change in E_0 is significant for reaction kinetic analysis and evaluating parameters for imaging. Due to the significant quenching of the acid-catalysts during PED, a decrease in the acid diffusion length is observed for PED durations at all heating temperatures.

For application perspectives, the time between UV exposure establishing an initial acid concentration and PEB, inducing acid-catalyzed deprotection, should be minimal. These results suggest that both exposure and laser PEB should be performed on-site in order to minimize PED. For this reason, all patterning tests performed at CNSE-Albany using EUV exposures were subjected to on-site laser PEB.

4.6 Conclusions

An alternate method for PEB utilizing a line-focused continuous wave CO_2 or diode laser was introduced. Nine resist systems were characterized using laser PEB for thermal stability, resist sensitivity, and acid diffusion for either DUV or EUV illumination. All of the investigated systems were thermally stable to temperatures at least 200 °C above their glass transition temperatures, which is due to the PEB duration in the sub-millisecond time frames. Despite five orders of magnitude difference in PEB duration, the sensitivity for hot-plate and laser PEB were similar at moderate laser PEB temperatures. To achieve an equivalent sensitivity to a 115 °C 60 s hot-plate PEB, laser powers reaching peak temperatures of 295-450 °C (20-30 W) were required with 500 μs laser PEB. Acid diffusion distances under laser PEB were measured using a PAG-containing/PAG-free bilayer structure, with minimal diffusion observed over similar laser-induced temperatures. Images formed using laser PEB, under DUV or EUV exposure at comparable resolution to hot-plate PEB, show simultaneous improvement in resist sensitivity (up to 30 %) and a decrease in roughness (as much as 25 %). These data demonstrate the potential for laser PEB to address some of the diffusion and sensitivity challenges in the future DUV and EUV lithography.

4.7 Acknowledgments

This work was supported by Intel Corporation and Semiconductor Research Corporation (Task ID: 2125.001). DuPont Electronic Materials and Taro Ishii at Mitsubishi Rayon America Inc. are acknowledged for providing materials. College of Nanoscale Science and Engineering, Albany, NY (Alin Antohe and Prof.

Gregory Denbeaux), SEMATECH (Karen Petrillo)and GLOBALFOUNDRIES in Albany, NY (Kenji Yoshimoto and Gerard Schmid), and Lawrence National Berkeley Laboratory Advanced Light Source in Berkeley, CA (Patrick Naulleau, Gideon Jones, and Brian Hoef) are gratefully acknowledged for EUV exposures and discussions. Patrick Naulleau and EUV SuMMIT are thanked for the imaging analysis. Florencia Paredes, Pratima Satish, Dong Chen, and Andrew Hurst are acknowledged for experimental contributions. Cornell Center for Materials Research (NSF-DMR 0520404) and the Cornell NanoScale Science and Technology Facility (NSF-ECS 0335765) are thanked for facility support. Manish Chandhok and Todd Younkin are gratefully acknowledged for mentoring, guidance, discussions, and encouragements. Jing Sha is thanked for being a wonderful colleague, a mentor, and a friend.

References

[1] H. Ito, C. G. Willson, and J. M. J. Frechet, "New UV resists with negative or positive tone", *Digest of Technical Papers of 1982 Symposium on VLSI Technology*, vol. 82, pp. 86–87, 1982.

[2] H. Ito and C. G. Willson, "Chemical amplification in the design of dry developing resist materials", *Polym. Eng. Sci.*, vol. 23, no. 18, pp. 1012–1018, 1983.

[3] H. Ito, "Chemical amplification for microlithography", *Adv. Polym. Sci.*, vol. 172, pp. 27–245, 2005.

[4] B. Wu and A. Kumar, "Extreme ultraviolet lithography: A review", *J. Vac. Sci. Technol. B.*, vol. 25, no. 6, pp. 1743–1761, 2007.

[5] R. L. Brainard, J. Cobb, and C. A. Cutler, "Current status of EUV photoresists", *J. Photopolym. Sci. Tec.*, vol. 16, no. 3, pp. 401–410, 2003.

[6] A. Saeki, T. Kozawa, and S. Tagawa, "Relationship between resolution, line edge roughness, and sensitivity in chemically amplified resist of post-optical lithography revealed by Monte Carlo and dissolution simulations", *Appl. Phys. Express*, vol. 2, pp. 075 006–1075006–3–, 2009.

[7] G. M. Gallatin, P. Naulleau, and R. Brainard, "Fundamental limits to EUV photoresist", *Proc. SPIE*, vol. 6519, p. 651 911, 2007.

[8] G. M. Gallatin, P. Naulleau, D. Niakoula, R. Brainard, E. Hassanein, R. Matyi, J. Thackeray, K. Spear, and K. Dean, "Resolution, LER and sensitivity limitation of photoresist", *Proc. SPIE*, vol. 6921, 69211E, 2008.

[9] T. Kozawa and S. Tagawa, "Radiation chemistry in chemically amplified resists", *Jpn. J. Appl. Phys.*, vol. 49, p. 030 001, 2010.

[10] T. Kozawa, A. Saeki, and S. Tagawa, "Point spread function for the calculation of acid distribution in chemically amplified resists for extreme ultraviolet lithography", *Appl. Phys. Express*, vol. 1, p. 027 001, 2008.

[11] B. Jung, J. Sha, F. Paredes, C. K. Ober, M. Thompson, M. Chandhok, and T. R. Younkin, "Sub-millisecond post exposure bake of chemically amplified resist by co_2 laser heat treatment", *Proc. SPIE*, vol. 7639, p. 76390L, 2010.

[12] B. Jung, C. K. Ober, M. Thompson, T. R. Younkin, and M. Chandhok, "Addressing challenges in lithography using sub-millisecond post exposure bake of chemically amplified resist", *Proc. SPIE*, vol. 7972, p. 797 219, 2011.

[13] S. Malik, J. Eisele, A. Whewell, L. Ferreira, T. Holt, and M. Bowden, "Post-exposure bake temperature considerations for high activation energy resist systems", *J. Photopolym. Sci. Tec.*, vol. 13, no. 4, pp. 513–518, 2000.

[14] S. Talwar, D. Markle, and M. Thompson, "Junction scaling using lasers for thermal annealing", *Solid State Technol.*, vol. 46, no. 7, pp. 83–86, 2003.

[15] S. Kang, W. L. Wu, K. W. Choi, A. de Silva, C. K. Ober, and V. M. Prabhu, "Characterization of the photoacid diffusion length and reaction kinetics in EUV photoresists with IR spectroscopy", *Macromolecules*, vol. 43, no. 9, pp. 4275–4286, 2010.

[16] V. M. Prabhu, S. Kang, J. Sha, P. V. Bonnesen, S. Satija, W. L. Wu, and C. K. Ober, "Neutron reflectivity characterization of the photoacid reaction-diffusion latent and developed images of molecular resists for extreme ultraviolet lithography", *Langmuir*, vol. 28, no. 20, pp. 7665–7678, 2012.

[17] B. Jung, J. Sha, F. Paredes, M. Chandok, T. R. Younkin, U. Wiesner, C. K. Ober, and M. O. Thompson, "Kinetic rates of thermal transformation

and diffusion in polymer systems measured during sub-millisecond laser-induced heating", *ACS Nano*, vol. 6, no. 7, pp. 5830–5836, 2012.

[18] E. Richter, S. Hein, and M. Sebald, "Novel diffusion analysis in advanced chemically amplified DUV resist using photometric methods", *J. Photopolym. Sci. Technol.*, vol. 12, no. 5, pp. 695–709, 1999.

[19] J. Sha, "Unconventional processing and characterization methods in lithography", PhD thesis, Cornell University, 2010.

[20] J. Jiang, B. Jung, M. O. Thompson, and C. K. Ober, "Line edge roughness of high deprotection activation energy photoresist by using sub-millisecond post exposure bake", *Proc. SPIE*, vol. 8682, 86821N, 2013.

[21] K. Natsuda, T. Kozawa, K. Okamoto, and S. Tagawa, "Study of acid-base equilibrium in chemically amplified resist", *Jpn. J. Appl. Phys.*, vol. 46, no. 11, pp. 7285–7289, 2007.

[22] T. B. Michaelson, A. T. Jamieson, A. R. Pawloski, J. Byers, A. Acheta, and C. G. Willson, "Understanding the role of base quenchers in photoresists", *Proc. SPIE*, vol. 5376, pp. 1282–1293, 2004.

[23] J. E. Meiring, T. B. Michaelson, A. T. Jamieson, G. M. Schmid, and C. G. Willson, "Using mesoscale simulation to explore photoresist line edge roughness", *Proc. SPIE*, vol. 5753, pp. 350–360, 2005.

[24] O. Nalamasu, E. Reichmanis, J. E. Hanson, R. S. Kanga, L. A. Heimbrook, A. B. Emerson, F. A. Baiocchi, and S. Vaidya, "Effect of post-exposure delay in positive acting chemically amplified resist: An analytical study", *Polym. Eng. Sci.*, vol. 32, no. 21, pp. 1565–1570, 1992.

[25] F. M. Houlihan, E. Chin, O. Nalamasu, J. M. Kometani, and R. Harley, *Correlation of the strength of photogenerated acid with the post-exposure delay effect in positive-tone chemically amplified deep UV resists*. American Chemical Society, 1995, pp. 84–109.

[26] Y. Wei and R. Brainard, *Advanced processes for 193-nm immersion lithography*. Society of Photo-Optical Instrumentation Engineers, 2009, pp. 100–107.

CHAPTER 5

CHEMICAL REACTION KINETICS OF A MODEL RESIST DURING LASER HEATING

5.1 Introduction and Motivation

Over the past four decades, photolithography has enabled advances in sub-micron scale patterning technology, leading to faster computing and advances in the microelectronics industry. Lithography involves patterning a radiation-sensitive polymer, known as a photoresist, which protects the underlying substrate during subsequent etching steps. Chemically amplified photoresists have been used for the past three decades in deep ultraviolet (DUV) lithography, because of their high sensitivity and excellent patterning performance. Chemical amplification involves photochemically generating a strong acid in the resist film, which cleaves (deprotects) tertiary esters along the polymer backbone during a subsequent heating step known as the post-exposure bake (PEB). The resist's solubility changes upon deprotection, facilitating its selective removal with a developing solvent [1]. Resist materials face numerous challenges as pattern dimensions approach sub-15 nm length scales, including the diffusion control of the acid-catalyst during the PEB. Furthermore, although the commercially optimized lithography process is famously reliable, its reaction pathways and kinetics are not fully understood at the molecular level. One of the key challenges is that these processes are difficult to study over a broad temperature range because of the resist's limited thermal stability.

Conventional PEB involves heating substrates to 90-150 °C for 30-120 s with temperature ramp rates on the order of 100 K/s. In contrast, continuous wave

(CW) laser heating sources can transiently heat thin polymer films to more than 400 °C above their conventional decomposition temperatures, providing access to new kinetic regimes with rates spanning eight orders of magnitude [2]. This process, known as laser spike annealing (LSA), was first utilized as a millisecond annealing technique to activate dopants while minimizing diffusion in ultra-shallow semiconductor junctions [3]. In LSA (Figure 1.20), a line-focused CW laser is scanned over the substrate to rapidly heat the surface for microseconds to milliseconds, after which cooling occurs quickly through conduction into the substrate. Laser-induced PEB is characterized by rapid heating at 10^4-10^5 K/s to peak temperatures of 200-600 °C, such that the ester cleavage reaction requires only 200-2000 μs to change the resist's solubility [2, 4]. By utilizing this laser technique for heating resist thin-films, the actual measurements of previously estimated kinetics and models at extreme temperatures can be obtained [5, 6].

A model 193 nm resist system, poly(2-methyl-2-adamantyl methacrylate-*co*-γ butyrolactone-2-yl methacrylate) (MAdMA-*co*-GBLMA) shown in Figure 5.1a, was studied over a temperature range from 115 °C to 560 °C and times from 200 μs to 180 s. The high sensitivity of this system to temperature and time made it an ideal candidate for kinetic investigations. Poly(MAdMA-*co*-GBLMA) is a chemically amplified resist where the acid-catalyzed cleavage of the adamantyl group from the methacrylate backbone modifies the solubility of the polymer matrix, leading to pattern formation. The rate of the reaction is directly coupled to the concentration of photo-generated acid-catalysts, which are formed by ultraviolet (UV) exposure of small molecule photo-acid generators (PAG) [1, 7]. The exposure to UV establishes an initial acid concentration which must be followed by PEB (to temperatures typically above 90 °C) to thermally activate

the deprotection reaction. Stabilization of the byproduct leads to a regeneration of the acid; this regenerated acid diffuses in the polymer matrix to another methyl adamantyl group, resulting in a chemical amplification of the deprotection reaction. This PEB is conventionally performed on a hot-plate at 90-150 °C for 30-120 s. Using a CW laser PEB source, the temperature and time range were extended to temperatures of 560 °C with times correspondingly reduced to 200 μs.

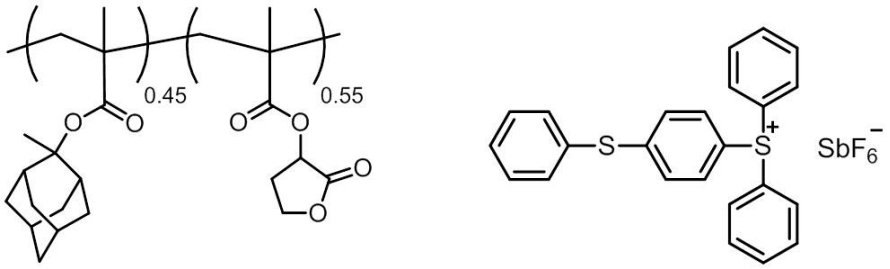

a) Poly(MAdMA-*co*-GBLMA) b) THSb

Figure 5.1: Chemical components used for kinetics measurements showing a) 2-methyl-2-adamantyl methacrylate-*co*-γ butyrolactone-2-yl methacrylate (MAdMA-*co*-GBLMA), a resist used for 193 nm optical lithography and b) triarylsulfonium hexafluoroantimonate salt (THSb) photo-acid generator.

While characterizing the chemical kinetic rates over this temperature and time ranges, unexpected behavior was observed in both ester cleavage reaction kinetics and diffusivity. For example, the diffusivity followed the expected William-Landel-Ferry (WLF) model to temperatures beyond T_g (~110 °C) [8]. At temperatures above 275 °C, however, the diffusivity transitioned into Arrhenius behavior with activation energy of 175 ± 25 kJ/mol. For deprotection, the apparent activation energy shifted from 21 ± 1 kJ/mol at high temperatures to 73 ± 11 kJ/mol at low temperatures. The underlying mechanism for such a large shift in E_A could not initially be identified [2].

This chapter discusses the experiments which have elucidated changes in the reaction pathways for this model polymer under low and high temperature PEB, which help to explain the large change in chemical reaction kinetics. The processes were monitored by characterizing byproducts of the reaction using Fourier transform infrared (FTIR) spectroscopy, nuclear magnetic resonance (NMR) spectroscopy, and gas chromatography and mass spectrometry (GC/MS). Identifying these changes in the chemical reaction pathways is a critical step to understanding the behavior of small molecules and polymer systems at extreme temperatures.

5.2 Materials and Methods

5.2.1 Glass Transition Measurements

Poly(2-methyl-2-adamantyl methacrylate-*co*-γ butyrolactone-2-yl methacrylate) (MAdMA-*co*-GBLMA) shown in Figure 5.1a and triarylsulfonium hexafluoroantimonate salt [9] (THSb) shown in Figure 5.1b were obtained from Mitsubishi Rayon Co., Ltd. and Sigma Aldrich. Poly(MAdMA-*co*-GBLMA) was used as a model polymer due to its relatively high glass transition temperature ($T_g \approx 160$ °C) [10]. Differential scanning calorimetry (DSC) was used to determine changes in the glass transition temperature of poly(MAdMA-*co*-GBLMA) as a function of THSb additives. Two polymers were dissolved in chemically inert dichloromethane and were extracted by evaporating the solvent in a vacuumed oven. Both standard and hermetic DSC holders were used for consistency. The glass transition temperature for poly(MAdMA-*co*-GBLMA) without

any additive was ~160 °C, consistent with reported values (Figure 5.2a). However, the glass transition temperature decreases rapidly as a function of THSb additives and with 5 wt.% THSb was measured to be ~110 °C (Figure 5.2b). The as-tested resist system contained poly(MAdMA-*co*-GBLMA) blended with 5 wt.% THSb in propylene glycol monomethyl ether acetate (PGMEA) solvent for spin-casting.

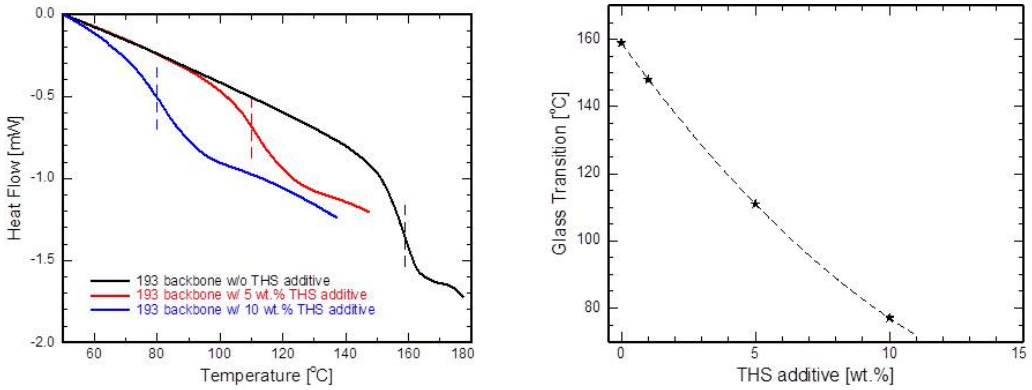

a) DSC measurements of poly(MAdMA-*co*-GBLMA)

b) Change in T_g due to plasticization

Figure 5.2: Characterization of the glass transition temperature (T_g). a) Identifying T_g as a function of THSb additives using differential scanning calorimetry (DSC). b) T_g vs. THSb concentration showing a relationship that is almost linear.

5.2.2 Sample Preparation

Resist films were spun onto silicon wafer substrates with 100 nm target thickness. All samples were soft baked on a vacuum-chuck hot-plate at 130 °C for 90 s to remove residual PGMEA solvent. Resist layers were then exposed to deep UV (λ = 235 – 260 nm) light at doses of 0.1-12 mJ/cm^2 to generate acid-catalysts from the THSb as schematically shown in Figure 5.3a [9]. Following either hot-plate or laser PEB to induce deprotection of the methyl adamantyl

esters as shown schematically in Figure 5.3b, samples were developed in 0.26 N tetramethylammonium hydroxide (TMAH) for 60 s at room temperature to remove regions with a modified solubility. The fraction of the film removed during the 60 s development is a direct measure of the deprotection reaction.

For diffusion studies, bilayer resist samples with a THSb-containing top layer (acid generating layer) and a THSb-free bottom layer were fabricated using a polydimethylsiloxane (PDMS) stamping technique as shown in Figure 4.5. First, a PDMS stamp (~5 mm in thickness and ~90 mm in diameter) was prepared and spun with a 100 nm of THSb-containing resist solution. Second, a silicon wafer substrate was spun with THSb-free resist solution to achieve ~100 nm thick film. Both substrates were soft baked on a vacuum hot-plate at 130 °C for 90 s. The PDMS with the THSb-containing layer was then stamped onto the wafer and soft baked for an additional 20 s at 70 °C for adhesion between the two polymer films prior to the removal of the PDMS stamp. Under UV exposure, the THSb in the top layer generated free acids that could diffuse into the bottom layer upon subsequent PEB.

Due to the potential for changes in the diffusion behavior from different glass transition temperatures in the top and bottom layers, diffusion measurements were also performed on bilayers where both layers contained the THSb photoacid generators. In these experiments, the top layer was exposed under UV to generate free acids for diffusion prior to lamination with the bottom layer. At high UV doses, the diffusion distance observed in these bilayers was essentially equivalent as that measured in films without THSb. However, this saturation was observed at lower UV doses for these bilayers (Appendix D).

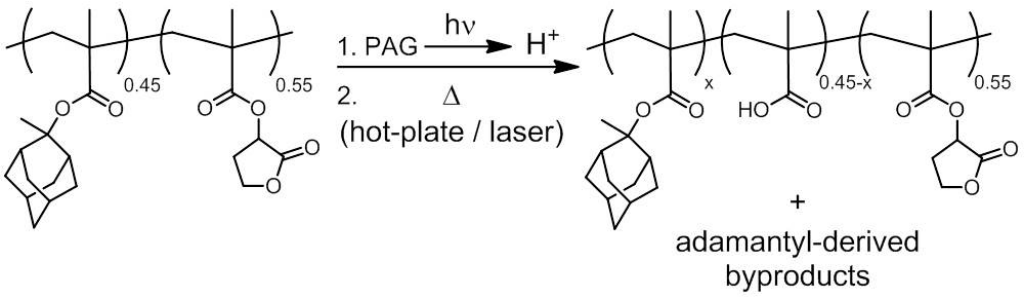

a) Poly(MAdMA-*co*-GBLMA) deprotection mechanism

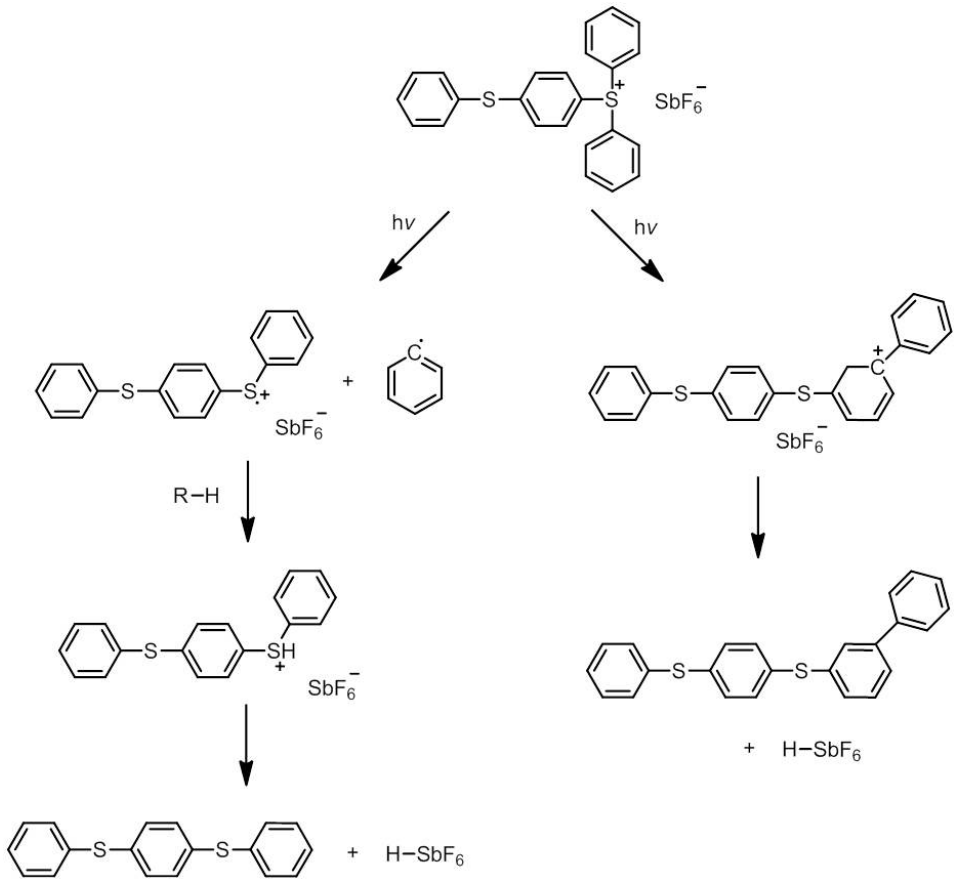

b) Acid-generation mechanism of THSb PAG upon DUV exposure

Figure 5.3: Reaction mechanism for a) poly(MAdMA-*co*-GBLMA) resist deprotection during PEB and b) THSb acid-generation upon UV exposure.

5.2.3 Sample Characterization

NMR measurements were performed using a Varian Inova 600 MHz NMR using a $^{1}H/^{13}C$, ^{15}N Z-PFG probe with a 20 Hz sample spin rate. Reaction byproducts were analyzed using heteronuclear single-quantum correlation and total correlation spectroscopy (HSQC-TOCSY) in order to investigate the decoupling between ^{13}C and ^{1}H. Gas chromatography and mass spectrometry (GC/MS) measurements were performed using a JEOL GCmate GC/MS double-focusing mass spectrometer with a 3 min solvent delay. Fourier transform infrared (FTIR) spectroscopic measurements were performed using a Bruker Hyperion 2000 with Tensor 27 in both transmission and reflection mode. Thermogravimetric and differential thermal analysis were performed using an Exstar TG/DTA 6200 by Seiko Instruments Inc.

5.3 Results and Discussion

5.3.1 Thermal Stability of a 193 nm Photoresist

The rates of MAdMA ester cleavage reactions were measured under conventional (hot-plate) and laser induced heating. Acid diffusion and ester cleavage are both thermally activated processes that require only milliseconds at high temperatures (laser), while reactions at lower temperatures require between 30 and 120 s to achieve comparable conversions. The thickness of the polymer film after development was used as a measure of the ester cleavage rate [11–13], and was determined as a function of heating temperature, time, and the initial acid

concentration (UV dose).

In the absence of acid, poly(MAdMA-*co*-GBLMA) resist was stable to much higher temperatures under laser-heating conditions as compared to conventional heating. Thermal stability over long time scales (seconds to minutes) was determined by thermogravimetric analysis (TGA) and by measuring the residual film thickness as a function of temperature and time on a vacuum-chuck hot-plate. Figure 5.4a indicates that both film thickness and polymer mass remain unchanged below 200 °C.

A ~60 % decrease in polymer thickness and weight percent is observed above 200 °C, corresponding to the loss of lactone and methyl adamantane esters as confirmed by NMR spectroscopy [14]. The methacrylate polymer backbone begins to decompose to form poly(methacrylic acid) above 300 °C (Appendix B). In contrast, poly(MAdMA-*co*-GBLMA) is stable to much higher temperature (~800 °C) under the short duration (500 μs) conditions associated with laser-heating (Figure 5.4b), and the stability temperature is inversely proportional to the heating duration (Figure 5.4c). When the heating duration is shortened to the sub-millisecond regime, the onset temperature for the ester and the backbone decompositions increases significantly.

These data demonstrate that organic polymers are stable to much higher temperatures than conventional limits as measured by TGA when the heating duration is significantly reduced. The rate of polymer decomposition can be estimated as the inverse of the heating duration at a given thickness loss, as shown in Arrhenius-like form in Figure 5.4d [15]. At temperatures above 160 °C, just above $T_g \approx 160$ °C, decomposition follows Arrhenius behavior with an activation enthalpy $E_A = 61 \pm 2$ kJ/mol, comparable to the cleavage energy

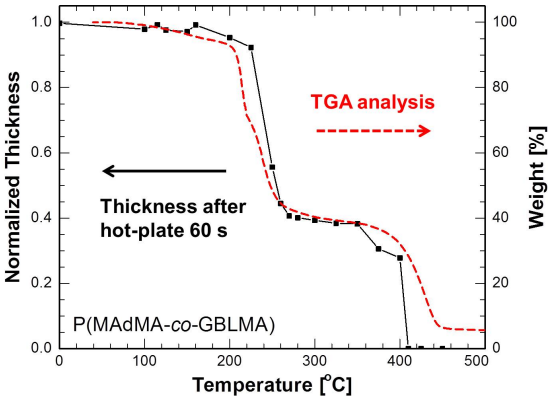

a) Thickness vs. weight % comparison

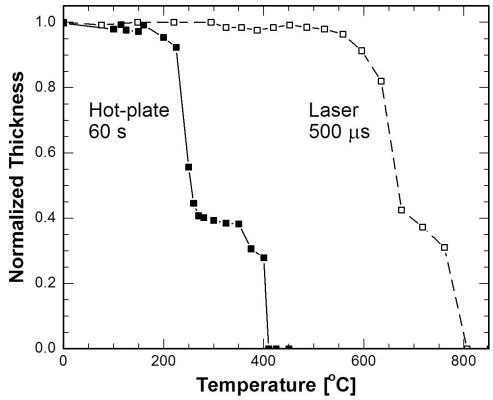

b) Stability comparision: heating temperature

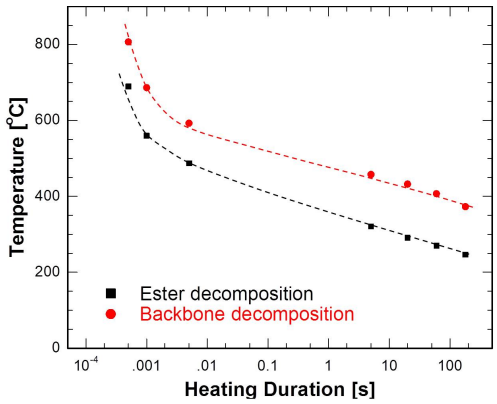

c) Stability comparision: heating duration

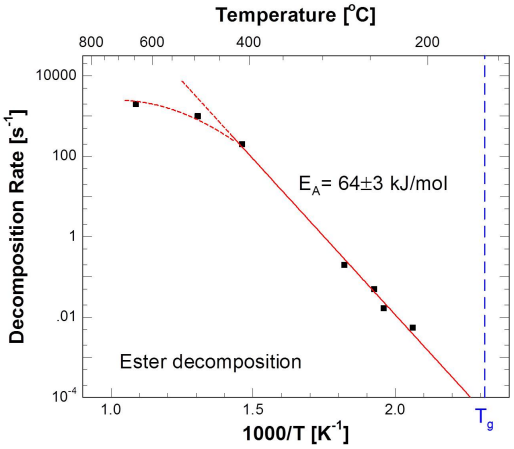

d) Activation energy for thermal deprotection

Figure 5.4: Thermal stability investigation of poly(MAdMA-*co*-GBLMA) 193 nm resist. a) A comparison between weight percent obtained using TGA and film thickness on Si substrate showing good agreement, b) extended polymer stability using laser-induced heating in the sub-millisecond time frames, c) stability of polymer backbone, methyl adamantyl and lactone side-groups as a function of heating duration, d) decomposition rate at 30 % thickness loss plotted as a function of inverse temperature.

of the side group [16, 17]. However, as temperatures exceed ~500 °C, the decomposition rate reaches a maximum value that is insensitive to further temperature increases, as evidenced by the asymptotic temperature stability at sub-

millisecond durations shown in Figure 5.4c. This saturation is unexpected and may be related to the competing interaction between decomposing side-group components and generating radicals stabilizing the process [18]. At low temperatures where the decomposition exhibit Arrhenius behavior, the reaction is limited purely by the cohesive energy between bonds holding the molecule and side-group together.

5.3.2 Deprotection Kinetics Measured using Hot-plate and Laser Heating

Taking advantage of the extended temperature stability on short times, the deprotection reaction kinetics were extensively investigated over unprecedented time frames ranging from sub-millisecond to minutes. The deprotection kinetics were probed and measured using contrast curves as shown in Figure 5.5a, where the remaining polymer film thickness was observed as a function of the initial (pre-heating) acid concentration, which was established experimentally by the UV exposure dose (mJ/cm^2). The dose required to remove the entire polymer film (E_0) is a function of both heating time and temperature with the representative data shown for 60 s hot-plate and 500 μs laser heating at various temperatures [19]. Due to the large difference in heating time (500 μs vs. 60 s), laser heating requires much higher temperatures to achieve a response similar to the hot-plate (*e.g.* compare laser curve at ~420 °C with the 150 °C hot-plate curve).

To compare the deprotection behavior over a range of temperatures and times, isotherms on a log-log E_0 versus heating time are shown in Figure 5.5b.

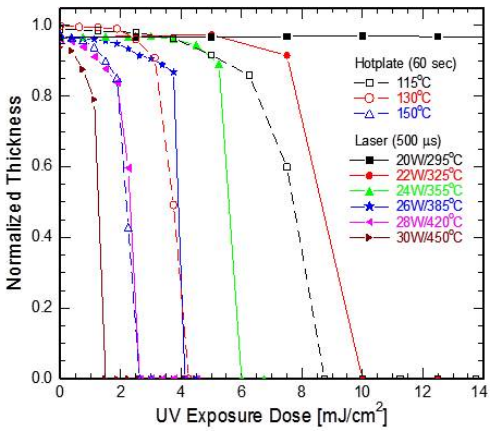

a) Contrast curve: laser vs. hot-plate

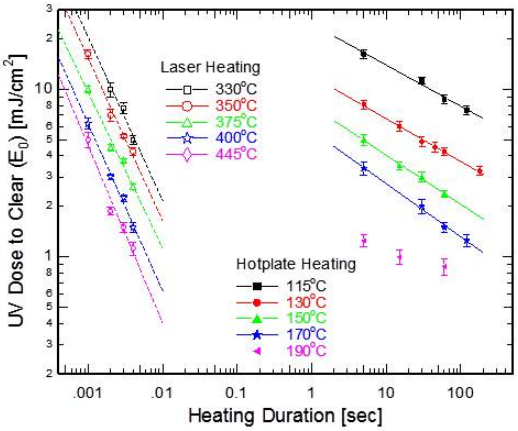

b) Isotherms of E_0 vs. heating duration

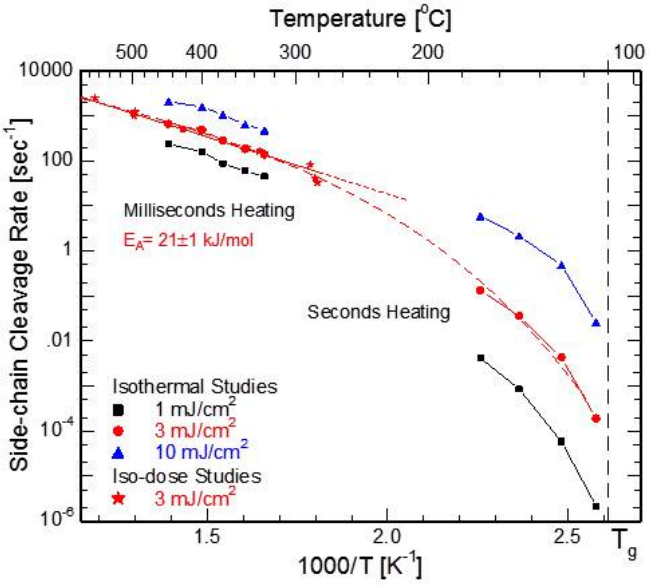

c) Deprotection rate at constant E_0 = 1, 3, and 10 mJ/cm^2

Figure 5.5: Probing deprotection kinetics of poly(MAdMA-*co*-GBLMA) during hot-plate or laser heating. a) Sensitivity curve for hot-plate and laser heating showing comparable E_0 despite five orders of magnitude change in heating duration compensated by high temperatures, b) E_0 vs. heating duration on a log-log scale showing drastic change in slope between two time frames, and c) deprotection rate vs. inverse temperature showing non-Arrhenius kinetics at constant E_0. Reprinted with permission from [2]. Copyright 2012 American Chemical Society.

At constant temperature, E_0 decreases with increasing heating duration due to the longer time available for the acid-catalyzed deprotection. The data suggest a power law dependence with widely different slopes from the two time frames: -1 for millisecond heating and -0.25 for seconds time frame heating.

It has been proposed that the deprotection should be governed by a first order differential equation

$$\frac{d\phi}{dt} = k_p H (1 - \phi) \tag{5.1}$$

where ϕ is the fraction of cleaved side-group, H is the concentration of the UV generated acid-catalysts, and k_p is a reaction rate constant [10]. The solution to this equation, $\phi = 1 - e^{k_p H t}$, reduces to $\approx k_p H t$ for short times. For a given polymer system, E_0 corresponds to a specific cleavage fraction where the solubility change is sufficiently large to enable full dissolution during the 60 s development. Similarly, the catalyst concentration H is directly proportional to the UV dose, which suggests that the product of E_0 and heating duration t should be a constant; increasing the acid concentration (E_0) by a factor reduces the time required by an equal amount. This dependence is $E_0 \propto t^{-1}$, corresponding to $n = -1$ in the generic form suggested by the experimental data.

The power-law slope observed in the millisecond regime was indeed close to unity, consistent with this simple first order, kinetically limited process for deprotection. If the acid concentration is reduced by a factor of two, the time required doubles to achieve the same solubility change. At lower temperatures and longer times, the result is very different. Halving the number of acids in the seconds time frame increases the required time by a factor of sixteen, suggesting complex reaction kinetics [2].

The behavior observed for this resist system is not unique. Similar behavior

was observed with another resist system poly(4-*t*-butoxycarbonyloxystyrene) (PBOCST) [17], whose chemical reactions involve a different mechanism with conversion of an *t*-butoxycarbonyl group to an isobutene as shown in Figure 5.6a. Slopes shown in Figure 5.6b (corresponding to Figure 5.5b), are ≈−0.5 for hot-plate and ≈−1.1 for laser heating. The simple first-order behavior of the laser regime appears universal while the complex hot-plate kinetic regime may vary with polymer systems and the relative temperature deviation $T - T_g$.

As underlying reactions are expected to be thermally activated, Figure 5.5c shows the deprotection rate (over eight orders of magnitude) as a function of inverse temperature for constant acid-catalyst concentrations (corresponding to UV exposures of 1, 3, and 10 mJ/cm^2). At high temperatures (300-600 °C), the rates exhibit Arrhenius behavior with an activation enthalpy E_A = 21 ± 1 kJ/mol, consistent with ester protonation and/or acid regeneration [18] steps during deprotection. However, as the system approaches T_g (≈110 °C), the cleavage rates decrease rapidly with a fingerprint typical of dynamics associated with segmental polymer motion near T_g. Between these limiting regimes, a crossover range exhibiting a power law dependence is expected [19]. At even lower temperatures below T_g, the behavior is expected to return again to Arrhenius behavior but with an activation enthalpy in the range of 100 kJ/mol [6, 11]. This transition may be partially linked to the segmental dynamics near T_g, but it is also coupled with changes in the fundamental reaction processes as shown below [6]. Direct observation of the transitional behavior and the newly observed Arrhenius behavior with low activation enthalpy at high temperature is possible only because of the ability to extend the temperature using laser heating technique.

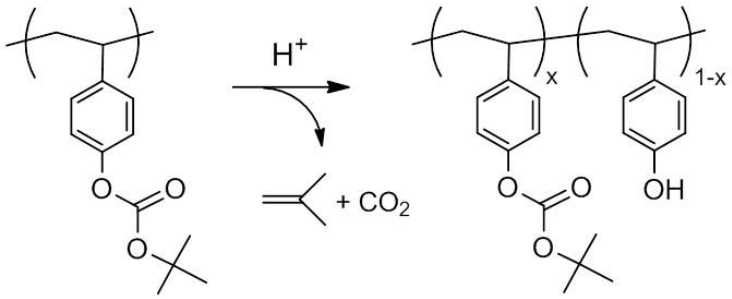

a) PBOCST deprotection mechanism

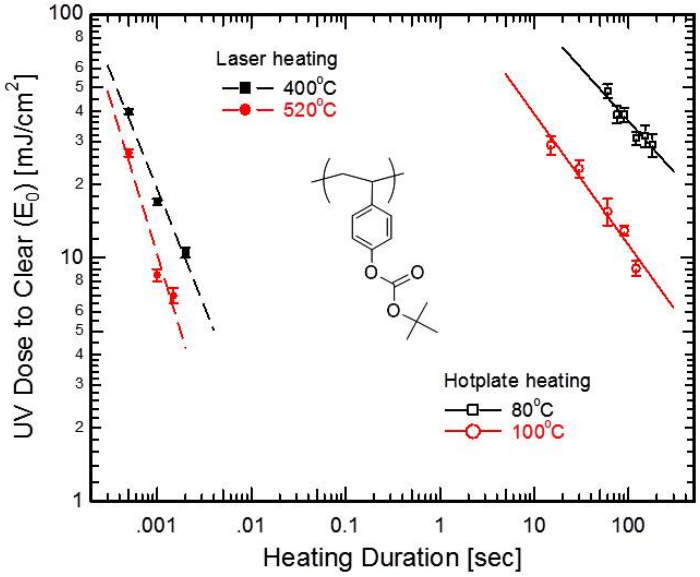

b) Isotherms of E_0 vs. heating duration

Figure 5.6: Probing deprotection kinetics of PBOCST during hot-plate or laser heating. a) Deprotection mechanism upon presence of acid and heat, and b) E_0 vs. heating duration on a log-log scale showing drastic change in slope between two time frames.

5.3.3 Acid Diffusion Measurements

Given the complexity of the low and high temperature regimes, diffusion of the photoacids enabling the deprotection reaction must also be considered. Substantial changes in the acid mobility would directly impact the deprotection kinetics. In contrast to complex deprotection kinetics, diffusion is a much simpler

random walk problem, albeit potentially impacted by structural changes arising from the deprotection kinetics of methyl adamantyl esters. Bilayer structures, consisting of an acid-containing top layer and an acid-free bottom layer, were treated by hot-plate or laser after UV exposure [17]. Acids initially present only in the top layer diffuse and subsequently deprotect the methyl adamantyl side-groups in the lower film. Thickness loss of the bottom layer after development thus measures the acid diffusion as shown in Figure 5.7a. T_g differences in the bilayers impacts the localized acid motion, but not the limiting diffusion distance in these films (Appendix D). Diffusion becomes significant on these length scales for hot-plate temperatures above 130 °C and for laser temperatures above ~385 °C (26 W).

The acid diffusivity $D = (\frac{\Delta x^2}{4t})$ based on diffusion from an initial concentration step [20], is shown in Figure 5.7b as a function of inverse temperature. For laser heating, the effective time at temperature is $1.2\tau_{dwell}$ based on an activation enthalpy of ~175 kJ/mol. At low temperatures (but still above T_g ~110 °C), acid diffusion in similar polymer systems has been shown to follow the Williams-Landel-Ferry (WLF) model, which links diffusion to free volume near the glass transition temperature [8, 21]. As with the deprotection dynamics, while the low temperature regime (<280 °C) appears linked to free volume near the glass transition, the high temperature regime (>300 °C) exhibits Arrhenius behavior. Surprisingly however, in contrast to the deprotection dynamics, the diffusivity is accelerated at high temperatures and exhibits an activation energy significantly higher than expected from extrapolation of the WLF behavior (contrast to Figure 5.5c. As these mechanisms act in parallel, the overall diffusivity can be modeled as a sum of Arrhenius behavior and the WLF model:

$$D = D_{\text{Arrhenius}} + D_{\text{WLF}} = D_0 \exp\left(-\frac{E_A}{k_b T}\right) + D_{T_g} \exp\left(\frac{C_{1g}(T - T_g)}{C_{2g} + (T - T_g)}\right) \tag{5.2}$$

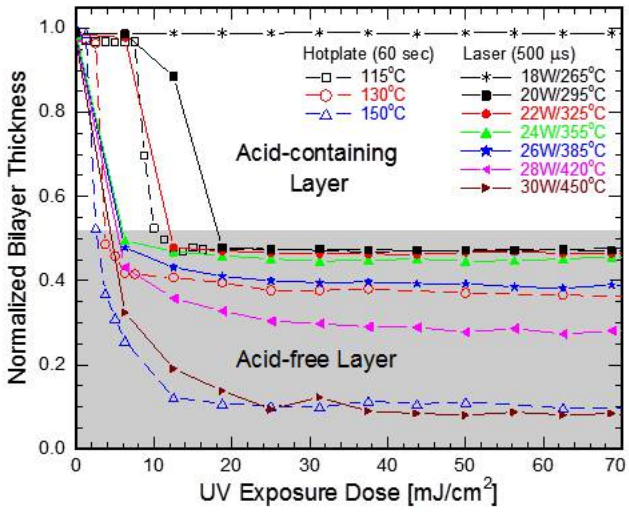

a) Bilayer structure consisting of acid-containing top layer

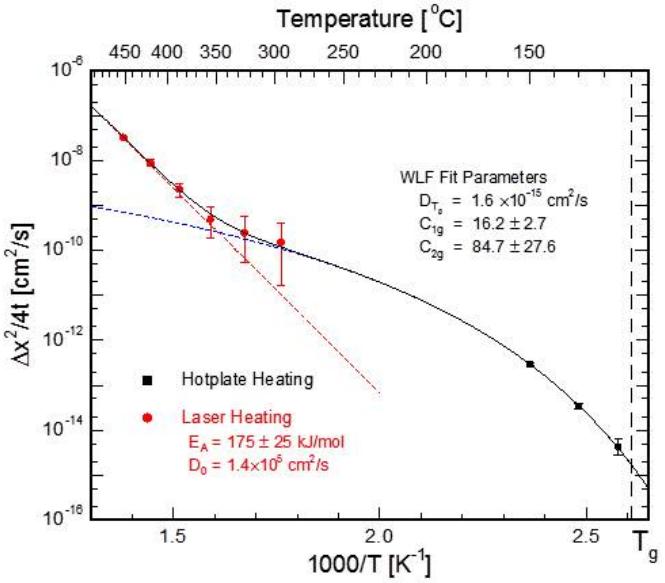

b) Meaured acid diffusivity

Figure 5.7: Photoacid diffusion in poly(MAdMA-*co*-GBLMA). a) Bilayer structure consisting of acid-containing top layer and an acid-free bottom layer. b) Acid diffusivity vs. inverse temperature showing a transition between WLF regime above the glass transition temperature and Arrhenius behavior at laser-induced higher temperatures. Reprinted with permission from [2]. Copyright 2012 American Chemical Society.

where D_{T_g} is the diffusivity at T_g. With T_g fixed at 110 °C, fits to the data yield $D_0 = 1.4 \times 10^5$ cm^2/s, $E_A = 175 \pm 25$ kJ/mol, $D_{T_g} = 1.6 \times 10^{-15}$ cm^2/s, $C_{1g} = 16.2 \pm 2.7$ and $C_{2g} = 84.7 \pm 27.6$. These WLF fit parameters are well within the range expected for similar polymer systems [22, 23], and the crossover from WLF to Arrhenius behavior at 350 °C occurs more than 200 °C below the thermal decomposition limit (Figure 5.4). However, Arrhenius activation energy of 175 kJ/mol is significantly higher than expected for typical diffusive processes in polymer liquids far above T_g (~60 kJ/mol) [24]. Ultimately, the agreement of this simple model with the experimental data over eight orders of magnitude is compelling evidence for the validity of this linked WLF and Arrhenius model. Indeed, observation of this unexpected crossover is possible only because of the extremely large temperature span enabled by this sub-millisecond heating technique.

5.3.4 Mechanisms for Behavior Shift between Hot-plate and Laser PEB

S. Kang *et al.* originally proposed a deprotection mechanism for poly(MAdMA-*co*-GBLMA) (Figure 5.3) where methyl adamantyl esters are ultimately eliminated to produce methylene adamantane [11]. They suggested that the reaction kinetics would be first order, but could not confirm directly [11, 12]. This result is in contrast to the complex-order kinetics observed in Figure 5.5b. The predicted model does, however, correspond the laser-induced high temperature regimes.

To uncover differences in the deprotection kinetics and diffusivity, the chem-

ical mechanism and the byproducts resulting from the acid-catalyzed reaction were investigated and characterized using FTIR spectroscopy. Figure 5.8 shows IR spectra obtained before and after deprotection of poly(MAdMA-*co*-GBLMA) using hot-plate heating at 130 °C for 60 s and using laser-induced heating at 355 °C for 500 μs. The UV exposure dose for all samples was beyond E_0 to ensure the initial concentration of acids was sufficient to complete the deprotection reaction throughout the polymer film. Independent of the heating method, data show peaks of carboxylic acids (1700 cm^{-1}), lactone (1770 cm^{-1}), and adamantyl ester (1740 cm^{-1}) consistent with the expected cleavage reaction shown in Figure 5.3. While peaks resulting from C-C double bonds (stretching vibration >1600 cm^{-1}) are nearly equivalent between hot-plate and laser heating methods, peaks resulting from C-C single bond stretching vibrations vary near 1100 cm^{-1}. Unfortunately bands assigned to C-C single bond stretch (1200-800 cm^{-1}) are generally weak and presents little value for identification of the chemical structure [25]. NMR spectroscopy was consequently performed to identify the variations in the deprotection reaction byproducts.

Byproducts resulting from the deprotection reactions at 115 °C (hot-plate 60 s) and at 385 °C (laser for 500 μs) were characterized using ^{1}H NMR (Figure 5.9). While the spectra are similar, there are substantial variations in the intensity of alkene peaks at 5.15 ppm and 4.45 ppm, suggesting differences in both concentration and structure of byproducts. The sharp peak at 4.45 ppm observed in films heated by the laser to 385 °C was identified as the small molecule methylene adamantane. This peak is notably almost non-existent for samples heated for 60 s. Conversely, a significant concentration of an unknown molecule resulting in an NMR peak at 5.15 ppm is observed following a low temperature, long time (hot-plate) heating.

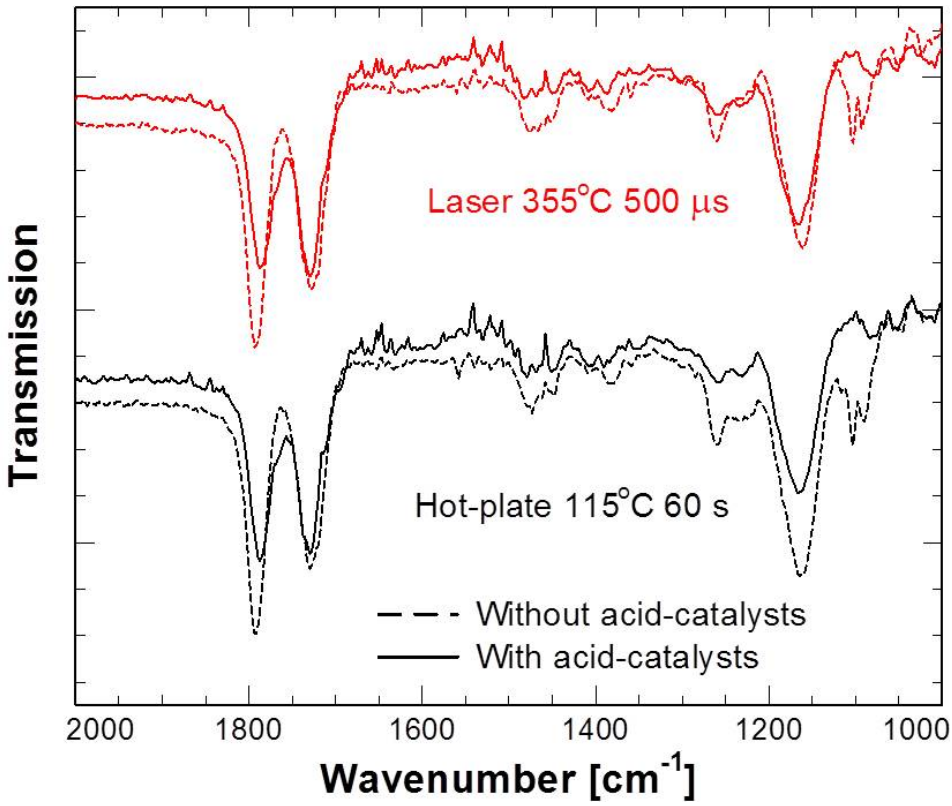

Figure 5.8: FTIR spectra of poly(MAdMA-*co*-GBLMA) with and without acid-catalyst and deprotected side groups after hot-plate or laser-induced heating.

To identify this unknown molecule, ^{1}H-^{13}C heteronuclear single-quantum correlation (HSQC) was employed. Figure 5.10 shows the 2D NMR results after acid-catalyzed deprotection reaction for hot-plate (red & blue for CH/CH_3 & CH_2 shifts) and laser heating (gray & black for CH/CH_3 & CH_2 shifts). While only slight differences between the byproducts are observed from alkane peaks (Figure 5.10a), key differences are observed for alkene peaks (Figure 5.10b) suggesting dimerization of two methylene adamantane byproducts. When peaks are assigned, both 2D NMR spectra agrees with the formation of methylene adamantane at 385 °C, while byproducts forming at 115 °C suggest a dimerization between two methylene adamantanes (Figure 5.10c).

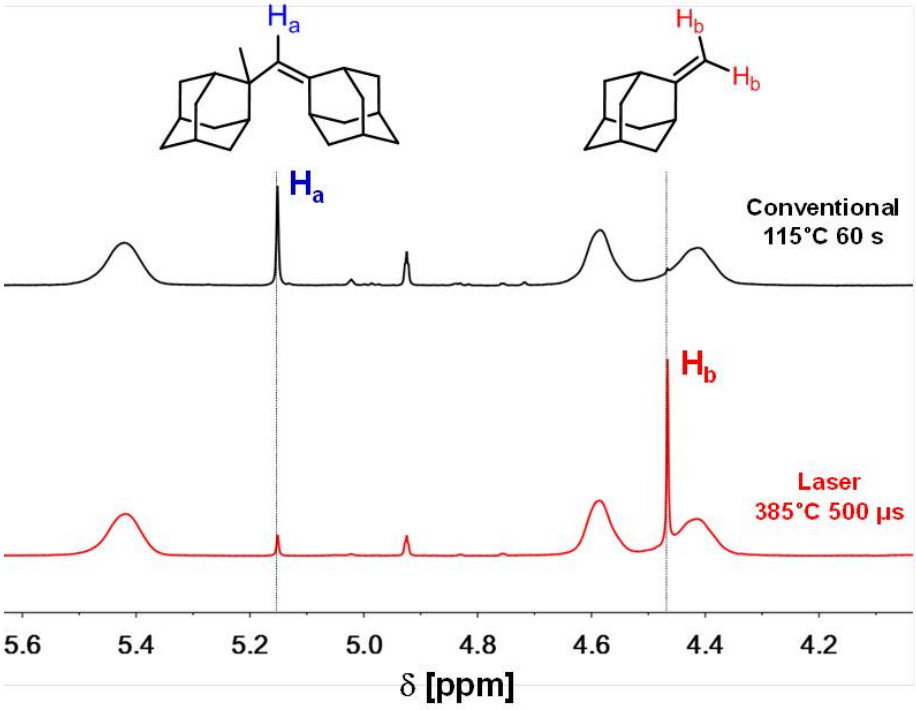

Figure 5.9: NMR spectra of poly(MAdMA-*co*-GBLMA) after deprotection induced by hot-plate or laser heating.

Gas chromatography-mass spectrometry (GC/MS) was also employed to confirm the identity of the byproducts seen by NMR. A comparison of a sample from laser induced heating with hot-plate heating (Figure 5.11) reveals significant differences in total ion count (proportional to concentration) for each reaction byproduct, especially at retention times of 7.5 min and 14.5 min.

These peaks correspond to methylene adamantane and adamantyl dimer respectively as determined from mass spectrometry as shown in Figure 5.12. While the GC peaks near 3 min are due to the solvents, the peak near 9 min represent a small concentration of 2-methyl-2-adamantanol (Figure 5.12b), which is formed by combining methylene adamantane with ambient water. Overall, the GC/MS results support the NMR conclusions; a significant concentration of the adamantyl dimer is observed at the low temperature and seconds time frame

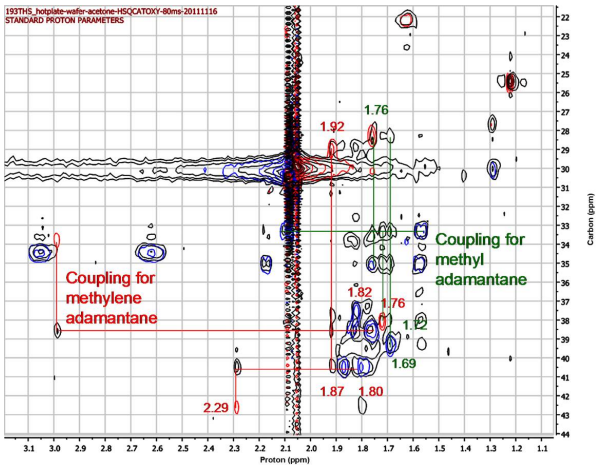

a) 2D NMR analysis for alkane shifts

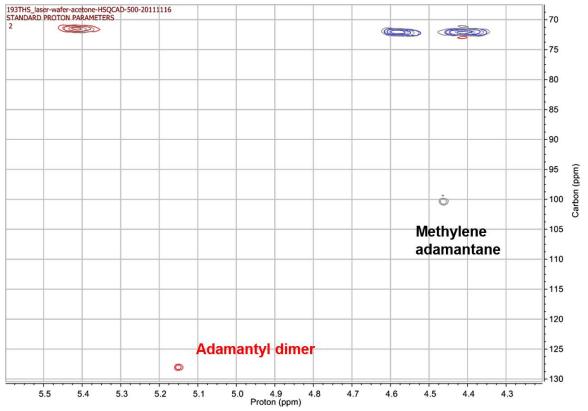

b) 2D NMR analysis for alkene shifts

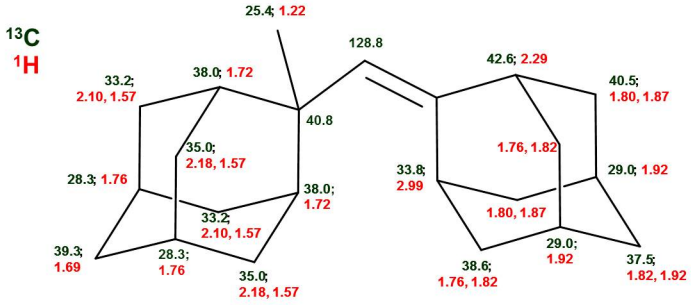

c) Peak assignments for adamantyl dimer based on NMR results

Figure 5.10: Two-dimensional (^{1}H-^{13}C) of poly(MAdMA-*co*-GBLMA) deprotection reaction byproducts after hot-plate or laser PEB. a) 2D NMR spectra analysis for alkane shifts, b) 2D NMR spectra analysis for alkene shifts, and c) peak assignments for the adamantyl dimer.

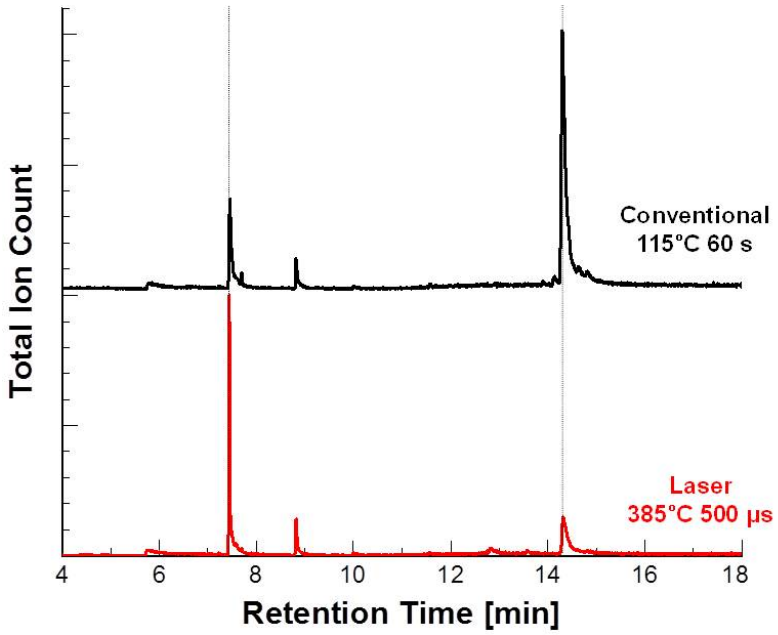

Figure 5.11: Gas chromatography of poly(MAdMA-*co*-GBLMA) showing the total ion current as a function of retention time after acid-catalyzed deprotection reaction using hot-plate (top) or laser (bottom).

heating, while a comparably higher concentration of methylene adamantane forms during the laser-induced high temperature and millisecond time frame heating. This result suggests that the side-group and the acid-catalyst interaction are limited by unexpected side reactions at low temperatures in the seconds time frames.

The different reaction outcomes at each heating condition are consistent with the thermodynamic parameters of elimination and dimerization reactions, as well as the limited molecular diffusion lengths that disfavor dimerization under the short-duration, local heating laser conditions [26]. The complexity of the ester cleavage reaction kinetics under conventional heating can be attributed to the competition between the ester cleavage reaction and methylene adamantane dimerization (Figure 5.13a). The dimerization affects the rate of acid-catalyzed

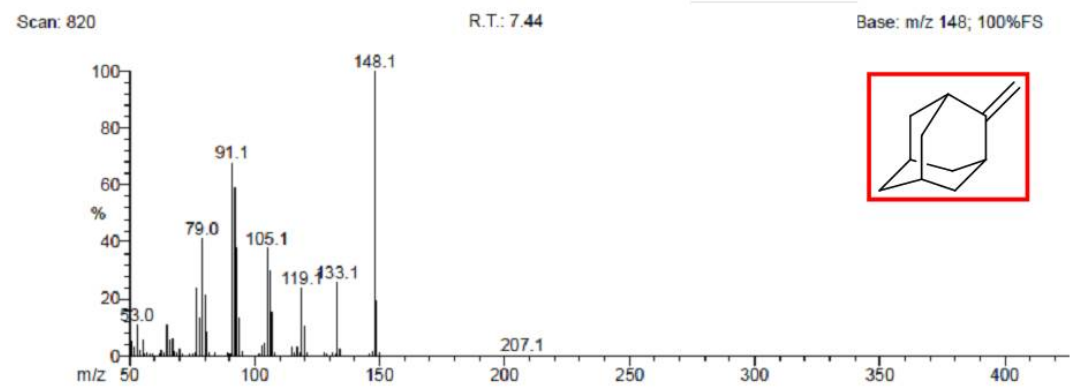

a) Methylene adamantane

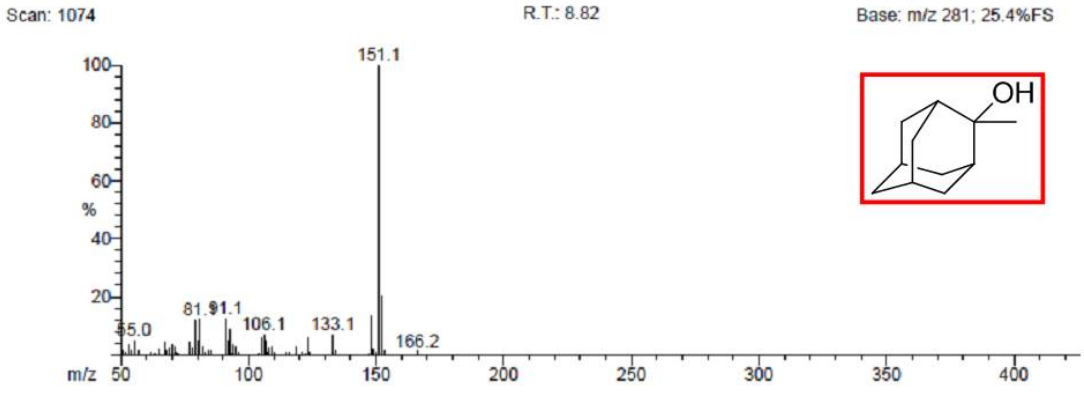

b) Methyl adamantanol

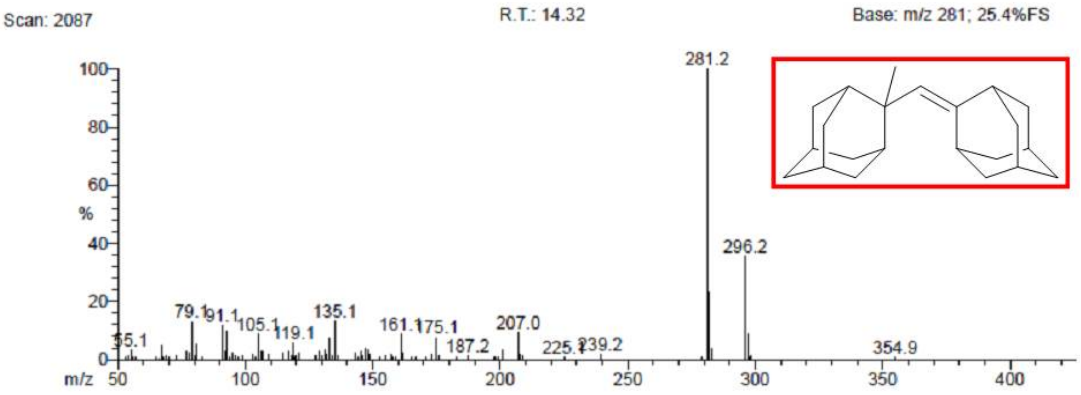

c) Adamantyl dimer

Figure 5.12: Mass spectrometry data and corresponding byproduct structure during the deprotection reaction of poly(MAdMA-*co*-GBLMA) showing a) methylene adamantane, b) methyl adamantanol, and c) adamantyl dimer.

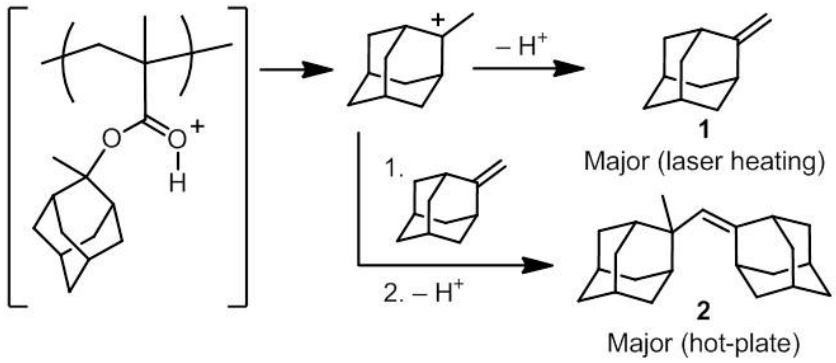

a) Byproducts formed during poly(MAdMA-*co*-GBLMA) deprotection

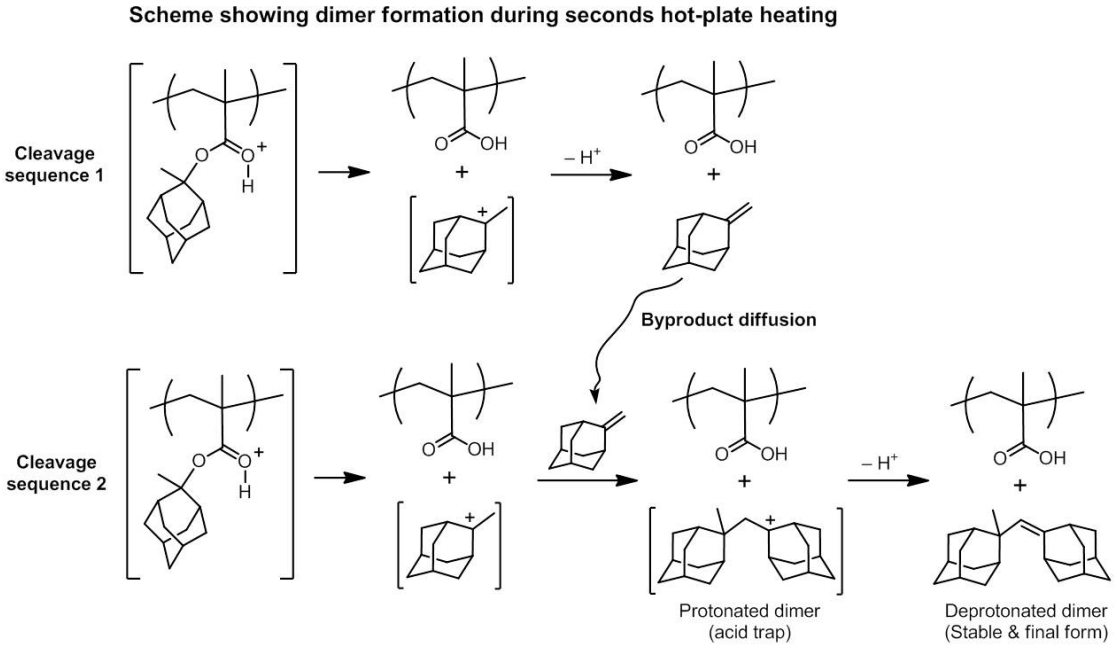

b) Proposed reaction path for dimer formation during hot-plate heating

Figure 5.13: Byproduct formation during poly(MAdMA-*co*-GBLMA) deprotection. a) Deprotection reaction resulting in methylene adamantane byproducts during laser-induced submillisecond heating and in adamantyl dimer during seconds hot-plate heating. b) Proposed reaction path for dimer formation during hot-plate heating. A generated methylene adamantane can diffuse in the resist matrix and form a dimer with nearby byproducts.

ester cleavage because its cationic intermediates act as traps for the photogenerated acid (Figure 5.13b) [27].

Under laser heating conditions, the ester cleavage reaction occurs with the expected first-order dependence on acid concentration in which methyl adamantium cation formation is likely to be rate-limiting. The dimerization side reaction impacts the apparent reaction order in acid because it can cause the available acid concentration in the polymer film to vary as a function of time and the ester cleavage reaction. Furthermore, the reaction kinetics are also coupled to the slower chain dynamics of the polymer [22–24]. At temperatures approaching the polymer T_g, chain motion of the polymer is limited and the average relaxation time increases, resulting in an increased and strongly temperature-dependent activation enthalpy for ester cleavage [23]. Conversely, chain motion becomes rapid at temperatures exceeding the glass transition by more than 200 °C, which lowers the activation barrier for acid-catalyzed ester cleavage. This mechanism establishes the temperature dependent activation enthalpy observed in Figure 5.5c. These two mechanisms are most likely the origin of the shift from at high temperature to at low temperature in the power law dependence of the heating time required for the solubility switch at a given initial acid concentration (Figure 5.5b).

5.3.5 Modeling Dimer Formation and Acid Trapping Kinetics

Modeling the reaction kinetics with the additional mechanisms introduces increased complexity to Equation 5.1. The ester cleavage rate must now reflect the free acid concentration, which varies as the concentration of methyl adamantine

and its dimer changes during heating.

The cleavage of the methyl adamantyl ester ultimately forms both methylene adamantane (MA) and dimer byproducts. Previously, the rate of this cleavage reaction was proposed to follow a form given in Equation 5.1. The time/dose dependence at low temperatures strongly suggests that the dimer acts as an acid trap once formed. Consequently, the effective active acid concentration becomes time-dependent and can no longer be modeled as a constant. We denote the free acid concentration as $H(t)$, which is equal to H_0 at $t = 0$. As shown in Figure 5.13b, the dimer is formed in the protonated state (trapping an acid), and can subsequently transition to a deprotonated form.

To characterize the trapping rates, let C_{MA} be the local concentration of the methylene adamantane, C^*_{dimer} the concentration of protonated adamantyl dimers, and C^0_{dimer} the concentration of deprotonated adamantyl dimers. In the most general case, and to the degree the activity is proportional to concentration, the rate of dimer formation and methylene adamantane loss are coupled. The fundamental deprotection rate equation must be modified to include the time-dependent acid concentration

$$\frac{d\phi}{dt} = k_p\, H(t)\, [1 - \phi(t)] \tag{5.3}$$

where $H(t)$ is the difference between the initial acid concentration and the concentration of protonated dimers.

$$H(t) = H_0 - C^*_{dimer} \tag{5.4}$$

The key reactions occurring dynamically include the formation of the protonated dimer and the subsequent deprotonation of the protonated dimer,

$$2\,[\mathrm{MA}] + [\mathrm{H^+}] \underset{k_2}{\overset{k_1}{\rightleftharpoons}} [\mathrm{Dimer^*}] \tag{5.5}$$

$$[\text{Dimer}^*] \underset{k_4}{\overset{k_3}{\rightleftharpoons}} [\text{Dimer}^0] + [\text{H}^+] \tag{5.6}$$

where it is assumed that only the protonated dimer can decompose back to the methylene adamantane pair. Defining rate constants k_1 and k_2 for the formation and separation of the protonated dimer, and rate constants k_3 and k_4 for the dimer protonation and deprotonation reactions, we have

$$\frac{dC^*_{dimer}}{dt} = k_1\, H(t)\, [C_{MA}]^2 + k_2\, C^*_{dimer} - k_3\, C^*_{dimer} + k_4\, H(t)\, C^0_{dimer} \tag{5.7}$$

$$\frac{dC^0_{dimer}}{dt} = k_3\, C^*_{dimer} - k_4\, H(t)\, C^0_{dimer} \tag{5.8}$$

$$\begin{aligned} \frac{dC_{MA}}{dt} &= C_{MAdMA}\, \frac{d\phi}{dt} - 2\, k_1\, H(t)\, [C_{MA}]^2 + k_2\, C^*_{dimer} \\ &= k_p\, H(t)\, C_{MAdMA}\, [1 - \phi(t)] - 2\, k_1\, H(t)\, [C_{MA}]^2 + k_2\, C^*_{dimer} \end{aligned} \tag{5.9}$$

where C_{MAdMA} is the initial concentration of side groups available for cleavage.

These equations depend critically on the five parameters k_1, k_2, k_3, k_4, and k_p. Of these constants, only k_p (deprotection rate) has been measured directly with a value ranging between 0.5-15 nm^3/s over a 20 °C temperature range [11]. All of these reaction rate constants are expected to follow Arrhenius behavior over the larger temperature range studied here. Several simplifying approximations may be applied to assess the plausibility of this model. The deprotonated dimer is likely the thermodynamically stable final state. Consequently, we neglect the reverse reactions with reaction rate constants k_2 and k_4 minimized ($k_2 \to 0$ and $k_4 \to 0$). This hypothesis is equivalent to suggesting that the absence of dimers under high temperature processing is a kinetic rather than a thermodynamic limitation.

The acid trapping efficiency is directly tied to the formation of the protonated dimer and reaction constant k_1. The secondary reaction (k_3) regenerates the active acid-catalyst and can be considered a second order effect. The ratio

k_1/k_p is therefore the critical parameter for establishing the impact of this trap mechanism. For small values of k_1/k_p, the ester cleavage occurs faster than the protonated dimer formation, and the acid concentration does not change significantly. These conditions are fulfilled during high temperature, short duration laser heating. Since no trapping occurs, the system follows the expected linear first order kinetics. At lower temperatures and longer heating durations, the k_1/k_p ratio is larger and dimerization occurs at a similar rate as ester cleavage. This effect results in a dynamic depletion of the active acid concentration and breakdown of linear kinetic behavior, leading to the apparent power-law behavior observed. Ultimately, it is the coupling of the dimer formation with the ester cleavage reaction that leads to the complex kinetic behavior.

Previous reports have acknowledged the presence of acid traps arising intrinsically within the resist resin and/or by base quencher additives [11, 28–30]. Most investigations, however, treats acid loss as a phenomenological process where trapping models are based only on empirical reference from kinetic measurements. Past studies neglect the reaction path leading to acid loss, making its subsequent effect on the deprotection kinetics challenging to predict and model. By using a model resist with a common adamantyl protecting group used for both deep UV and extreme UV lithography, the observed dimer formation provides chemical insight to previously estimated models and simulations.

The time required to achieve the solubility switch versus the acid concentration (UV exposure dose) under isothermal conditions was empirically observed to follow a power law dependence (Figure 5.5b), with $n \approx -1$ in the laser temperature regime and $n \approx -0.25$ in the hot-plate temperature regime. The coupled differential equations (Equations 5.7-5.9) were numerically integrated to deter-

mine the time required to achieve ϕ = 70 %, which is the deprotection level required for the solubility switch [31]. Results are shown in Figure 5.14 where the required acid to side group ratio is shown as a function of the time required to reach the solubility switch for a range of k_1/k_p values.

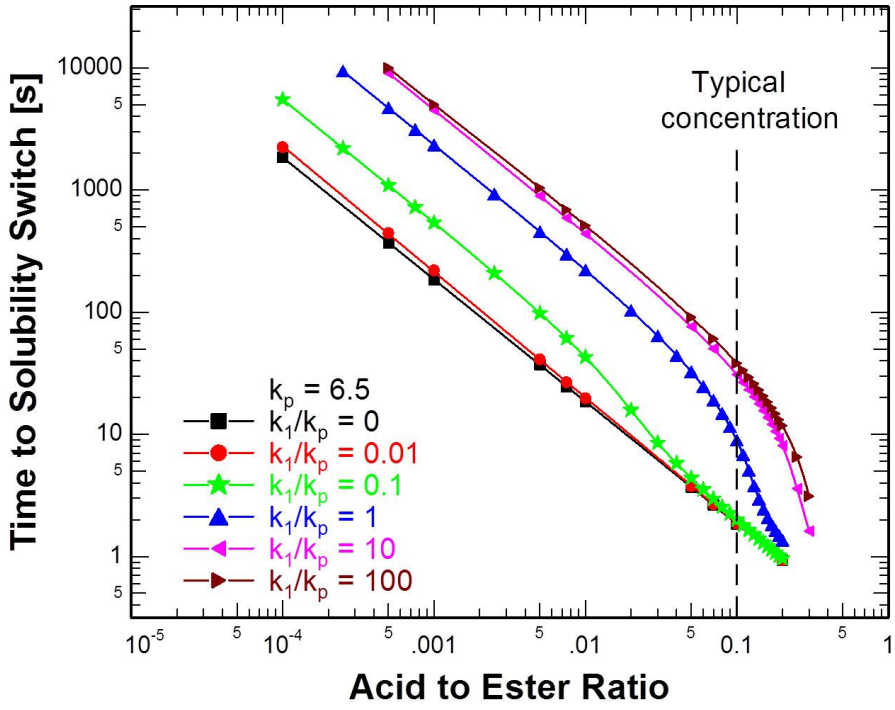

Figure 5.14: Simulated deprotection kinetics using the proposed model from Equations 5.7-5.9. The coupled differential equations were numerically integrated to determine the time required to achieve complete deprotection as a function of acid concentration for a range of k_1/k_p values. The transition corresponds to a shift in the rate-limiting mechanism for deprotection.

The time-scale for the deprotection is determined primarily by k_p, where the time shifts inversely with changes in k_p. For this graph, a value of k_p = 6.5 nm^3/s was estimated from experimental measurements at a bake temperature of 110 °C [11]. Reverse reaction rate constants, k_2 and k_4, were set to zero corresponding to thermodynamically stable products from the forward reactions. To avoid complete trapping of acids in the dimer, k_3/k_p was set to 0.01. The key pa-

rameter is the relative rates of dimer formation to the deprotection k_1/k_p. As $k_1/k_p \to 0$, the system approaches simple first order linear kinetics with the dose and time inversely related to each other. For any given acid concentration, the minimum time required for the solubility switch is along these curves shown in Figure 5.14. We believe that this corresponds to the conditions under laser PEB in the sub-millisecond time frames.

As the ratio k_1/k_p approaches unity (low temperature regime), the rate of dimer formation and deprotection are comparable. Under these conditions, the active acid concentration becomes time dependent and the average is reduced. At high acid concentrations, the cleavage reaction is effectively complete before dimers begin to form, resulting in the asymptotic approach to the $k_1/k_p = 0$ curve. At very low acid concentrations, dimer formation is favored and the effective acid concentration is determined by the transition to the deprotonated dimer, resulting in a much slower net ester cleavage rate. As k_1/k_p is increased further, the critical acid concentration for transition between these two regimes increases.

At both high and low acid concentrations, the curves approach an inverse relationship between the time and the acid concentration (below 1 s and above 100 s). However, the relationship in the transition exhibits much shallower slopes (exponent n). At an acid to ester ratio of ~0.1, the slope of the non-linear region in Figure 5.14 is approximately -0.3, which is comparable to the -0.25 slope experimentally observed (Figure 5.5b).

The transition corresponds to a shift in the rate-limiting mechanism for deprotection. At low k_1/k_p values, the cleavage reaction is simply limited by the diffusion of active acids. However, at high k_1/k_p values, release of acids from the

protonated to the deprotonated dimer state effectively determines the cleavage rate. As k_1 and k_p will exhibit different activation energies, transition from the low to high k_1/k_p regime with temperature is reasonable. Indeed, the modeled rate equations and their simulation are a powerful tool to predict the deprotection kinetics. While the absolute rate constants are not known, these results suggest that this mechanism can readily explain the observed shift in exponent between laser and hot-plate regimes.

5.4 Conclusions

Cleavage kinetics, decomposition behavior, acid diffusivity, and reaction pathways of a model photoresist polymer containing a methyl adamantyl ester acid-labile group have been extensively studied over a >500 °C window using transient laser-induced heating. The measured ester cleavage rates and acid diffusion show non-Arrhenius behavior over the eight orders of magnitude in kinetic rates studied. While the ester cleavage kinetics were measured to be first order under high temperature millisecond heating, they were more complex and exhibited a power law behavior when the films were heated near T_g for a few seconds. Different molecular byproducts were formed under each condition. At high temperatures, ester cleavage predominantly forms methylene adamantane. In contrast, longer duration conventional heating at lower temperatures produces an adamantyl dimer, which is identified for the first time. This compound is a likely contaminant that limits the lithographic performance of these resist systems.

The change in kinetics is proposed to originate from the formation of a proto-

nated dimer acting as a catalyst trap, which decreases the active acid concentration available for ester cleavage. This hypothesis is consistent with a new mathematical model that includes both methylene adamantane and adamantyl dimer formations, and that reproduces the experimentally observed ester cleavage kinetics. At laser-induced high temperatures, the suppressed dimer formation results in a fixed concentration of active acid-catalyst, giving rise to first-order cleavage kinetics. Under conventional heating conditions, the active acid concentration is effectively decreased as a consequence of protonated adamantyl dimer formation, complicating the kinetics of the ester cleavage reaction. Laser-induced heating can be utilized to investigate otherwise unattainable temperatures and kinetic regimes within polymer films and also provides a means to bypass undesirable processes occurring under conventional heating methods.

This work highlights the utility of the laser-induced sub-millisecond heating technique to characterize reaction rates and pathways over a wide range of temperature and time. For lithography, this capability provides critical understanding of catalyst utilization and trapping mechanisms that limit patterning performance, which will contribute to next-generation photoresist design. In addition, laser induced heating permits direct measurements of previously estimated kinetics and can validate predicted models [5, 6] at extreme temperatures. When combined with existing methods to identify the chemical structure of these polymers, the laser-induced heating technique opens up new opportunities to study chemical processes at high temperatures, and we anticipate that this capability will prove useful for a diverse range of applications beyond photoresist polymers.

5.5 Acknowledgments

Intel Corporation and Semiconductor Research Corporation (Task ID: 2125.001) provided funding for this work. Poly(MAdMA-*co*-GBLMA) was generously provided by Mitsubishi Rayon America Inc. (Taro Ishii). Professor Ulrich Wiesner is acknowledged for his expertise in polymer physics and helpful discussions. Dimer analysis could not have been possible without the support of Ivan Keresztes at Cornell's NMR facility (NSF-CHE 7904825; NSF-PGM 8018643). This work made use of facilities in the Cornell Center for Materials Research (NSF-DMR 0520404) and the Cornell NanoScale Science and Technology Facility (NSF-ECS 0335765). Pratima Satish, Florencia Paredes, and David Bunck are recognized for their experimental support. Big thanks to Marie Krysak, Brandon Wenning, and David Calabrese for lessons in chemical synthesis. Genggeng Qi helped greatly by providing equipment time for TGA measurements. Special thanks to Manish Chandhok and Todd Younkin for mentoring, guidance, discussions, and encouragements throughout this project.

References

[1] H. Ito, "Chemical amplification for microlithography", *Adv. Polym. Sci.*, vol. 172, pp. 27–245, 2005.

[2] B. Jung, J. Sha, F. Paredes, M. Chandok, T. R. Younkin, U. Wiesner, C. K. Ober, and M. O. Thompson, "Kinetic rates of thermal transformation and diffusion in polymer systems measured during sub-millisecond laser-induced heating", *ACS Nano*, vol. 6, no. 7, pp. 5830–5836, 2012.

[3] T.Yamamoto, T. Kubo, T. Sukegawa, E. Takii, Y. Shimamune, N. Tamura, T. Sakoda, M. Nakamura, H. Ohta, T. Miyashita, H. Kurata, S. Satoh, M. Kase, and T. Sugii, "Junction profile engineering with a novel multiple laser spike annealing scheme for 45-nm node high performance and low leakage CMOS technology", *Int. Elec. Devices Meet.*, vol. 1, pp. 143–146, 2007.

[4] K. Iyengar, B. Jung, M. Willemann, P. Clancy, and M. O. Thompson, "Experimental determination of thermal profiles during laser spike annealing with quantitative comparison to 3-dimensional simulations", *Appl. Phys. Lett.*, vol. 100, no. 21, p. 211 915, 2012.

[5] P. G. Debenedetti and F. H. Stillinger, "Supercooled liquids and the glass transition", *Nature*, vol. 410, pp. 259–267, 2001.

[6] K. Chen, E. J. Saltzman, and K. S. Schweizer, "Segmental dynamics in polymers: from cold melts to ageing and stressed glasses", *J. Phys. Condens. Matter*, vol. 21, p. 503 101, 2009.

[7] H. Ito and C. G. Willson, "Chemical amplification in the design of dry developing resist materials", *Polym. Eng. Sci.*, vol. 23, no. 18, pp. 1012–1018, 1983.

[8] M. L. Williams, R. F. Landel, and J. D. Ferry, "The temperature dependence of relaxation mechanism in amorphous polymers and other glass-forming liquids", *J. Am. Chem. Soc.*, vol. 77, no. 14, pp. 3701–3707, 1955.

[9] J. L. Dektar and N. P. Hacker, "Photochemistry of triarylsulfonium salts", *J. Am. Chem. Soc.*, vol. 112, no. 16, pp. 6004–6015, 1990.

[10] S. Kang, B. D. Vogt, W. L. Wu, V. M. Prabhu, D. L. VanderHart, A. Rao, and E. K. Lin, "Characterization of compositional heterogeneity in chemically amplified photoresist polymer thin films with infrared spectroscopy", *Macromolecules*, vol. 40, no. 5, pp. 1497–1503, 2007.

[11] S. H. Kang, V. M. Prabhu, B. D. Vogt, E. K. Lin, W. L. Wu, and K. Turnquest, "Effect of copolymer composition on acid-catalyzed deprotection reaction kinetics in model photoresists", *Polymer*, vol. 47, no. 18, pp. 6293–6302, 2006.

[12] G. Wallraff, J. Hutchinson, W. Hinsberg, F. Houle, P. Seidel, R. Johnson, and W. Oldham, "Thermal and acid-catalyzed deprotection kinetics in candidate deep ultraviolet resist materials", *J. Vac. Sci. Technol. B*, vol. 12, no. 6, pp. 3857–3862, 1994.

[13] U. Okoroanyanwu, *Chemistry and lithography*. New York, New York: John Wiley & Sons, Inc. and SPIE, 2010, pp. 563–603.

[14] L. F. Thompson, C. G. Willson, and M. J. Bowden, *Introduction to microlithography*. ACS Professional Reference Book, 1994, pp. 212–232.

[15] J. H. Flynn and L. A. Wall, "A quick, direct method for the determination of activation energy from thermogravimetric data", *Polym. Sci. Pol. Lett.*, vol. 4, no. 5, pp. 323–328, 1966.

[16] K. C. Chenoweth, S. Cheung, A. C. T. van Dulin, W. A. Goodard, and E. M. Kober, "Simulations on the thermal decomposition of a poly(dimethylsiloxane) polymer using the ReaxFF reactive force field", *J. Am. Chem. Soc.*, vol. 127, no. 19, pp. 7192–7202, 2005.

[17] V. A. Bershtein and V. A. Ryzhov, "Far infrared spectroscopy of polymers", *Adv. Polym. Sci.*, vol. 114, pp. 43–121, 1994.

[18] Y. Kodera and B. J. McCoy, "Distribution kinetics of radical mechanisms: Reversible polymer decomposition", *AlChE J.*, vol. 43, no. 12, pp. 3205–3214, 1997.

[19] S. Malik, J. Eisele, A. Whewell, L. Ferreira, T. Holt, and M. Bowden, "Post-exposure bake temperature considerations for high activation energy resist systems", *J. Photopolym. Sci. Tec.*, vol. 13, no. 4, pp. 513–518, 2000.

[20] A. A. Gusev, F. Muller-Plathe, M. F. van Gunsteren, and U. W. Suter, "Dynamics of small molecules in bulk polymers", *Adv. Polym. Sci.*, vol. 116, pp. 207–247, 1994.

[21] M. D. Stewart, M. H. Somervell, H. V. Tran, S. V. Postnikov, and C. G. Willson, "Study of acid transport using IR spectroscopy and SEM", *Proc. SPIE*, vol. 3999, pp. 665–679, 2000.

[22] J. D. Ferry, *Viscoelastic Properties of Polymers*. New York, New York: John Wiley & Sons, 1980, pp. 264–315.

[23] R. D. Priestley, L. J. Broadbelt, J. M. Torkelson, and K. Fukao, "Glass transition and α-relaxation dynamics of thin films of labeled polystyrene", *Phys. Rev. E*, vol. 75, no. 6, p. 061 806, 2007.

[24] F. Bueche, *Physical properties of high polymers*. New York, New York: Interscience, 1962, pp. 90–93.

[25] R. M. Silverstein, G. C. Bassler, and T. C. Morrill, *Spectrometric identification of organic compounds*. New York, New York: John Wiley & Sons, Inc., 1991, pp. 91–132.

[26] N. L. Allinger and J. T. Sprague, "Conformational analysis. LXXXIV. A study of the structures and energies of some alkenes and cycloalkenes by the force field method", *J. Am. Chem. Soc.*, vol. 94, no. 16, pp. 5734–5747, 1972.

[27] G. H. Fredrickson and H. C. Andersen, "Kinetic Ising model of the glass transition", *Phys. Rev. Lett.*, vol. 53, no. 13, pp. 1244–1247, 1984.

[28] Y. Kawai, A. Otaka, A. Tanaka, and T. Matsuda, "The effect of an organic base in chemically amplified resist on patterning characteristics using KrF lithography", *Jpn. J. Appl. Phys.*, vol. 33, pp. 7023–7027, 1994.

[29] F. A. Houle, W. D. Hinsberg, M. Morrison, M. I. Sanchez, G. Wallraff, C. Larson, and J. Hoffnagle, "Determination of coupled acid catalysis-diffusion processes in a positive-tone chemically amplified photoresist", *J. Vac. Sci. Technol. B*, vol. 18, no. 4, pp. 1874–1885, 2000.

[30] D. L. Goldfarb, M. Angelopoulos, E. K. Lin, R. L. Jones, C. L. Soles, J. L. Lenhart, and W. Wu, "Confinement effects on the spatial extent of the reaction front in ultrathin chemically amplified photoresists", *J. Vac. Sci. Technol. B*, vol. 19, no. 6, pp. 2699–2704, 2001.

[31] A. Rao, S. Kang, B. D. Vogt, V. M. Prabhu, E. K. Lin, W. L. Wu, K. Turnquest, and W. D. Hinsberg, "Dissolution fundamentals of 193 nm methacrylate based photoresist", *Proc. SPIE*, vol. 6153, p. 615 310, 2006.

CHAPTER 6

LASER-INDUCED MILLISECOND RESIST HARDBAKE

6.1 Introduction and Motivation

For over 40 years, photolithography has been the key driver for advances in microelectronics, leading to faster and more efficient computing. At the most basic level, photolithography involves patterning a radiation-sensitive polymer which acts as a stencil for underlying films during subsequent etching steps [1–3]. Most chemically amplified photoresist patterning using deep ultraviolet (DUV) and extreme UV (EUV) light sources involves radiatively generating a strong acid in the resist film which cleaves (deprotects) esters along the polymer backbone during a subsequent heating step known as the post-exposure bake (PEB). The resist's solubility changes upon deprotection and enables its selective removal with a developing solvent [3–5]. Although resist materials and their patterning chemistries continue to evolve to achieve even higher resolutions, key concerns remain for controlling the critical dimension (CD) and line width roughness (LWR) of developed patterns, where 11 nm half-pitch resolutions will require less than 1.0 nm and 0.9 nm (3σ) control in CD and LWR respectively. Research to date has focused on improving the pattern resolution during UV exposure, post-exposure bake, and development. In contrast, processes to improve resist metrics after development have received only modest attention.

An ideal post-develop process would reduce LWR without changes to CD and pattern profile (sidewall angle). Processes that have been previously explored to reduce LWR after development include chemical rinsing, smoothing

by vapor-induced melting of the resist surface, smoothing by resist flow using additional heating (hardbake), and controlled etching of the resist surface [6]. While these processes have demonstrated reduced roughness, significant changes in the CD and pattern profiles were observed due to the swelling of the polymer and/or loss in resist thickness. Smoothing by polymer flow using a 10-30 s hardbake above the resist's glass transition temperature (T_g), for example, reduced the LWR up to 15 % but excessive flow in the lateral direction changed the profile dimension and the sidewall angle from its original pattern [6, 7]. If the heating duration was minimized and controlled to prevent the excessive flow of the resist polymer while maintaining the thermal budget required to induce polymer flow, an ideal post-develop technique might be established.

Conventional heating methods using furnaces or vacuum-chuck hot-plates involve heating substrates in the seconds time frame with temperature ramp rates on the order of 10-100 K/s. In contrast, continuous wave (CW) laser heating sources can transiently heat thin polymer films above their T_g's in sub-millisecond time frame at 10^4-10^5 K/s to peak temperatures beyond the polymer decomposition [8, 9]. This process, known as laser spike annealing (LSA), was first utilized as a millisecond annealing technique to activate dopants while minimizing diffusion in ultra-shallow semiconductor junctions [10, 11]. In LSA (Figure 6.1), a line-focused CW laser is scanned over the substrate to rapidly heat the surface for microseconds to milliseconds, after which cooling occurs quickly through conduction into the substrate. In this work, LSA is used to anneal fully developed resist patterns at temperatures of 295-450 °C for 500 μs. At this unprecedented hardbake duration and temperatures beyond the resist's T_g, the patterned polymer is expected to flow and minimize its surface energy resulting in a reduction in LWR without damaging the sidewall angle and the

CD, as shown schematically in Figure 6.1. While characterizing the CD and the LWR on three different resist polymer systems using laser hardbake, we observed LWR reduction up to 50 % with minimal (less than 4 %) change in CD. Roughness reduction using this laser technique may ultimately enable the controlled reflow of organic polymers in nanometer-scale surface patterning that will complement high resolution patterning.

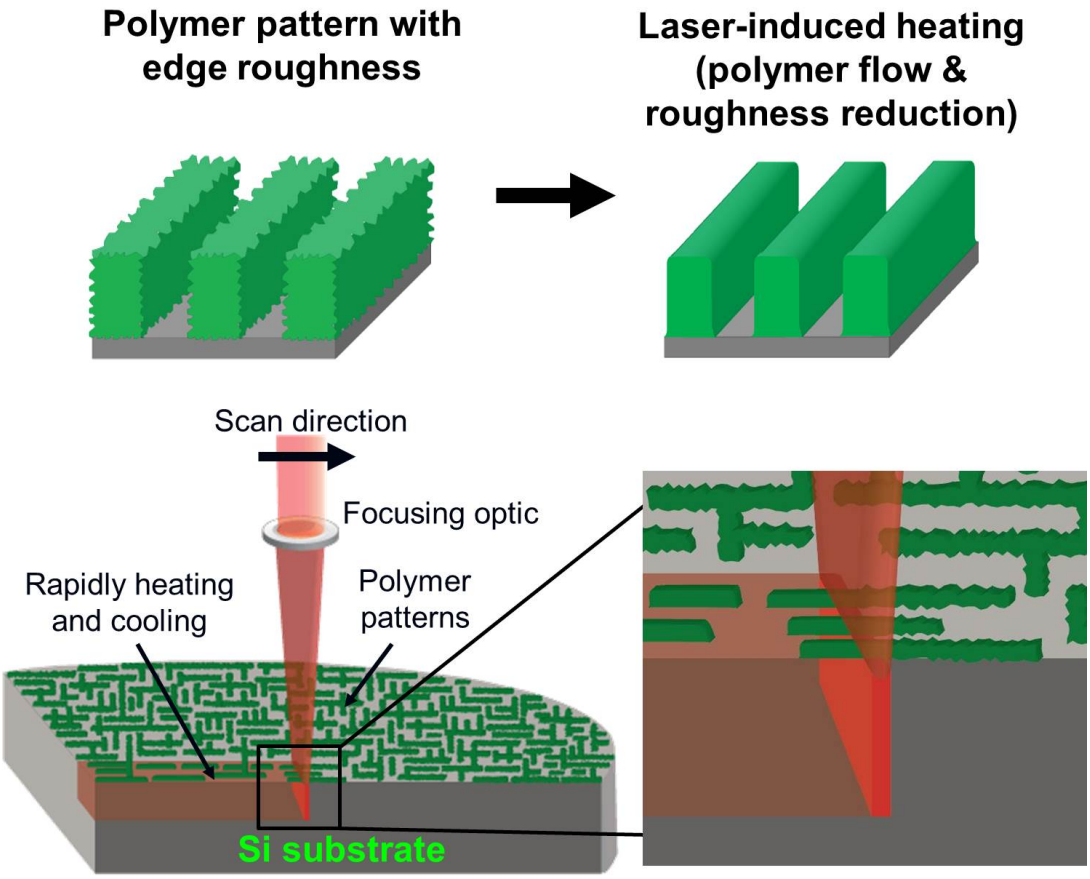

Figure 6.1: Schematics of laser-induced resist hardbake process. Patterned resist polymers are heated using a transient laser. When heated above the glass transition temperature, the polymer flows and minimizes the surface energy to reduce pattern roughness.

6.2 Sample Preparation & Characterization

Three commercially available resist polymers were spun on Si wafer ($\rho \sim 0.01$-0.02 Ω·cm) with target thicknesses at 35-50 nm and were exposed at EUV (13.5 nm) wavelengths. The investigated systems included an acrylate-based resist platform (hereby referred to as acrylate-based polymer) where the deprotection mechanism during PEB converts esters along the polymer backbone into carboxylic acids, and two additional hybrid polymers designed to be thermally sensitive (hereby referred to as hybrid polymer A and hybrid polymer B). After EUV exposure, samples underwent conventional hot-plate PEB using optimal conditions and were developed using tetramethylammonium hydroxide (TMAH, 0.26 N). The developed patterns, 30 nm lines and spaces, were subsequently hardbaked using either a hot-plate at 90-150 °C for 30 s or a laser at 175-450 °C for 500 μs.

Following hardbake, resist patterns were imaged using Leo 1550 FESEM with constant magnification at 200k. SuMMIT [12] was used to quantify CD and LWR selected from a minimum of eight lines from a single SEM image. For consistency, SEM images of the original and hardbaked patterns were obtained from adjacent areas to minimize systematic variations across the wafer. At least five SEM images were analyzed at a given hardbake condition to average CD and LWR values. To visualize the resist profile and to quantify the surface roughness, resist profiles were measured by an AFM (Dimension Icon by Bruker) using high resolution tips designed specifically for measuring high aspect ratio trenches. CDI carbon nanotube tips with diameters less than 10 nm and heights greater than 500 nm were obtained from K-TEK Nanotechnology LLC.

6.3 Results and Discussion

6.3.1 Analysis on CD and LWR using SEM images

Figure 6.2 shows SEM images of 30 nm patterns before and after laser hardbake using hybrid polymer A. While the original pattern shows significant roughness on the edges, noticeable smoothing of the resist profile is observed as the hardbake temperature increases. Once the laser hardbake temperature reaches 420 °C, however, excessive polymer flow is observed in the lateral direction where the CD and the sidewall angle become degraded. This smoothing behavior is not unique to a single polymer system. The two additional resist polymers, acrylate-based polymer and hybrid polymer B, exhibited similar smoothing beyond a material-dependent threshold temperature (Appendix E).

Quantitative changes in CD and LWR as a function of laser hardbake temperature are shown in Figure 6.3 for all three polymer systems, and compared with the values from the original pattern. For all systems, CD of the resist profile is essentially constant near targeted 30 nm with slights variations over the wafer substrate (black curves). Similarly, LWR remains near 4-6 nm with slightly greater variability. When values are compared for patterns before and after laser hardbake, CD changes by less than 1 nm at temperatures up to 385 °C for 500 μs. At higher temperatures, CD increases rapidly for all three polymers as the original profiles deteriorate due to flow. The LWR shows minimal change up to 205 °C but then decreases sharply from 5.5 nm to 3.8 nm at 385 °C for the acrylate-based polymer, from 3.9 nm to 2.3 nm at 355 °C for hybrid polymer A, and from 5.0 nm to 2.7 nm at 325 °C for hybrid polymer B with respect to their original LWR. Once the hardbake temperature exceeds 420 °C, LWR sharply in-

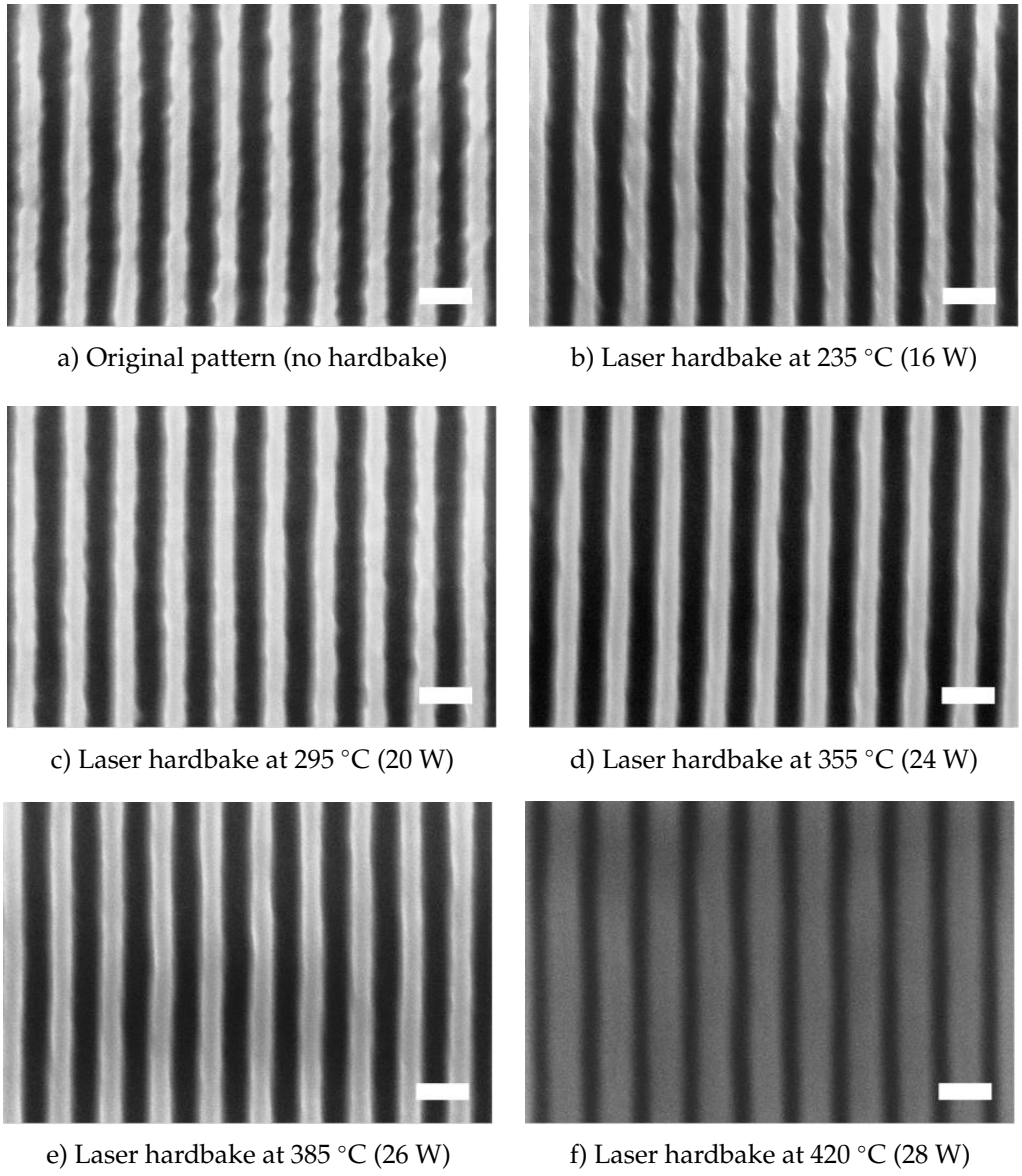

a) Original pattern (no hardbake)

b) Laser hardbake at 235 °C (16 W)

c) Laser hardbake at 295 °C (20 W)

d) Laser hardbake at 355 °C (24 W)

e) Laser hardbake at 385 °C (26 W)

f) Laser hardbake at 420 °C (28 W)

Figure 6.2: SEM images of 30 nm line/space patterns generated in the hybrid polymer A followed by laser-induced hardbake for 500 μs. Images show a) the original pattern, b) 235 °C, c) 295 °C, d) 355 °C, e) 385 °C, and f) 420 °C. While the original patterns show significant roughness on pattern edges, resist smoothing through polymer flow is observed for increasing hardbake temperatures. At 420 °C however, excessive flow is apparent where CD is damaged. All scale bars correspond to 60 nm.

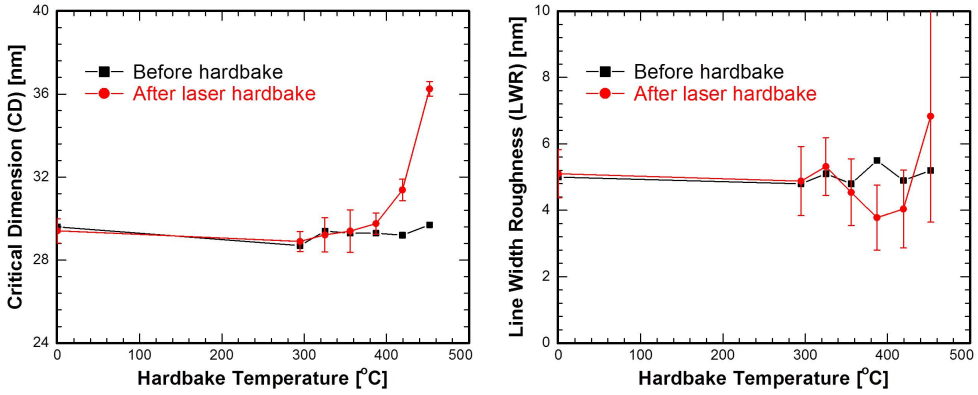

a) Acrylate-based polymer CD

b) Acrylate-based polymer LWR

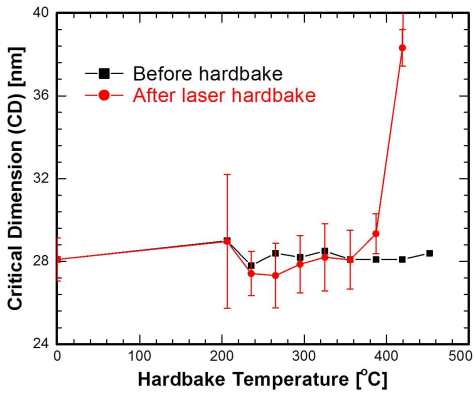

c) Hybrid polymer A CD

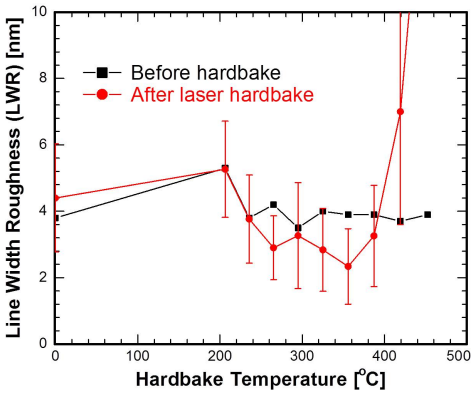

d) Hybrid polymer A LWR

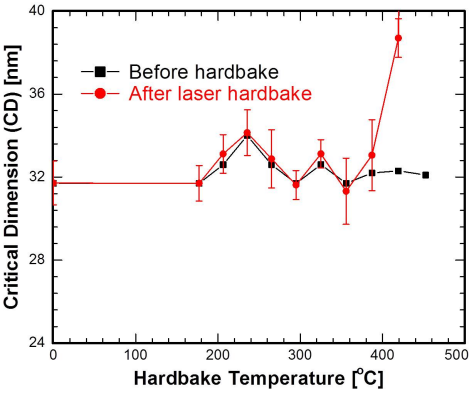

e) Hybrid polymer B CD

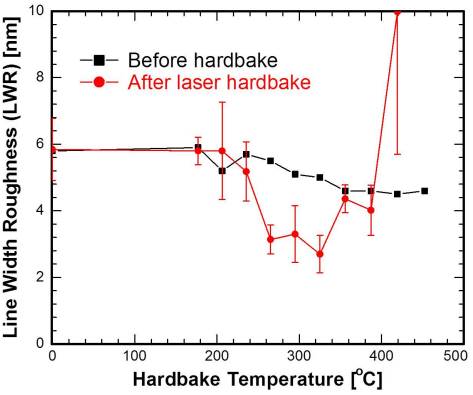

f) Hybrid polymer B LWR

Figure 6.3: Quantitative values of a,b,c) critical dimension (CD) and d,e,f) line width roughness (LWR) as a function of laser hardbake temperature for three investigated resist polymers. Black points are initial measurements prior to hardbake; red points are the corresponding features after laser hardbake. For all polymers, a favorable trade-off between LWR reduction up to 45 % and CD change less than 2 nm occurs at temperatures where polymer flow is optimized and controlled. Laser hardbakes were performed at τ_{dwell} = 500 μs.

creases for all three polymer systems. At the optimum heating temperature respective to the polymer system, up to 45 % reduction in LWR is observed using the sub-millisecond laser hardbake.

Controlled polymer flow with minimal change in CD occurs at 385, 355, and 325 °C for the acrylate-based polymer, hybrid polymer A, and hybrid polymer B respectively. At these temperatures, the polymer's viscosity decreases sufficiently to flow on nanometer scales within the 500 μs time frame and smoothen by surface energy minimization. However, the time is insufficient to obscure large scale flow over larger dimensions. Increasing the hardbake temperature above 420 °C reduces the viscosity to a level that flow occurs rapidly over these larger dimensions, resulting in a drastic increase in both CD and LWR. While these critical temperatures are significantly higher than the T_g of all three polymers (≈100 °C), the increase is not surprising as the five orders of magnitude decrease in heating duration compensates the lower viscosity. A similar shift in another thermal threshold was observed for decomposition of an acrylate-based resist system, increasing by 400 °C above its conventional limits from seconds to sub-millisecond time frames [8].

The optimum hardbake temperature for these three polymer systems were between 300 °C and 420 °C. However, even a short range flow may modify the resist sidewall angle and impact subsequent etch processes. AFM analysis of the resist profiles was used to evaluate any changes in local topography.

6.3.2 AFM Analysis

Figure 6.4 shows AFM images of the acrylate-based resist measured after varying hot-plate and laser temperatures. Features in these images are 80 nm wide trenches separated by 320 nm. These wider spaced features were used to ensure that the AFM accurately reflected the depth of the trenches and to observe flow over dimensions beyond the minimum feature size. Figure 6.4a shows typical original patterns prior to any thermal processing. For hot-plate hardbake, the bottom of the trench has begun to collapse toward a v-shape profile at both 90 °C and 115 °C for 30 s. Although some surface roughness reduction is apparent at both temperatures, thinning of trenches (CD loss) is significant. These results are consistent with the results and trends observed using conventional hardbake in the seconds time frames [6, 7, 13, 14]. For sub-millisecond hardbake however, there are only minimal change in the trench profile below 385 °C. At 385 °C, the critical temperature for the acrylate-based polymer, the surface roughness rapidly decays with slight rounding of the sidewall angle. Smoothing of the sidewalls and near the bottom of the trench was also observed, but the bottom of the trenches remained well defined and show minimal change. As the hardbake temperature is increased further to 420 °C, significant loss of the sidewall angle due to flow is readily apparent even for the 500 μs laser-induced heating.

6.3.3 Comparison on Trench Profile and Surface Roughness

Profiles of the resist height as a function of position for these trenches are shown in Figure 6.5 for the original pattern, hot-plate hardbake at 90 °C, and laser hard-

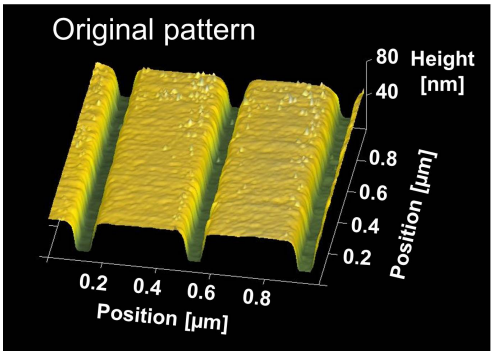

a) Original pattern (no hardbake)

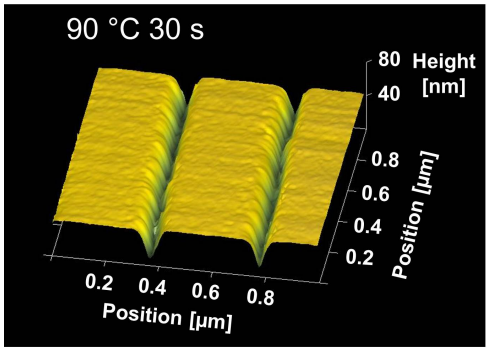

b) Hot-plate hardbake at 90 °C 30 s

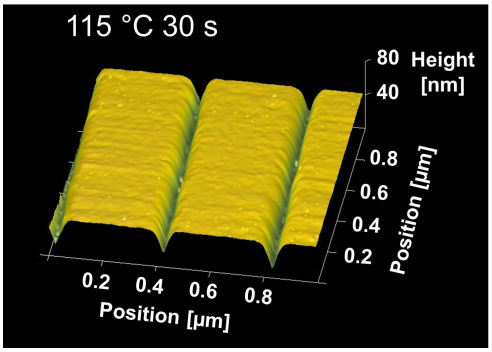

c) Hot-plate hardbake at 115 °C 30 s

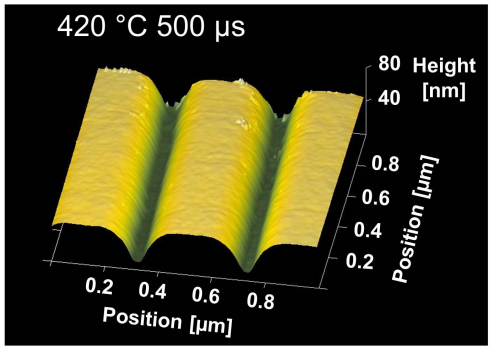

d) Laser hardbake at 355 °C 500 μs

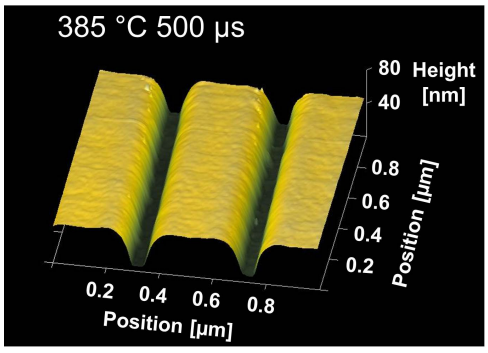

e) Laser hardbake at 385 °C 500 μs

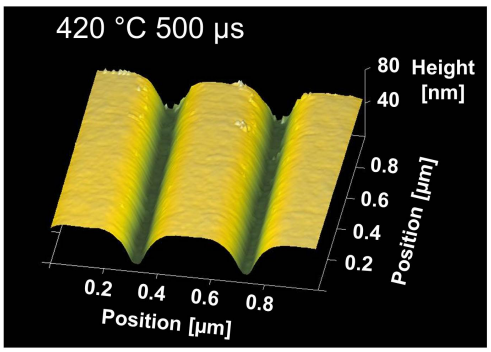

f) Laser hardbake at 420 °C 500 μs

Figure 6.4: Resist profiles obtained from AFM measurements as a function of hardbake temperature using the acrylate-based polymer showing a) the original pattern, b,c) hot-plate hardbake at 90 °C and 115 °C for 30 s, and d,e,f) laser hardbake at 355 °C, 385 °C, and 420 °C for 500 μs respectively. While surface roughness is reduced for both hardbake methods, trenches remain intact only for the laser-induced sub-millisecond anneal.

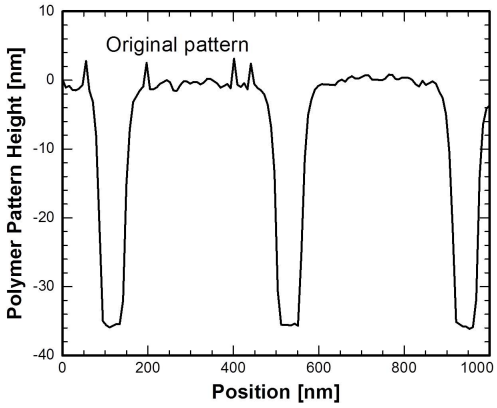

a) Original pattern (no hardbake)

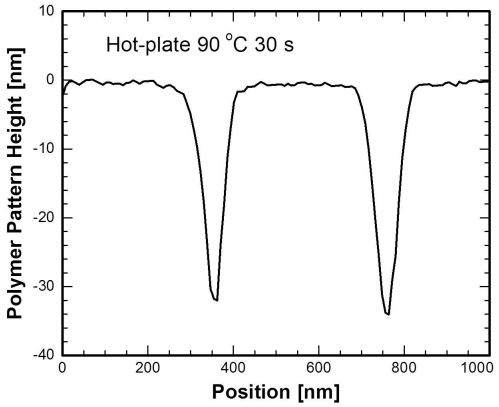

b) Hot-plate hardbake at 90 °C 30 s

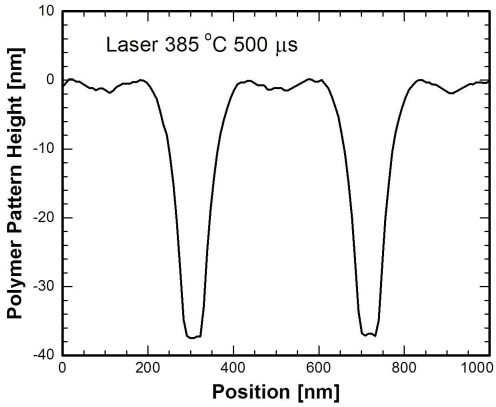

c) Laser hardbake at 385 °C 500 μs

Figure 6.5: AFM traces of the acrylate-based resist height plotted as a function of scan position for a) the original pattern, b) hot-plate hardbake at 90 °C for 30 s, and laser hardbake at 385 °C for 500 μs. Polymer flow on the seconds time frame degrades the resist sidewalls and trench profile. In contrast, there are only minimal changes in the trench profile after sub-millisecond hardbake.

bake at 385 °C. Loss of the sidewall angle and CD at the trench bottoms is most severe under hot-plate processing, with almost complete loss of the trench bottom and depth. Resist flow in this case occurs predominately in the trenches with much less change on the surface of the resist patterns. In contrast, the laser hardbake shows primarily surface flow, surface smoothing, and corner smoothing with minimal damage in the trench profile, where the change is limited to

the top 10 nm of resist. As a resist stencil for the subsequent etching step, the profile after laser hardbake remains viable while the complete CD loss using hot-plate hardbake would be ineffective.

To characterize the surface roughness reduction of the acrylate-based polymer, quantitative measures were obtained from comparable areas (100 nm by 850 nm on the resist surface) in the AFM images. Figure 6.6 shows the average roughness (R_a), root mean square (RMS) roughness (R_q), and maximum roughness (R_{max}) for both hot-plate and laser hardbake. Using hot-plate hardbake, a

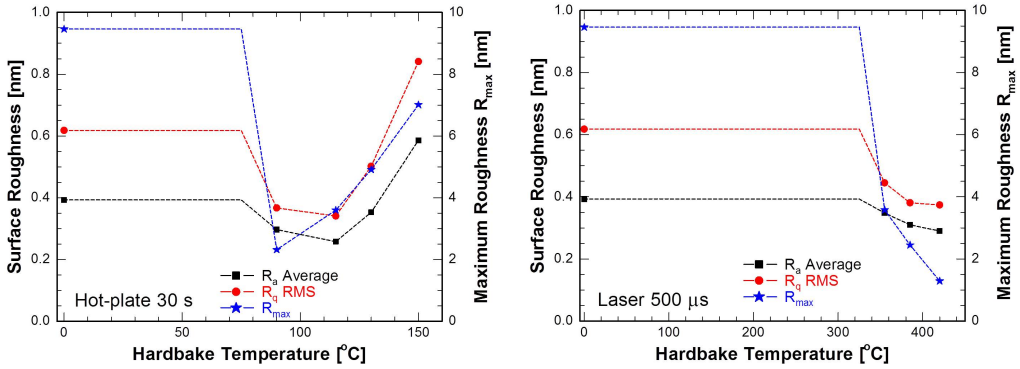

a) Roughness after hot-plate hardbake b) Roughness after laser hardbake

Figure 6.6: Surface roughness measurements of the acrylate-based resist pattern showing the average roughness, root mean square roughness, and maximum roughness (R_a, R_q, and R_{max} respectively) as a function of hardbake temperature using a) hot-plate or b) laser-induced heating. Up to 40 % reduction in R_q is observed from polymer flow using either heating methods. Scale for R_{max} is on the right axis.

minimum in all three measures was observed at temperatures between 90 °C and 115 °C. While the R_q is reduced up to 45 % at 115 °C, this reduction is not useful given the collapse of the sidewall profiles due to the excessive polymer flow. As the temperature is increased further, large scale flow of the resist results in rapidly increasing roughness which ultimately approaches and exceeds the initial values. Similar reductions up to 40 % in R_q are observed using laser

hardbake at 385 °C, but trench profiles remain nearly intact in contrast to hot-plate hardbake. With increasing laser hardbake temperature, all roughness measurements continue to decrease suggesting an increase in resist flow during the 500 μs heating. The large decrease, up to 75 % in R_{max}, for both hardbake methods is due to the loss of the sharp bumps, up to 10 nm in height, initially present on the surface. Removal of such high spatial frequency roughness is expected to occur first as the resist flow distance increases exponentially with temperature. Collectively, these data indicate that the acrylate-based polymer is more sensitive to large scale flow and profile damage during the seconds hardbake as compared with the sub milliseconds hardbake at much high temperatures.

The CD and LWR values obtained from SEM analysis indicated an optimal laser hardbake range between 300 °C and 420 °C for the investigated three polymer systems. For the acrylate-based polymer at 385 °C, LWR is reduced up to 30 % with less than 1 nm change in CD, and with R_a and R_q reduced by 21 % and 38 % respectively. As both LWR and surface roughness are similarly impacted by the viscous polymer flow, the consistent reductions between these two values are expected and observed. As the temperature is increased above T_g, the reduced viscosity of the polymer enables flow to minimize the surface energy and hence reduces both LWR and surface roughness. As the viscosity decreases rapidly with temperature, the temperature range for hardbake is relatively narrow for surface smoothing without excessive flow resulting in the loss of CD and sidewall angle. The polymer flow observed using the hot-plate hardbake at 90 °C for 30 s is comparable to the flow observed using laser-induced heating at 385 °C for 500 μs. The polymer viscosity change is expected to be inversely proportional to the heating duration, and the threshold for polymer flow shifts from 90 °C to 385 °C as heating duration is decreased by five orders

of magnitude. This result suggests an activation enthalpy of 34.2 kJ/mol for Arrhenius-like activated flow process, where the value is comparable to that of typical polymers [15, 16].

Fundamentally, the polymer flow induced from either hot-plate and laser hardbake is related to the decreased viscosity and the behavior should be comparable. However, the data show substantial smoothing without damage to the CD and sidewall profiles for laser heating, while the trenches are almost completely lost with similar surface smoothing for hot-plate heating. Two possible explanations can be attributed for this difference in flow behavior. First, the polymer on the sidewalls may be chemically different than the polymer on the surface due to the partial deprotection of the polymer during PEB and pattern development. For the acrylate-based polymer, this would imply a higher concentration of carboxylic acids and deprotection byproducts formed along the sidewalls during PEB, compared to more thermally stable carbonyl esters on the surface. These deprotection byproducts can act as plasticizers effectively lowering the T_g during the seconds time frame, resulting in substantial polymer flow in the sidewall compared to the surface, and leading to the rapid loss of CD and trench profiles. For sub-millisecond heating at temperatures far above T_g, additional flow due to the slight changes in T_g would be far less significant. Second, polymer flow at the bottom of the trench will be modified by the surface wetting of the polymer with the Si substrate. Changes in the delicate balance between surface energies at the polymer/Si interface and the polymer/vapor interface may delay wetting and flow at high temperatures, ultimately preventing the collapse of the trench profiles during laser hardbake. Further studies of the flow behavior over varying time frames and conditions are necessary to resolve this issue.

6.4 Conclusions

A laser-induced sub-millisecond heating is introduced as a post-develop process for controlling and minimizing LWR with minimal CD loss. Three different polymers were patterned and subjected to laser hardbake at peak temperatures between 175-450 °C for 500 μs. Results were compared with conventional hot-plate hardbake performed at temperatures of 90-150 °C for 30 s. For both heating methods, pattern smoothing due to polymer flow above its T_g was observed. At the optimal laser heating conditions, LWR was reduced up to 45 % with less than 1 nm change in CD. Surface roughness was also decreased up to 40 % with minimal change to the sidewall angle. While comparable reduction in surface roughness was observed for hot-plate hardbake, significant damage to the CD and the sidewall angle was observed in the trench profiles. These data demonstrate the potential for a sub-millisecond laser induced heating to address some of the roughness challenges in photoresist polymers.

6.5 Acknowledgments

Ruben Martinez and Steve Shim at K-TEK Nanotechnology LLC and Ragona Scientific are gratefully acknowledged for providing carbon nanotube AFM probes. Intel in Hillsboro, OR provided EUV exposures and development of high resolution features. This work made use of facilities in the Cornell Center for Materials Research (NSF-DMR 0520404) and the Cornell NanoScale Science and Technology Facility (NSF-ECS 0335765). Work at Cornell University was supported by Intel Corporation. Manish Chandhok is gratefully acknowledged for guidance and mentoring of this work.

References

[1] H. Ito, C. G. Willson, and J. M. J. Fréchet, "New UV resists with negative or positive tone", *Digest of Technical Papers of 1982 Symposium on VLSI Technology*, vol. 82, pp. 86–87, 1982.

[2] H. Ito and C. G. Willson, "Chemical amplification in the design of dry developing resist materials", *Polym. Eng. Sci.*, vol. 23, no. 18, pp. 1012–1018, 1983.

[3] H. Ito, "Chemical amplification for microlithography", *Adv. Polym. Sci.*, vol. 172, pp. 27–245, 2005.

[4] W. H. Zhou, S. M. Kuebler, K. L. Braun, T. Yu, J. K. Cammack, C. K. Ober, J. W. Perry, and S. R. Marder, "An efficient two-photon-generated photoacid applied to postive-tone 3D microfabrication", *Science*, vol. 296, no. 5570, pp. 1106–1109, 2002.

[5] G. M. Wallraff and W. D. Hinsberg, "Lithographic imaging techniques for the formation of nanoscopic features", *Chem. Rev.*, vol. 99, pp. 1801–1821, 1999.

[6] M. Chandhok, K. Frasure, E. Putna, T. R. Younkin, U. S. W. Rachmady, and W. Yueh, "Improvement in linewidth roughness by postprocessing", *J. Vac. Sci. Technol. B*, vol. 26, no. 6, pp. 2265–2270, 2008.

[7] M. Padmanaban, D. rentkiewicz, S. Lee, C. Hong, D. Lee, D. Rahman, R. Sakamuri, and R. R. Dammel, "Effect of hard bake process on LER", *Proc. SPIE*, vol. 5753, pp. 862–869, 2005.

[8] B. Jung, J. Sha, F. Paredes, M. Chandok, T. R. Younkin, U. Wiesner, C. K. Ober, and M. O. Thompson, "Kinetic rates of thermal transformation

and diffusion in polymer systems measured during sub-millisecond laser-induced heating", *ACS Nano*, vol. 6, no. 7, pp. 5830–5836, 2012.

[9] K. Iyengar, B. Jung, M. Willemann, P. Clancy, and M. O. Thompson, "Experimental determination of thermal profiles during laser spike annealing with quantitative comparison to 3-dimensional simulations", *Appl. Phys. Lett.*, vol. 100, no. 21, p. 211 915, 2012.

[10] S. Talwar, D. Markle, and M. Thompson, "Junction scaling using lasers for thermal annealing", *Solid State Technol.*, vol. 46, no. 7, pp. 83–86, 2003.

[11] T. Yamamoto, T. Kubo, T. Sukegawa, E. Takii, Y. Shinmamune, N. Tamura, T. Sakoda, M. Nakamura, H. Ohta, T. Miyahita, H. Kurata, S. Satoh, M. Kase, and T. Sugii, "Junction profile engineering with a novel multiple laser spike annealing scheme for 45-nm node high performance and low leakage CMOS technology", *Int. El. Devices Meet.*, vol. 1, pp. 143–146, 2007.

[12] M. D. Shumway, P. Naulleau, K. A. Goldberg, and J. Bokor, "Measuring line roughness through aerial image contrast variation using coherent extreme ultraviolet spatial filtering techniques", *J. Vac. Sci. Technol. B*, vol. 23, no. 6, pp. 2844–2847, 2005.

[13] B. J. Rice, H. Cao, M. Chandhok, and R. Meagley, "Effects of processing parameters on line width roughness", *Proc. SPIE*, vol. 5039, pp. 384–392, 2003.

[14] R. Peters, K. Lucas, J. Cobb, C. Parker, K. Patterson, R. McCauley, M. Ercken, F. van Roey, N. Vandenbroeck, and I. Pollentier, "Line-edge roughness reduction and CD slimming using hardbake processing", *Proc. SPIE*, vol. 5038, pp. 1131–1142, 2003.

[15] P. B. Macedo and T. A. Litovitz, "On the relative roles of free volume and activation energy in the viscosity of liquids", *J. Chem. Phys.*, vol. 42, pp. 245–256, 1965.

[16] G. P. Johari and M. Goldstein, "Viscous liquids and the glass transition. II. Secondary relaxations in glasses of rigid molecules", *J. Chem. Phys.*, vol. 53, pp. 2372–2388, 1970.

CHAPTER 7

EXPLOSIVE CRYSTALLIZATION AND STRUCTURAL CHARACTERIZATION OF AMORPHOUS SILICON BY CO_2 LASER SPIKE ANNEALING

7.1 Introduction and Motivation

Crystallization of thick (>100 nm) amorphous silicon (a-Si) films deposited on insulating substrates are attractive for large area electronic applications such as photovoltaic (PV) cells and three dimensional integrated circuits [1, 2]. Over the past 30 years for example, PV cells based on polycrystalline silicon (poly-Si) have been receiving increased attention due to the availability of high-rate deposition technologies for poly-Si films, in order to fabricate efficient cells with thicknesses less than 25 μm. Poly-Si cells provide an opportunity to gain the efficiency of bulk Si cells (limited to 31 %) at the cost of thin-film PV technologies [3, 4]. In order to attain poly-Si film at low-cost, a-Si is deposited onto a low-cost substrate such as glass or polymer and is annealed for crystallization. The efficiency of poly-Si cells is currently as high as 8.2 %, which is lower than thin-film modules such as a-Si cells at ~10 % [1, 4]. The main reason for the reduced efficiency is due to the electronic transport properties, where the carrier lifetime depends on the grain size of poly-Si established by the nucleation and growth kinetics from its amorphous form [1]. Larger grain size and smaller grain density improves the carrier lifetime resulting in an increased power conversion efficiency, and is generally explored through various annealing methods.

Previously, it has been shown that irradiation of a-Si film with short laser pulses can result in rapid crystallization process [5–8]. Pulsed laser irradia-

tion (*e.g.* Nd:YAG and excimer) and crystallization necessarily require heating into the melt. In contrast, laser spike annealing (LSA) normally operates as a non-melt process using a solid-state diode or CO_2 laser at temperatures up to substrate melt for dwell times (τ_{dwell}) ranging from 10 μs to 10 ms. Since the spike annealing process is in the sub-millisecond time regime, the nucleation and growth of poly-Si is also expected to occur in sub-millisecond potentially yielding large grain structures with low grain densities suitable for PV applications.

Amorphous silicon is a metastable phase that undergoes a first order transformation to the diamond cubic crystalline phase. Since a-Si is a continuous network of Si atoms, the entire network re-arranges to minimize its free energy when annealed at high temperatures. Above 500 °C, a solid phase transformation into the thermodynamically stable crystalline phase occurs since a-Si has a higher free energy by ~0.11 eV/atom. If the a-Si layer is on top of a single crystal substrate, the transformation will occur at the interface by solid phase epitaxy. If there is no pre-existing crystal template, nucleation of crystalline clusters must occur before solid phase growth can occur. For a-Si, a crystalline cluster can nucleate homogeneously within the amorphous film or heterogeneously on discontinuities such as interfaces, extended defects, and precipitates [9]. Since the occurring type of nucleation heavily depends on the defect concentration and the deposition method, mixed nucleation is also a possibility. Once nucleation has occurred, growth proceeds as a simple Arrhenius-activated process with a velocity given by:

$$v(T) = v_0 \exp\left(-\frac{E^*}{k_b T}\right) \tag{7.1}$$

where v_0 is an orientation-dependent velocity prefactor, k_b is Boltzmann's constant, T is heating temperature, and E^* is a well-defined activation energy at

2.4 eV [10]. As shown in Equation 7.1, the fastest growth is achieved through highest temperatures.

During LSA of a-Si thin-films, an anomalous mode of crystallization is observed. The behavior is comparable to the explosive crystallization of a-Si, which can occur during a sub-millisecond heating if the feedback of the latent heat released from crystallization causes an acceleration of the crystallization. While the behavior and structure of explosive crystallization in Si have been extensively studied using nanosecond pulse lasers [5–8], the explosive crystallization of Si during microsecond CO_2 LSA is unknown and has to be reconsidered using large area scanned laser sources. This chapter explores an explosive crystallization behavior and resulting structural analysis of silicon using sub-millisecond CO_2 laser spike annealing.

7.2 Sample Preparation and Characterization

Approximately 300 nm of a-Si was prepared on thermal oxide using sputter deposition as schematically shown in Figure 7.1. The purity of the silicon target used for the deposition was 99.9+ %. Prior to deposition, the substrate surface was etched by ion beam cleaning in order to improve the quality of the thin-film by removing a layer of SiO_2. For a silicon substrate, the applied RF power was 2 kW which resulted in an a-Si deposition rate of 1.6 nm/min. All depositions were carried out *in situ* with 40 sccm of Ar gas. The deposition pressure for ion beam cleaning and silicon was approximately 1.5 mTorr and 5 mTorr, respectively.

Heavily doped substrates ($\rho \sim 0.01$-0.02 Ω·cm) were used to ensure free-

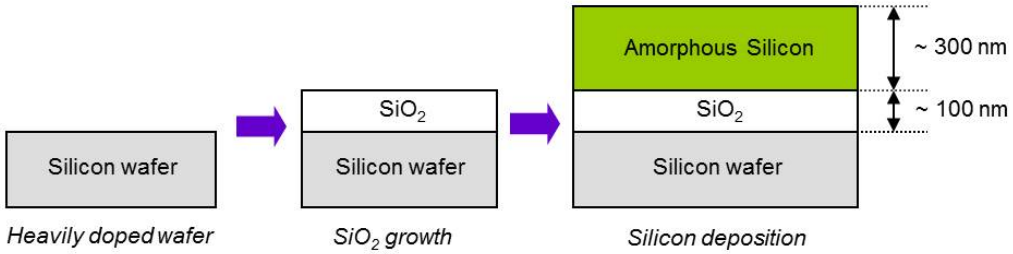

Figure 7.1: Schematic cross-section diagram showing the sample preparation of a-Si on SiO_2 before laser spike annealing.

carrier absorption of the CO_2 laser at 10.6 μm. The as-deposited a-Si film was relaxed by furnace annealing at 500 °C for 30 min in a nitrogen environment. Substrate was subsequently annealed with the laser at peak temperatures ranging from 800 °C (40 W) to 1400 °C (70 W) for 500 μs. Images of poly-Si were obtained through optical microscopes and Leica 440 SEM.

To analyze the explosive crystallization in detail, transmission electron spectroscopy (TEM) was used (Tecnai G2 F20) to image the cross-section and their relative diffraction patterns. Scattering vector, Q, was determined by the following equation

$$Q = \frac{1}{d_{hkl}} = \frac{\left(h^2 + k^2 + l^2\right)^{1/2}}{a} \tag{7.2}$$

where a is the lattice constant of silicon. For diamond cubic structures, the allowed diffraction planes are {111}, {220}, {311}, {400}, {331}, {422}.

7.3 Results and Discussion

Laser spike annealed a-Si using a CO_2 laser develops in three different stages as shown in Figure 7.2. At low temperature, Figure 7.2a reveals two distinguishable area: amorphous phase covering the majority of the area and a transformed region represented in a band caused by the substrate annealing at 900 °C (52 W). As the annealing temperature increases, two additional features can be observed: a feather-like thread nearly orthogonal to the beam path and a band of small crystallites along the center of the beam path. The width of each region (amorphous) increases with laser peak temperature. This increase is a result of the Gaussian temperature profile for each scan as discussed in Chapter 2.

The small crystallites observed for peak temperatures above 1110 °C unfortunately do not represent individual grain structures. Each crystallite has "scalloped microstructures" which are observed to be columnar crystals growing radially in a rosette-like pattern. These structures are commonly observed in explosively crystallization of Ge [11, 12]. Explosive crystallization of a-Si occurs when the annealing temperature is lower than the melting point of crystalline Si but greater than the melting point of a-Si. Under pulsed laser annealing, the melting temperature of a-Si is 200 ± 50 K lower than its crystalline form [12]. The solidification of liquid Si (l-Si) can occur on existing grain structures and/or nucleation near grains [6], where explosive liquid-phase nucleation (ELPN) can occur during the millisecond laser scan. The ELPN process during laser annealing is shown schematically in Figure 7.3, where a-Si is melted into metastable l-Si which becomes unstable with respect to its crystalline state [6].

In order to distinguish the transformed regions quantitatively, plan-view

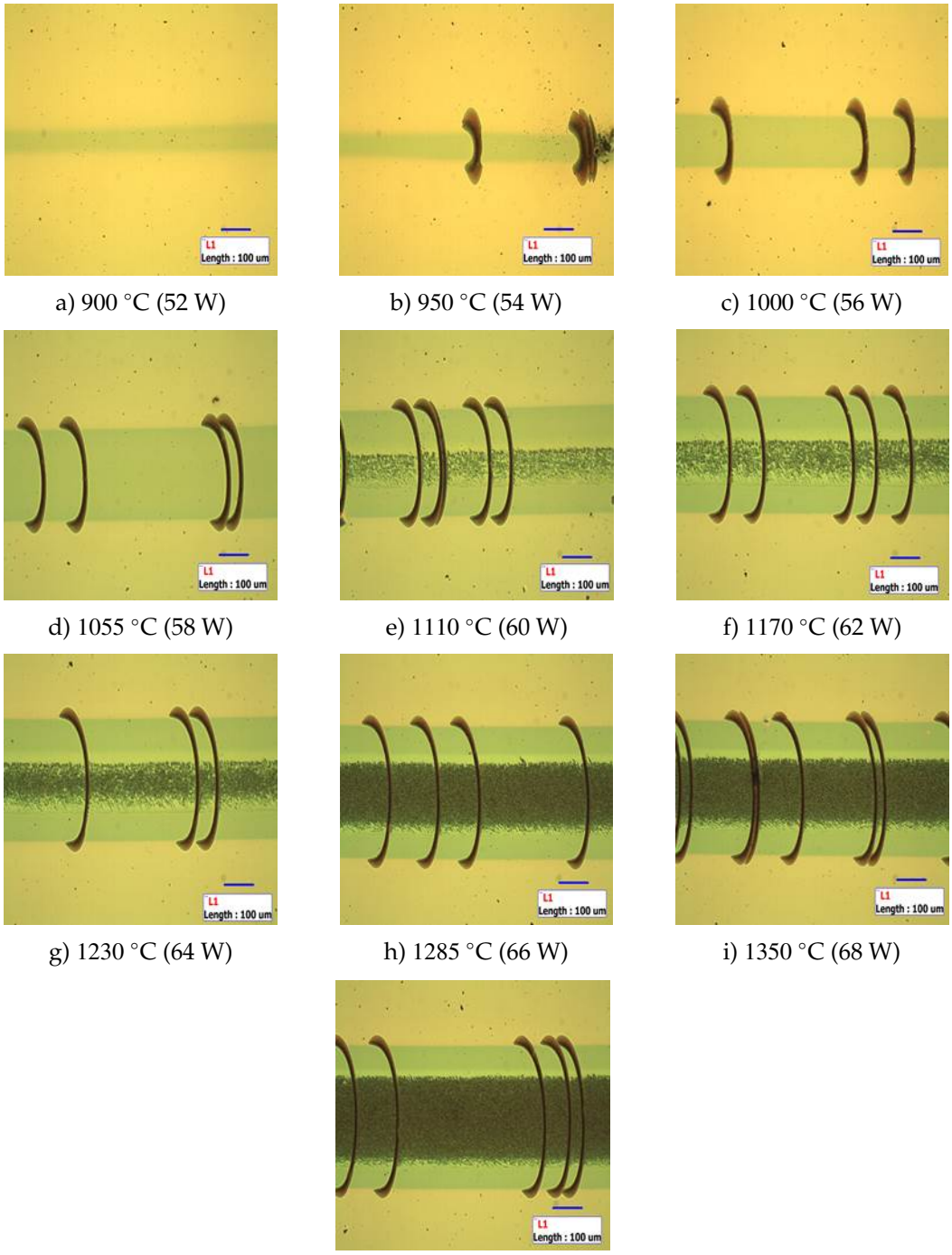

a) 900 °C (52 W) b) 950 °C (54 W) c) 1000 °C (56 W)

d) 1055 °C (58 W) e) 1110 °C (60 W) f) 1170 °C (62 W)

g) 1230 °C (64 W) h) 1285 °C (66 W) i) 1350 °C (68 W)

j) 1400 °C (70 W)

Figure 7.2: Bright field images of CO_2 laser spike annealed a-Si film at 500 μs. Laser scan direction is from left to right. All scale bars correspond to 100 μm.

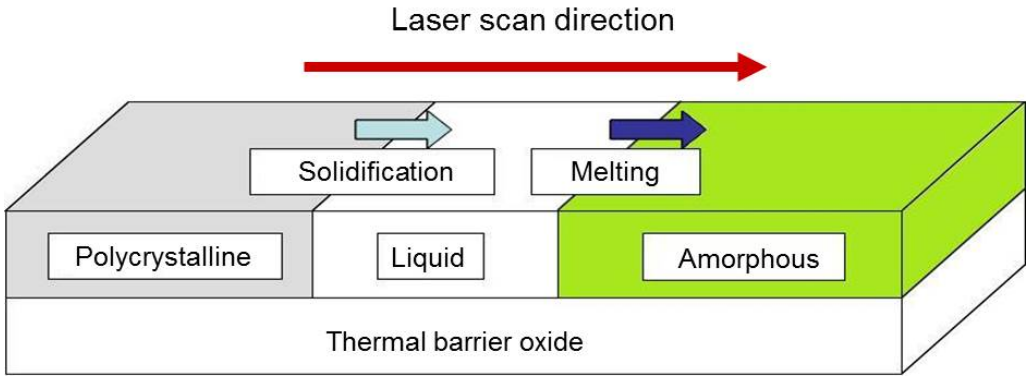

Figure 7.3: Schematic drawing of an explosive liquid-phase nucleation process. Silicon is melted and then solidified through laser spike annealing [11].

TEM samples were prepared and analyzed. The corresponding images and diffraction patterns were obtained using selected area electron diffraction of 40 μm radius. Each investigated area is labeled corresponding to Figure 7.4a. Diffraction in Figure 7.4b is consistent with a conventional amorphous phase. Figure 7.4c and 7.4f each represent the transformed regions above and below the small crystallites formed along the center of the beam path for peak temperatures 1055 °C (58 W) or higher. The diffraction patterns and TEM images of these transformed regions reveal that they are fine-grained polycrystalline phases formed by conventional nucleation and growth. The grain size in this region is <200 nm. Crystallites formed along the center of the beam path are much larger and patterns show individual grain diffraction (Figure 7.4e) rather than the concentric rings of fine grain material. The structure in this region consists of polycrystalline with larger grains, which likely requires transition to partial melt with accelerated growth dynamic.

The distribution function vs. scattering vector, Q, is plotted in Figure 7.5. Peaks for the center crystallites (Figure 7.4e) are diminished even for the

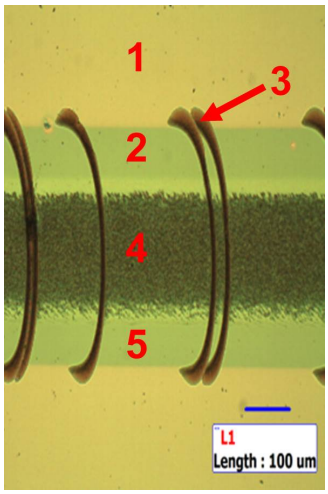

a) Optical view

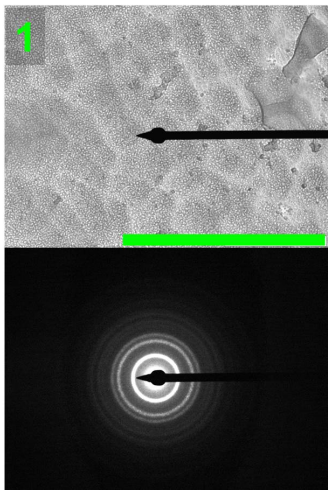

b) Amorphous silicon

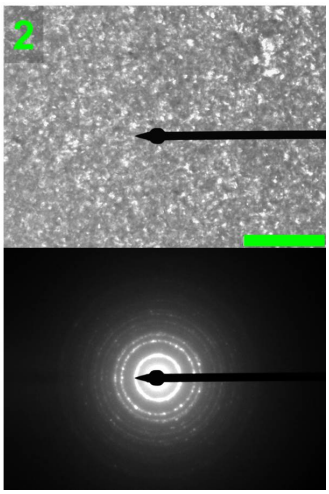

c) Fine-grained region above the band of explosive crystallites

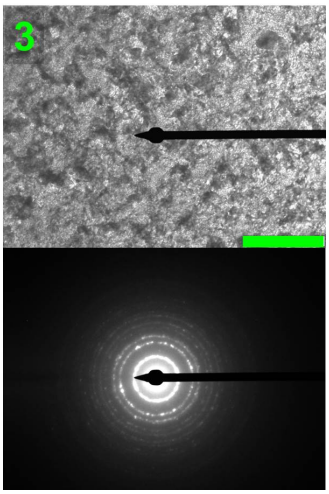

d) Explosive feather like threads

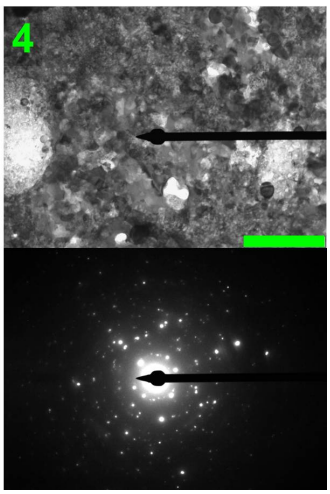

e) Center at the band of explosive crystallites

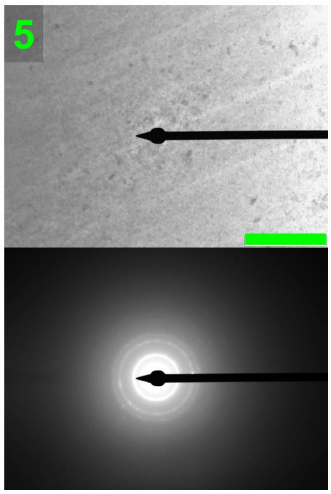

f) Fine-grained region below the band of explosive crystallites

Figure 7.4: Plan-view TEM images and corresponding selected area electron diffraction patterns. a) Optical image marking positions for b) amorphous silicon, c) fine-grained region above the band of explosive crystallites, d) explosive feather-like threads, e) center at the band on explosive crystallites and f) fine-grained region below the band of explosive crystallites. All scale bars for TEM images correspond to 1 μm.

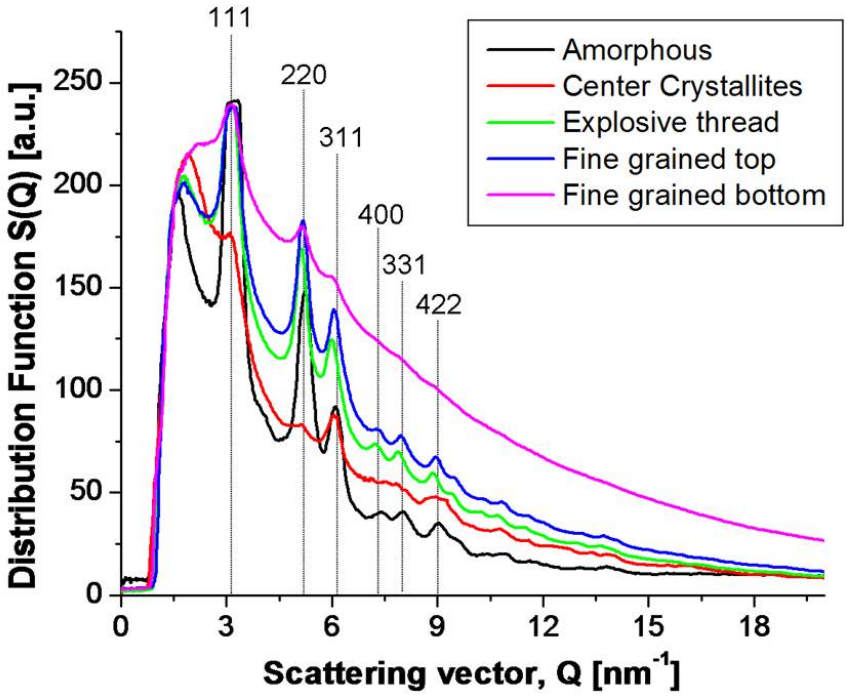

Figure 7.5: Distribution function based on the selected area electron scattering. All peaks are labeled with allowed diffraction planes in a diamond cubic structure. The unlabeled initial peak represents the scattering caused by the metal pin shown in Figure 7.4.

strongest diffraction peak at (111) plane. Thus the crystallites are not fine-grained polycrystalline but instead are composed of large grain structures. The TEM images also reveal that the surface is extremely rough, which is not a characteristics of a solid phase processes. Instead, it follows a trait of ELPN, where the amorphous phase melts into a metastable liquid in the temperature range $T_{ma} < T < T_{mc}$. This liquid state is unstable compared to the crystalline state, and can solidify directly from existing poly-Si grains or nucleation near grains [6]. The final phase due to ELPN is expected to be polycrystalline with large grains. At laser temperature of 1285 °C (66 W), the average grain size obtainable from the ELPN is approximately 500 nm. The range of the grain sizes vary

from hundreds of nanometers to over a micron, which is a consequence of the random nucleation and growth behavior.

Diffraction patterns in Figure 7.4d reveals that the feather-like thread is a mix of small and fine grains. It is similar to that of the fine-grained region shown in Figures 7.4c and 7.4f, but the numbers of small grain are larger in the feather-like threads. This observation also can be realized by the much lower magnitude of the fine-grained bottom peak compared to that of the explosive thread in Figure 7.5. These feather-like threads generate randomly as shown in Figure 7.2 and are the most interesting phase created through the CO_2 laser spike annealing. The lengths of these threads are clearly increasing with the increasing laser power as observed in Figures 7.2b through 7.2j.

Figure 7.6 shows dark field images of these feather-like threads and reveal that they are indeed crystalline. At low substrate temperature of 850 °C (50 W), these threads initiate from a defect on the sample. As seen in Figure 7.2, ELPN does not occur until the substrate temperature is above 1110 °C (60 W). We suggest that these defects increase the local heat absorption and raise the temperature locally to initiate an explosive crystallization in its liquid state. Even with a dwell time of microseconds, once explosive crystallization begins, a thin self-propagating liquid travels through the a-Si at velocities of 10-20 m/s, generating fine-grained poly-Si [5, 12].

To better understand the formation of these threads, the structure was examined by SEM (Figure 7.7). The "defect" nucleating these threads are apparent in Figures 7.7b, 7.7d, and 7.7e, indicating that the propagation of these threads is in the direction of the trailing end of the laser beam. It is likely that the fine-grained polycrystalline formed at the leading edge rapidly becomes unstable as

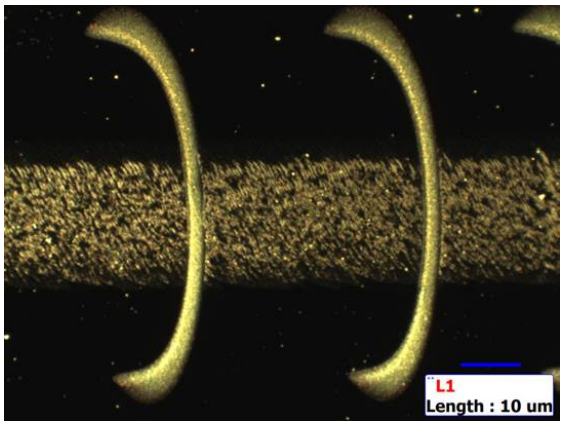

a) Explosive threads

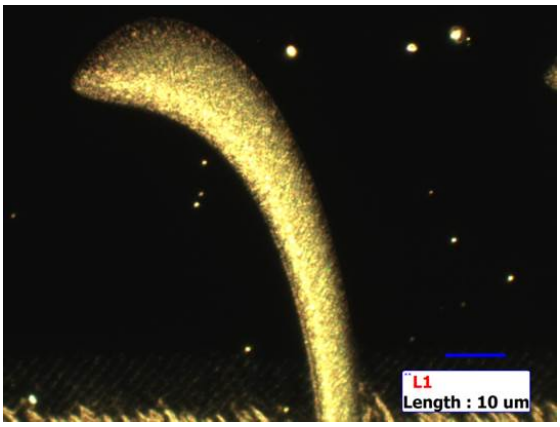

b) Explosive thread top

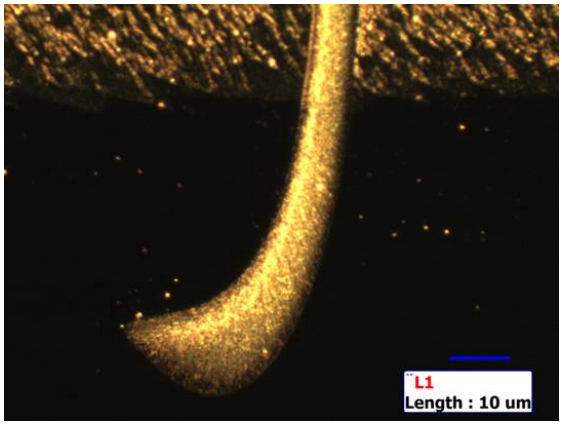

c) Explosive thread bottom

Figure 7.6: Dark field focusing on the explosive threads showing a) the overall explosive thread, b) top portion of the explosive thread, and c) bottom portion of the explosive thread. Laser scan direction is from left to right. All scale bars correspond to 10 μm.

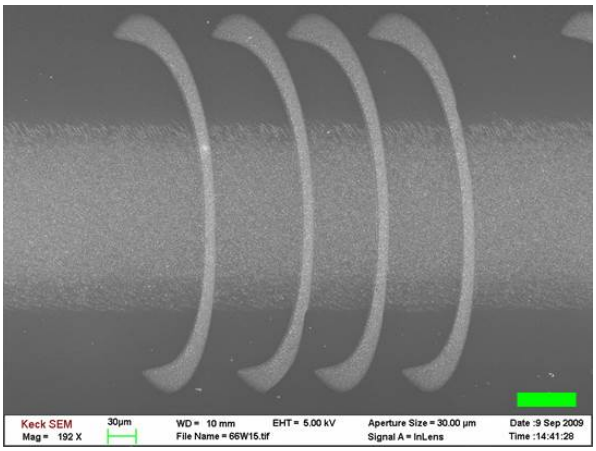

a) Explosive threads 1285 °C (66 W)

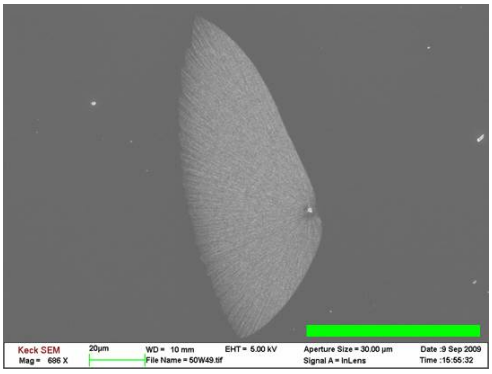

b) Thread formation 850 °C (50 W)

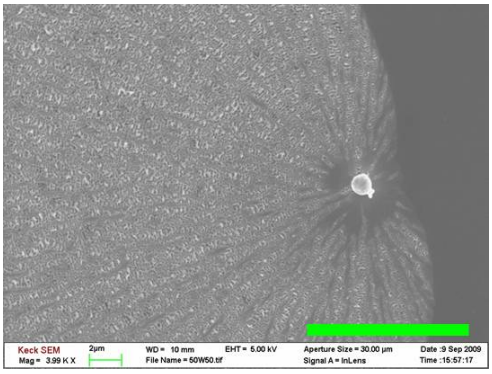

c) Thread formation 850 °C (50 W)

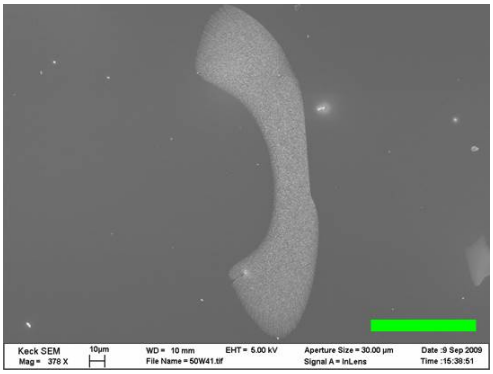

d) Thread formation 900 °C (52 W)

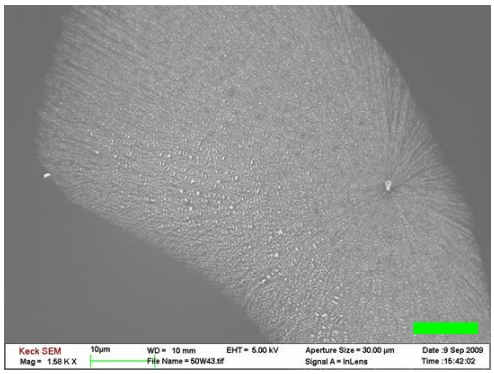

e) Thread formation 900 °C (52 W)

Figure 7.7: SEM images focusing on the explosive threads at various laser powers. Laser scan direction is from left to right at 500 μs dwell. Scale bars correspond to 60 μm for (a,b,d) and 10 μm for (c,e).

the temperature drops in front of the laser beam. The slow decrease in temperature behind the laser permits the explosive process to continue for much greater distances. However at higher laser temperatures, this fine-grained polycrystalline phase will stabilize and prevent the propagation of the explosive crystallization. In other words, the shape of this explosive thread develops a curvature with increasing laser temperatures along with the increasing area of the stable fine-grained polycrystalline phase.

7.4 Conclusions

Explosive crystallization of a-Si is observed for CO_2 laser spike annealed substrate temperatures above 850 °C (50 W). The explosive liquid phase nucleation of a-Si generates explosive crystallites along the center of the beam path which consists of large grains up to a micron in size. The explosive crystallites border fine-grained polycrystalline phases on either ends. A propagation of explosive crystallization in its liquid state is also observed as feather-like threads almost orthogonal to the beam direction. Generation of these threads is random and is initiated by defects on the sample. The structure of these threads is similar to that of fine-grained polycrystalline phase. In order to prevent the explosive crystallization during CO_2 spike annealing at higher temperatures than 850 °C (50 W), Si film less than 300 nm or much shorter beam dwells of <10 μs are required.

7.5 Acknowledgments

This project was funded by the Engineering Learning Initiatives (ELI) research sponsorship program at Cornell University through Professor Michael O. Thompson. Assistance from John Grazul, Luis Estevez, and Florencia Paredes in CMP, TEM, and general experimental support is gratefully acknowledged. This work made use of facilities in the Cornell Center for Materials Research (NSF-DMR 0520404) and the Cornell NanoScale Science and Technology Facility (NSF-ECS 0335765). Michael Willemann and Shahyaan Desai are especially acknowledged for encouragements and helpful discussions on the project and processing techniques.

References

[1] K. Chopra, P. Paulson, and V. Dutta, "Thin-film solar cells: An overview", *Prog. Photovoltaics*, vol. 12, no. 2-3, pp. 69–92, 2004.

[2] A. Topol, C. L. Tulipe, L. Shi, D. Frank, K. Bernstein, S. Steen, A. Kumar, G. Singco, A. Young, K. Guarini, and M. Leong, "Three-dimensional integrated circuits", *IBM J. Res. Dev.*, vol. 50, no. 4-5, pp. 491–506, 2006.

[3] M. A. Green, *Third generation of photovoltaics: Advanced solar energy conversion*. Berlin, Germany: Springer, 2003, pp. 1–6.

[4] M. A. Green, K. Emery, Y. Hishikawa, W. Warta, and E. D. Dunlop, "Solar cell efficiency tables (version 39)", *Prof. Photovolt: Res. Appl.*, vol. 20, pp. 12–20, 2012.

[5] M. Thompson, G. Galvin, J. Mayer, P. Peercy, J. Poate, D. Jacobson, A. Cullis, and N. Chew, "Melting temperature and explosive crystallization of amorphous silicon during pulsed laser irradiation", *Phys. Rev. Lett.*, vol. 52, no. 26, pp. 2360–2363, 1984.

[6] H. Geiler, E. Glaser, G. Gtz, and M. Wagner, "Explosive crystallization in silicon", *J. Appl. Phys.*, vol. 59, no. 9, pp. 3091–3099, 1986.

[7] G. Gtz, "Explosive crystallization process in silicon", *Appl. Phys. A*, vol. 40, no. 1, pp. 29–36, 1986.

[8] K. Murakami, K. T. O. Ery and, and K. Masuda, "Explosive crystallization starting from an amorphous-silicon surface region during long-pulse laser irradiation", *Phys. Rev. Lett.*, vol. 59, no. 19, pp. 2203–2206, 1987.

[9] C. Spinella, S. Lombardo, and F. Priolo, "Crystal grain nucleation in amorphous silicon", *J. Appl. Phys.*, vol. 84, no. 10, pp. 5383–5414, 1998.

[10] L. Csepregi, E. F. Kennedy, J. W. Mayer, and T. W. Sigmon, "Substrate-orientation dependence of the epitaxial regrowth rate from siâăřim-planted amorphous si", *J. Appl. Phys.*, vol. 49, p. 3906, 1978.

[11] A. Chojnacka, "Explosive crystallization of germanium films: kinetics and morphologies", PhD thesis, Cornell University, 2002.

[12] C. Csari, G. Nihoul, J. Marfaing, W. Marine, and B. Mutaftschiev, "Amorphous-crystalline interfaces after laser induced explosive crystallization in amorphous germanium", *Surf. Sci.*, vol. 162, pp. 724–730, 1985.

CHAPTER 8

CONCLUSIONS AND FUTURE WORK

8.1 Conclusions

Microlithography and laser spike annealing (LSA) are both critical techniques that have helped to drive the dimension scaling in the semiconductor industry. While remarkable advancements in lithography techniques have been established using chemically amplified resist systems, challenges arise in bypassing the trade-off in high resist sensitivity, controlled acid diffusion, and high resolution. Using a LSA system, thermally sensitive resist polymers were heated to temperatures beyond their conventional limits for sub-millisecond time frames. With the five orders of magnitude decrease from conventional heating durations, these thermally sensitive organic systems showed an extension in their thermal stabilities up to 1050 °C.

Compared to conventional hot-plate heating, high resolution (up to 50 nm lines/spaces) patterns formed using laser heating under DUV or EUV exposure showed simultaneous improvement in resist sensitivity (up to 30 % enhancement) and in roughness (up to 25 % reduction). To understand this improvement, deprotection kinetics and reaction pathways of a 193 nm resist system with methyl adamantyl esters were extensively studied over eight orders of magnitude. Across this temperature range, the behavior was non-Arrhenius. While the deprotection kinetics were measured to be first order at high temperature millisecond heating, the kinetics were more complex and exhibited a power law behavior for heating near the glass transition for seconds durations. The change in kinetics was due to the differences in the reaction byproduct,

where single ester cleavage occurs with formation of methylene adamantane only at laser-induced high temperatures, while an adamantyl dimer formation is observed for conventional seconds heating. The path to adamantyl dimer formation is acid-catalyzed, which acts as an acid trap and delays the overall deprotection kinetics. A mathematical model is proposed that incorporates this behavior, with simulation confirming the experimentally observed deprotection kinetics. At laser-induced high temperatures, both dimer formation and trap efficiency are decreased resulting in a fixed concentration of active acid-catalyst.

In an alternate approach to control the roughness, fully developed resist patterns were hardbaked at peak temperatures between 295-450 °C for 500 μs using CO_2 LSA. Surface smoothing due to flow of the polymer resist at the elevated temperatures was observed, which resulted in roughness reduction on pattern edges by >30 % with a <1 nm change in feature sizes. The hot-plate induced hardbake at optimal temperature also minimized roughness by ~40 %, but AFM images reveal loss of the vertical sidewall profile and substantial changes in the feature size.

In a conventional investigation of bulk nucleation and growth kinetics, the sub-millisecond CO_2 LSA was used to study the explosive crystallization of amorphous Si at temperatures above 850 °C (50 W). While a mix of fine-grained and large-grained polycrystalline phases were observed, a propagation of Si in its liquid state was observed creating a feather-like threads orthogonal to the scan direction. Generation of these threads is random and is initiated by defects on the sample. To prevent the explosive crystallization during CO_2 LSA at higher temperatures, Si film thinner than 300 nm or much shorter beam dwells of <10 μs are needed.

These results demonstrate the utility of laser-induced sub-millisecond heating to characterize reaction kinetics over a wide range of temperature and time, while identifying fundamental changes in mechanisms. For thermally sensitive polymers, the laser-induced heating allows the measurement of previously estimated kinetics and predicted models at previously unattainable temperatures. For microlithography, the laser-induced heating on resist polymers may address some of the diffusion and sensitivity challenges in future DUV and EUV lithography. Combined with existing methods to characterize material properties, the LSA technique has been shown to be a viable method for investigating reaction kinetics at high temperatures for millisecond time frames, not only for conventional semiconductor materials such as Si, but also for thermally sensitive organic systems.

8.2 Future work

8.2.1 Resist patterning using laser-induced millisecond heating

Laser-induced heating was demonstrated as an alternative post-exposure bake method at high temperatures (200-450 °C) for millisecond time frames (0.5-2 ms). As schematically shown in Figure 4.17b, resist systems with higher activation energy in deprotection than in acid diffusion will enhance the resist sensitivity, while controlling the acid diffusion required to minimize the line edge roughness (LER) even for sub-50 nm high resolution patterns. The trade-off in resolution, LER, and sensitivity can be shifted to time and temperature regimes corresponding to laser PEB conditions, potentially opening up new op-

tions for high resolution patterning at enhanced sensitivity with controlled acid diffusion.

While laser heating tools are readily available, resist systems with the appropriate activation characteristics are required to ensure optimal patterning performance during millisecond PEB. Ideally, these resist systems should incorporate base quenchers and additives to be comparable to commercially available systems used in the current semiconductor industry. However, most next-generation commercial resists have the reversed activation characteristics, making them better suited for hot-plate PEB conditions as illustrated in Figure 4.17a. Unfortunately, chemical compositions of most commercial systems are unknown, and the patterning performance cannot be readily linked with the chemical structure, deprotection reaction, and catalyst diffusion of the resist system.

To further demonstrate the appropriate activation characteristics leading to an optimized patterning performance using laser heating, chemical modification via changing protecting groups, photoacid generators, base quenchers, and additives should be performed in-house and should be tested for imaging as well as their reaction kinetics to confirm the relative activation energy behavior.

8.2.2 Thermal stability and kinetics of organic systems during laser-induced heating

Extension of the thermal stability of organic systems was demonstrated using laser heating in the sub-millisecond time frame (Chapter 3). Since this stability

extension appears universal across all organic systems, reaction kinetics can be characterized at previously unattainable heating conditions for a deeper fundamental understanding.

At laser-induced high temperatures and sub-millisecond time frames, reaction kinetics may or may not follow Arrhenius behavior depending on the changes in the reaction pathways as shown in Chapter 5. It was also demonstrated that using conventional characterization techniques such as FTIR, NMR, and GC/MS, the physical changes in chemical structures can be identified and be used to explain the kinetic changes under laser-induced heating conditions.

The temperature and time regimes from laser-induced heating open up an entirely new area for kinetic investigations on thermally-sensitive organic systems. In particular, laser-induced heating can directly measure chemical reaction kinetics under conditions that were only modeled and estimated due to the challenges reaching the required temperatures and the thermal instability of organic systems at high temperatures.

8.2.3 Laser-induced millisecond hardbake on open-source resist systems

Roughness reduction of fully developed patterns at elevated temperatures was demonstrated using sub-millisecond heating. The reduction occurs by smoothing of the resist polymer's surface and trenches with the degree of smoothing dependent on the chemical structure and flow properties, such as the glass transition temperature (T_g). While the concept has been proven using commercial

resist systems (Chapter 6), the flow characteristics could not be linked with the unknown chemical components of these commercial systems. Since flow is more apparent for high resolution features, a patterning method capable of consistently printing <30 nm feature sizes using an open-source (known chemical composition) resist polymer is required. These patterns could then be heated using to quantify the flow behavior in millisecond times.

The laser hardbake using an open-source resist was attempted using an imprint technique with a Nanoimprint NX-2500 available in Cornell NanoScale Science and Technology Facility (CNF). A high resolution, EUV exposed resist patterns on a Si substrate was obtained from Warren Montgomery (College of Nanoscale Science and Engineering (CNSE) - Albany). The resist patterns contained a wide range of features including 1:1 ratio contact holes and lines/spaces. As shown in Figure 8.1a, 25 nm lines/spaces was the limit for the lithographic patterns. To obtain the Si template for imprint, the Si substrate was etched in a continuously flowing C_4F_8 and SF_6 at a 3:1 ratio as shown in Figure 8.1.

While 60 s etch completely removes the resist layer and prevents selective etching, a 30 s etch yielded a 76.4 nm Si trench as confirmed through AFM after stripping the resist layer. The Si templates were used to imprint patterns on a 193 nm resist, poly(MAdMA-*co*-GBLMA), (Figure 5.1a) spun onto a Si substrate (100 nm film). The patterned template and the resist-coated substrate were put into contact at ~300 psi and 185 °C (sufficiently above $T_g \approx 160$ °C) to induce polymer flow for 45 s. The Si template was then peeled from the resist on substrate by hand, creating enough static force between the template and the resist which removed parts of the film. Figure 8.2 shows the imprinted resist patterns

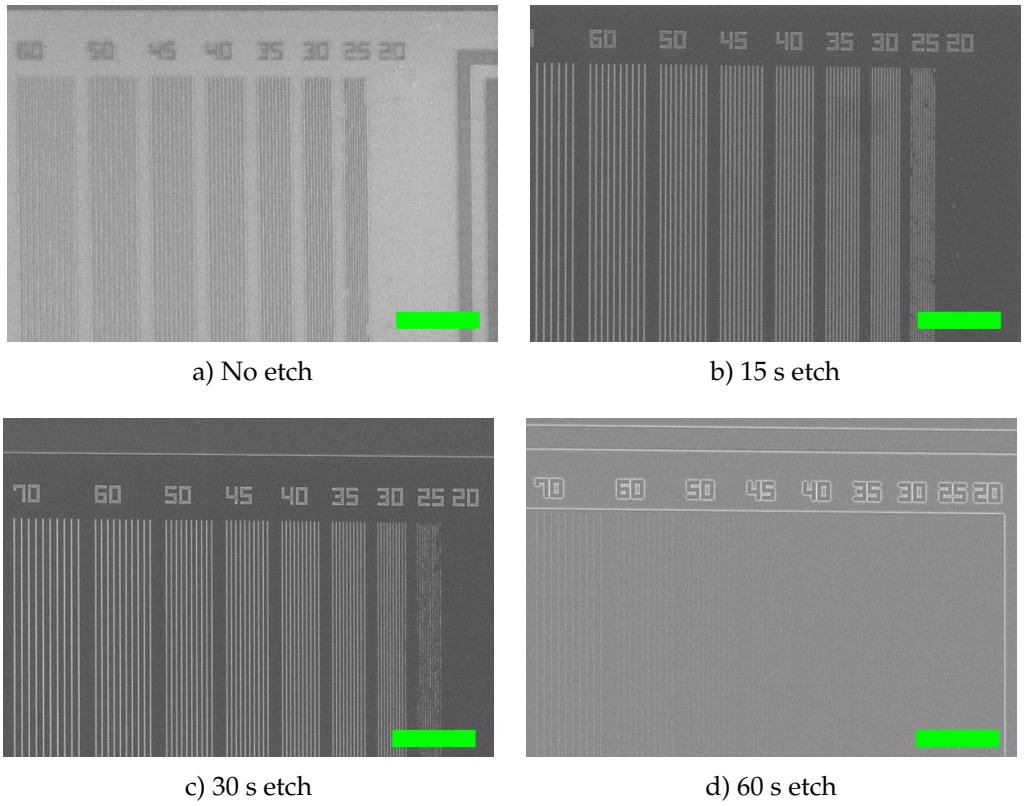

a) No etch b) 15 s etch

c) 30 s etch d) 60 s etch

Figure 8.1: SEM images of Si substrate with patterned resist etched in C_4F_8 and SF_6 gases at 3:1 ratio for a) 0 s (no exposure), b) 15 s, c) 30 s, and d) 60 s. The resist resolution is limited at 25 nm lines/spaces. While the 30 s etch yields a 76.4 nm of Si trench upon resist strip, 60 s etch becomes too long as the resist stencil layer is completely removed. All scale bars represent 4 μm.

showing 35 nm lines/spaces and contact holes.

High resolution resist patterns at 35 nm lines/spaces from a successful imprint are viable for laser hardbake and subsequent flow characterizations. However, consistency in imprint is required in order to characterize the flow behavior as a function of peak temperatures. As shown in Figure 8.3, a significant part of resist surface is removed when the Si template is pulled apart from the resist on the Si substrate causing inconsistency in imprint lithography.

Several approaches were pursued to minimize the resist removal during

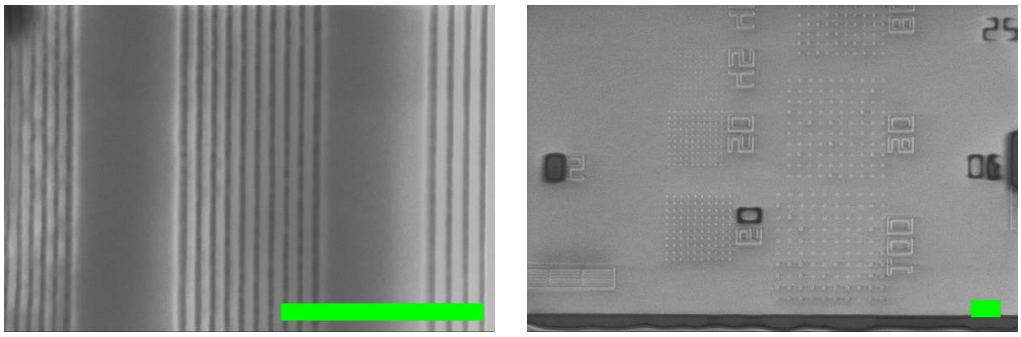

a) Imprinted 35 nm lines/spaces b) Imprinted contact holes

Figure 8.2: SEM images of 193 nm resist poly(MAdMA-*co*-GBLMA) patterns imprinted on Si substrates showing a) 35 nm lines/spaces and b) contact holes. High resolution imprint is possible with resists with known composition, but consistency is an issue. All scale bars represent 1 μm.

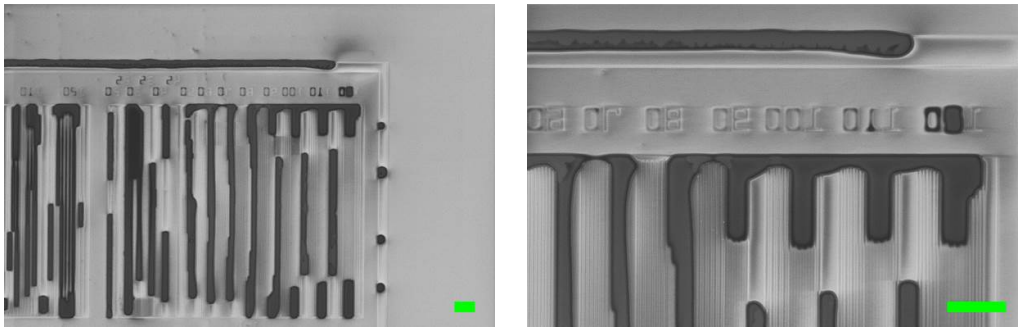

a) Resist peel after template removal b) Resist peel after template removal

Figure 8.3: SEM images of 193 nm resist poly(MAdMA-*co*-GBLMA) patterns on substrate after Si template have been pulled off. Consistency is an issue for imprint using NX-2500. All scale bars represent 2 μm.

the peeling step, including pulling the Si template in the direction of the lines/spaces to minimize lateral variations in CD, and coating the Si template with a monolayer of 1,1,2,2-perfluorooctyl silane (FOTS), which is a widely used polymer for anti-stiction coating in microelectromechanical systems (MEMS). Despite these efforts, inconsistency in both feature widths and edge roughnesses were visible. One alternative path is to cure the resist using ultraviolet

exposure during the imprint process, which crosslinks the resist polymer and makes them more stable during the template removal. This experiment requires a clear template such as polydimethylsiloxane (PDMS) with high resolution patterns.

8.2.4 Crystallization of a-Si in microsecond time frames

While the investigation of explosive crystallization behavior of a-Si at millisecond time frames is certainly interesting, it is difficult to make use of the poly-Si with inconsistent structural and electrical properties. Ultimately for device applications, a large-grained poly-Si is desired where laser-induced high temperatures can accelerate the growth kinetics while suppressing the explosive behavior at sufficiently short dwell times. While the spike annealing at 500 μs was demonstrated as shown in Chapter 7, shorter dwells are required to prevent the explosive crystallization behavior. For the next-generation of experiment, laser spike annealing in the order of a 50 μs or below should be pursued.

APPENDIX A

TEMPERATURE SIMULATION USING CLASP

While temperatures were measured experimentally, comparison with computational estimates is helpful to confirm their validity. To simulate the temperature during millisecond LSA, Cornell Laser Annealing Simulation Package (CLASP) was used to compare temperatures. CLASP, initiated and developed by M. O. Thompson, K. Iyengar, and P. Clancy, simulates LSA including temperature-dependent material thermal properties, optical coupling through band-to-band and free carrier absorption, and optical coupling arising from thin-film interference effects. The software was obtained directly from Michael O. Thompson (mot1@cornell.edu).

User inputs to CLASP include, but not limited to, laser wavelength (980 nm or 10.6 μm), beam FWHM, scanning velocity (τ_{dwell}), substrate doping concentration, and the line power density (W/cm) along the long axis of the line-focused beam. The line power density assumes a uniform beam intensity profile along the long axis, which is a 2D estimate valid near the peak of the spatial Gaussian intensity distribution (Figures 2.20 and 2.21).

CLASP approximates the beam as infinitely long and experimental laser powers must be converted to the equivalent line power density at the peak. The line power density as a function of position is denoted as $I(x)$. The integral of $I(x)$ over the long axis of the beam gives the total laser power. For a laser power of 64 W at τ_{dwell}, $\int_{-\infty}^{\infty} I(x)dx$ = 64 W. For the CO_2 laser, the beam intensity profile follows a Gaussian distribution (Equation 2.2). Normalizing to an intensity of I_0

at the peak at $x = 0$, this can be expressed as

$$I(x) = I_0 \exp\left[-\frac{x^2}{2\sigma^2}\right] \tag{A.1}$$

which has an integral of $\sqrt{2\pi\sigma^2}\, I_0$. Expressing in terms of the integrated total laser power P_0,

$$I(x) = P_0 \frac{1}{\sqrt{2\pi\sigma^2}} e^{\left(-\frac{x^2}{2\sigma^2}\right)} \tag{A.2}$$

and hence

$$I_0 = \frac{P_0}{\sqrt{2\pi\sigma^2}} \tag{A.3}$$

It is more convenient to work with the beam FWHM which is related to σ via FWHM $= \sqrt{8\ln 2}\,\sigma \approx 2.355\,\sigma$. Expressing I_0 in terms of the laser power P_0 and the FWHM, we have

$$I_0 = \frac{\sqrt{8\ln 2}\, P_0}{\sqrt{2\pi}\,\mathrm{FWHM}}\ (\mathrm{W/cm}). \tag{A.4}$$

From Equation A.4, a laser power P_0 of 64 W is equivalent to a line power density of 1022.2 W/cm for the CO_2 FWHM of 588.2 μm. These line power density are summarized in Table A.1.

The Si reflectivity at 10.6 μm was directly measured to be 22 % on the Si substrates with doping concentrations of $\sim 4.8 \times 10^{18}$ cm^{-3} ($\rho \sim 0.015$ Ω·cm for p-type). These conditions were used to simulate the temperature profiles during the CO_2 LSA. Conversely, substrates with doping concentrations of $\sim 9.0 \times 10^{14}$ cm^{-3} ($\rho \sim 15.0$ Ω·cm) were used to simulate the temperature profile of the 980 nm diode LSA.

Both temporal profiles and peak temperatures up to Si melt were obtained for dwells ranging from 250 to 1000 μs. The substrate thickness was set to 525 μm, the standard thickness for a 4 inch Si wafer. The boundary condition at the back interface was clamped (sample on vacuum chuck) while the edges

Table A.1: Calculated line power density for CO_2 and diode laser corresponding to their long axis FWHM using Equation A.4

Power [W]	CO_2 Laser [W/cm]	Diode Laser [W/cm]
10	160	40
20	320	75
30	480	115
40	640	155
50	800	190
60	960	230
70	1120	270
80	1280	305
90	1440	345
100	1600	385

were free. The initial substrate temperature was set to 300 K. While the simulated peak temperatures showed great match with the measured values using the CO_2 laser, this was less true for the 980 nm diode laser at 10 ms τ_{dwell}. The mismatch using the diode laser is potentially related to the fact that the diode intensity profile was not Gaussian and the strong dependence of optical properties at 980 nm with temperature, and the operation in thermally thin substrate region. Temperatures measured for $\tau_{dwell} < 10$ ms are required to compare the shape of the curves.

APPENDIX B

SUPPLEMENTAL DATA FOR POLYMER THERMAL STABILITY

B.1 Organic polymers: TGA, film thickness, and decomposition kinetics

For all investigated polymer systems, the thermogravimetric analysis (TGA) measuring the weight as a function of heating temperature was essentially equivalent to the normalized film thickness on a heated Si substrate. Figure B.1 shows this behavior for polymer systems based on a organic backbone. Since the loss in polymer film thickness was comparable to the weight loss obtained from TGA analysis, thermal stability limits can be obtained using hot-plate or laser-induced heating for thin-film polymers. The stability measured by film thickness loss during hot-plate induced seconds or laser-induced sub-millisecond heating are shown in Figure B.2.

For a given polymer system, the stability curve shapes between the two heating regimes are essentially equivalent, suggesting similar decomposition behavior. In contrast to poly(MAdMA-*co*-GBLMA) decomposition in Chapter 5, most of these systems exhibited a single step decomposition and threshold. The decomposition thresholds for all systems are remarkably extended up to 1050 °C, ~500 °C higher than the conventional limits, when the heating duration is reduced to 50 μs. Taking advantage of this extension in thermal stability, decomposition kinetics were observed by plotting the decomposition rate to 20 % film thickness loss as a function of inverse temperature as shown in Figure B.3.

For all investigated systems, the decomposition rate follows Arrhenius be-

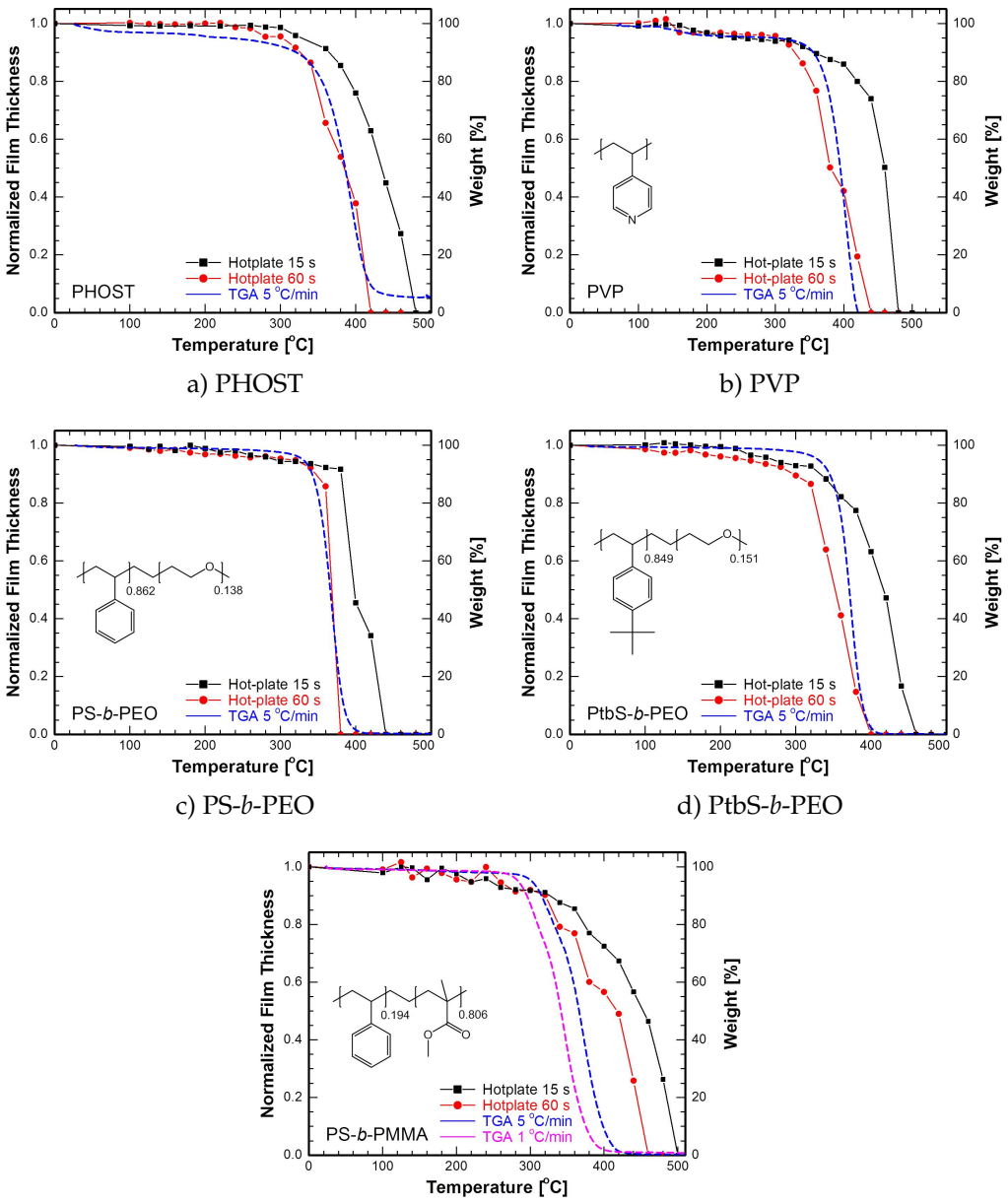

Figure B.1: Normalized film thickness as a function of heating temperature using a vacuum-chuck hot-plate for a) PHOST, b) PVP, c) PS-*b*-PEO, d) PtbS-*b*-PEO, and e) PS-*b*-PMMA. Loss in film thickness is comparable with the weight loss as plotted (dashed lines) on the right axis.

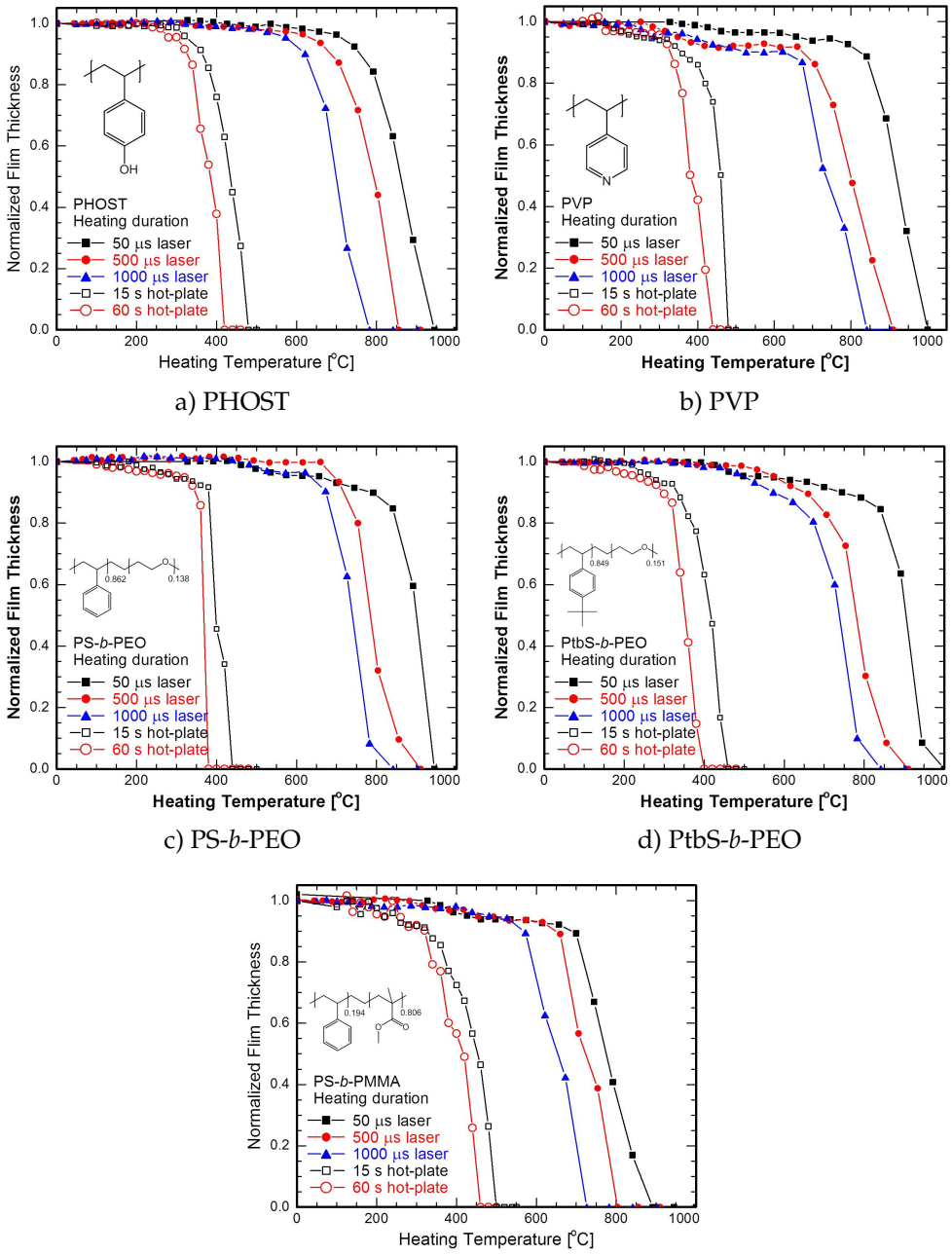

Figure B.2: Polymer film thickness loss as a function of temperature during hot-plate seconds and laser-induced sub-millisecond heating for a) PHOST, b) PVP, c) PS-*b*-PEO, d) PtbS-*b*-PEO, and e) PS-*b*-PMMA. For a given polymer system, stability curve shapes between the two heating durations are essentially equivalent, suggesting a similar decomposition behavior of the respective polymers. The decomposition thresholds is extended up to 1050 °C as the heating duration is reduced to 50 μs.

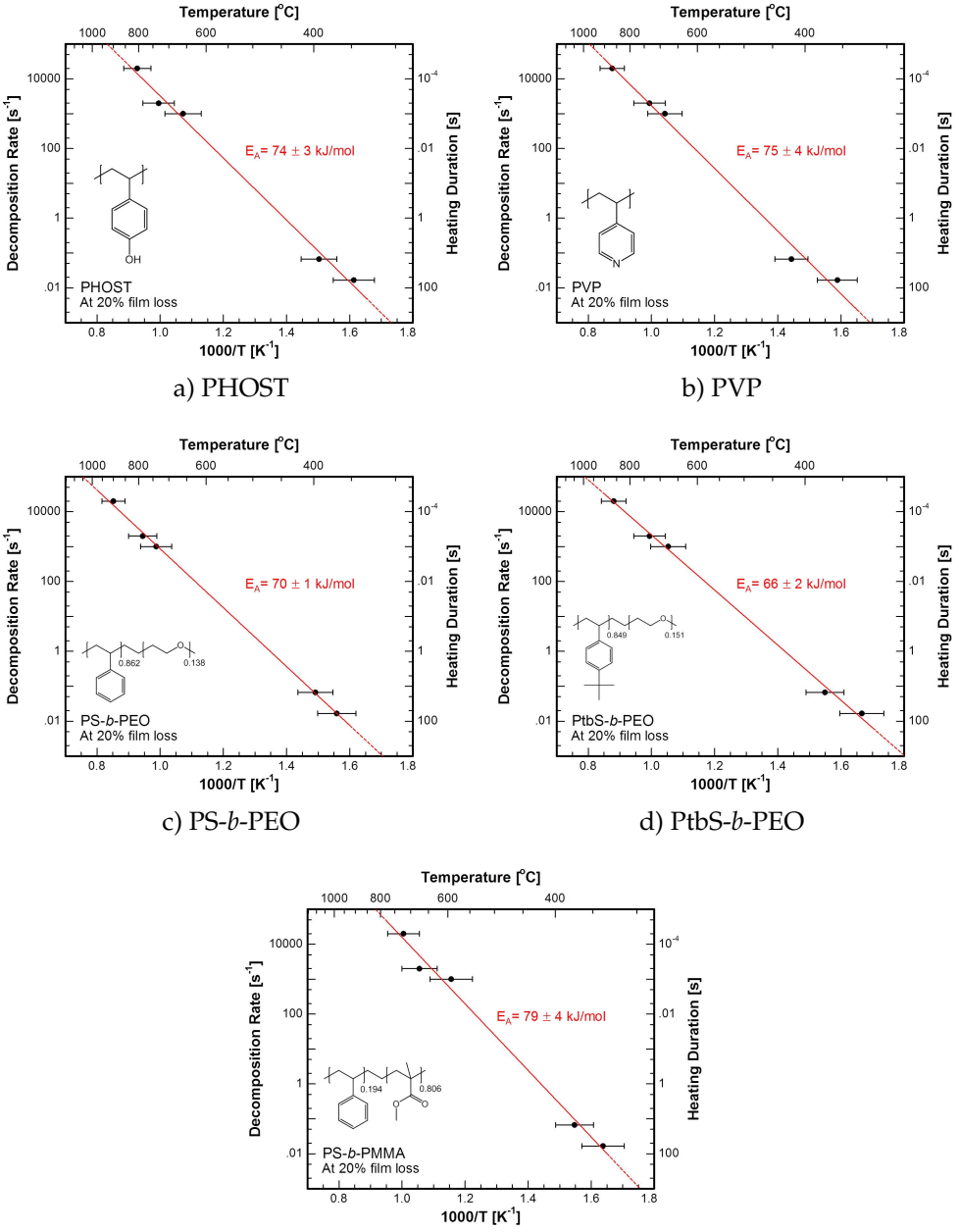

Figure B.3: Polymer decomposition rate as a function of inverse temperature at 20 % thickness loss for a) PHOST, b) PVP, c) PS-*b*-PEO, d) PtbS-*b*-PEO, and e) PS-*b*-PMMA. The decomposition rate follows Arrhenius behavior across the temperature range from hot-plate to laser-induced temperatures. The activation energy of all systems are similar suggesting the critical step is decomposition of the common organic backbone.

havior from hot-plate induced to laser-induced heating conditions. The similarity in E_A are similar due to the comparable decomposition barrier of the organic backbone.

B.2 Conjugated and Si-containing polymers: TGA, film thickness, and decomposition kinetics

Comparable TGA studies and film thickness measurements were made on conjugated and Si-containing polymers as shown in Figure B.4. As before, the loss in polymer film thickness was comparable to the weight loss obtained from the TGA at long times and thermal stability limits were obtained from hot-plate to the laser-induced time frames. The stability behavior measured by film thickness loss during hot-plate seconds or laser-induced sub-millisecond heating are shown in Figure B.5.

For a given polymer system, the stability curve shapes between the two heating regime are similar, suggesting comparable decomposition behavior. The decomposition thresholds is extended to as high as 1100 °C, ~500 °C higher than the conventional limits, as the heating duration is reduced to 50 μs. Taking advantage of this extension in thermal stability, decomposition kinetics are plotted (decomposition rate to 20 % film thickness) as a function of inverse temperature (Figure B.6). For all of these systems, the decomposition rate follows Arrhenius behavior across hot-plate and laser-induced heating conditions. The activation energies of the purely organic systems were essentially identical to the organic systems (~75 kJ/mol). However, with the addition of inorganic Si in the polymer backbone, the activation energy increases significantly as previously dis-

cussed in Chapter 3. While similar investigation on pure PSS would be ideal for distinguishing the decomposition behavior between PEDOT and PSS, obtaining a uniform film of PSS on a Si substrate was challenging.

B.3 FTIR Analysis on Decomposition

Fourier transform infrared spectroscopy (FTIR) was used to confirm the equivalent decomposition mechanism of the investigated organic, conjugated, and Si-containing polymers across hot-plate and laser heating. Ester, ether, and alcohol vibrational stretches for each polymer are shown as a function of heating temperature: PS-*b*-PMMA (Figure B.7), MEH-PPV (Figure B.8), PEDOT:PSS (Figure B.9), 4:1 PS-*b*-PDMS (Figure B.10), and 16:13 PS-*b*-PDMS (Figure B.11).

To quantify the data, all peaks were integrated and were plotted as a function of heating temperature as shown in Figure B.12. For all investigated polymers, comparable changes in integrated peaks are observed with increasing temperature between hot-plate and laser-induced heating. For most investigated polymers (all systems except for PS-*b*-PMMA), a sharp increase in C=O aromatic ester is observed, likely due to the decomposition of other components giving rise to alkenyl vibrational stretches.

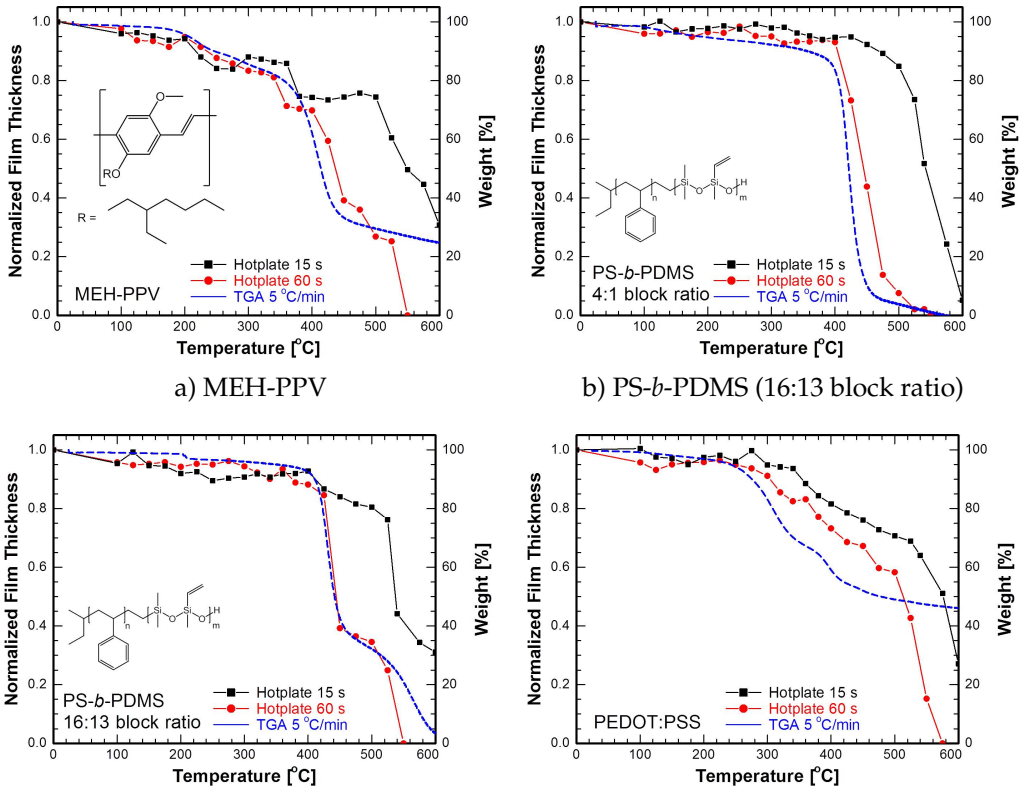

a) MEH-PPV

b) PS-*b*-PDMS (16:13 block ratio)

c) PS-*b*-PDMS (1:1 ratio)

d) PEDOT:PSS

Figure B.4: Normalized film thickness as a function of heating temperature using a vacuum-chuck hot-plate for a) MEH-PPV, b) PS-*b*-PDMS (16:13 block ratio), c) PS-*b*-PDMS (16:13 block ratio), and d) PEDOT:PSS. Film thickness is comparable to TGA weight as plotted (dashed lines) on the right axis.

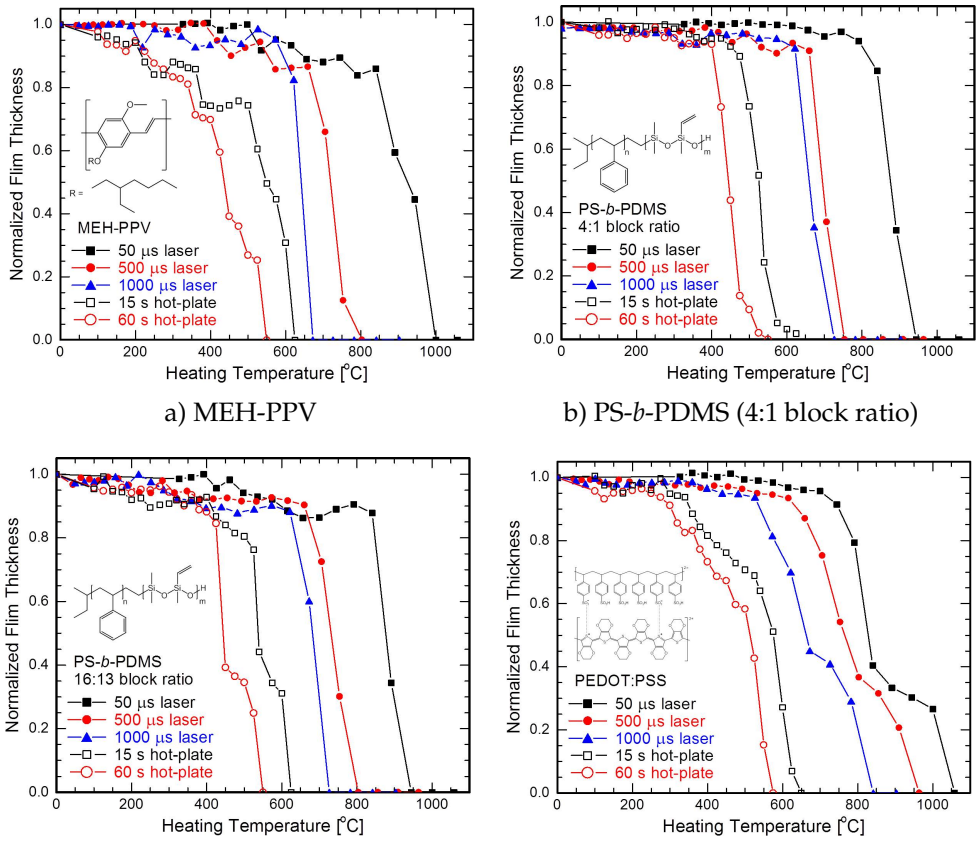

a) MEH-PPV

b) PS-*b*-PDMS (4:1 block ratio)

c) PS-*b*-PDMS (16:13 block ratio)

d) PEDOT:PSS

Figure B.5: Polymer film thickness loss as a function of temperature during hot-plate seconds and laser-induced sub-millisecond heating for a) MEH-PPV, b) PS-*b*-PDMS (4:1 block ratio), c) PS-*b*-PDMS (16:13 block ratio), and d) PEDOT:PSS. For a given polymer system, stability curve shapes between the two heating durations are essentially equivalent, suggesting a similar decomposition mechanisms. The decomposition threshold is extended to as high as 1100 °C as the heating duration is reduced to 50 μs.

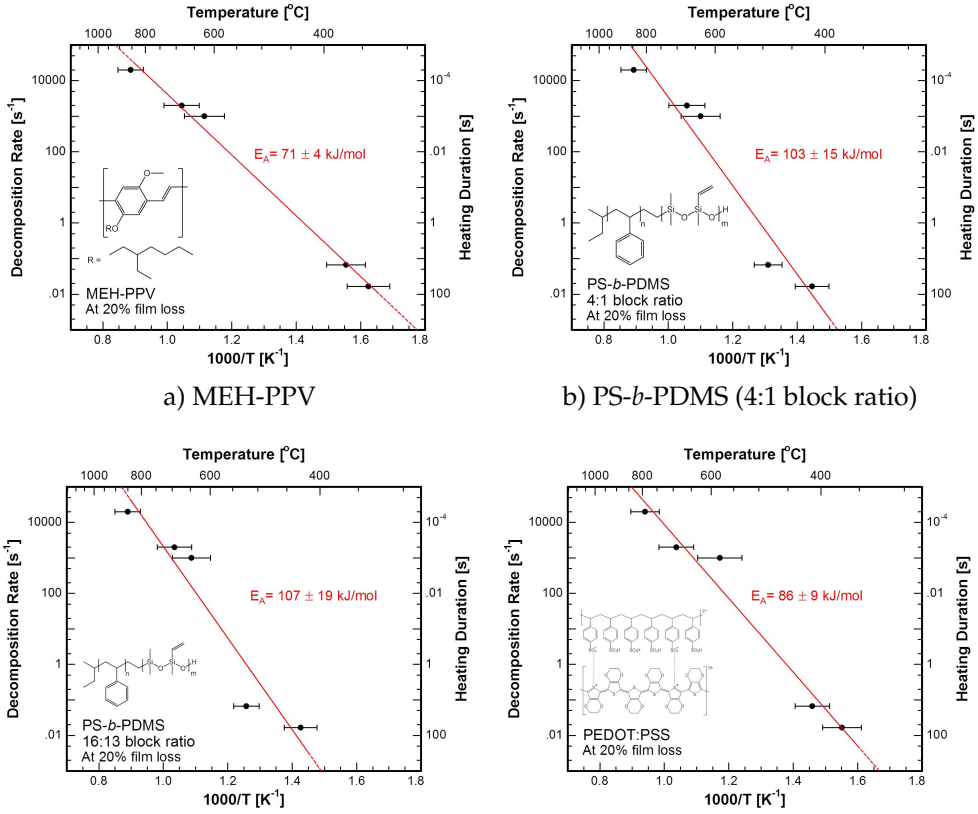

Figure B.6: Polymer decomposition rate as a function of inverse temperature at 20 % thickness loss for a) MEH-PPV, b) PS-*b*-PDMS (4:1 block ratio), c) PS-*b*-PDMS (16:13 block ratio), and d) PEDOT:PSS. The decomposition rate follows Arrhenius behavior across hot-plate and laser-induced temperatures. With inorganic elements incorporated into the polymer matrix, the activation energy increases.

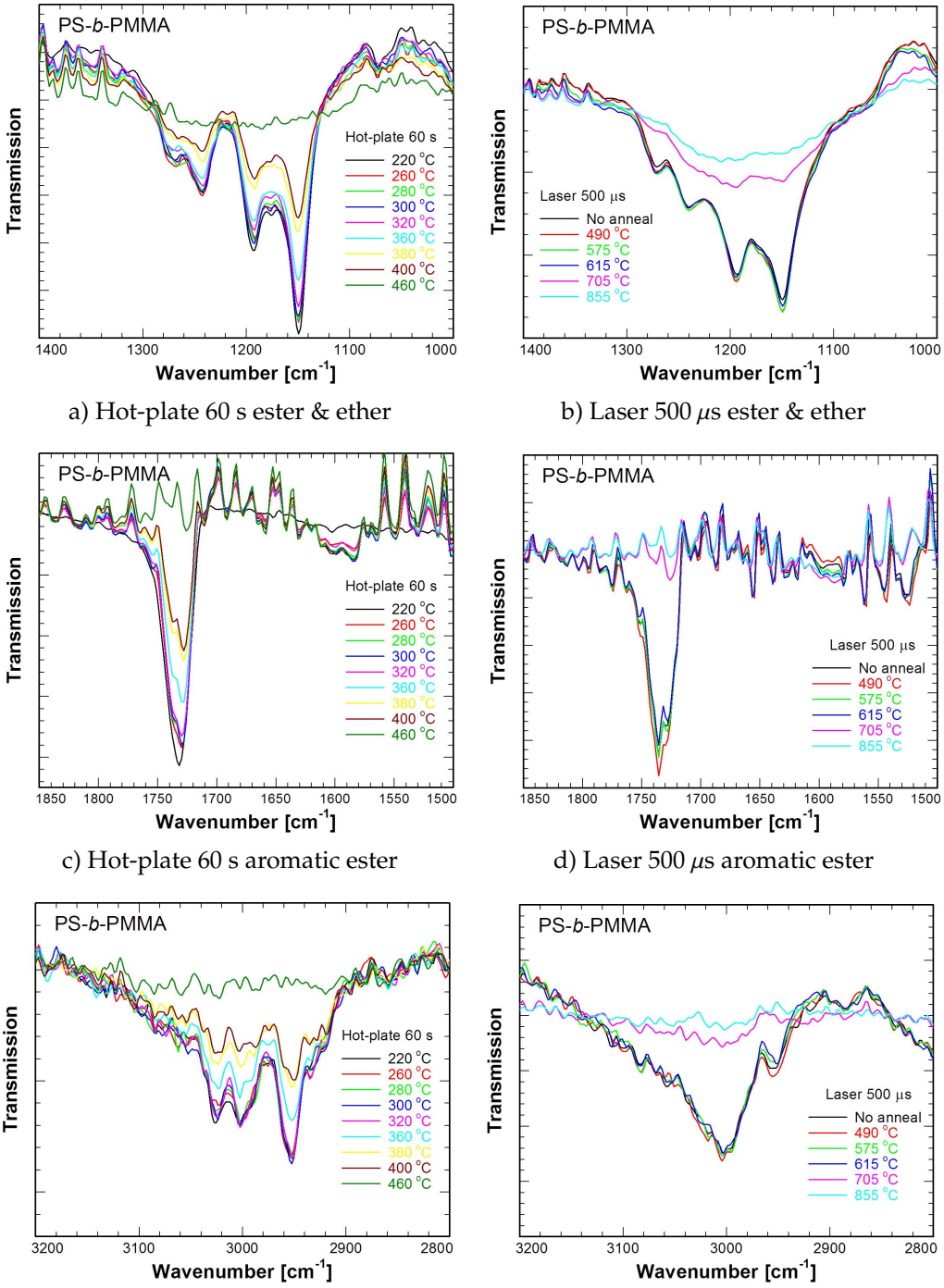

a) Hot-plate 60 s ester & ether

b) Laser 500 μs ester & ether

c) Hot-plate 60 s aromatic ester

d) Laser 500 μs aromatic ester

e) Hot-plate 60 s alcohol

f) Laser 500 μs alcohol

Figure B.7: FTIR peak comparison between hot-plate and laser heating for vibration stretches of a,b) ester and ether, c,d) aromatic ester, and e,f) alcohol for PS-*b*-PMMA. All peaks decrease as a function of heating temperature.

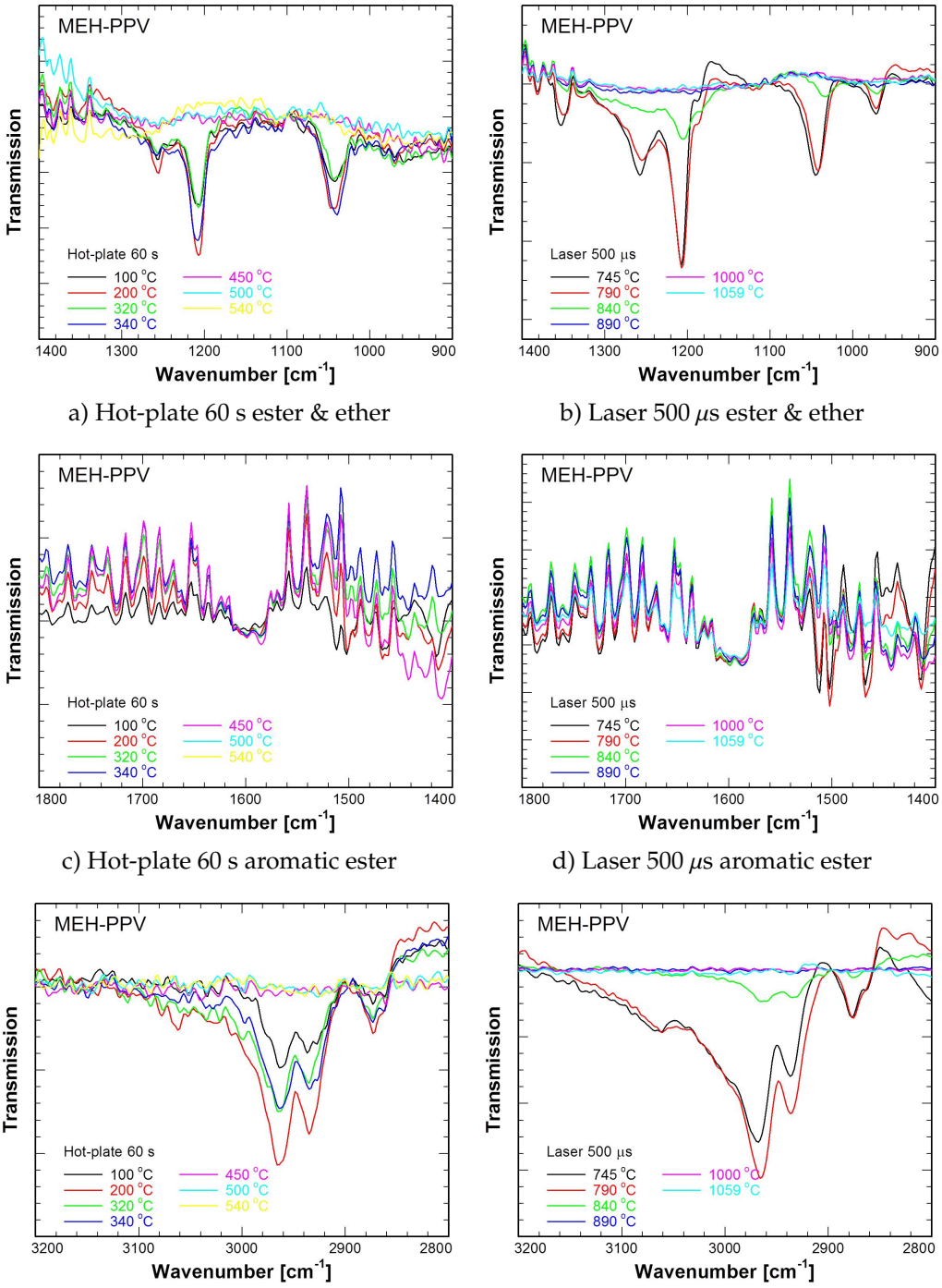

a) Hot-plate 60 s ester & ether

b) Laser 500 μs ester & ether

c) Hot-plate 60 s aromatic ester

d) Laser 500 μs aromatic ester

e) Hot-plate 60 s alcohol

f) Laser 500 μs alcohol

Figure B.8: FTIR peak comparison between hot-plate and laser heating for vibration stretches of a,b) ester and ether, c,d) aromatic ester, and e,f) alcohol for MEH-PPV. All peaks decrease as a function of heating temperature.

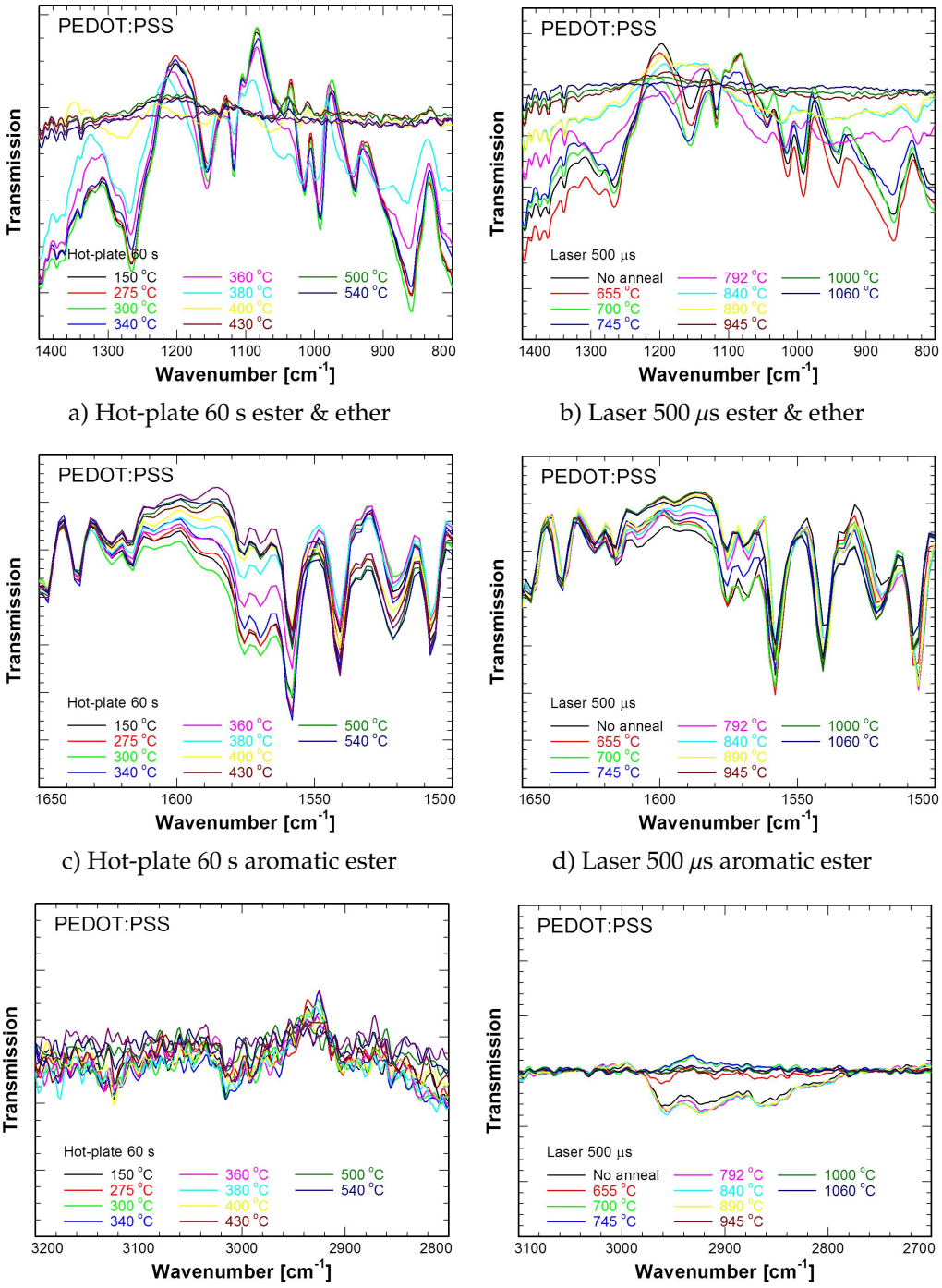

a) Hot-plate 60 s ester & ether

b) Laser 500 μs ester & ether

c) Hot-plate 60 s aromatic ester

d) Laser 500 μs aromatic ester

e) Hot-plate 60 s alcohol

f) Laser 500 μs alcohol

Figure B.9: FTIR peak comparison between hot-plate and laser heating for vibration stretches of a,b) ester and ether, c,d) aromatic ester, and e,f) alcohol for PEDOT:PSS. All peaks decrease as a function of heating temperature.

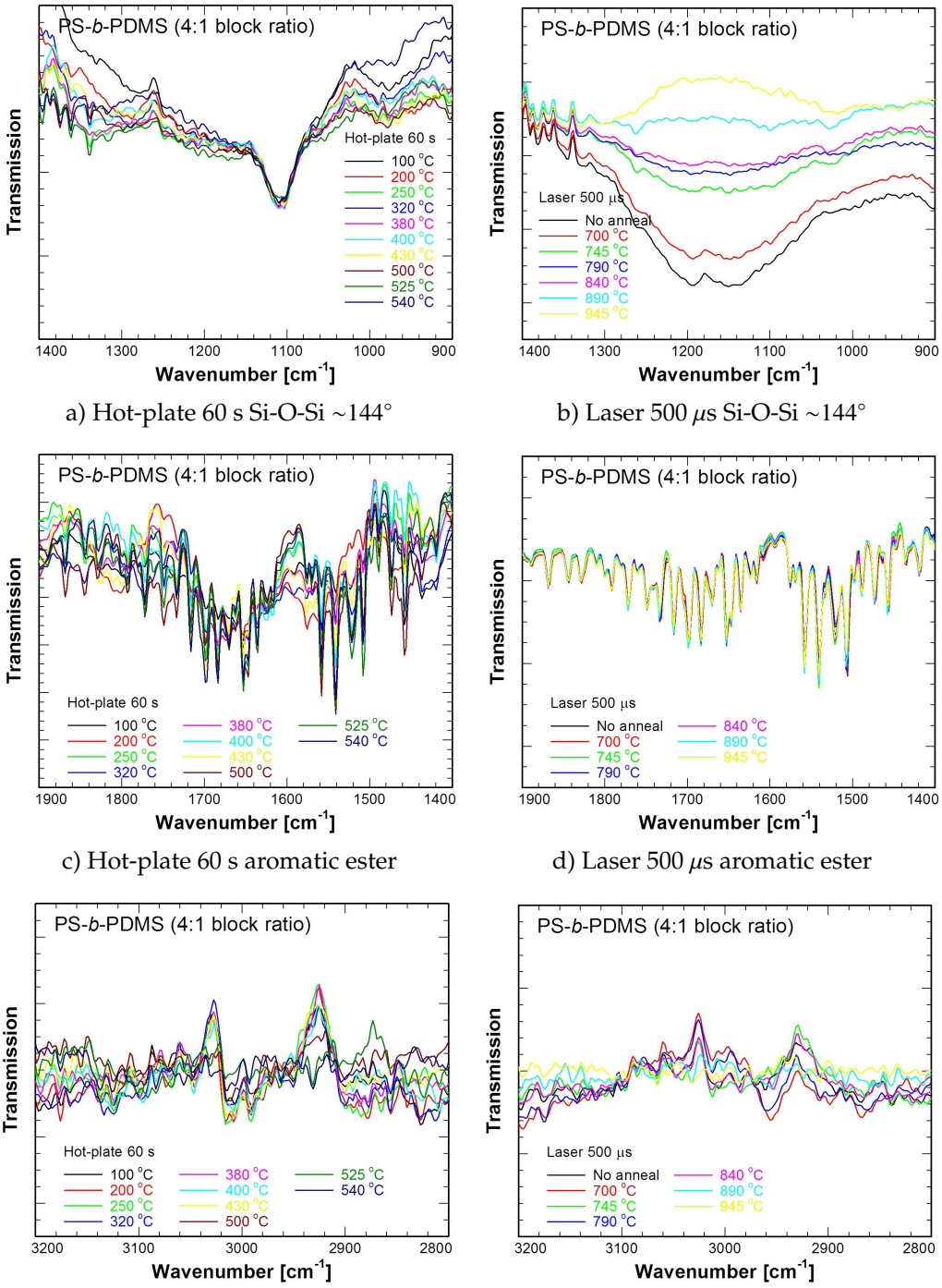

a) Hot-plate 60 s Si-O-Si ~144°

b) Laser 500 μs Si-O-Si ~144°

c) Hot-plate 60 s aromatic ester

d) Laser 500 μs aromatic ester

e) Hot-plate 60 s alcohol

f) Laser 500 μs alcohol

Figure B.10: FTIR peak comparison between hot-plate and laser heating for vibration stretches of a,b) Si-O-Si ~144°, c,d) aromatic ester, and e,f) alcohol for PS-*b*-PDMS (4:1 block ratio). All peaks decrease as a function of heating temperature.

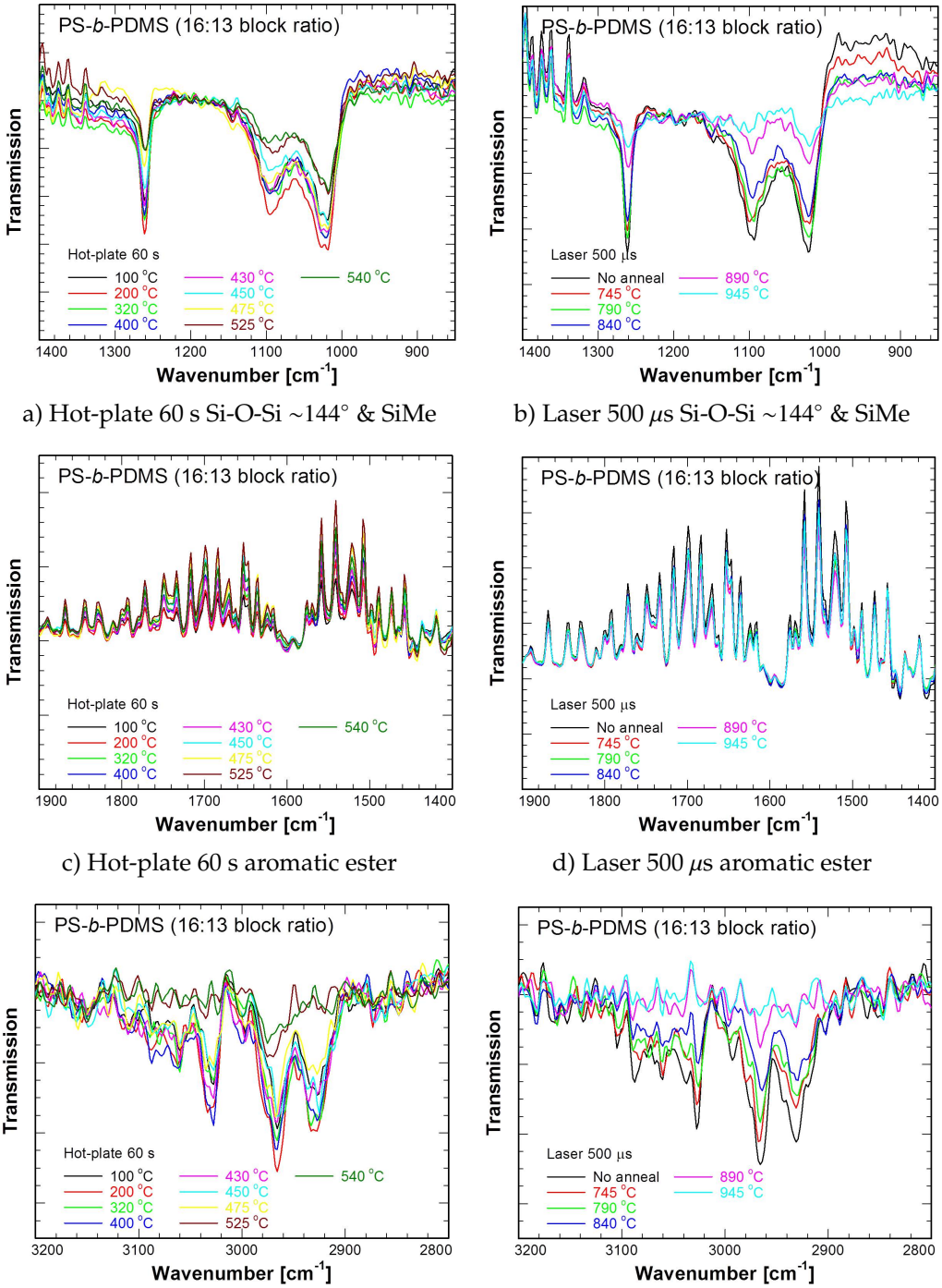

a) Hot-plate 60 s Si-O-Si ~144° & SiMe

b) Laser 500 μs Si-O-Si ~144° & SiMe

c) Hot-plate 60 s aromatic ester

d) Laser 500 μs aromatic ester

e) Hot-plate 60 s alcohol

f) Laser 500 μs alcohol

Figure B.11: FTIR peak comparison between hot-plate and laser heating for vibration stretches of a,b) Si-O-Si ~144° & SiMe, c,d) aromatic ester, and e,f) alcohol for PS-*b*-PDMS (16:13 block ratio). All peaks decrease as a function of heating temperature.

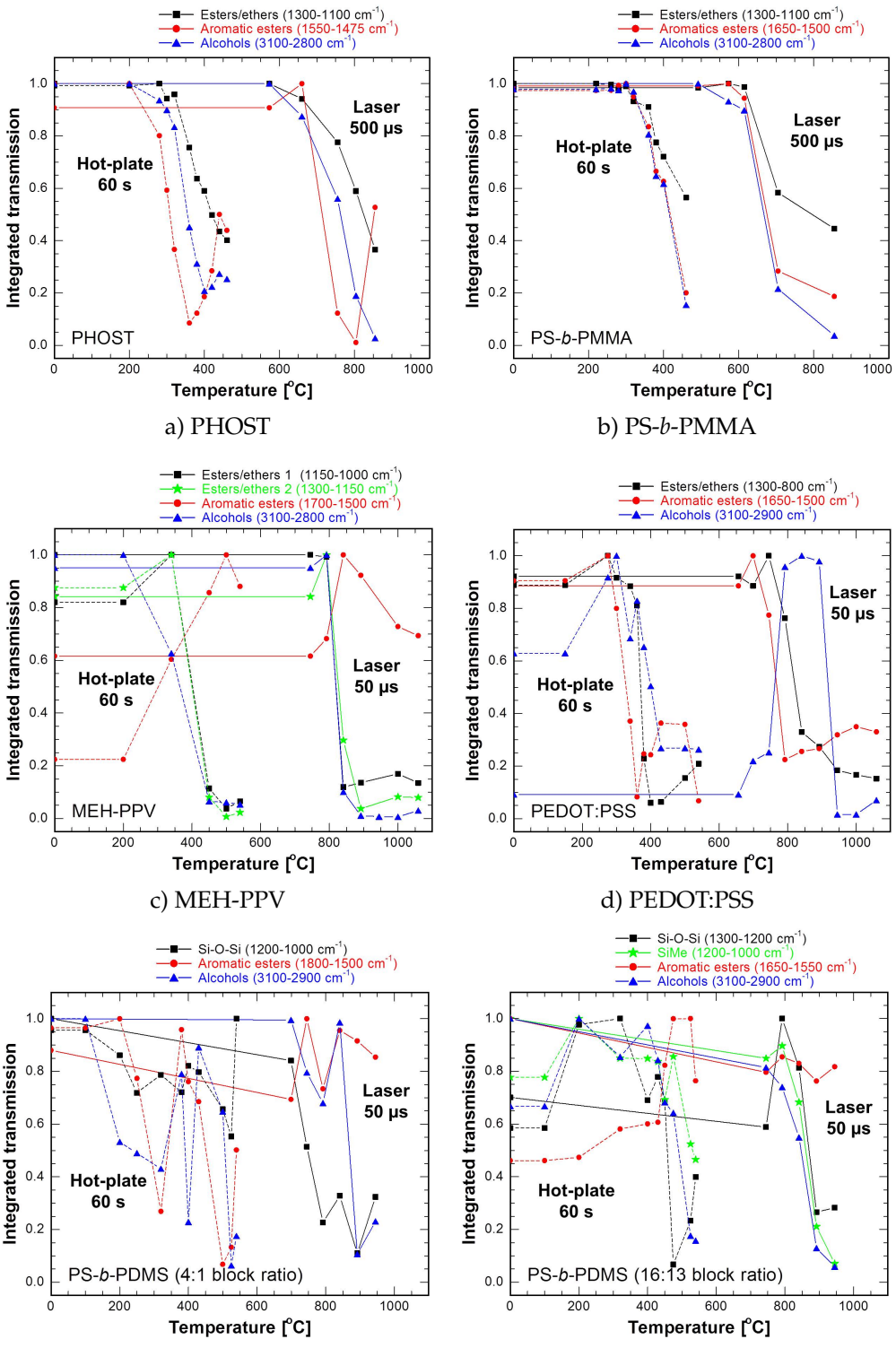

Figure B.12: Integrated FTIR peaks for a) PHOST and b) PS-*b*-PMMA, c) MEH-PPV, d) PEDOT:PSS, e) PS-*b*-PDMS (4:1 block ratio), and f) PS-*b*-PDMS (16:13 block ratio) resulting from a 60 s hot-plate or a 500 μs laser heating.

APPENDIX C

OPTICAL COUPLING OF CO_2 LASER TO RESIST THIN-FILM

In Chapter 4, sensitivity of chemically amplified resists and EUV resists showed up to 46 % enhancement using CO_2 laser at λ = 10.6 μm. This sensitivity enhancement corresponds to an accelerated deprotection kinetics at laser-induced high temperature (265-560 °C) compared to conventional hot-plate PEB temperatures (90-150 °C). Since the deprotection reaction is a thermally-activated process, this sensitivity enhancement under laser-induced high temperature is expected to be purely thermal. In addition to the thermal effect, an interaction between 10.6 μm (0.117 eV) photon and polymer's stretching and/or bending modes (at 943.4 cm^{-1}) may occur, resulting in an accelerated deprotection reaction through a direct photochemical effect.

To test this hypothesis, it was necessary to decouple the heating effect from the CO_2 illumination. The concept of the experiment was to use a conventional hot-plate to establish a PEB temperature while simultaneously illuminating the resist-coated substrate with 10.6 μm beam and inspect for IR-assisted PEB. The major challenge in the experiment was to minimize the sample heating induced by the CO_2 laser during the hot-plate PEB.

A 193 nm resist with THSb PAG (Figures 4.3b and 4.4b) was spun on an intrinsic Si wafer as a 100 nm film. The intrinsic Si wafer is essentially transparent to the 10.6 μm beam. The resist-coated wafers were exposed under UV light with dose gradient extending beyond the respective E_0 at 115 °C as schematically shown in Figure C.1a. To minimize the CO_2 laser-induced heating of the substrate, the CO_2 beam was expanded to an ~1 in diameter beam using a di-

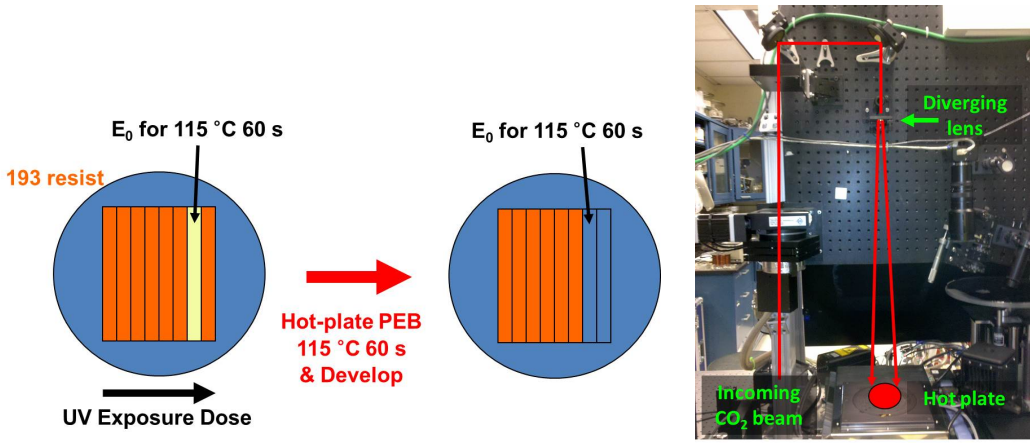

a) UV dose gradient on 193 nm resist b) Expanded CO_2 beam

Figure C.1: Experimental setup for IR-assisted deprotection. a) Schematic of intrinsic Si substrate coated with 100 nm of 193 nm resist with THSb PAG. b) Expanded CO_2 beam to minimize the laser-induced heating of the substrate.

verging lens as shown in Figure C.1b.

In addition to the expanded CO_2 beam, a brass sheet with 0.4 mm holes spaced by 1/8 inch (3.175 mm) over an 1 in^2 area was fabricated and placed on top of the wafer substrate to minimize the CO_2 transmission to ~1.6 % as schematically shown in Figure C.2.

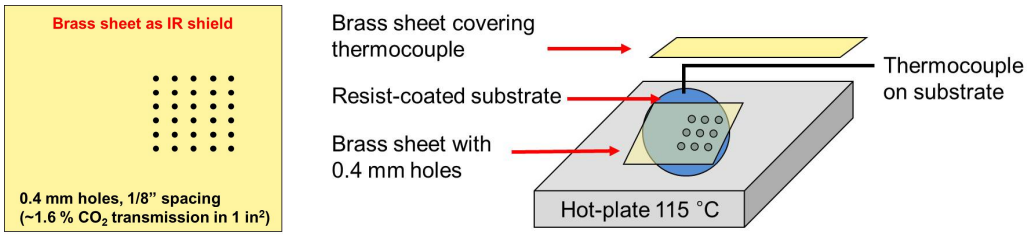

a) Brass sheet with holes b) Schematic experimental setup

Figure C.2: Schematics of a) brass sheet and b) experimental setup to minimize the CO_2 transmission onto the resist-coated substrate which results in the laser-induced heating of the substrate. Holes on the brass sheet allows selective transmission of the CO_2 beam.

The resist-coated substrates were heated on the hot-plate at 115 °C for 60 s to sufficiently induce the deprotection for UV dose at or greater than E_0, while simultaneously being exposed to CO_2 illuminations at power densities up to 20 W/cm^2. In addition to the thermocouple on the vacuum-chuck hot-plate, a second thermocouple was placed on top of the sample to measure the negligible sample temperature change (<1 °C) upon IR illumination. After 60 s of hot-plate heating with CO_2 illumination, the sample was removed from the hot-plate and developed in TMAH.

If resist deprotection was IR assisted, a series of holes would be expected within the regions deprotected by pure thermal process, as shown schematically in Figure C.3a. Conversely, no features would be expected if the deprotection was purely thermal. Figure C.3b shows a photo of the developed sample after 60 s hot-plate heating with CO_2 illumination at 20 W/cm^2. There was no evidence of any holes on the resist film suggesting that the sensitivity enhancement observed during laser PEB is purely a thermal effect. This result was confirmed using a second brass shield with wider holes (1/8 inch) to increase area of the CO_2 illumination.

CO_2 photochemical effects for power densities up to 20 W/cm^2 was shown to be non-existent. While resist film experience much higher power density (~65 kW/cm^2), multi-photon excitation of radicals is unlikely as the threshold power density for such effects is ~100 MW/cm^2.

For the 193 nm resist system, the sensitivity enhancement can be attributed to the trapping of the acid-catalyst that occurs only for the seconds duration hot-plate heating as addressed in Chapter 5. The trapping of the catalyst is bypassed using laser PEB either due to the thermal instability of the trap at high

temperature or insufficient time for trap formation in the sub-millisecond time frame.

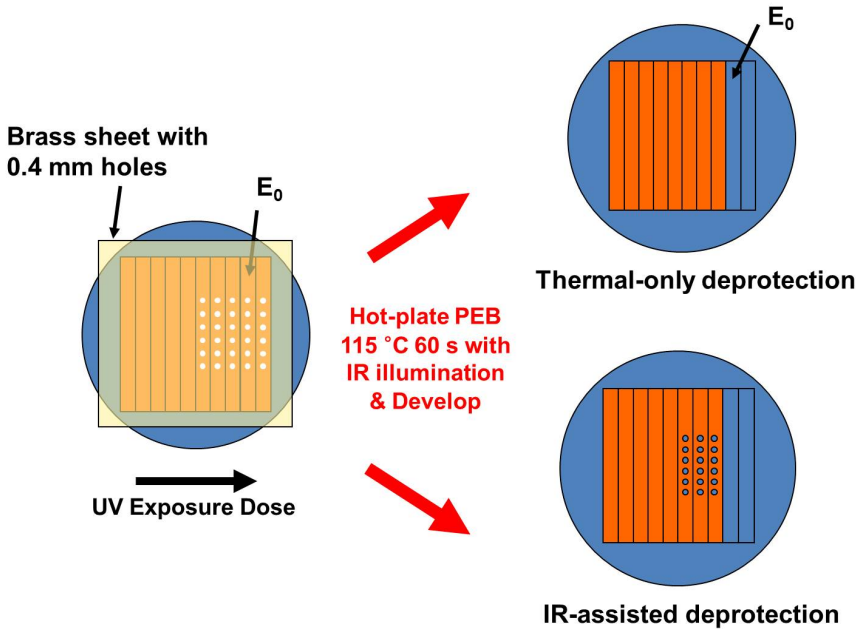

a) Thermal vs. IR-assisted deprotection

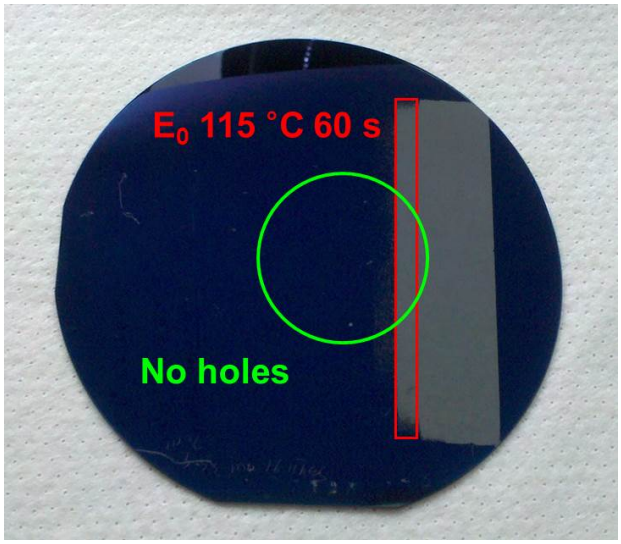

b) Sample after hot-plate & IR illumination

Figure C.3: IR-assisted deprotection experiment results. a) Concept and expectation between thermal-only deprotection or IR-assisted deprotection after 60 s hot-plate PEB with CO_2 illumination at 20 W/cm^2. For IR-assisted deprotection, additional resist removal is expected upon deprotection in areas without brass shield on top. b) Sample photo showing no additional holes on the resist film suggesting that the sensitivity enhancement during laser PEB is purely a thermal effect.

APPENDIX D

SUPPORTING EXPERIMENTS AND ANALYSIS ON 193 NM RESIST KINETICS

D.1 Plasticization effect on Bilayers

When THSb photo-acid generator (PAG) was introduced into a poly(MAdMA-*co*-GBLMA) resist matrix, a significant decrease in resist glass transition temperature (T_g) was observed. For 5 wt.% THSb addition w.r.t. the resist, a THSb concentration of interest for deprotection and diffusion studies, a ~50 °C decrease in T_g was observed (Figure 5.2b). For bilayer studies, THSb concentration in poly(MAdMA-*co*-GBLMA) matrix may increase the free volume and impact the acid motion, and hence it is critical to introduce PAG into the non-photoactivated layer.

Figure D.1a shows the conventional bilayer fabrication method which activates the PAG after the two layers are stamped together. In this configuration, there is no concern of photo-activation in the PAG-free bottom layer. Upon acid-generation and heating, however, the effective diffusivity occurs in a partially plasticized resist.

If PAG is added to the bottom layer, photo-activation must be prevented by exposing only the top layer before stamping, in order to properly analyze acid diffusion as schematically shown in Figure D.1b. Although more difficult to fabricate, proper "tracer-like" diffusion measurements can be performed with the top and the bottom layers identical.

A comparison of the two bilayer techniques is shown in Figure D.2, where

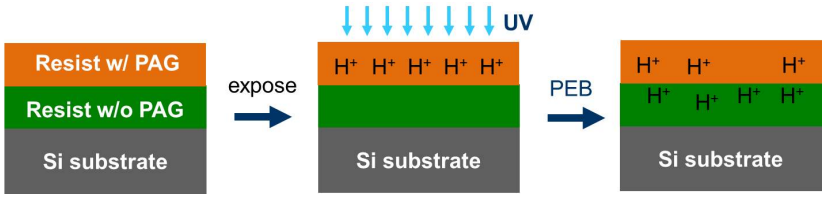

a) Conventional bilayer fabrication method

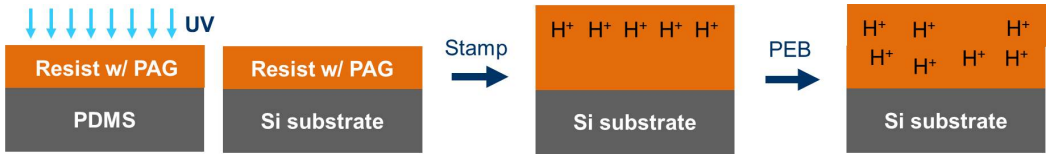

b) Improved (correct) bilayer fabrication method

Figure D.1: Bilayer fabrication method using a) conventional PAG-free bottom layer and b) PAG-containing bottom layer to ensure consistent acid motion in plasticized resist matrix.

solid curves represent bilayer analysis with PAG-containing top and bottom layers, while the dashed curve at 385 °C represents bilayer analysis with a PAG-containing top layer and a PAG-free bottom layer. For the conventional PAG-free bottom layer (dashed curve), the acid diffusion length increases in a "tailing" manner with increasing exposure dose (initial acid concentration), due to ongoing plasticization during the post-exposure bake (PEB). At the same PEB temperature, acid diffusion into the PAG-containing bottom layer, represented in the solid curve, does not show this behavior since the bottom layer is already plasticized. However, the final acid diffusion length for both curves becomes insignificant as local acid diffusion saturates in the chemical amplification scheme.

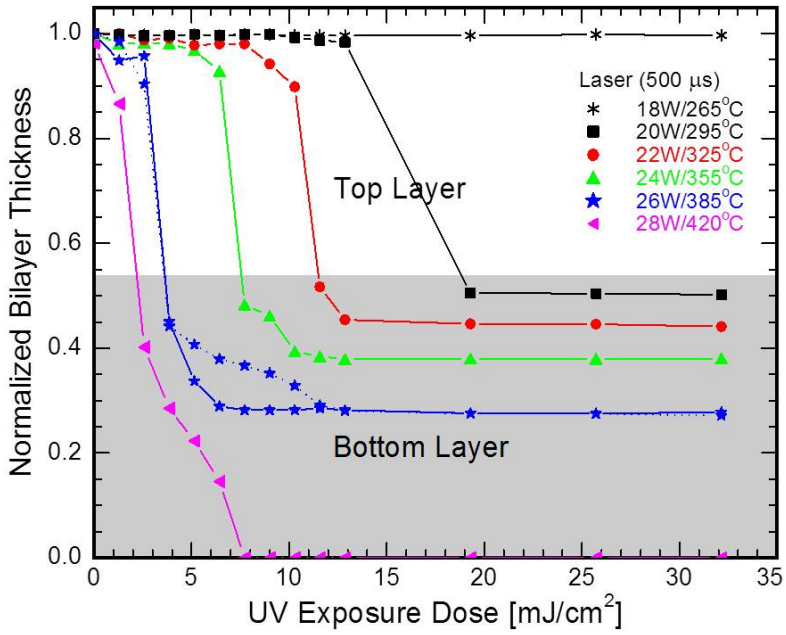

Figure D.2: Diffusivity measurements using bilayers of poly(MAdMA-*co*-GBLMA) with PAG-containing top/bottom layers (solid curves). At 385 °C, the corresponding curve from a PAG-containing top layer with a PAG-free bottom layer is shown as the dashed curve.

D.2 NMR analysis during decomposition of poly(MAdMA-*co*-GBLMA)

To identify the decomposition behavior of intrinsic poly(MAdMA-*co*-GBLMA) resulting in an intermediate thickness loss of ~60 % (Figure 5.4a), nuclear magnetic resonance (NMR) spectroscopy was used (Figure D.3). At temperatures of 210, 225, and 240 °C for 60 s heating, peaks corresponding to shifts in methyl adamantyl esters (~1.6 and ~1.7 ppm) and lactone esters (~4.4, ~4.6, and ~5.4 ppm) exhibit a steady decrease in intensity, suggesting the decomposition of less thermally stable acrylate components of the polymer. Beyond 300 °C, the poly(methyl methacrylate) backbone begins to decompose and forms

a poly(methacrylic acid) as shown by a shift in the peak from ~1.1 ppm to ~1.4 ppm.

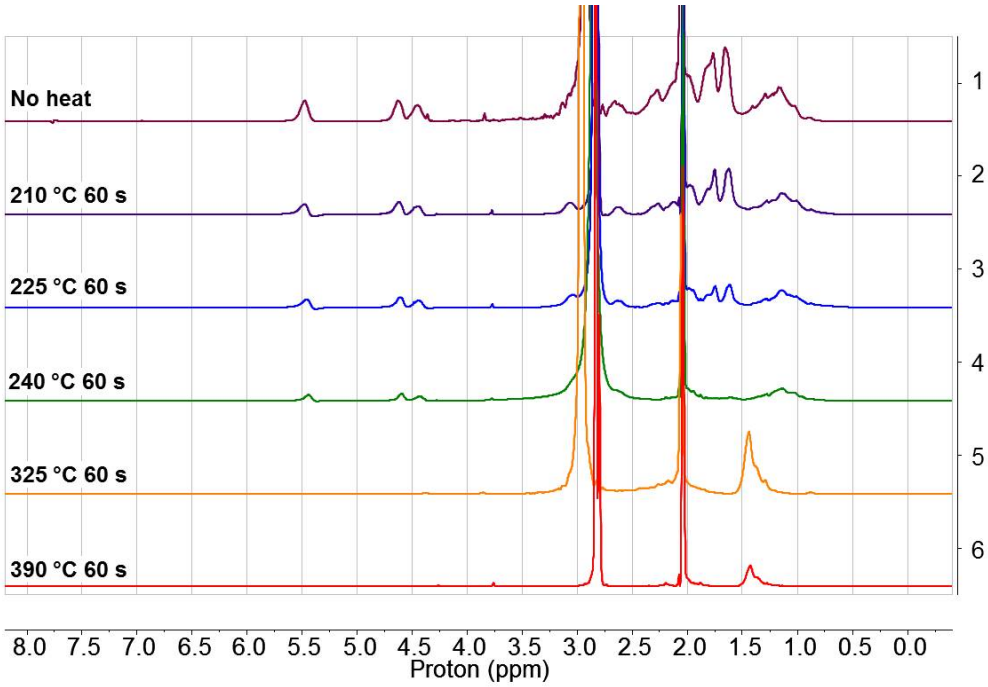

Figure D.3: NMR of poly(MAdMA-*co*-GBLMA) film as a function of heating temperature. For temperatures up to 240 °C, decomposition of both methyl adamantyl and lactone esters is observed. By 390 °C, the entire polymer including the backbone begins to decompose.

D.3 Fourier Transform Infrared Spectroscopy (FTIR)

To confirm the same acid-catalyzed side chain cleavage mechanisms between the hot-plate and laser PEB, the polymer film was analyzed using FTIR after heating. While no significant change in peaks were observed for C-C double bond stretching vibration (Figure 5.8), slight variations in the background peaks were observed near the ether stretching vibrations near 1100 cm^{-1} as shown

in Figure D.4. However, as bands assigned to C-C single bond stretch (1200-800 cm^{-1}) are generally weak and show little value for identification of the chemical structure, NMR spectroscopy and GC/MS analysis were used to identify changes during deprotection.

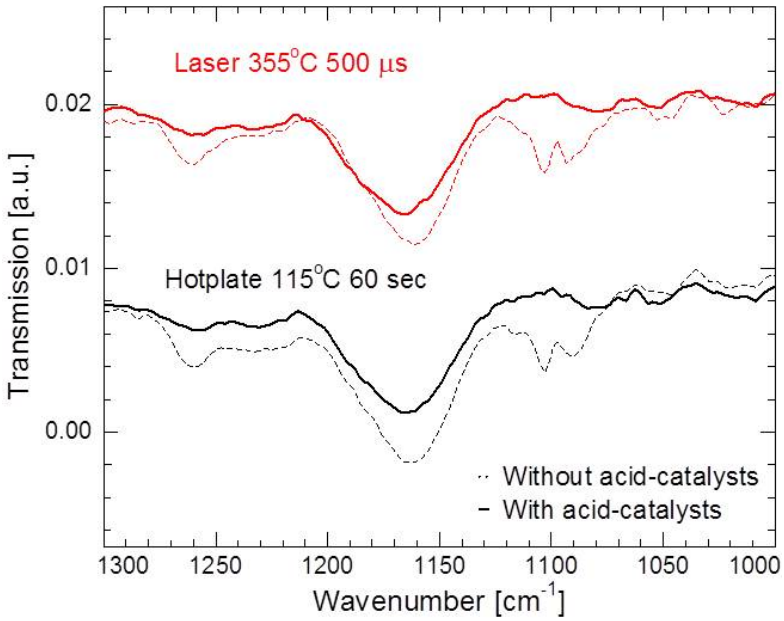

Figure D.4: FTIR spectra of poly(MAdMA-*co*-GBLMA) with and without acid-catalyst and cleaved side chains after hot-plate or laser-induced heating.

APPENDIX E

SUPPORTING INFORMATION FOR LASER HARDBAKE

E.1 Laser Hardbake on Additional Resist Systems

In addition to the temperature-sensitive hybrid polymer A analyzed in Chapter 6, two additional polymer systems were studied. One was an acrylate-based polymer where the deprotection mechanism involves conversion of esters along the polymer backbone into carboxylic acids. The other was a temperature-sensitive hybrid polymer B. The SEM images of the patterns before and after laser hardbake at 500 μs is shown in Figures E.1 and E.2 for acrylate-based polymer and hybrid polymer B respectively. For both polymer systems, the original pattern shows significant roughness on the edges before noticeable smoothing as the hardbake temperature increases.

E.2 Power spectral density of patterns at optimal hardbake conditions

For all patterns subjected to laser hardbake, the power spectral density (PSD) (Fourier amplitude as a function of spatial frequency of the line patterns) was analyzed and compared. Figure E.3 compares the line-edge roughness PSD of the original pattern with the hardbaked pattern at the polymer's optimal heating condition. This condition was chosen for maximum reduction in LWR with minimal CD change. While the shape of the curve is comparable before and after laser hardbake (confirming minimal CD change), original patterns show

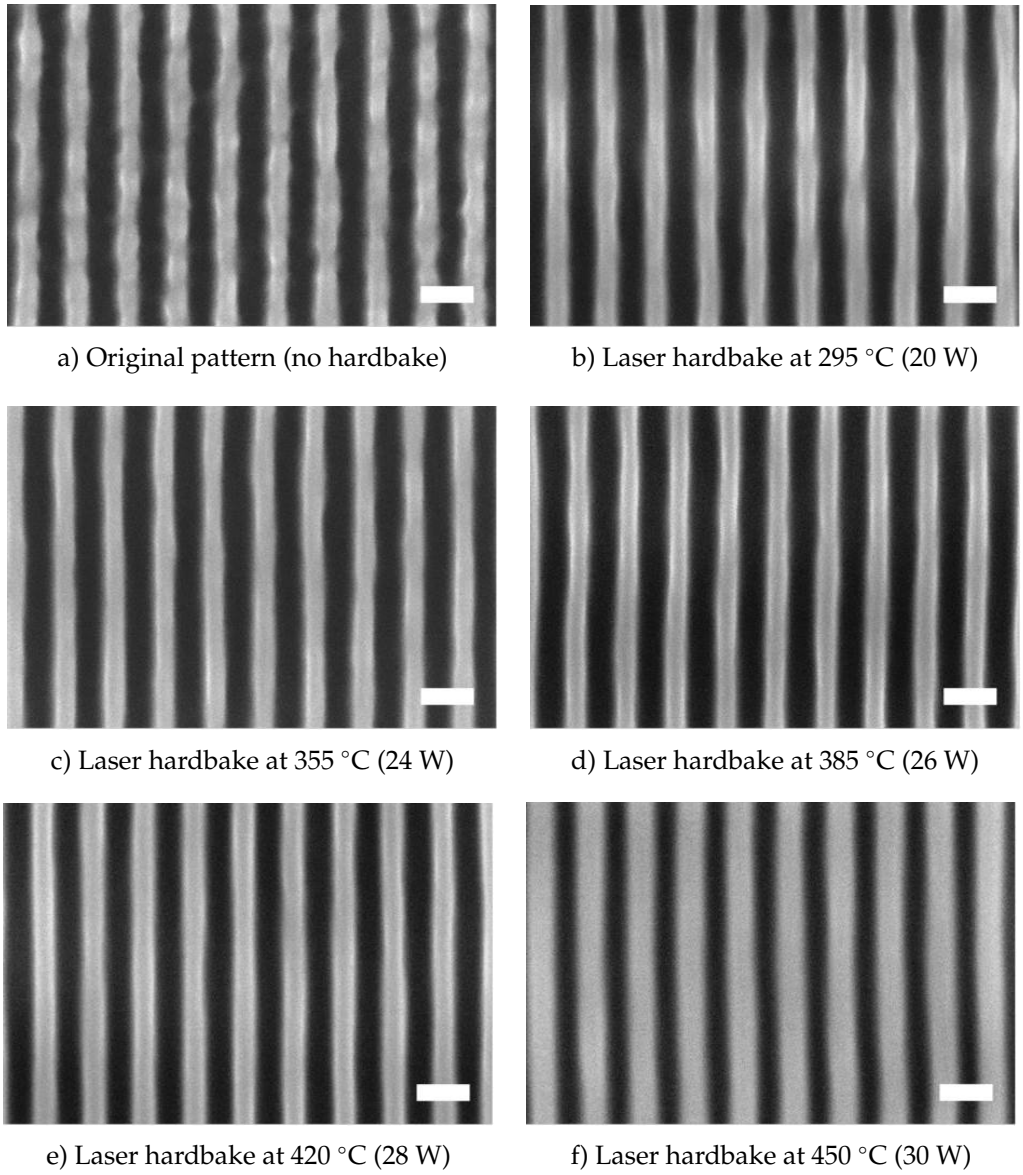

a) Original pattern (no hardbake)

b) Laser hardbake at 295 °C (20 W)

c) Laser hardbake at 355 °C (24 W)

d) Laser hardbake at 385 °C (26 W)

e) Laser hardbake at 420 °C (28 W)

f) Laser hardbake at 450 °C (30 W)

Figure E.1: SEM images of 30 nm line/space patterns generated in the acrylate-based resist polymer followed by laser induced hardbake for 500 μs. Images show a) original pattern, b) 295 °C, c) 355 °C, d) 385 °C, e) 420 °C, and f) 450 °C. While the original patterns show significant roughness on pattern edges, resist smoothing through polymer flow is observed for increasing hardbake temperatures. At 450 °C however, excessive flow is apparent. All scale bars correspond to 60 nm.

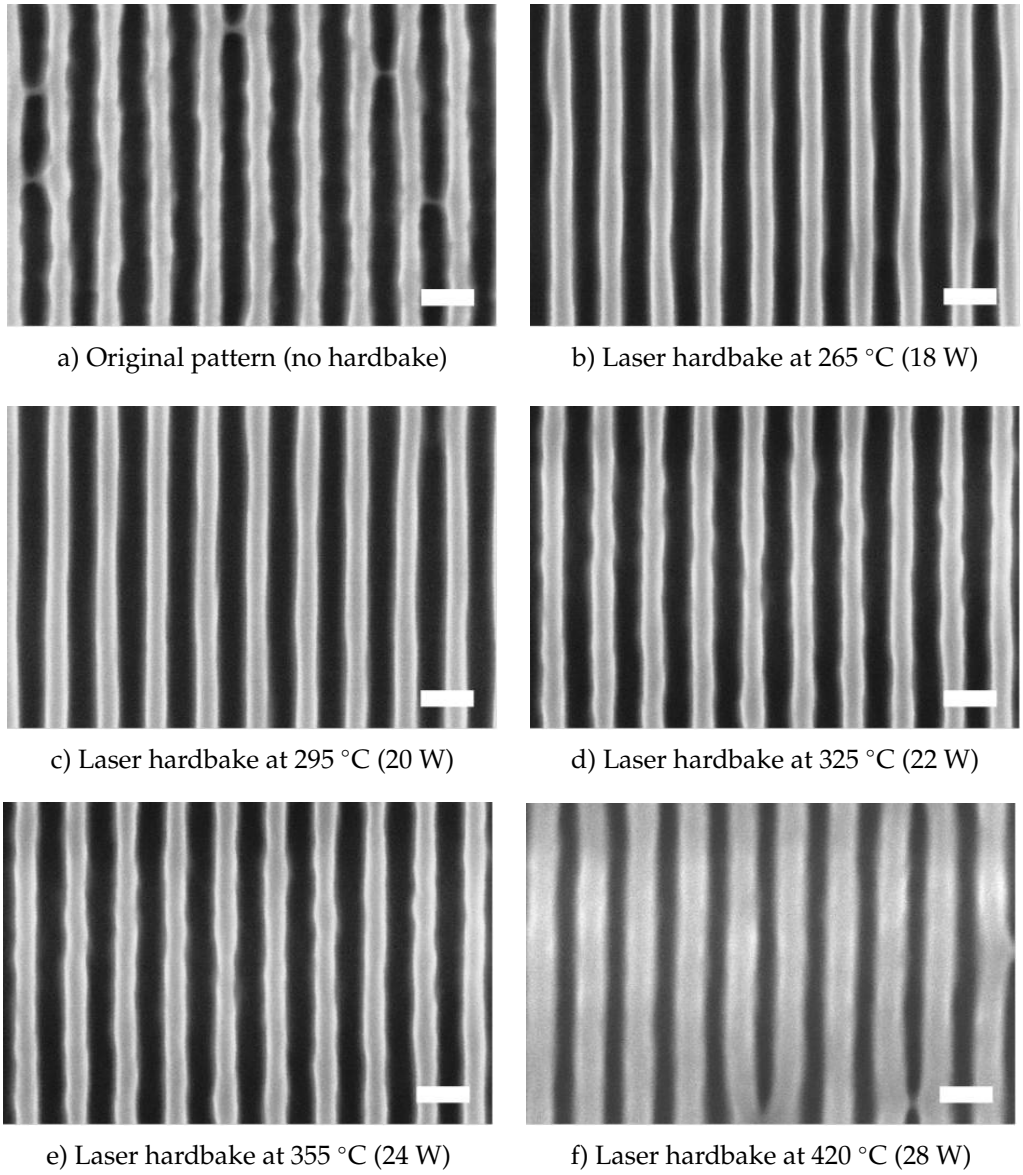

a) Original pattern (no hardbake)

b) Laser hardbake at 265 °C (18 W)

c) Laser hardbake at 295 °C (20 W)

d) Laser hardbake at 325 °C (22 W)

e) Laser hardbake at 355 °C (24 W)

f) Laser hardbake at 420 °C (28 W)

Figure E.2: SEM images of 30 nm line/space patterns generated in the hybrid polymer B followed by laser-induced hardbake for 500 μs. Images show a) original pattern, b) 265 °C, c) 295 °C, d) 325 °C, e) 355 °C, and f) 420 °C. While the original patterns show significant roughness on pattern edges, resist smoothing through polymer flow is observed for increasing hardbake temperatures. At 420 °C however, excessive flow is apparent. All scale bars correspond to 60 nm.

random peaks at low frequencies up to 10^2 μm^{-1} corresponding to the significant roughness on pattern edges which are reduced upon laser hardbake in PSD.

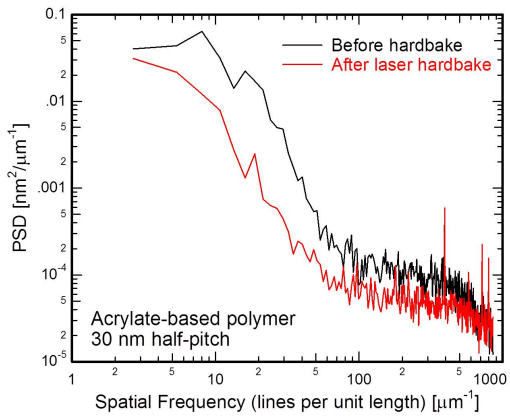

a) Acrylate-based polymer

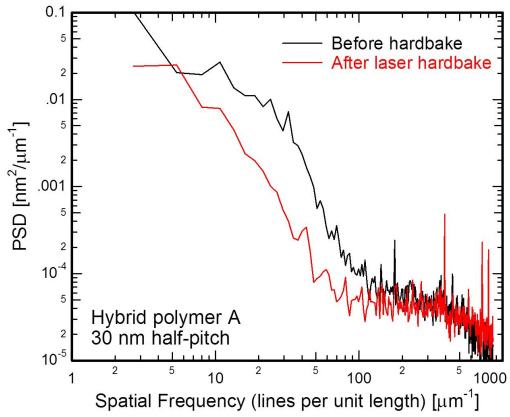

b) Hybrid polymer A

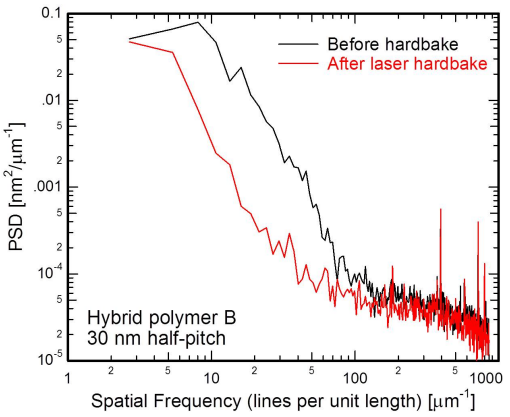

c) Hybrid polymer B

Figure E.3: Power spectral density (PSD) as a function of spatial frequency for three polymers before and after laser hardbake at optimal heating conditions. Compared to the original patterns, significant smoothing of the curve in the frequency range from 10-100 μm^{-1} confirms the roughness reduction while the similarity in PSD curve shape suggest minimal change to the overall CD.